

Nano- to catchment-scale investigations of metal
transport processes in mining-impacted river systems

Patrizia Onnis

A thesis submitted in partial fulfilment of the requirements of Liverpool John
Moores University for the degree of Doctor of Philosophy

October 2019

Dedicated to everyone who turned failure into a bittersweet power.

Abstract

Millennia of metal mining has left across the world an extensive physical legacy of contaminated mine waste and a substantial impact on the environment. In mining-impacted rivers, efforts to monitor metal mine contamination and remediation strategies to achieve good water quality are often of limited efficiency and success due to the variability of processes which control metal dispersion. This thesis aims to identify nano- to catchment-scale drivers of metal dispersion by: assessing the role of river catchment geomorphology in metal storage; quantifying metal sources across streamflow conditions; and investigating the metal-bearing nanoparticle flux in the river water.

This study investigated metal dispersion at the Nant Cwmnewyddion and the Nant Magwr, two rivers draining the abandoned lead and zinc mining area of Wemyss and Graiggoch Mines (central Wales). Sediment geochemistry and metal content were characterised and combined with river catchment geomorphological descriptions to identify areas of metal storage. A multi-tracer approach, which combined continuous tracers with slug (gulp) injections, allowed metal sources to be apportioned at a highly resolved spatial scale, enabling variations in metal load across streamflows to be accounted for. Metal-bearing nanoparticle flux was quantified using a novel, efficient sampling method and their size, morphology and chemistry characterised with a multi-method approach with the employment of several instruments.

The findings of this study suggest that river catchment geomorphology can influence on sediment geochemical processes (such as redox and dissolution), and highlight areas of metal source transformation. Descriptions of river catchment geomorphology can therefore be employed as a low-cost approach to initially identify potential metal sources and focus geochemical sediment analysis. The multi-tracer method successfully estimated point and diffuse metal source contributions throughout the river and across streamflows. These estimates were only possible due to the multi-tracer methods, therefore, the integration of this method in monitoring protocols is proposed for future studies of metal dispersal in rivers. Furthermore, the study provided important information concerning environmental nanoparticle chemistry, particle size distribution, and aggregation state within the river, allowing their role in metal transport to be better understood. In conclusion, this research extended the understanding of the spatial and temporal variability of zinc and lead dispersion mechanisms and showed the high potential of adopting a multi-method approach to apportioning metal sources at the catchment scale.

Contents

1. Introduction	1
1.1 Metal mining-impact on river systems	1
1.2 Metal dispersion drivers across catchments and streamflows	3
1.2.1 Metal presence in mining-impacted rivers	3
1.2.2 Geochemical and geomorphological drivers of metal dispersion	4
1.2.3 Metal source apportionment across streamflows	4
1.2.4 The role of nanoparticles in metal transport	5
1.3 Research aim, and objectives	6
1.4 Structure of Thesis	7
2. The local research context	8
2.1 Justification of the study site	8
2.2 The geographical and mining asset of the study site	9
2.3 Conclusions	14
3. Methods and Materials	15
3.1 Characterising soil contamination at the catchment scale	15
3.1.1 Sediment geochemical and mineralogical analysis	15
3.1.2 River catchment geomorphology	16
3.2 Monitoring streamflow variability and metal source apportionment	17
3.2.1 Streamflow definition	17
3.2.2 Streamflow estimation by continuous tracer injection	18
3.2.3 Streamflow estimation using slug injections	19
3.3 Waterborne nanoparticles sampling and analysing	21
3.3.1 Sampling protocol and nanoparticles storage time	21
3.3.2 Nanoparticle abundance, geochemical and morphological characterisation	23
3.4 Conclusions	26
4. Geochemical and morphological drivers of Pb and Zn release at the catchment scale	27
4.1 Introduction	27
4.2 Method and materials	29
4.2.1 Sampling description and grain size analysis	30
4.2.2 Sediment geochemical and mineralogical analysis	31
4.2.3 River catchment geomorphological description	32
4.3 Results	33
4.3.1 General observation and granulometric description of the sample sites	35
4.3.2 Metal sediment content distribution along the catchment	35
4.3.3 Proposed sediment mineralogy and related metals	39
4.3.3 River catchment geomorphological description	48

4.4 Discussion	50
4.4.1 Geochemistry of sediments along the catchment	50
4.4.2 Fluvial morphological control on Zn and Pb bearing minerals distribution	53
4.5 Conclusions	58
5. Source apportionment of Zn and Pb metal over the range of streamflows at the catchment-scale	59
5.1 Introduction	59
5.2 Method and Materials	61
5.2.1 Streamflow range definition	61
5.2.2 Streamflow estimation with the continuous tracer injection method	61
5.2.3 Streamflow estimation using slug injection method	64
5.2.4 Metal load analysis	65
5.2.5 Source apportionment	66
5.3 Results	67
5.3.1 Streamflow range definition	67
5.3.2 Spatial detailed streamflow variations along the river	67
5.3.3 Temporal streamflow variations along the river	68
5.3.4 General water chemistry and metal load variations	69
5.3.5 Metal source apportionment and temporal-spatial variations	70
5.4 Discussion	85
5.4.1 Zinc and Pb source apportionment across streamflows	85
5.4.2 Distribution and storage processes of Zn and Pb and their implication for remediation strategies	88
5.5 Conclusions	92
6. The role of environmental nanoparticles in metal transport in mining impacted rivers	93
6.1 Introduction	93
6.2 Methods and materials	96
6.2.1 Sampling protocol and nanoparticles storage time	96
6.2.2 Nanoparticle characterisation experiment	99
6.2.3 River water metal partitioning	102
6.3 Results	103
6.3.1 Evaluation of sampling procedure and storage	104
6.3.2 Particle size distribution – DLS and AFM results	105
6.3.3 Geochemical nanoparticle characterisation - TEM results	109
6.3.4 River water metal partitioning	113
6.4 Discussion	117
6.4.1 Optimal methods for fluvial sampling of nanoparticles	117
6.4.2 Nanoparticle size distribution variations along the river	118
6.4.3 Metal-bearing nanoparticle, source and transport along the river	120
6.4 Conclusions	123

7. General Discussion and Conclusions	124
7.1 Key findings and hypothesised processes	124
7.1.1 Point and diffuse source mechanisms and apportionment along the river	125
7.1.2 Point and diffuse source mechanisms and apportionment across streamflows	126
7.1.3 The role of nanoparticles in metal transport in river systems	127
7.1.4 General geochemical and hydrological processes driving Zn and Pb dispersion	128
7.1.5 Conclusions	130
7.2 Management implications of research findings	130
7.2.1 Water quality management and metal source apportionment	131
7.2.2 Sediment quality management and metal source investigation	132
7.2.3 The importance of metal-nanoparticles in remediation strategies	133
7.2.4 Conclusions	134
7.3 Final remarks and future directions	1352
7.4 Conclusions	136
Appendices	138
References	199

List of Figures

Figure 2.1	Geology and topography of the Nant Cwmnewyddion and the Nant Magwr. Source: DiGMapGB-50 [SHAPE geospatial data], Scale 1:50000, Tiles: ew178, Updated: 1 October 2013, BGS, Using: EDINA Geology Digimap Service (www.digimap.edina.ac.uk , Downloaded: 2016-06-03), modified with ArcGIS v.10.	10
Figure 2.2	Annual hydrograph of 2016 (a) and 2017 (b) station 63001 on the Ystwyth at Pont Lolwyn downstream the Nant Magwr confluence. Red and blue areas represent lowest and highest flows on each day over the period of record (NRF, 2019).	12
Figure 2.3	Monthly rainfall in Wales 2016 (blue) and 2017 (red) in millimeters (Met Office, 2020).	13
Figure 3.1	Curve of river water EC values after salt injection at 5 second interval. The bell-shaped curve shows smaller value in the sides and the peak in the central area. Slops are different, quick rise on left, first to the peak, and smooth slope on right, after the peak.	20
Figure 3.2	River water filtration system with prefiltration steps (63 and 1 μm), 0.45 μm water sample, followed by 10 kDa ultrafiltration for dissolved metals and centrifuged recovery.	23
Figure 4.1.	Map of the sampling areas along the Nant Cwmnewyddion and the Nant Magwr, the fluvial and glacial deposits and the mine areas. WM: Wemyss Mine; CW: tributary at Wemyss mine; TO: upstream the mine areas; GG: Graiggoch Mine; DC: depositional area at middle river length; RB: floodplain upstream (ups) and downstream (ds) areas. DiGMapGB-50 [SHAPE geospatial data], Scale 1:50000, Tiles: ew178, Updated: 1 October 2013, BGS, Using: EDINA Geology Digimap Service (www.digimap.edina.ac.uk , Downloaded: 2016-06-03), modified with ArcGIS v.10.	31
Figure 4.2.	Sampling area views. WM: Wemyss Mine with CW: tributary at Wemyss Mine; TO: upstream the mine areas. River paths is indicated with the blue dashed line. Graiggoch Mine with GG labeled samples. Depositional area at middle river length with 1 to 2 m river bank and percolating red water visible on the bottom left. Floodplain view of a meander corner. River flow direction is indicated by a blue arrow.	32
Figure 4.3.	Grain size percentage averaged for all the sampling areas from the upstream site WM until the most downstream RB d/s.	37
Figure 4.4.	Iron, Pb and Zn sediment concentrations in weight % along the river. Please refer to Figure 4.3 for a complete legend of the background image.	38
Figure 4.5.	Sample T0 M2, upstream mine site. a) Overview of the sample showing plant and shale fragments, angular and acicular minerals (quartz, phyllosilicate, rutile and zirconium) sometime agglomerate and cemented by a Fe-Oxide	41

paste. b) Detailed image of a phyllosilicate agglomerate cemented by a Fe oxide paste enriched in Pb bearing phases likely represented by anglesite, plumbojarosite and pyromorphite.

- Figure 4.6. Sample WM K4, Wemyss Mine tips. a) Overview of the sample showing angular and acicular minerals (monazite, rutile, feldspar and phyllosilicate) sometime agglomerate and cemented in 1 – 0.5 mm cluster. Any Pb or Zn bearing metals were observed in this area. b) Low brightness image of galena grains showing the cubical fractures. c), d) and e) Element map of the galena grain showing respectively Si, S and Pb intensity. 41
- Figure 4.7. Sample WM K4, Wemyss Mine tip. Detailed elementary maps acquired with Jeol8100 Superprobe (WDS) on an amorphous cement phase of Fe Oxide (Fe) enriched in Zn, Pb, S and Mn. Trapped and surrounding minerals are mainly represented by silicate (Si) and rutile (Ti). 42
- Figure 4.8. Sample CW J1, Mill Race headwater sediment. Detailed elementary maps acquired with Jeol8100 Superprobe (WDS) on a galena grain showing cubical fractures and weathered edges. Zinc, Co and Cd low levels of concentration are associated with the grain. 43
- Figure 4.9. Sample GG L1, Graiggoch Mine river bank sediment. On the right, mudstone grain with silicate and monazite minerals covered by Zn- bearing Fe oxides associated with pyromorphite (s.47). On the left, mineral phase of Mn and Pb oxide associated with low concentration of Fe, Zn, Cu and Co (s.44). 44
- Figure 4.10. Sample GG L1, Graiggoch Mine river bank sediment. a) Image of a anthropogenic fragment of fabric containing aluminium (s. 99) and copper fragments (s.96) surrounded by silicate minerals. Sn, Zn and Cr are associated with these metals and weathered phases. 45
- Figure 4.11. Sample DC E7, depositional area at the river middle length. Amorphous Fe-oxide cementation around silicate, rutile and sphalerite (s.46) minerals. Lead-sulfate (s.49) and trace amount of Ni, Cr and Zn are often associated to the Fe- oxide cement composition. 45
- Figure 4.12. Sample DC F2, depositional area at the river middle length. Overview of the riverbank sample collected at 60 cm above the river water level showing plant fragment, weathered detritus and bulk minerals. Grain of sphalerite (s.91) sometime associated with lead (s.88) are easily spotted in the sample. 46
- Figure 4.13. Sample DC F2, depositional area at the river middle length. Detail od Pb- and Zn- sulfur grains and weathering processes found in proximity of a fragment high in carbon concentration (S.109, S.117). On the right, EDS maps show S, Pb and Zn distribution. 46
- Figure 4.14. Sample DC F1d, depositional area at the river middle length. Details of a river bank sample collected at the water level showing well shaped galena minerals (s.64) and secondary minerals, likely anglesite and/or plumbojarosite (s.60) formed in the weathered detritus. 47

Figure 4.15.	Sample RB up/s C1, upper part of the floodplain. Detailed elementary maps acquired with Jeol8100 Superprobe (WDS) on a Fe oxide associated with Pb concentrations.	47
Figure 4.16.	Topography and slope map of the research site. Elaborated with ArcGIS from 1 meter resolution LIDAR images (Natural Resources Wales information ©).	49
Figure 4.17.	Wemyss Mine summary of sediment geochemistry and fluvial morphological parameters to identify the main processes driving Pb and Zn dispersion.	54
Figure 4.18.	Graiggoch Mine summary of sediment geochemistry and fluvial morphological parameters to identify the main processes driving Pb and Zn dispersion.	55
Figure 4.19.	Depositional area at the middle river length summary of sediment geochemistry and fluvial morphological parameters to identify the main processes driving Pb and Zn dispersion.	56
Figure 4.20.	Depositional area at the middle river length summary of sediment geochemistry and fluvial morphological parameters to identify the main processes driving Pb and Zn dispersion.	57
Figure 5.1	Tracer injection and slug sample sites along the Nant Cwmnewyddion and the Nant Magwr. Listed in red the distance from the injection site (T0, 0m) to the tracer transport (T1, T2, T3, and T4) and slug sites. WM: Wemyss Mine; MR: Mill Race; FA: Frongoch Adit; GG: Graiggoch Mine; DC: depositional area at middle river length; RB: floodplain upstream (up/s) and downstream (d/s) areas. DiGMapGB-50 [SHAPE geospatial data], Scale 1:50000, Tiles: ew178, Updated: 1 October 2013, BGS, Using: EDINA Geology Digimap Service (www.digimap.edina.ac.uk , Downloaded: 03-06-2016), modified with ArcGIS v.10.	63
Figure 5.2	Bromide concentrations (blue), streamflow estimations (orange) and relative error bars along the first 0-2614 m where 0 is the continuous tracer injection site (T0). WM: Wemyss Mine; MR: Mill Race; FA: Frongoch Adit; NC: Nant Ceunant; GG: Graiggoch Mine.	68
Figure 5.3	Streamflow maximum, minimum and average derived with the continuous tracer and slug injections.	69
Figure 5.4	Spatial profile of Zn, Pb, Fe and SO ₄ concentrations derived with the continuous tracer injection. WM: Wemyss Mine; MR: Mill Race; FA: Frongoch Adit; NC: Nant Ceunant; GG: Graiggoch Mine.	72
Figure 5.5	Spatial profile of pH (blue) and EC (orange) acquired during the continuous tracer injection.	73
Figure 5.6	Spatial profile of Zn, Pb, Fe and SO ₄ concentrations derived with the continuous tracer injection. WM: Wemyss Mine; MR: Mill Race; FA: Frongoch Adit; NC: Nant Ceunant; GG: Graiggoch Mine.	74

Figure 5.7	River segment contribution and attenuation percentages of Zn, Pb, and Fe derived with the continuous tracer injection.	77
Figure 5.8	Minimum, maximum, and average Zn concentrations along the river.	79
Figure 5.9	Minimum, maximum, and average Pb concentrations along the river.	80
Figure 5.10	Minimum, maximum, and average Fe concentrations along the river.	81
Figure 5.11	Minimum, maximum, and average SO ₄ concentrations along the river.	82
Figure 5.12	Total and cumulative Zn loads under low, moderate and high streamflow conditions.	83
Figure 5.13	Total and cumulative loads of filtered (a) and unfiltered (b) Pb under low, moderate and high streamflow conditions.	83
Figure 5.14	pH variations along the river across high (HF), moderate (MF) and low (LF) flows conditions.	85
Figure 6.1	The Nant Cwmnewyddion and the Nant Magwr map showing waterborne nanoparticle sampling site. Listed in red the sampling sites and distance from T0 (0m). GG: Graiggoch Mine; DC: depositional area at middle river length; RB: floodplain (upstream site). DiGMapGB-50 [SHAPE geospatial data], Scale 1:50000, Tiles: ew178, Updated: 1 October 2013, BGS, Using: EDINA Geology Digimap Service (www.digimap.edina.ac.uk , Downloaded: 03-06-2016), modified with ArcGIS v.10.	97
Figure. 6.2	Example of river water filtration with 63 and 1 µm pre-filters and 0.45 µm filter.	99
Figure 6.3	DLS size distribution by intensity for sample T0, T2, GG, DC and RB at week I (plain line) and week II (dashed line).	104
Figure 6.4	Table (on top) reporting the peak size (d.nm) and intensity (%) individuated manually in the DLS graphs of size distribution by intensity reported below (T0, T2, GG, DC and RB).	107
Figure 6.5	AFM results for sample T2, GG, DC and RB. a) Cumulative PSD curve expressed in percentage. b-e) Histograms of particle size distribution curve for T2 (b), GG (c), DC (d) and RB (e). Particles bigger than 24 nm are counted in the 24%.	108
Figure 6.6.	Zinc, Pb, Fe, Al, Mn, Cd and Co concentration (on the left) and load (on the right) partitioned as truly dissolved (filtered at 2.5 nm), nanoparticle (2.5-450 nm) and suspended particles (>450 nm).	114

List of Tables

Table 4.1	Metal concentration (g/kg) and pH values averaged for each transect, plus minimum (min), maximum (max) and average for the whole area. Suggested metal concentration limit are reported as TEL (threshold effect level) and PEL (predicted effect level) from the Environment Agency sediment quality guideline (2008).	36
Table 4.2	Iron, Pb and Zn concentrations of the 10 sediment samples selected for geochemical and mineralogical analysis.	39
Table 4.3	Lead concentrations of Wemyss and Graiggoch Mines from this study and previous literature (Palumbo-Roe et al, 2013 modified).	51
Table 4.4	Comparison of Zn and Pb total concentrations measured in river sediment in Wales and England (Byrne et al, 2010 modified).	52
Table 5.1	Inflow and seepage filtered Fe, Pb and Zn concentrations. Filtered and unfiltered concentration are reported for DC seepage. WM: Wemyss Mine; MR: Mill Race; GG: Graiggoch Mine; DC: depositional area at middle river length; LB: left bank inflow.	70
Table 5.2	River segment contribution to Zn, Pb and Fe load expressed in %. WM: Wemyss Mine; MR: Mill Race; FA: Frongoch Adit; NC: Nant Ceunant; GG: Graiggoch Mine; NG: Nant Gilvern; Forested: Areas with dense vegetation; Shaft: mining work area with shafts.	76
Table 5.3	Effective inflows and measured inflow concentrations (n.d. not measured value).	78
Table 5.4	Zinc and lead cumulative loads and attenuation percentages under low (HF), moderate (MF) and high flows (HF).	84
Table 5.5	Load contributions of Wemyss Mine (WM), Frongoch Adit (FA) and Graiggoch Mine (GG) and potential remediation effects at 2614 m on loads and concentrations of Zn and Pb. Values are calculated from continuous tracer injection loads estimated under moderate flow (30/07/2016, MF).	90
Table 6.1	Time frame of nanoparticle analysis at FENAC (Facilities for Environmental Nanoscience Analysis and Characterisation) laboratories carried out in September 2017.	100
Table 6.2	DLS results from main experiment at week I and week II. Z-ave: Z-average hydrodynamic diameter; SD: standard deviation; PDI: polydispersity index; Peak: intensity-weighted size distribution peak; *, <i>In range figure low</i> : instrument expert advice on result quality indicating the presence of large or sedimenting particles; ^, <i>Cumulative fit error high</i> : instrument expert advice on result quality indicating the sample is too polydispersed for cumulant analysis.	105

Table 6.3	AFM results for sample T2, GG, DC and RB. Reported are the number average, $N(z)$, calculate as $\sum n_i z_i / \sum n_i$ and weighted average, $S(z)$, calculated as $\sum n_i z_i^2 / \sum n_i z_i$ where “z” is the particle height and “n” is the number of particle; minimum (MIN) and maximum (MAX) particle values; polydispersity (P) equal to $S(z)/N(z)$; concentration of particle on the acquired images ($n/\mu\text{m}^2$).	108
Table 6.4	Description of particles from TEM image observations reporting morphology and potential mineralogy of T2 (a), GG (b), DC (c) and RB (d). The full list of images is reported in the Appendix 6.e.	111
Table 6.5	Partitioned loads of truly dissolved (filtered at 2.5 nm), nanoparticle (2.5-450 nm) and suspended particles (>450 nm).	116

Declaration of copyright

I confirm that no part of the material presented in this thesis has previously been submitted by me or any other person for a degree in this or any other university. In all cases, where it is relevant, material from work of others has been acknowledgment.

The copyright of this thesis rests with the author. No quotation from it should be published without prior written consent and information derived from it should be acknowledged.

Acknowledgement

I gratefully acknowledge receipt of a PhD scholarship, funded by Liverpool John Moores University.

I want to express my gratitude and appreciation to my director of studies Dr. Patrick Byrne for all the support and for his continuous motivation, help and guidance. I also want to thank my advisor Prof. Karen Hudson-Edwards for her valuable, constant and insightful comments which were essential in shaping this research; and my supervisors Prof. Tim Stott and Prof. Chris Hunt for their insightful comments and encouragement throughout key milestones of this research. Dr. Briant Kimbal, Dr. Rob Runkel, and Dr. Giovanni De Giudici are acknowledged for their precious advice in key stages of this research.

Special thanks to Hazel Clark and David Williams at Liverpool John Moores University (LJMU) for their crucial help during my first days in the lab and for their expertise throughout this work. I am sincerely thankful to Dr. Rob Allen, Dr. Nicola Dempster and Dr. Paul Gibbson and Dr. Phil Salmon that provided technical support. I grateful acknowledge all the people who helped me in the field and lab work, especially George, Dario, Ilaria, Lewis, Silvia, Emanuele, and Christine. Furthermore, I would like to thanks Natasha for helping with the sediment sampling and the pXRF analysis.

My sincere thanks also goes to Dr. Christine Elgy, Prof Eugenia Valsami-Jones, and Ben who provided me an opportunity to join their team as intern, and who gave access to the laboratory and FENAC facilities. Without they precious support it would not be possible to conduct this research. NERC and CEH are gratefully acknowledged for funding the FENAC grant.

I would like to thank all the people from the Natural Resources Wales that provided me all the information on the study site. Special gratitude to Tom Williams, Paul Edwards and Peter Stanley. Richard and Johns, whom became an importance source of support and help during this research, granted access to privately owned land in the study area.

I thank my dear friends and supporters Ilaria Frau, Dr. Christine Hamilton, and Dr. Tim Lane for their constant advice, critiques, proof reading, laughs and moral support. Another thank you goes to my friends Lorena Zara, Marta Fiacconi, Silvia, Daniel, Le Nane and my son Ignazio for checking constantly on my mental health and research progress.

I am extremely grateful to my family for their love and constant support while dealing with the distance. Last but not the least, I would like to thank you Dario who sustains me every day.

Lot of other people contributed to this research and supported me. I would not be here and achieved so much without you all. Thank you!

Chapter 1. Introduction

1.1 Metal mining-impact on river systems

Metal exploitation started during the Bronze Age and carries on today due to its essential role in our life. The environment is adversely impacted by the contaminated mine wastes resulting from historical mining activities. Some of the first documented evidence of mine waste impacts in the UK was reported by the River Pollution Committee (1874). It describes *poisonous slimes* destroying vegetation, killing livestock and making river banks more susceptible to erosion. In recent decades, the environmental impacts of mining activities has received increased attention, with several studies reporting high concentrations of contaminants (such as Zn, Pb and Cd) and acidity associated with mine wastes (Johnson and Hallberg, 2005, Nordstrom, 2009).

Mine wastes are heterogeneous materials consisting of ore, gangue, industrial minerals, metals, coal or mineral fuels, ash, processing chemicals, and fluids, including waters used in the mining process (Kossoff et al., 2014). In the past, crude and inefficient mining techniques produced metal-enriched mine waste that may release contaminants. Most of the mine working and wastes are located along streams, and as a result they represent the volumetrically largest waste streams in the world (Hudson-Edwards et al., 2011).

Contaminated waste in sediment and water is easily mobilised by geochemical and geomorphological processes (Nordstrom, 2011a). Mine wastes are eroded and transported along the river channels, and deposited in channels or in alluvial valleys (Lewin and Macklin, 1987). Metal-bearing minerals are dispersed in the river system and constitute potential sources of contaminants for the ecosystem, via sediments, water or organisms (Dennis et al., 2009). By the end of this century, metal dispersion from historical mining is very likely to increase as extreme rainfall events are predicted to become more frequent as a consequence of climate change (IPCC, 2013). Heavy rainfall and large floods are forecast to erode mine tips and rework contaminated floodplains at a higher rate than that at present (Foulds et al., 2014).

Metal contamination and remediation strategies are current worldwide challenges (Naidu et al., 2019), with numerous nations introducing standard quality guidelines (Byrne et al., 2010). In 1992 at the Oslo-Paris Convention (OSPAR), countries bordering the north-east Atlantic reported that the flux of metals at the tidal inlets of large rivers can provide a way to monitor freshwater contaminations and their interactions with marine habitats (OSPAR, 2019). Governments monitoring land pollution and the interaction with tidal environments have collected water data

following standard procedures, and produced a database (Mayes et al., 2013). The EU, with the Water Framework Directive (2000/60/EC) and the EU Dangerous Substances Directive (76/464/EEC), focus their attention on reaching good water quality standards. From 2000, they imposed EU environmental quality standards (EQS) to reach good chemical and ecological status by 2015 or, if failed, by second and third management cycles ending respectively in 2021 and 2027 (European Commission, 2012). Concerning sediment quality, there are currently no EU guidelines regarding river bed sediments. In the UK the sediment environmental quality (SEQS) and assessment procedures have been introduced to control the total metal concentration in the sediment (Environment Agency, 2008a).

Water and soil quality guidelines have amplified attention to the monitoring and remediation of mine wastes. Nowadays, mining companies are decreasing their impact on the environment by reducing the amount of waste, stabilising contaminated sediments and recycling wastewater in the mining process (Hudson-Edwards et al., 2011). The importance of managing historical mine waste in river ecosystems has been recognised (Byrne et al., 2010); research focuses on remediation procedures and technologies that are designed to limit the impact of contaminated mine wastes (Mayes et al., 2008). These can be categorised into active and passive treatments, and physical stabilisation technologies (Byrne et al., 2012). Active treatments use electrical energy and require maintenance and particular set-up procedures whilst passive remediations use natural energy (topographical gradients and metabolic energy) and are, as a result, less expensive (Skousen et al., 2017). To reduce sediment dispersion, physical stabilisation technologies, such as capping procedures or phyto-stabilisation, have been developed (Tordoff et al., 2000). However, these strategies tend to be limited as the extent of metal mine sources or metal load variations across streamflows is often unknown.

River systems affected by historical mining can release a significant amount of metals from diffuse sources, preventing the good quality status of water and soil (Mayes et al., 2008). Diffuse sources include waste piles leached by run-off or eroded diffuse seepages, contaminated groundwater, and hyporheic zones, and re-mobilisation of a contaminated river bank or bed sediments stored in river channels or floodplains (Jarvis et al., 2006, Gandy et al., 2007). Dispersion of metals from diffuse sources depends on geochemical processes at the micro- and nano-scale (metal-bearing mineral dissolution or precipitation, interactions among metals, water, and organic or inorganic surfaces) and at the catchment scale (streamflow variations, hyporheic and groundwater interactions, contaminated sediment transport) (Nordstrom, 2011a). Knowledge of the metal contribution from diffuse sources is of imperative importance to ensure remedial works are effective. However,

apportioning metal source apportionment and understanding the mobilisation of metals can be difficult to accomplish (Gozzard et al., 2011).

1.2 Metal dispersion drivers across catchments and streamflows

Determining the apportionment of metal sources is difficult to achieve due to multiple, temporally variable, processes occurring at the nano- to catchment scales. Metals in mining areas are sourced by the mineral ores, weathered by geochemical processes and dispersed through the river system by geomorphological processes (Hudson-Edwards et al., 2001). Once released in the water, metals contribute to the river metal load, the extent of which is dependent on streamflow conditions (Cánovas et al., 2018). Furthermore, metal water transport can occur in dissolved phases (ions) or as metal-bearing phases of various nature and size (few nanometres to several micrometres) (Plathe et al., 2013). Therefore, a multi-disciplinary approach is essential to providing a more complete understanding of the processes driving metal dispersion and to quantify metal source contribution.

1.2.1. Metal presence in mining-impacted rivers

Sulfides (such as galena, sphalerite, and pyrite) are the primary minerals occurring in the mined ore. Their oxidation and dissolution can enrich solutions in metals and in some cases decrease the pH. The mineral weathering rates depend on various factors such as water chemistry, pH and electrical conductivity (EC), biological influences and mineral size (Nordstrom, 2009). Metals can be transported in the water or stored in mineral phases such as carbonate, silicate, phosphate and sulfate (CSPS) minerals or Fe- and Mn-oxyhydroxides (Hudson-Edwards et al., 1996, Hammarstrom et al., 2005). Zinc tends to stay in solution under circum-neutral pH (Lee et al., 2002); it can be temporarily stored in bio-precipitation (Medas et al., 2012), adsorbed on organic matter, clay minerals and Fe- and Mn-oxyhydroxides, or exchanged with carbonate minerals (Cravotta, 2008, Van Damme et al., 2010). These reactions are reversible and observed during diurnal Zn cycles (Frau et al., 2012, Nimick et al., 2011). Compared to Zn, Pb is more sediment-bound (Zhu et al., 2007). Lead is often found associated with Fe- and Mn-oxyhydroxides and CSPS minerals (Lynch et al., 2018); its adsorption is highly influenced by soil pH and the organic ligand concentration (Yang et al., 2006). A variety of metal-bearing minerals are found along the river systems, therefore, a geochemical and mineralogical sediment analysis extended to a catchment scale provides information about weathering reaction, mineral parageneses and potential metal release (Hudson-Edwards et al., 1998). The geochemical settings where metal-bearing minerals are formed (controlled by pH, EC, and water or sediment chemistry) can change across space and time due to

geomorphological processes (passive dispersal and active transformation) (Miller, 1997) and hydrological processes (pore water saturation, river water level, flood or drought events) (Lynch et al., 2014).

1.2.2 Geochemical and geomorphological drivers of metal dispersion

Sediment metal concentrations can decrease downstream due to dilution by uncontaminated sediment, hydraulic and density sorting, re-mobilization of polluted sediment and geochemical processes (Miller, 1997). However, they can also increase due to chemical mobilisation and metal-enriched inflows (tributaries, hyporheic water, and groundwater) (Hürkamp et al., 2009, Palumbo-Roe et al., 2012). Sediment dispersion is ruled by morphological degradation and aggradation processes which can change the distribution of sediment load along the stream (Miller, 1997). Sediment erosion at the mine tips can be exacerbated by a lack of vegetation on the slope due to its phytotoxicity (Tordoff et al., 2000). Sediments are distributed along the stream channels in areas with low slope gradient, re-worked during floods (Palumbo-Roe et al., 2016) and deposited on floodplains (Dennis et al., 2009). The stability of precipitated phases and element mobility varies along the river system. Generally, geochemical parameters, such as pH and redox, depend on water presence, pore water chemistry, temperature, mineralogy and fluvial morphological features (Lynch et al., 2014). The physical and chemical dynamics of the hyporheic zone are influenced by its sedimentology (grain sorting and size, clay and organic matter presence), geology (lithology and structural patterns), geomorphology (streambed topography, slope) and hydrology (water flows, permeability) (Macklin et al., 2006, Brown et al., 2007). Processes that occur in the hyporheic zone, such as acid-base and redox reactions, precipitation, dissolution, and sorption (Larson et al., 2013), can trap or release metals (Palumbo-Roe et al., 2013). River catchment geomorphological factors, such as topography, slope, grain size and landscape parameters (vegetation and aggradation or degradation processes) influence water path and sediment load transport, and, therefore, geochemical parameters (redox and pH variations). As a consequence, investigation of geomorphological factors together with sediment geochemistry is a fundamental step to understand metal-sediment borne distribution and storage at the catchment scale.

1.2.3 Metal source apportionment across streamflows

The contribution of metal sources to the river metal load varies with streamflows (Gozzard et al., 2011). In river water, high metal concentrations are usually observed under low flow conditions and after the first rainstorm following a dry period due to high volumes of water flushing soluble

secondary minerals into the river channel (Nordstrom, 2009). Furthermore, high flow events can increase metal mobility representing a hazardous situation for organisms (Gutierrez et al., 2016).

The geochemical and physical variables impacting on metal release are influenced by streamflows. Firstly, metal-bearing minerals should be present in the area and contain a sufficient amount of metals (Nordstrom, 2011). The soil moisture level and the geochemical conditions, such as redox and pH, can control mineral dissolution rate, or metal de-adsorptions (Lynch et al., 2014). Water flow paths, such as translator flows from the river bank and upwelling through the hyporheic zone, can transport metals with greater magnitude during high flow conditions (Byrne et al., 2013). Several studies have tried to quantify metal source contributions but encountered limitations when diffuse sources are present (Mighanetara et al., 2009, Gozzard et al., 2011). Conversely, studies which identified spatial patterns of metal load contribution stressed the limitation due to streamflow variability (Runkel et al., 2013). However, apportionment of point and diffuse metal sources at a catchment scale and across streamflows are fundamental to prioritise remediation strategies and reach good water status.

1.2.4 The role of nanoparticles in metal transport

Natural nanoparticles can form via weathering (rock and mineral mechanical or dissolution/precipitations processes), in river water or as a result of volcanic and hydrothermal activities, and human activities (including mining operations) (Sharma et al., 2015). These particles can vary in size (few to thousand nanometers) and compositions (inorganic, organic or a mixed composition) (Buffle et al., 1998). The importance of nanoparticles in metal dispersion has been recognised in the literature (Hochella et al., 2008, Vasyukova et al., 2012); in mining-impacted river systems nanoparticles have been observed to both bear and transport metals (Wigginton et al., 2007, Plathe et al., 2013). Nanoparticle mobility, and in general aggregation, dissolution and transformation processes, are influenced by pH, ionic strength and aqueous or solid-phase chemistry (Sharma et al., 2015). Metal-nanoparticle interactions are potentially controlled by nanoparticle morphology, chemical composition, and abundance (Baalousha and Lead, 2007).

Monitoring water quality filters of 0.45 or 0.22 μm are employed to separate particulate phases from 'dissolved elements'. Generally, metals contained in the dissolved phases are considered more bioavailable than those bound to the particulate phases. Although, particles can pass through these filters and show their own toxicity, bioavailability and chemical properties (American Public Health et al., 2005, Baun et al., 2008). Consequently, metal transport and chemistry linked to metal-bearing particles included in the 'dissolved fraction' have been underlooked.

Studies encounter limitations in designing efficient sampling and storage techniques that preserve nanoparticle stability and avoid aggregation, precipitation, adsorption on other phases or dissolution (Pokrovsky et al., 2010, Lapworth et al., 2013). In addition, analysis of nanoparticle properties, such as abundance, morphology, chemistry, requires a multi-method approach that utilises several instruments (Baalousha and Lead, 2012). Therefore, natural nanoparticle studies still encounter complexity in understanding their role in metal dispersion and quantification of the metal-bearing nanoparticle flux in river systems.

1.3 Research aim and objectives

The existing literature provides invaluable knowledge on metal dispersion processes in metal mine-impacted river systems. However, efforts to control metal mine contamination encounter limited efficiency in attempting to reach good quality in river water. Thus, it is clearly evident that gaps in understanding and quantifying metal sources, dispersion and transport are still present.

The overall AIM of this thesis is to investigate nano- to catchment-scale drivers of metal dispersions and metal source apportionment under different streamflow conditions.

Understanding metal drivers in mining-impacted rivers involves studying the transport mechanisms and metal dispersion processes occurring at multiple scales. At a catchment scale, it remains unclear the role that river geomorphology plays in enhancing geochemical settings where metals can be stored or released. In addition, due to the unknown location of metal sources and complex hydrology, accurate metal source apportionment across streamflows cannot be accomplished with current methods. Furthermore, several studies suggest that nanoparticles transport metals, but previous investigations have not been sufficiently detailed to quantify the associated metal flux and provide a comprehensive nanoparticles characterisation at a catchment scale.

This aim is investigated by the following OBJECTIVES:

- 1) to identify the role of soil geochemistry and river catchment geomorphology in metal storage (Chapter 4);
- 2) to quantify metal sources in mining-impacted rivers under different streamflow conditions (Chapter 5);
- 3) to investigate the role of nanoparticles in transporting metals in mining-impacted rivers (Chapter 6).

1.4 Structure of the Thesis

The background and rationale of the research are presented in Chapter 1. The site description is presented in Chapter 2 and a general review of the field and laboratory methods is provided in Chapter 3.

A specific literature review and method descriptions are presented for each data chapter, together with relative results and discussions. Chapter 4 describes the research investigating the role of catchment morphology and soil geochemistry in metal storage. Chapter 5 details the study on metal source apportionment across streamflows. Chapter 6 presents the study on the role of nanoparticles in transporting metals in mining-impacted rivers. Finally, Chapter 7 summarises and discusses the key findings in relation to some of the wider issues surrounding metal mine contamination and management.

Chapter 2. The local research context

2.1 Justification of the study site

The study site is the river system that drains the Wemyss and Graiggoch Mines in central Wales, UK (Figure 2.1). These former Zn and Pb mines are drained by the Nant Cwmnewyddion which flows east to the Nant Magwr and then into the Afon Ystwyth. This area contains examples of historical metal mines that are a testimony to centuries of ore exploitation that occurred worldwide in the 18th to 20th centuries (Hudson-Edwards et al., 2011, Byrne et al., 2017). In the UK, metal-enriched veins were exploited from the Bronze Age (Environment Agency, 2008b), with metal extraction and export occurring extensively till the 1920s when metal prices decreased and new large ore bodies were found in Australia, South America and the Iberian Peninsula (Lewis and Macklin, 1987). Approximately 3,000 abandoned mines remain in the UK, with over 1,000 located in Wales (Environment Agency, 2002, Jarvis et al., 2008).

Significant quantities of metals remain in the mine wastes, which can be mobilised and transported from the mine spoil into catchments (Macklin et al., 2006). In Wales and England, metal mines are thought to release at least 193 tons of Zn and 18.5 tons of Pb into the Atlantic annually (Mayes et al., 2010). Generally, the metal loads appear to be positively correlated to the drainage area of their associated river basins. Among the exceptions are the Afon Ystwyth and Goch, located in Wales, which have a larger contribution of Zn compared to their catchment area. This suggests that within their catchment small tributaries release high amount of Zn (Mayes et al., 2013). Furthermore, the Afon Ystwyth reports high Pb load and yield (kg/year/km²).

In Wales and England, the total extension of metal sources in mining-affected catchments is unknown. Mayes et al. (2013) investigated the contribution of historically mined ore fields to the total metal load registered at the Atlantic coast by comparing mining archives with data for mine drainage metal load, geology and land-use. Mine associated metal loads are believed to contribute 52% of the total Zn and 47% of the total Pb to the Atlantic. Point source account for 16% Zn and 6.3% Pb, meaning diffuse sources are the main contributor of mine metal load (Mayes et al., 2013). Diffuse metal sources to the catchments are represented by mine spoil heaps, metal-enriched groundwater (often connected to underground mining work) and metal-

enriched sediments stored in river channels and floodplains (Macklin et al., 2006, Dennis et al., 2009, Gozzard et al., 2011,).

The Environment Agency (2002) identified the 50 most contaminating mine sites in Wales, with the Wemyss, Graiggoch, and Frongoch Mines listed in the top seven. Sources of mine contamination present in these catchments cause downstream rivers to be classified as 'poor' by the Water Framework Directive standards, due to their elevated Pb, Zn and Cd concentrations. Along the Afon Ystwyth, significant increases in Zn, Cd and Pb concentrations occur at the Nant Magwr confluence (Environment Agency, 2012b), with a total of 19 km of river reach impacted (NRW, 2016). According to a sampling campaign undertaken by the Environment Agency (2012a) upstream of the Nant Cwmnewyddion confluence, the concentration of Zn in the Nant Magwr was 23.9 µg/l. This is considered the background concentration of Zn due to the mineralised nature of the catchment (Environment Agency, 2012a). In addition, the Nant Cwmnewyddion above the Nant Magwr was defined as fishless by a fish population survey (NRW, 2016). Potential sources of the metals include the Wemyss Mine waste heaps at the Nant Cwmnewyddion headwaters, Frongoch Adit and Graiggoch Mine hillside (Atkins, 2008, Environment Agency, 2012a, NRW, 2016). Wemyss spoil heaps have been estimated to contribute about 530 kg/yr Zn, 132 kg/yr Pb and 2.28 kg/yr Cd (Stokes, 2002). Proposed remedial measures have included capping the spoil and diverting adjacent rivers to reduce infiltration, metal leaching and contaminant sediment erosion (NRW, 2016). Since the 1840s Frongoch Adit connected Frongoch Mine underground to the Nant Cwmnewyddion. Frongoch Mine is an important mine site lying on the east edge of the studied catchment. In March 2011 remediation work was undertaken at the Frongoch Mine site. Superficial water was channeled to avoid interaction with mine waste heaps and tailings. This reduced the flow in the Frongoch stream, the Nant Cell, and the Frongoch Adit but increased Zn and Pb concentrations at Frongoch Adit (Environment Agency, 2012b). In summary, this area represents a metal impacted river system with complex multiple sources requiring a priority guide for the remediation.

2.2 The geographical and mining asset of the study site

The field area is mainly underlain by rocks of the Devil's Bridge Formation of Upper Llandovery age (Telychian age, 438.5-433.4 Ma, in the Silurian Period) (BGS, 2004). This formation comprises alternating mudstones and sandstones or thick series of mudstones (Figure 2.1). The sequences are folded, with a vertical orientation of strata notable in the upper part of the riverbed and in some outcrops. A large normal fault has a direction southwest-northeast strike and is associated

with narrow quartz and sulfide veins (Palumbo-Roe and Dearden, 2013). The veins contain the Frogoch mineral lode comprising Cu, Pb, Zn, and Ag.

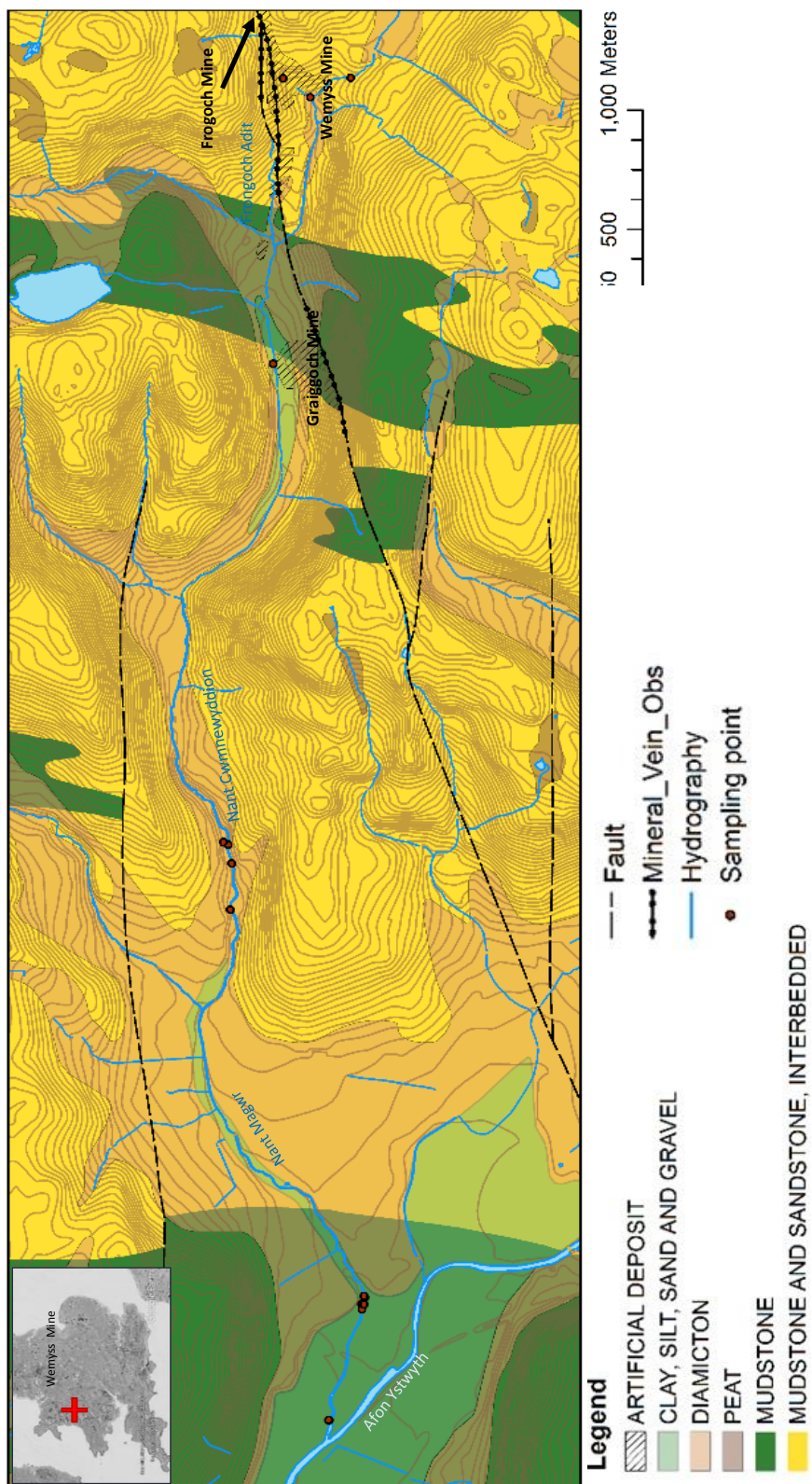


Figure 2.1 Geology and topography of the Nant Cwmnewyddion and the Nant Magwr. Source: DIGMapGB-50 [SHAPE geospatial data], Scale 1:50000, Tiles: ew178, Updated: 1 October 2013, BGS, Using: EDINA Geology Digimap Service (www.digimap.edina.ac.uk, Downloaded: 2016-06-03), modified with ArcGIS v.10.

The hills around the Nant Cwmnewyddion catchment are also covered by glacial deposits (diamicton) and more recent fluvial – alluvium deposits (clay, silt, sand, and gravel). The weathering of the mudstones has produced peat and clay loam. The deposits produced by the mine works are reported as artificial deposits in Figure 2.1. The permeability of the Silurian basement is considered low and only related to its fracturing or restricted to mined areas.

Graiggoch, Wemyss and Frongoch Mines exploited the Frongoch mineral load. Wemyss and Frongoch were joined in the 1840s under the same owner, with Wemyss Adit extended to serve Frongoch Mine, becoming Frongoch Adit. From 1898 to 1904 the mines were acquired by 'Société Anonyme Minière', a Belgian company. They modernised the mining system, introducing electricity by utilising hydropower at Pont Ceunant and building a large ore dressing mill at Wemyss (NRW, 2016). This area falls into the Ceredigion Uplands, a Special Landscape Area (SLA) of national importance in terms of its outstanding ecological and cultural value. In the last two decades buildings at Pont Ceunant saw the Environment Agency, the Welsh Mine Preservation Trust and locals involved in archeological and protection works (Welsh Mines Preservation Trust, 2009). Furthermore, the Dyfed Archaeological Trust (DAT) Archeological Services, commissioned by the NRW, assessed part of Wemyss Mine area as areas of high archeological potential (DAT Archeological Services, 2016). Finally, the Welsh Mine Society and the Ceredigion Council highlighted the landscape value and the Countryside Council for Wales reported the presence of six rare lichens plus Sea Campion plants (Environment Agency, 2002). However, the land is mostly used for grazing and occasionally with recreational scope. These characteristics are typical of abandoned metal mining areas, often included in national and international heritage scheme protection and provide unique habitats for rare organisms (Environment Agency, 2008).

The minerals present in the ore veins are sulfides, including galena, sphalerite, and occasional pyrite, as well as gangue minerals comprising mainly quartz and local ankerite. Palumbo-Roe and Dearden (2013) analysed the mineralogy of the mine waste and reported bulk minerals such as quartz, feldspar, illite, and chlorite, plus Pb-bearing minerals including anglesite, plumbojarosite, and galena. In addition, Palumbo-Roe and Dearden (2013) calculated the organic matter concentration from weight loss using loss-on-ignition (LOI). Wemyss Mine wastes show a high variability in organic matter concentrations from 0.49 % to 22.9 wt. % whereas Graiggoch Mine wastes show a smaller range between 0.72% and 4.38 wt. %.

Annual hydrograph records at the downstream Ystwyth gauge station 63001 (Ystwyth at Pont Llolwyn). Figure 2.2 shows high inter- and intra-annual variability. The gauge record illustrates a fast-flush river system with the water level rising and decreasing quickly. Lynch et al. (2017) identify extended periods (weeks) with streamflow higher or lower than annual mean. The observed high variability is typical of the UK climate, a temperate marine climate, influenced by the North Atlantic oscillation, storm tracks and blocking (Watts et al., 2015).

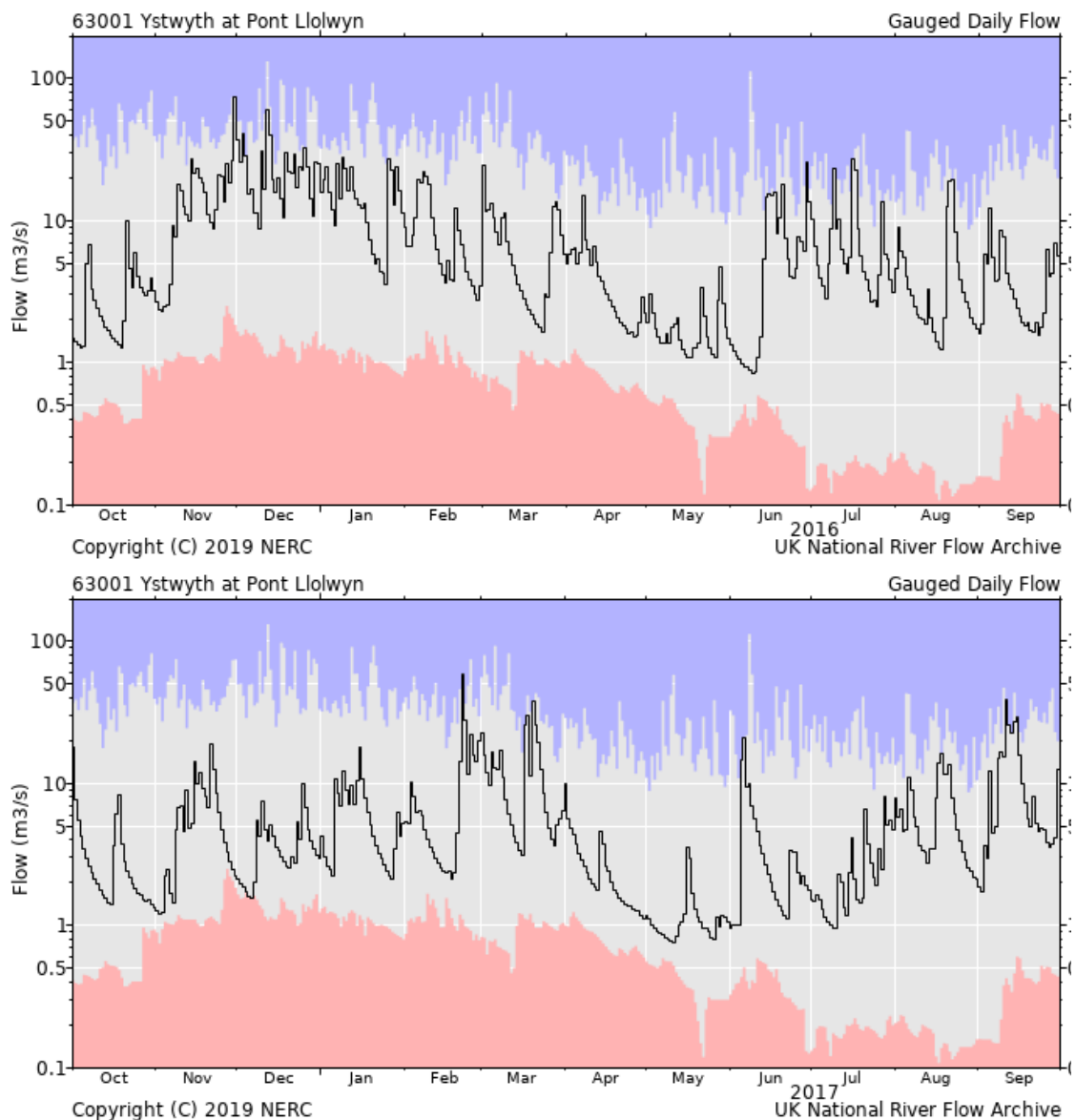


Figure 2.2 Annual hydrograph of 2016 (top) and 2017 (bottom) station 63001 on the Ystwyth at Pont Llolwyn downstream the Nant Magwr confluence. Red and blue areas represent the lowest and highest flows on each day over the period of record (NRF, 2019).

Croxton et al. (2006) highlighted the local and regional spatial variations of weather conditions due to the topography, altitude and sea closure. Walsh's monthly precipitation averages are presented in Figure 2.3 for the years 2016 and 2017 (Met Office, 2019). Their annual means are similar (about 114 mm), but monthly variations are observed during winter. Observing the longest dataset for UK, England and Wales Precipitations (EWP) starting in 1766, large variabilities are clear in winter (Dec-Feb) and summer (Jun-Aug) from year-to-year. Averages can vary from 88.9 mm (1964) to 423 mm (1915) in winter, and 66.9mm (1995) and 409.7mm (1912) in summer (Jenkins et al., 2009). Among the variabilities, in the last 50 years, winters are becoming wetter because of heavy precipitation events and summers are decreasing in precipitations (UKCP09). The increase of rainfall in Wales is expected to rise river flows by 20.8% by 2050 and 27.6% by 2080 for medium emission (P50) scenarios (UKCP09).

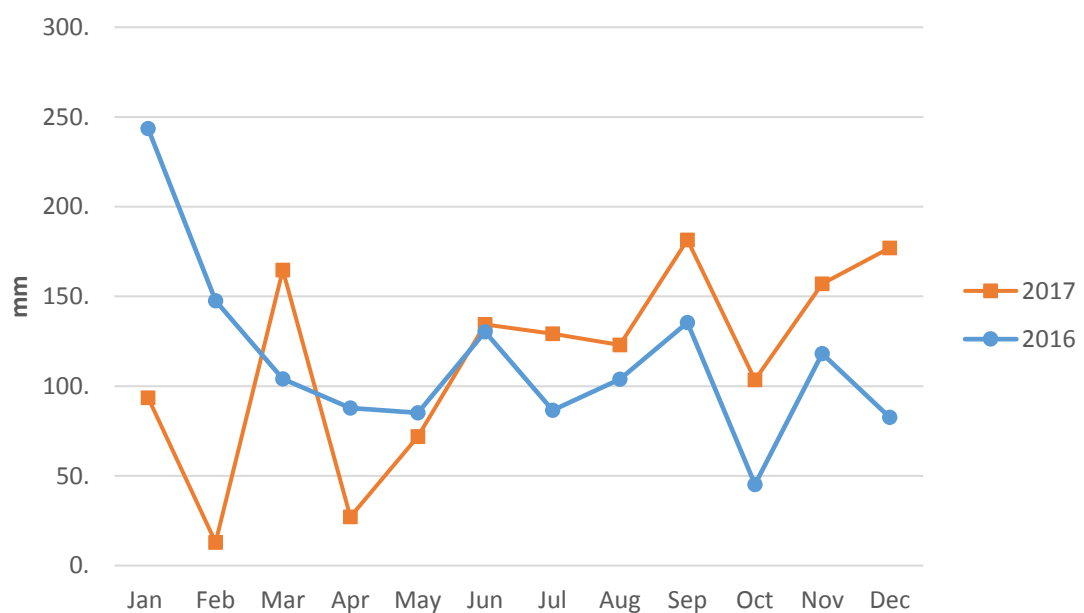


Figure 2.3 Monthly rainfall in Wales 2016 (blue) and 2017 (red) in millimeters (Met Office, 2020).

2.3 Conclusions

The major conclusions from this chapter are:

- The Nant Cwmnewyddion and the Nant Magwr drain Pb and Zn veins exploited by Wemyss, Graiggoch and Frongoch Mines.
- By reporting low water quality due to Zn and Pb contamination, these river systems are typical mining-affected catchments.
- Wemyss Mine, Graiggoch Mine, and Frongoch Mine are classified among the top seven most contaminating mine site in Wales.
- The magnitude and spatial variability of Zn and Pb sources along the catchment are not well constrained.
- The variable hydrological regime limits metal source apportionment utilising traditional methods.

Chapter 3. Methods and materials

3.1 Characterising soil contamination at the catchment scale

Sediment samples were collected along Nant Cwmnewyddion and Nant Magwr that analysed for their metal concentrations and geochemistry. Preliminary metal sediment concentrations were measured with a portable X-ray fluorescence (pXRF) and were reported in a spatial trend map. The geochemistry and mineralogy of the sediment samples were then investigated with X-ray diffractometry (XRD), scanning electron microscopy (SEM) and electron microprobe micro-analysis coupled with energy dispersive X-ray spectroscopy (Kovacs et al., 2006). In addition, sediment geochemistry and metal concentrations were compared to river catchment geomorphologic factors such as topography, slope, landscape, and grain size distribution. The justification and background information of the laboratory methods and field techniques are here reported. A more detailed description of the sampling approach and methodology is given in Chapter 4.

3.1.1 Sediment geochemical and mineralogical analysis

The pXRF analyser is currently used in research and as standardised procedures for sediment characterisation (Radu and Diamond, 2009, Foulds et al., 2014). This technique is non-destructive and allows fast acquisition of chemical data (Kalnicky and Singhvi, 2001). However, results can suffer from low quality. For example sediment moisture content and the physical matrix effect (particle size, sorting, and morphology) can impact data quality and generate an underestimation of Zn and Pb concentrations (Kalnicky and Singhvi, 2001). As discussed in Chapter 4, the pXRF Genius 9000XRF model Skyray (Liverpool John Moores University) was used to analyse the sediment collected along the catchment. The results were used for a qualitative description of metal dispersion due to the equipment's low data accuracy.

The spatial variability of contaminants can be illustrated using geographic information systems (GIS). Spatial metal trends and hot spots of contamination were identified by measuring metal concentration with pXRF and documenting the location of sample points with GPS (Hürkamp et al., 2009, Kincey et al., 2018). A spatial trend can be generated for a wider area using interpolation algorithms, such as Kriging in ArcGIS (Kincey et al., 2018). Kriging interpolation can result in extremely high values therefore knowledge of mining location and potential depositional areas is required when interpreting metal spatial trends (Chen et al., 2012). In Chapter 4, data interpolations for Zn, Pb and Fe concentrations were determined using the Kriging algorithm in ArcGIS v.10.

Sediment mineralogy can be investigated with XRD analysis (Hudson-Edwards et al., 1996). The optimal condition for data quality is the presence of crystalline phases in the sample. However, sediment metal-bearing minerals are often poorly crystalline or amorphous (Hudson-Edwards et al., 1996) and are present in low concentrations (Horie and Fujita, 2011). Therefore, the recognition of sediment minerals with XRD can be limited (Hudson-Edwards, 2003). In Chapter 4 qualitative sediment mineralogy was investigated with a Rigaku Miniflex XRD with 30 kV/ 15 mA Cu X-ray (Liverpool John Moores University).

The chemical composition, mineralogy, and morphology of sediment grains can be studied with SEM and EDS (Kennedy, 2002). These instruments allow the acquisition of grain images and element concentrations giving micro-scale information on the size, shape, composition, and nature (organic, inorganic, artificial) of the sediment grains (Caboi et al., 1993, Palumbo-Roe et al., 2013). In Chapter 4, SEM observations performed with a FEI-Quanta 200 SEM coupled with an EDS INCA-X-act Oxford Instruments are presented (Liverpool John Moores University). Detailed information on chemical composition and morphology of sediment grains can be accurately obtained with electron microprobes coupled with EDS analytical systems (Hudson-Edwards et al., 1996). Sediments prepared in epoxy-impregnated polished mounts allow particle-by-particle investigation (Davis et al., 1993, Kennedy, 2002). Backscatter images allow the recognition of bright phases composed of denser elements. In Chapter 4 analyses were performed with the microprobe Jeol8100 Superprobe (WDS) coupled with an Oxford Instrument INCA microanalytical system (University College of London).

3.1.2 River catchment geomorphology

Understanding of the role of river catchment geomorphology on metal distributions is restricted by the complexity and variety of stream systems. Downstream decreases in metal concentration have been observed in several studies (Miller, 1997, Hudson-Edwards, 2003, Byrne et al., 2010). Miller (1997) attributes the downstream trend to aggradation and degradation of mine waste along the channel, dilution of contaminated sediment by clean sediment, hydraulic sorting based on density, size and shape, and biogeochemical reactions. Statistical approaches based on regression or mixing models have attempted to model downstream metal decay (Lewin and Macklin, 1987). The downstream concentration decay appears to be metal-specific, due to its biogeochemistry and associated material as denser material remains closer to the source (Macklin et al., 1992). Mixing models can account for dilution processes due to clean sediment or multiple source areas (Marcus, 1987). However, the fit between the data and statistical models tends to be poor despite similar

general trends (Miller, 1997). Modelling limitations arise from the variability of geomorphological processes that are not systematic along the channel. A detailed semi-quantitative approach is therefore essential for linking river catchment geomorphology to metal concentration distribution along the catchment. The semi-quantitative approach used as part of this thesis is outlined in Chapter 4. The investigated factors include topography, slope, grain size distribution, and landscape observations (vegetation presence, channel and overbank description, and use of land). Geomorphological analysis of topography and slope allows identification of areas where contaminated sediments are potentially trapped or mixed with clean sediments (Foulds et al., 2014). Landscape observations and grain size distribution give information on aggradation or degradation processes which can indicate release or storage of metal-bearing sediments (Hudson-Edwards et al., 2001).

3.2 Monitoring streamflow variability and metal source apportionment

Metal source apportionment along Nant Cwmnewyddion and Nant Magwr was estimated by combining two tracer injections, the continuous tracer injection and the gulp-injection, referred to as the 'slug injection'. The range of streamflows was defined using a historical series of streamflows. Metal concentrations in river water were analysed, ensuring good quality of data, and, multiplied by the streamflows, used to calculate metal loads. The justification and background information about the streamflow estimation methods are reported here; for a detailed description of the sampling locations, methodology settings and metal load calculations refer to Chapter 5.

3.2.1 Streamflow definition

Streamflow is often represented as historical daily flow series using percentile values (0-100), which indicate the percentage distribution (Helsen and Hirsch, 2002). Hydrological studies tend to rank streamflow as the percentage exceedance (Q), calculated as 100 minus the percentile (Gozzard et al., 2011). Generally, for a historical distribution of streamflow measurements a Q value between 25% and 75% indicates moderate streamflow. This means that all streamflow above the 75th percentile are low flows (often exceeded), and those below the 25th percentile are high flows (less likely to be exceeded) (USGS, 2019). In the UK, the National Stream Flow Archive (NRFA) provides data series from numerous gauging stations across the country (NRFA, 2019). Hydrological data spanning 1963 to 2017 from the gauge station 63001 (Ystwyth at Pont Llolwyn, SN5902477289) are

summarised in Chapter 5. This gauge station is located along the Afon Ystwyth downstream of the confluence with Nant Magwr and Q values were calculated from its daily flow.

3.2.2 Streamflow estimation by continuous tracer injection

Estimating streamflow in mountain streams, where historical mines are situated (Hudson-Edwards et al., 2011), is difficult to achieve using traditional methods. These methods, such as flow metering, acoustic doppler, and thin plate weirs, can underestimate streamflow, not account for subsurface flows (hyporheic or groundwater inputs), or introduce uncertainty due to irregular stream cross-sections and bed stream roughness (Runkel et al., 2013, Byrne et al., 2017). As a result, new methods based on tracer dilution and mass conservation were developed to accurately estimate streamflows in complex stream systems. Tracer methods have been designed during the US Geological Survey Toxic Substance Hydrology Program (Kilpatrick and Cobb, 1985, Kimball et al., 1998, Kimball, 2002, Moore, 2004b). Until now, these approaches have been used mainly in the US, for the abandoned Mine Lands Initiative (Kimball et al., 1998), and executed only a few times in Europe (Kimball et al., 2007, De Giudici et al., 2017).

In continuous tracer injections, a geochemical tracer is injected into the stream water at a controlled rate. After an elapsed time, the tracer is dispersed homogeneously downstream of the injection and a steady-state concentration (noted as a plateau) is observed. Streamflow values can be calculated based on the mass conservation principle (Kimball, 2002, Moore, 2004b). The stream water dilutes the injected tracer therefore knowledge of the tracer concentration in the stream and the injection parameters (tracer concentration and streamflow), can be used to estimate streamflow at the sampled points. Streamflow is calculated as:

$$Q = \left(\frac{q (C_{inj} - C_{bg})}{C_p - C_{bg}} \right)$$

where C_{inj} = injectate concentration

Q = stream streamflow C_{bg} = salt concentration in natural water (background)

q = injection streamflow C_p = tracer concentration during plateau

Sampling points are carefully pre-selected through walkovers and map investigations. They are up- or downstream of suspected contaminant sources, inflows, stream channel variations (lithology, vegetation density or type, sedimentology) or geochemical precipitation (Kimball, 2002). Sampling

multiple points along the stream creates a spatially detailed streamflow profile based on a dense grid of samples. The continuous tracer injection, combined with synoptic sampling, captures spatial variation in water chemistry and streamflows (Runkel et al., 2013). Tracer and metal concentrations are measured for each sample, with metal concentrations multiplied by the respective streamflows providing load values. The spatially detailed loads along the river highlight metal sources and sinks (Runkel et al., 2013).

Tracer type, concentration, and volume of injectate are chosen based on stream characteristics. NaBr, LiBr, and LiCl are commonly used as salt tracer, with selection based on stream tracer background concentration and aqueous pH. Bromide can be released as a conservative tracer in circum-neutral streams, whilst Li can be used as a conservative tracer under acidic conditions (Runkel et al., 2013). Such conservative tracers (Li, Cl, Br) are not affected by geochemical processes at the given stream conditions. The tracer is injected with an automatic pump usually connected to a data logger which keeps the injection rate constant (Moore, 2004b), or a peristaltic pump. The injection point should be in a well-mixed stream segment, such as upstream of a turbulent flow area. This provides mixing between tracer solution and river water. The tracer volume and the injection rate depend on the stream streamflow and length. Adequate time is needed for the tracer to reach plateau at the most downstream point and for operators to complete the sampling. Limitations of this technique relate to errors associated with field equipment, sampling, geochemical diurnal variations, laboratory measurements, loss of tracer due to permeable geological basement or tracer dilution due to rainfall occurring during the injection (Schmid et al., 2010).

Typically, continuous tracer experiments are carried out during low flow conditions (generally with a streamflow of 100L/s) to provide easier control over the logistic of injections (volume of tracer required for reaching plateau) and which are believed to have the highest metal concentrations (Runkel et al., 2013). Continuous tracer injections are usually completed in small streams characterised by widths less than 2 m and that have linear chemical variations (Kimball, 2002, Moore, 2004a). The continuous tracer injections described in Chapter 5 were the first of their kind to be executed in highly variable weather conditions, typical of an oceanic temperate climate.

3.2.3 Streamflow estimation using slug injections

Slug injections can provide an estimation of streamflow in high gradient streams. Slug injections are based on tracer mass conservation. Detailed methodology descriptions of this technique are reported by Moore (2004a, 2004b, 2005) and Richardson et al. (2016). The method requires limited

equipment, a bucket, pre-weighed bags of salt and an electric conductivity (EC) meter, and is thus easy to execute in remote sites. A tracer solution, created by mixing a known amount of salt in stream water, is injected in the stream. Downstream of the injection site, the salt wave is recorded by the EC meter at regular intervals (generally 1 to 5 seconds). The graph of EC values against the time-lapse illustrates an asymmetric bell shape with a central peak and a final smooth tail (Figure 3.1). EC measurements should be taken from the centre of the stream, downstream of the tracer injection at 10 to 25 times the stream width depending on the fluvial topography. Injection and monitoring sites should allow full mixing of the tracer and inflows, and slow water pools should be avoided. The change in EC due to the trace traveling in the stream water usually last between 2 and 30 minutes depending on the tracer longitudinal dispersion and is proportionally inverse to stream velocity. The EC value increase in the stream water should be 50-200% of EC background (Moore, 2004a).

To calculate the streamflow EC measurements are first converted into the tracer concentrations. A known amount of salt is added gradually into the stream water and the EC increments are monitored. Tracer concentrations are then plotted against the EC increments, and the slope of the obtained regression curve is used as the coefficient K. The tracer concentrations are derived by multiplying the EC values to K. Finally, the streamflow is calculated by dividing the tracer mass by the summation of tracer concentration multiplied by the sample time interval.

Being easy to execute in remote sites, suitable for irregular stream cross-sections and for a range of streamflows, slug injections were employed to estimate streamflows in Chapter 5.

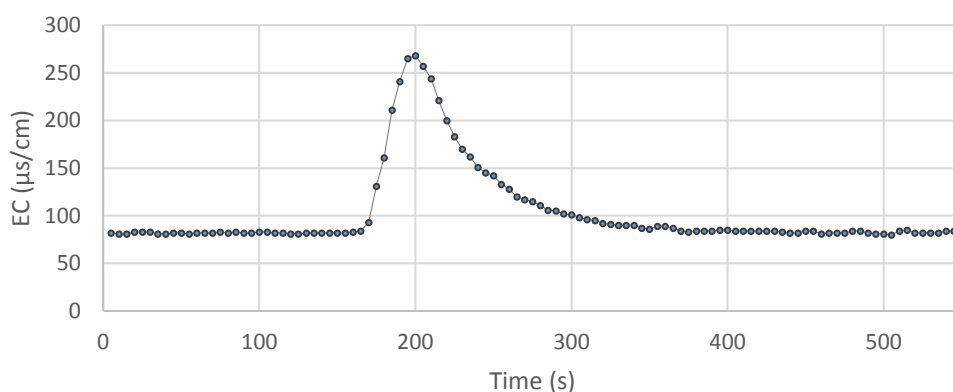


Figure 3.1 Example of EC values in river water after salt injection at 5-second interval. The bell-shaped curve shows smaller value in the sides and the peak in the central area. Slops are different, quick rise on left, first to the peak, and smooth slope on right, after the peak.

3.3 Waterborne nanoparticles sampling and analyses

Nanoparticle abundance, geochemistry, and morphology were investigated in the Nant Cwmnewyddion and the Nant Magwr. An optimal sampling method was developed prior to conducting the experiment. This investigation was possible thanks to the FENAC/2016/11/008 grant, which allowed access to the UK Facility for Environmental Nanoscience Analysis and Characterisation (FENAC) at the University of Birmingham. The design of the sampling protocol was carried out at Liverpool John Moores University. The justification and background information about the sampling and the FENAC employed techniques are here reported. Details on further techniques and water chemistry investigations are provided in Chapter 6.

3.3.1 Sampling protocol and nanoparticles storage time

Accurate nanoparticle characterisation is dependent on accurate sampling techniques. Several researchers have tried to develop an optimal approach for sampling nanoparticles (Pokrovsky and Schott, 2002, Pokrovsky et al., 2010, Lapworth et al., 2013), highlighting the complexity due to contamination and fragile nanoparticle stability. Pokrovsky et al. (2010) investigated trace elements and organic carbon seasonal fluxes in the Severnaya Dvina River, Russia. In-situ filtration (5 and 0.22 μm , 100, 10 and 1 kDa) and dialysis (1 and 10kDa) were performed and the results compared. The ultrafiltration was performed in a non-cascade series, with 25 nm, 100 kDa, 10 kDa and 1 kDa fractions filtered from the 0.22 μm sediment fraction. This technique, executed with Amicore filter and membranes, regenerated cellulose and required 6-12 hours. In contrast, dialysis techniques can take up to 24-48 hours. During this time frame, hydrological and geochemical variations occur (such as precipitations or diurnal element cycles). Samples may therefore be unrepresentative of their environment and may contain artefacts (Court, 2014). In Chapter 6, a filtration system comprised of pre-filtration steps (63 and 1 μm) and 0.45 μm , followed by 10 kDa, ultrafiltration were developed, reducing contamination issues and allowing rapid sample processing (Figure 3.2).

In water quality monitoring protocols, the filtration step at 0.45 μm represents the cut off size below which elements present are considered 'dissolved' (American Public Health et al., 2005). In Chapter 6 this filtration step is used to compare metal concentration and load transported in nanoparticles (passing through 0.45 μm), truly dissolved (< 2.5 nm) phases and suspended particles (0.45 μm) (Kimball et al., 1995). River water pre-filtration, before 0.45 μm size, is fundamental to avoid clogging of the filter (Lapworth et al., 2013). Pre-filtration steps at 63 μm and 1 μm were completed to reduce clogging of the 0.45 μm filter, this is outlined in Chapter 6.

Fractions below 1 kDa are considered truly bioavailable metals because they are similar in size to the cell wall transport channels in bacteria and plants (Vasyukova et al., 2012). Despite this, no significant differences in metal concentration were measured between 14 and 1 kDa in the study completed by Court (2014). As a result, truly dissolved elements are defined with a 10 kDa size that corresponds to the 2 -2.5 nm size, depending on the nominal molecular weight limit, in Chapter 6. Some organic molecules containing metals can pass through the filter, but a smaller filter could generate a clogging of the filter pores. Two kinds of 10 kDa membranes have been used 1) Regenerated Cellulose Amicon Ultracentrifugation (Merckmillipore); 2) Polyethersulfone membrane Vivaspin 500 (SLS).

Limitations in sampling nanoparticles rise from sample contamination and particle instability. Once removed from their native environment, nanoparticles can easily transform (Lapworth et al., 2013, Johnson et al., 2014). In order to verify the time window of the nanoparticle stability and the efficiency of the sampling methodology, a trial experiment was conducted (see Chapter 6). Precautions outlined by Pokrovsky et al. (2010) were adopted to avoid contamination. Before filtration, the units were cleaned by flushing them with 18 M Ω cm⁻¹ MilliQ water, then ~0.1 M ultrapure HNO₃, and finally, MilliQ water. During the filtration, the first 50 mL of filtrate was discarded. The filters were replaced every time the flow rate decreased (indicating membrane clogging). Potential contaminations with Cu, Zn and Pb were measured and these elements were discarded for the interpretation of ultrafiltration results. Therefore, for the experiment outlined in Chapter 6, all the equipment was cleaned in 10% nitric acid for 24 h, rinsed 5 times with MilliQ water and left soaking in MilliQ for 24 h to neutralise the equipment surface. A filtration set was prepared for each site. The filtration system was developed considering the time to be elapsed, ease in the execution and reduced contamination effects. In addition, before sampling the river water, the filtration system was thoroughly rinsed with 18 M Ω cm⁻¹ MilliQ and a blank collected.

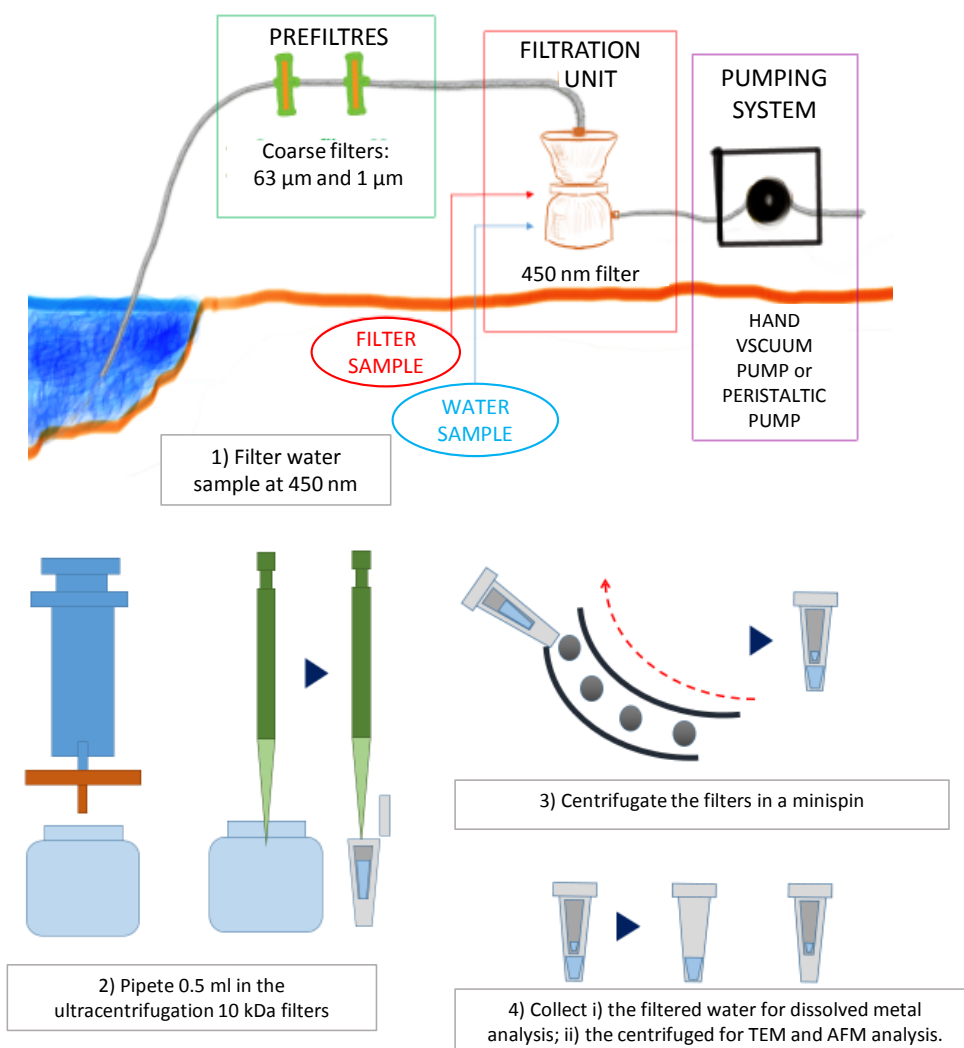


Figure 3.2 River water filtration system with prefiltration steps (63 and 1 μm), 0.45 μm water sample, followed by 10 kDa ultrafiltration for dissolved metals and centrifuged recovery.

3.3.2 Nanoparticle abundance, geochemical and morphological characterisation

The study of nanoparticles is often limited by the availability of appropriate analytical tools in a laboratory (Baalousha and Lead, 2012). This is particularly problematic for investigating natural nanoparticles whose parameters are unstable therefore requiring prompt and complete analysis to be carried out quickly under controlled conditions. Furthermore, environmental nanoparticles can have low concentrations and a large range of sizes (<20 nm to colloidal scale). Generally, natural

nanoparticles are considered as a fraction of heterogeneous and polydisperse phases, colloids, with at least one dimension between 1-1000 nm (Baalousha and Lead, 2013). Studying their characteristics is extremely challenging particularly due to their various chemical and mineralogical characteristics, and so a multi-method analysis is necessary.

The experiment described in Chapter 6 was possible thanks to access to FENAC which was equipped with: Malvern Zetasizer HPPS Nano ZS including Dynamic Light Scattering (DLS) and Zeta potential analysis; PSIA XE-100 Atomic Force Microscope (AFM); JEOL 2100 at 200 keV Transmission Electronic Microscopy coupled with Energy-dispersive X-ray Spectroscopy. DLS and Zeta potential are non-invasive techniques that provide particle size distribution (PSD) and surface charge. Microscopic techniques such as AFM and TEM can help to determine PSD, particle morphology and chemistry.

DLS can quickly detect the average size of nanoparticles from 0.03 nm to 10 μm and provide info on the PSD. Checking signal reproducibility can highlight particle size changes over time. DLS measures the light scattered by the sample over the analysis time. The light intensity fluctuates according to the function of the particle diffuse coefficient. Particle size, expressed as hydrodynamic diameter, is extrapolated by the diffusion coefficient. The conversion of the signal intensity into the particle size requires assumptions, such as spherical shape and homogeneous density. These assumptions are a limitation for the data elaboration and interpretations of natural particles due to their high complexity (Baalousha and Lead, 2012). As discussed in Chapter 6, the Malvern DLS instrument provided cumulant analysis (the z-average hydrodynamic diameter, also named dDLS, and the polydispersity index, PDI) and distribution analysis (an intensity-weighted size distribution). Cumulant (Z-average hydrodynamic diameter, polydispersity index) and distribution parameters (peaks of the intensity-weighted size distribution) are the data representing the particle size (Baalousha and Lead, 2012). Detailed information is reported in section 6.2.

Measures of surface charge (zeta potential, mV) are important for understanding the stability of suspended particles. When zeta potential is c. 0 mV flocculation and sedimentation can occur, and when it is higher than 30 mV or lower than -30 mV the nanoparticles are stable in solution. The surface charge analysis consists of applying an electric field (voltages) to the sample cell which contains two gold electrodes. In the Malvern Zeta Potential instrument, the electric field induces particle movement which is recorded as a phase change in light scattered by the particles (electrophoresis). The phase change depends on the electrophoretic mobility of the particles and used to calculate the Zeta potential (Malvern, 2012). Zeta potential parameters are reported as Phase plot and Distribution data. Distribution data are represented by a signal (counts) and zeta

potential (mV) curve, from which information on average and main peaks is extracted and listed against the run name. Values can be highly heterogeneous and an average among sample runs difficult to calculate. Detailed information is reported in section 6.2.

The AFM has been used to investigate the nanoparticle size (Baalousha and Lead, 2007). The AFM combines the electron microscopes with the measure of particles providing images of nanoparticle agglomerate under normal working conditions (no vacuum) and controlled levels of humidity. The sample supported by a mica layer is scanned by a tip that reconstructs a topographic image of the nanoparticles. This technique is useful for measuring sample structures with high carbon and water contents, as natural nanoparticles in the aquatic system will contain humic substances and therefore may be unstable under the vacuum. For the experiment in Chapter 6, the scan acquisition was carried out at environmental conditions to ensure a better quality of size acquisition (Baalousha and Lead, 2012). AFM images require a brief correction before elaboration, usually a polynomial fitting approach is employed to flatten the image. These images provide height dimensions for the nanoparticles by dragging a line through the image and generating the mica topographic profile. For each observed particle, the height values are reported in a table. The acquisition method distorts the width, therefore, only the height dimension is considered. The nanoparticles are counted when the height of the peak is three times bigger than the background. The background values may be mainly due to organic matter, such as humic acids, which commonly range around 1 to 3 nm or larger in case of agglomeration (Baalousha and Lead, 2007, Baalousha and Lead, 2013). At least 190 heights should be counted (Baalousha and Lead, 2012, Baalousha et al., 2014). Parameters representing the data are height averages, number average and weight average, and the polydispersity (Lapworth et al., 2013, Baalousha and Lead, 2007). Refer to Chapter 6 for details on method execution and data elaboration.

TEM coupled with EDS analysis can result in the acquisition of particle images providing nanoparticle shape, structure and composition information (Echigo et al., 2012). From the images and EDS spectra, size and morphology, as well as chemistry and mineralogy information were reported for each sample. Refer to Chapter 6 for details on method execution and data elaboration.

The quality of data provided by microscopic techniques, AFM and TEM, is dependent on the sample preparation techniques. Washing steps or chemistry reactions between the substrate and the nanoparticles can generate issues related to non-uniform distribution of nanoparticles or induced aggregation (Baalousha et al., 2014). Sample preparations can be done with passive (adsorption, sorption, and drop deposition) or active methods (e.g. the ultracentrifugation) (Baalousha and Lead, 2012). The chosen method, outlined in Chapter 6, is the passive adsorption on thin-layer

method on freshly cleaved mica substrates. A passive method and the use of untreated substrate were preferred to avoid artefact and nanoparticle degradation. Baalousha and Lead (2013) used the adsorption method, followed by washing which gave accurate images and decreased artefacts due to sample preparations. See Chapter 6 for detailed information on sample preparation.

3.4 Conclusions

The major conclusions from this chapter are:

- Spatial variation of sediment metal concentrations along the river was investigated with a pXRF and illustrated in a map elaborated in GIS (Chapter 4).
- The sediment chemistry and mineralogy were analysed with the XRD, SEM and an electron microprobe (Chapter 4).
- River catchment geomorphological description focused on topography, slope, grain size distribution and landscape observation, such as vegetation presence, channel and overbank observations, and use of land (Chapter 4).
- Linear variations of streamflows, metal concentrations and loads were estimated by coupling a continuous tracer injection with a detailed synoptic sampling (Chapter 5).
- Streamflow and metal load under different flow conditions were estimated using slug injections (Chapter 5).
- An efficient method for filtering and sampling nanoparticles from river water was designed (Chapter 6).
- River water samples were partitioned into truly dissolved (< 2.5 nm), nanoparticle (2.5-450 nm), and suspended particles (> 0.45 μm) fractions (Chapter 6).
- Nanoparticle abundance, geochemical and morphological characterisation were undertaken at FENAC laboratories using DLS, Zeta potential, AFM and TEM instruments (Chapter 6).
- Spatial variation of metal loads for dissolved, nanoparticle and suspended particle fractions were estimated along the river (Chapter 6).

Chapter 4. Geochemical and morphological drivers of Pb and Zn release at the catchment scale

4.1 Introduction

Centuries of mine exploitation have resulted in the accumulation of ore and waste materials in the headwaters of river systems (Kossoff et al., 2014). Consequently, metal-enriched sediments are redistributed in catchments by geomorphological processes to achieve morphological equilibrium (Lewin and Macklin, 1987). High metal concentrations decrease sediment quality and pose risks to ecosystems. Hence, contaminated sediment dispersion is a current issue still seeking policy guidelines (Byrne et al., 2010).

Metal enriched sediment can be eroded, transported or deposited in catchments and the metals can be temporarily stored in minerals or released into the river water or the ecosystem. The estimation of sediment metal concentrations at the catchment scale is difficult due to the variability of parameters such as sediment transport processes, vegetation distribution, streamflow, and metal geochemistry. Previous studies have attempted to understand links between metal sediment concentrations, geomorphology and mineral presence (Hudson-Edwards et al., 1996, Hudson-Edwards et al., 2001, Foulds et al., 2014, Kincey et al., 2018), but these have been limited due to neglecting either the geomorphological or mineralogical aspects. A clearer understanding of metal sources at the catchment scale can be provided by mixing the three components of geomorphology, mineralogy and metal sediment distribution.

Along river headwaters, river channels and floodplains erosional and depositional areas can drive metal dispersion (Miller, 1997). In an English mine site, Kincey et al. (2018) quantified the mine waste erosion from mine heaps located in the river headwater and entering the river system of Garrigill Burn, a tributary of the upper South Tyne. Erosional processes such as gullying, bank erosion and mass movements were observed with laser scanning data acquisition. These processes released 434 t of contaminated sediment during the 18 months of monitoring. Lead and Zn concentrations, measured *in situ* with a pXRF, were above the threshold guideline values. This study highlighted the exposure of the mining area to erosion due to unstable slopes, loose material and lack of sediment storage. Large losses of sediments were recorded, particularly during infrequent high magnitude storms (Kincey et al., 2018). However, the study lacked a thorough mineralogical

investigation and an assessment of possible sediment storage areas which could have helped to predict contaminated sediment accumulation processes and potential release of metals at the catchment scale. Other studies investigated sediment remobilization and dispersion in four Welsh catchments (the Afon Leri, Afon Rheidol, Afon Clarach, and Afon Ystwyth) that occurred in 2012 after an intense rain event (Foulds et al., 2014). These authors investigated the metal concentrations distribution along the catchment and compared data with previous floodplain sediment metal concentrations (deduced from samples collected at 0.45 m deep). The 1980s channel of the Afon Ystwyth had lower metal concentrations than the 2012 data up to 15 km downstream of the mine site. Samples from 15 to 40 km downstream showed similar concentrations from 1980 to 2012. This pattern was explained by the localisation of the mining workings in the upper 14 km of the catchment. Foulds et al. (2014) identified two main processes involved in the sediment transport: i) direct erosion of unstable loose sediment mainly represented by mine waste at headwaters; ii) bank erosion and lateral and vertical accretion of floodplain deposits common of piedmont areas. Furthermore, variations in sediment transport velocity, controlled by change of slope or enlargement of the channel, were proposed to create low energy zones that trapped sediments. The authors proposed that these processes may confine sediment to tributaries, preventing it from reaching the main river channel. The study showed that a topographical observation of possible sediment traps along tributary channels connecting mining areas to larger rivers could ensure a better understanding of the sediment mass movement along the river. The study lacked in mineralogical investigations and river water metal transport estimations. Such information may have shown areas at risk of metal remobilisation.

Mine wastes dispersed into the catchment carry ore minerals, such as galena and sphalerite, or secondary metal-bearing minerals, such as sulfates, phosphates, carbonates and Fe or Mn oxyhydroxides (Hudson-Edwards et al., 1996, Hudson-Edwards et al., 2001). The stability of these minerals depends strictly on biogeochemical settings (pH, oxygen concentration, metal sediment, and water concentration, water saturation, bacterial activity). Therefore, geochemical and mineralogical analysis is necessary to better identify the presence of metal-bearing phases and their stability. The study of Hudson-Edwards et al. (1996) provided a mineralogical characterisation of sediments sampled at mine-waste tips, riverbanks, mining-age alluvium and suspended sediment. At the studied river (the Tyne River Basin) the primary minerals were the sulfide minerals galena, sphalerite, and chalcopyrite. They were mostly localised at the mine tips and their dissolution enhanced the formation of secondary carbonate, silicate, phosphate and sulfate minerals (CSPS). Oxidative or acidic conditions can dissolve sulfide minerals and yield soluble CSPS. Furthermore, oxyhydroxides can replace CSPS or precipitates, forming more stable metal-bearing mineral phases.

Iron- and Mn-oxyhydroxides were more abundant downstream with Mn-oxyhydroxides progressively decreasing in abundance. Integrating mineralogical information with river catchment geomorphological descriptions can help to extrapolate local sample-scale information to the catchment scale with more confidence.

Understanding the drivers of metal transport and transformation at the catchment scale requires the observation of geological and geomorphological features. Subsequently, sediment mineralogical and geochemical analysis must be undertaken to estimate the storage or release capacity of potential metal sources dispersed in the catchment. Recently, the knowledge of sediment geochemistry characterisation and metal enriched sediment dispersion has increased, although there is still a lack of understanding of the role of fluvial morphology in enhancing geochemical settings and metal release. River segments characterised by high slope and erosional rates can be characterised by primary minerals continuously washed away and exposed to weathering processes. On the other hand, depositional areas provide permeable riverbeds and banks that can potentially promote geochemical processes typical of hyporheic zones or clay embankments with low permeability and reductive conditions (Palumbo-Roe et al., 2012).

The specific aim of this chapter is to identify the effects of sediment geochemistry and fluvial morphology on Zn and Pb storage at the catchment scale. The objectives are i) to characterise the geochemistry of the sediment dispersed in the catchment; ii) to propose a fluvial morphological control on Zn- and Pb- bearing mineral distribution along the catchment.

4.2 Method and materials

The Nant Cwmnewyddion and the Nant Magwr show variation in river catchment geomorphological features, such as slope, topography and grain size distribution. These features were investigated with topographical analysis of DTM maps and granulometric description of sediment samples. Geochemical characterisation of the sediment samples was carried out using a portable X-ray Fluorescence (pXRF) instrument. Ten samples collected from the river banks were selected as a subset for detailed mineralogical and elemental analysis.

4.2.1 Sampling description and grain size analysis

Along the Nant Cwmnewyddion and the Nant Magwr, five areas of sampling were identified based on the location of mining and depositional areas (Figure 4.1 and 4.2). The areas are:

i) upstream of the mine tips, considered as the 0 m point (T0);

- ii) the mine tips around Wemyss Mine (171 m) both at the headwater (CW) and further downstream of Mill Race Stream (WM);
- iii) along the Graiggoch Mine (1110 - 2620 m) river segment ;
- iv) around a middle reach (3000 – 4070 m) depositional area (DC);
- v) the floodplain at about (5800 m and 6740 m) (respectively RB UPS and RB DS).

In each area a series of solid samples were collected along transects perpendicular to the river corridor on the 18-19-20 and 26 July 2016. The transect position depended on fluvial morphological observations (such as depositional or erosional areas), geological and sedimentological features (as sediment texture, rocky outcrop), sediment formation and vegetation obstructions. Seventeen transects were located as follows: eight (transect RB A, B, C, D, I, DEP A, DEP B and DEP C) in the floodplain area; five (transect DC D, E, F, G and H) in the depositional area around 3 Km (DC); one (transect GG L) nearby Graiggoch Mine; three (transect T0 M, CW J and WM L) in the upstream part (WM, CW and T0). A total of 68 samples were collected (refer to Appendix 4.a for a complete sample and transect list). Prior to sample collection, roots, leaves, and pebbles were removed from the sediment. Soft sediment was sampled with a trowel or hand Augers to a maximum depth of 40 cm. The samples from the river bank were sampled both with a trowel or, where possible, with a PVC cast.

The samples were transported to the laboratory, left to dry at room temperature (21°C), and characterised in terms of their pH and grain size distribution. pH was measured with the pH paper test. Different grain sizes were separated on a vibration platform (Fritsch) using Endcotts sieves. Following Wentworth size classes, the sieving separated: very coarse sand (2 – 1 mm), coarse sand (1 – 0.5 mm), medium sand (0.5 – 0.25 mm), fine sand (0.25 – 0.125 mm), very fine sand (0.125 mm - 63 µm) and silt and clay (less than 63 µm).

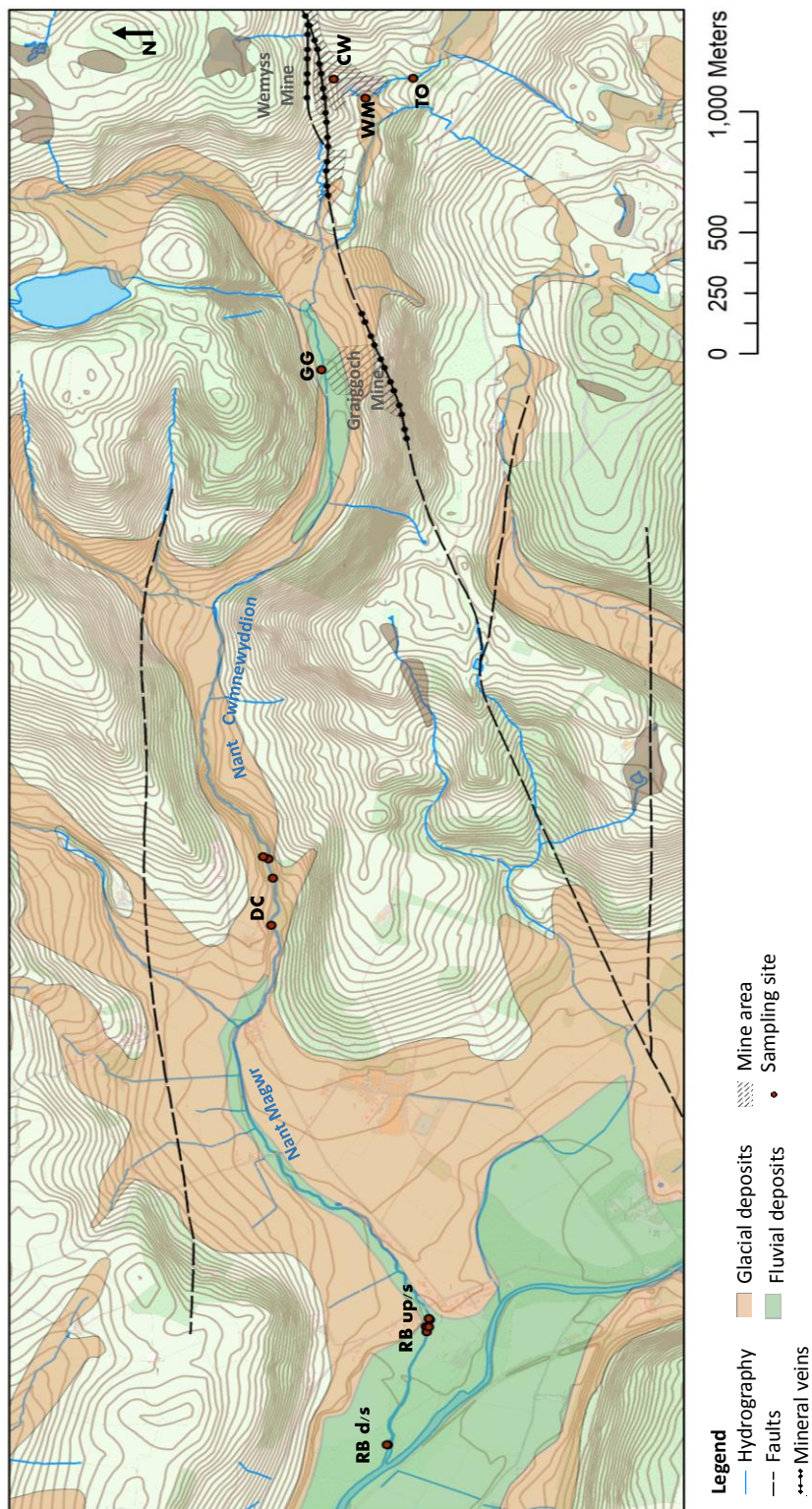


Figure 4.1. Map of the sampling areas along the Nant Cwmnewyddion and the Nant Magwr, the fluvial and glacial deposits, and the mine areas. WM: Wemyss Mine; CW: tributary at Wemyss mine; TO: upstream the mine areas; GG: Graiggoch Mine; DC: depositional area at middle river length; RB: floodplain upstream (ups) and downstream (ds) areas. DiGMapGB-50 [SHAPE geospatial data], Scale 1:50000, Tiles: ew178, Updated: 1 October 2013, BGS, Using: EDINA Geology Digimap Service [online: www.digimap.edina.ac.uk] Downloaded: 03/06/2016), modified with ArcGIS v.10.

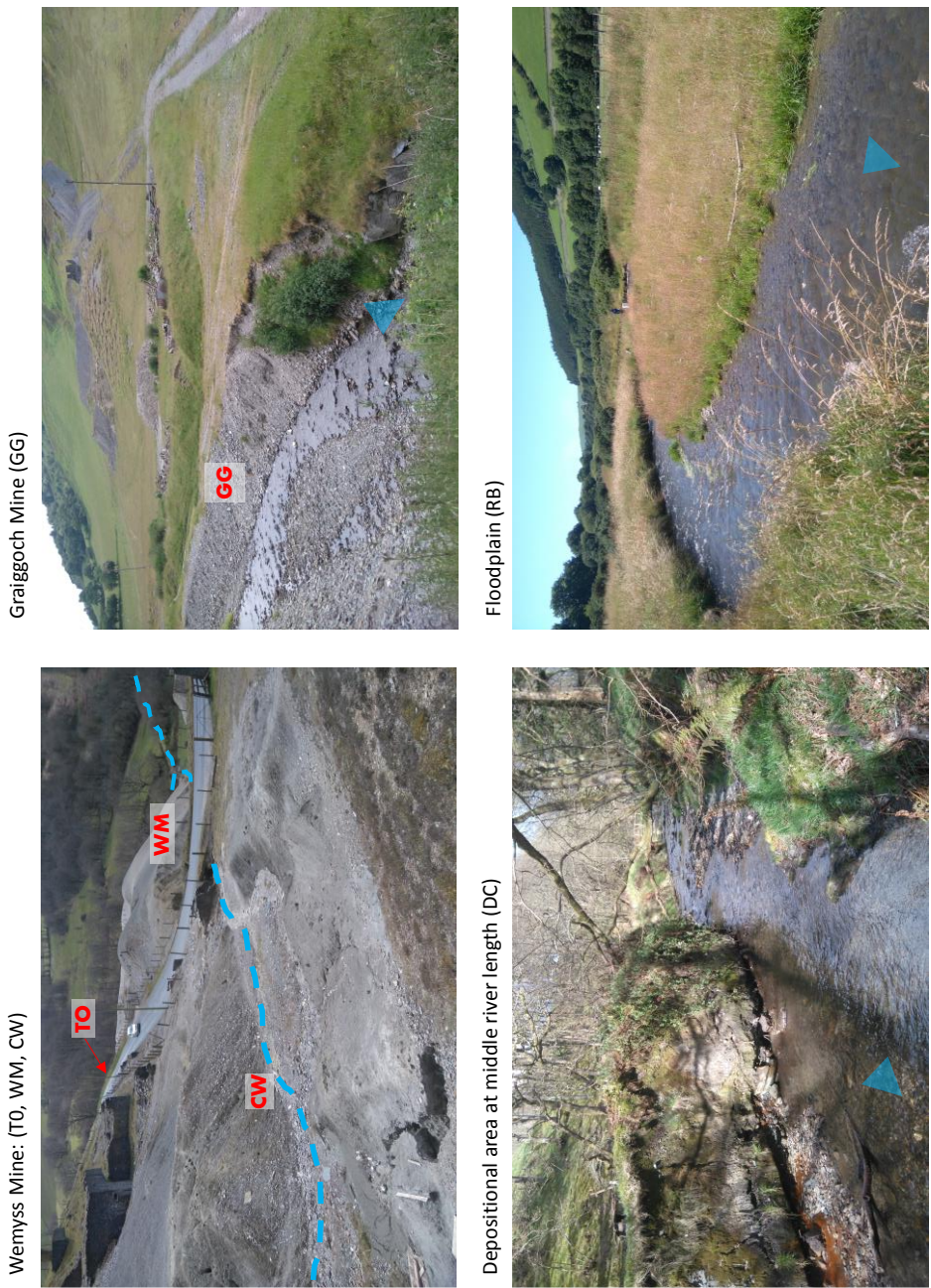


Figure 4.2. Sampling area views. WM: Wemyss Mine with CW: tributary at Wemyss Mine; TO: upstream the mine areas. River paths are indicated with the blue dashed line. Graiggoch Mine with GG labeled samples. Depositional area at middle river length (DC) with 1 to 2 m river bank and percolating red water visible on the bottom left. Floodplain (RB) view of a meander corner. River flow direction is indicated by a blue arrow.

4.2.2 Sediment geochemical and mineralogical analysis

The elemental compositions of the sediment were investigated with the pXRF Genius 9000XRF model Skyray. The p-XRF analysis was carried out for each size fraction to reduce physical matrix effects and repeated six times to increase data precision and to enable the standard deviation to be calculated. Element peak positions were determined with a standard of silver. Although, Pb, Zn, Cu, Fe, Rb, K, Bi, Nb, Zr, Sr, Ni, Ti, Co, and Mn were acquired only Zn, Pb and Fe values are here presented. The whole sample metal concentration was then calculated as the weighted average of the metal concentration related to their respective size fraction weights. For each transect an arithmetic average of metal concentration was calculated to homogenise the values and obtain a representative value of the sampled area.

Portable XRF (pXRF) data were used to determine the spatial distributions of Fe, Zn and Pb concentrations along the river. Values were interpolated using the Kriging algorithm of ArcGIS to produce a map of the studied catchment reporting the metal weight percentage along the river. The maps were then clipped using the river buffer polygon (10 m from the river polyline). Please refer to section 3.1.1 for further information on the pXRF instrument and the ArcGIS map elaboration.

A subset of 10 samples was selected for mineralogical and morphological characteristics thorough XRD (X-ray diffractometer), SEM (scanning electron microscope) and Superprobe analysis. The selection criteria were based on the proximity of the sample to the river water (e.g. samples on the riverbank) and on the metal concentrations obtained with pXRF analysis. Samples with higher concentrations were preferred to better identify sediment mineralogy. In the upstream part of the study river, represented by T0, WM, CW, and GG, the samples with the highest metal concentration were chosen for each area (Figure 4.1). Therefore, four samples in total were collected from transect M in T0, J in CW, K in WM and L in GG. For the middle length of the river (DC) three samples were selected, two from a riverbank both at water level and at 55 cm from it (transect F, samples F1 and F2), and one from a depositional part of a meander (transect E). Three samples were selected from the floodplain (RB), two samples at 5.9 km where the river corridor is channeled at water level and at 30 m from it (transect C, samples C1 and C2) and one at 6.7 km collected on the erosional side of a meander (transect A).

For XRD and SEM analysis the finest granulometric fraction (<63 μm) was analysed because previously found carrying the highest metal concentrations (Chilleri et al, 2019). The mineralogy of the finest sediment size (<63 μm) was analysed with the Rigaku Miniflex XRD. The 2θ angle data

collected (3-75 degree) were imported as a txt file into the data processing software package Sieve for PDF2. Background noise was removed from the raw XRD pattern, but no further smoothing tools were applied. Peaks were recognised using both automatic peak mode and manually checked. The recognised peaks (expressed with *d-spacing* and *intensity*) were matched with the mineral database PDF (Powder Diffraction File) by ICDD (International Center for Diffraction Data) based on known chemistry (lithology and elemental chemistry information). The XRD results were used for a qualitative description of the sediment mineralogy.

SEM observations were performed with an FEI-Quanta 200 SEM coupled with an EDS INCA-X-act-Oxford Instruments (EDS). Samples were dusted lightly onto carbon stubs. No carbon or gold coating was applied as no advantages in image quality with these were observed after a primary test. The sample was first investigated to observed grain heterogeneity at 1 mm scale, then images were acquired at larger scales (100 to 10 μm). X-ray spectra were acquired as single point or chemical maps at 20 KeV (Oxford Instrument, 2008). The peak presence and intensities of Ca, Na, K, Mg, K, Ti, Cu, Zn, Pb, Al, Si, Cl, P, C, S, N, and O were verified in each spectrum. Trace elements were often associated with high standard deviations and thus their concentrations were not considered. Analysis of the whole portion sieved at 2 mm was carried out with a Jeol8100 Superprobe (WDS) with an Oxford Instrument INCA microanalytical system (EDS). Samples were mounted in epoxy-impregnated polished mounts (Davis et al., 1993). Metal-bearing phases were detected using backscatter electron images (BSEM) and energy dispersive detection (EDS). The brightest spots were zircons and monazite, and decreasing the contrast slightly enabled Pb-bearing minerals to be spotted. Once identified, spots of interest were scanned as points or chemically mapped using EDS. Please refer to section 3.1.1 for further information on the instruments.

4.2.3 River catchment geomorphological description

The river catchment geomorphology was described using topography, slope and the grain size distribution of the riverbank, as these have been shown to be the major controls on physical transport and deposition (Macklin et al., 1992, Zhu et al., 2007, Foulds et al., 2014). Topographic features, such as river channel shape and proximity of valley sides and slope calculation, were extrapolated using ArcGIS v.10 from a meter definition LIDAR-Digital Terrain Model (DTM) of the area (Welsh 1m LIDAR, Natural Resources Wales information ©). Raster DTM data are mosaic to a single DTM layer with 'Mosaic to New Raster' following the specific: 'Pixel Type: 8_BIT_unsigned', 'Number of band: '. The 'height contour' and 'slope' tools of ArcGIS Spatial Analysis tools were used to produce height contour and slope maps of the area. The slope is expressed in degrees. A river profile is extrapolated using the 'stack profile' tool from the functional surface in the 3D analyst

tool from the DTM layer. From the attribute tables the data are exported for calculating slope degree using Excel functions. River segments are selected for each sampling area through slope map and stack profile observations. Finally, landscape observations were collected during the three years of research. They include nearby vegetation presence, channel and overbank characteristics, use of land and occurring fluvial morphological transformations. Please refer to section 3.1.2 for further information on fluvial morphology parameters and data elaboration.

4.3 Results

4.3.1 General observation and granulometric description of the sample sites

The sediment pH varied between 4.5 and 5.0 (Table 4.1) with the highest reading recorded in the floodplain samples. Percentages of grain size fractions are presented in Figure 4.3 as site averages. The river banks are generally sandy with silts and clays accounting for between 17% and 36% of the total grain sizes. The highest percentage of silt and clay size is recorded at the most downstream sampling point (RB DS) and the lowest at the first sampled point of the floodplain (RB UPS). The same amounts of silt and clay are observed at GG and DC (24%). Abundant riparian vegetation is observed at T0 and DC, and poor vegetation at GG.

4.3.2 Metal sediment concentration distribution along the catchment

Averaged sediment concentrations of Fe, Pb and Zn are reported here, for a complete list of results refer to Appendix 4.b. Based on the transect averages, Fe, Pb and Zn concentrations vary between 37.3 – 92.6, 0.00 – 24.7 and 0.3 – 4.6 g/kg, respectively (Table 4.1). The highest metal values are shown in the upstream part of the river, but high Zn, Pb, and Fe concentrations are also observed further downstream and in the floodplain. The metal distribution along the river is illustrated in Figure 4.4. The three elements show different patterns: Fe concentrations increase downstream; Pb concentrations are higher in the upstream part where the heaps of mine waste are concentrated, and generally, decrease downstream; Zn concentrations are also highest around the mine spoil but they are also high downstream.

Table 4.1. Metal concentration (g/kg) and pH values averaged for each transect, plus minimum (min), maximum (max) and the average for the whole area. Suggested metal concentration limits are reported as TEL (threshold effect level) and PEL (predicted effect level) from the Environment Agency sediment quality guideline (2008).

River area	Sample	Fe g/kg	Pb g/kg	Zn g/kg	pH
T0	T0 M	37.3	7.4	1.3	4.7
WM	CW J	46.4	24.7	1.5	4.4
WM	WM K	47.1	23.8	4.6	4.6
GG	GG L	64.7	4.5	1.0	4.7
DC	DC D	67.3	5.3	0.9	4.8
DC	DC E	56.6	3.8	0.8	4.7
DC	DC F	53.2	20.3	1.5	4.5
DC	DC G	61.8	11.3	1.1	4.6
DC	DC H	67.6	11.1	0.9	4.8
RB	RB B	92.6	2.6	1.3	5
RB	RB C	76.9	11.0	2.7	5
RB	RB DEP C	58.4	2.2	2.0	5
RB	RB D	79.2	7.4	1.4	5
RB	RB I	82.0	8.3	1.5	4.7
RB	RB DEP B	66.8	1.7	1.6	5
RB	RB DEP A	66.3	2.2	1.6	5
RB	RB A	82.0	0	0.3	4.9
min		37.3	0	0.3	4.4
max		92.6	24.7	4.6	5.0
average		65.1	8.7	1.5	4.8
TEL		-	0.035	0.123	
PEL		-	0.091	0.315	

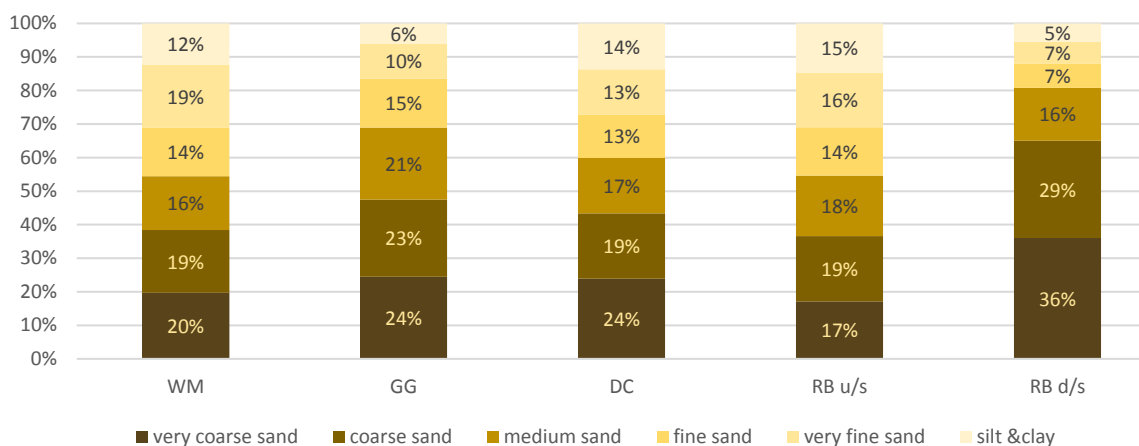


Figure 4.3. Grain size percentage averaged for all the sampling areas from the upstream site WM until the most downstream RB d/s.

Although the T0 area is located upstream of the mine tips, its sediment has high Pb and Zn concentrations. For the selected sample XRF results show peaks of 18.4 and 29.2 g/kg for Pb and Zn, respectively. Therefore, its description will be associated with the Wemyss Mine (WM) and Mill Race sediment (CW) which have similar mineralogical associations. The area shows a range of Fe concentrations between 47.1 – 37.3 g/kg, Pb concentrations between 24.7 – 7.4 g/kg and Zn concentrations between 4.6 and 1.3 g/kg (Table 4.1). The values of selected samples are between the average ranges for Fe, but they show higher concentrations in Pb for CW and WM and in Zn for the T0 sample (T0 M2, CW J1 and WM K4 in Table 4.2). Graiggoch Mine sediments have an average of 64.7 g/kg for Fe, 4.5 g/kg for Pb and 1.0 g/kg for Zn (Table 4.1). The selected sample has a slightly lower Fe and Pb concentration than the averages (GG – L1 in Table 4.2). The sediment in this area has lower Pb concentrations than those in the mine heaps in the upper part. Along the depositional area observed at middle river length (DC) metal concentration ranges 67.6 – 53.2 g/kg for Fe, 20.3 – 3.8 g/kg for Pb and 1.5 – 0.8 g/kg for Zn (Table 4.1). The values of the selected samples are within the indicated range with the exception of a lower Zn concentration in DC – F2 (Table 4.2). The sediment samples collected from the floodplain have Fe concentrations between 92.6 – 58.4 g/kg, Pb 1.10 g/kg or less and Zn between 0.3 and 2.7 g/kg (Table 4.1). The lowest values of Pb and the highest of Fe are measured in the further downstream samples (RB DS – A1 in Table 4.2).

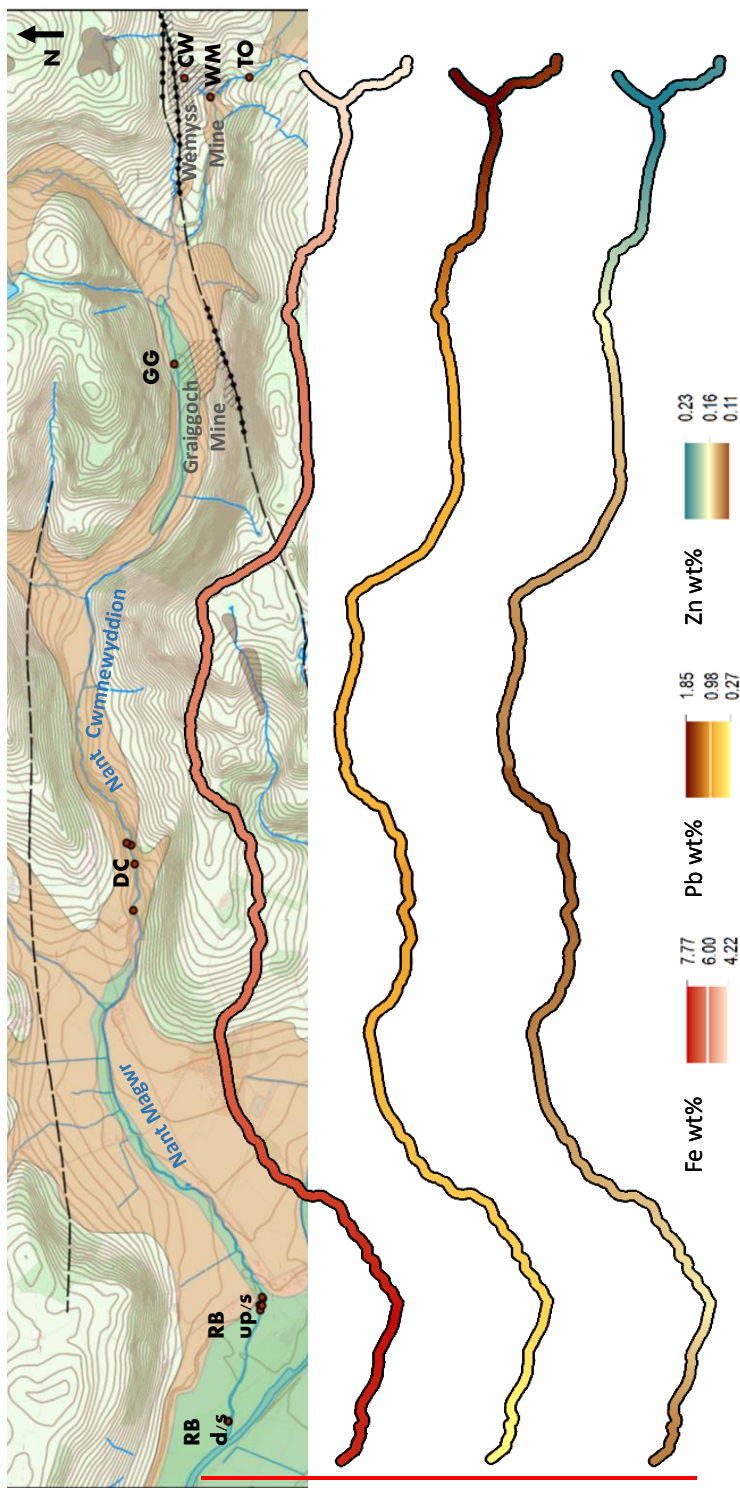


Figure 4.4. Iron, Pb and Zn sediment concentrations in weight % along the river. Please refer to Figure 4.3 for a complete legend of the background image.

Table 4.2 Iron, Pb and Zn concentrations of the 10 sediment samples selected for geochemical and mineralogical analysis.

Sample	Fe g/kg	Pb g/kg	Zn g/kg
T0 - M2	40.4	18.4	29.2
CW - J1	43.7	42.5	0.9
MP - K4	43.3	31.6	13.3
GG - L1	50.2	2.9	1.1
DK - E7	57.8	3.2	0.8
DK - F 1d	50.2	0	2.2
DK - F2	50.1	16.1	0.3
RB UP/S - C1	76.3	9.3	2.8
RB UP/S - C2	77.6	12.7	2.6
RB D/S - A1	84.7	0	0.4

4.3.3 Proposed sediment mineralogy and related metals

XRD results indicate the presence of a common association of bulk minerals over all the catchment. These are mainly represented by quartz, feldspar, rutile, illite, and chlorite. The upstream samples are characterised by the presence of sulfate minerals, such as anglesite or hydrated Pb sulfate, and Cu-bearing jarosite. Oxide and hydroxide minerals are low in Fe and enriched in Al, Mn, and Ti. Phosphate containing Mg – Al or Fe – Mn phases are also observed. In Graiggoch Mine secondary minerals are jarosite, pyromorphite, and Mn hydroxide. At the middle length of the river the presence of sulfide is more evident, such as sphalerite and Cu – Fe, Cu – Fe – As and Pb - Sb sulfides. In addition, traces of Mn, Fe and Al hydro-oxide and anglesite are reported. In the floodplain the minerals present are sulfides such as sphalerite and galena, sulfate probably in the form of a Ca – Zn jarosite and Pb-bearing hydrate phosphate which is likely pyromorphite. Finally, metal-bearing oxides and hydroxides are observed, including Mn hydroxide, Cu oxide, Fe oxide, Fe – Mo oxide hydrate, Bi – As – Mo oxide, Pb – Fe – Mn oxide, Mg – Mn – Zn hydroxide hydrate and Ni – Ti – Sb oxide. XRD data are reported in Appendix 4.c.

SEM results are reported briefly here; further sample details (including images) and EDS spectra are available in Appendix 4.d. Samples from the upstream part of the system have phyllosilicate minerals in foliated aggregated particles often associated with Zn and Pb high concentrations. Molybdenum is occasionally highly concentrated and it occurs with sulfate within Zn and Pb phases. Cobalt is associated with Fe in phyllosilicate minerals. More detailed information is reported in Appendix 4.d.1 (WM – K4) and Appendix 4.d.2 (T0 – M2). SEM images and spectra of the GG samples reveal significant quantities of euhedral quartz. Acicular crystals of rutile ranging in diameter from

1000 to 70 nm are also present. Significant quantities of Zn and Pb are associated with phyllosilicate phases. A layer of Fe, Mn, and S associated with O (likely a sulfate) appears to cover the phyllosilicate phases. More detailed information on the GG – L1 sample is included in Appendix 4.d.3. The SEM images and element analysis of sample DC highlight significant concentrations of Pb, As and Sb, often within phyllosilicate minerals. No Zn-bearing minerals or phases were identified by XRD or SEM. This is in accordance with the Zn average of the pXRF results which indicate lower concentrations of Zn in this area. Appendix 4.d.4,5,6,7 and 8 reports more detailed information on DC – F1d and F2. The SEM data for floodplain samples show that Pb and Zn are associated with elements found in phyllosilicates (Mg, Fe, Si, Al, and O), suggesting their uptake on the mineral surface. Moreover, S and P are often associated with Pb, Zn, and these phyllosilicate elements. Molybdenum has a significant presence, both associated with phyllosilicate minerals or with S. Iron hydroxides are present as layering cementing clay crystals in aggregate. Nanosized minerals are observed in some SEM images; their compositions can be related to silicate, aluminosilicates or Mn – Fe oxides. Appendix 4.d.9, 10 and 11 reports detailed information on RB – C1 and C2 samples.

Images and spectra acquired with the Jeol8100 Superprobe show a general presence of mudstone detritus and bulk minerals as quartz, feldspar, and phyllosilicate. Zircon, monazite, rutile, and ilmenite are found in all the samples.

An overview image of sample T0 M2 (0 m) shows root and seed fragments, 50 – 500 um mudstone clasts and sub-angular aggregates of well-shaped minerals (quartz, rutile, zircon, and phyllosilicate) cemented by an amorphous phase (Figure 4.5.a). Mainly Fe-oxides form this cementing phase with low concentration of Pb, S, Cl, and P in the spectra background (Figure 4.5.b). Small amounts of Cr and Ni (0.32 wt. %) are associated with phyllosilicate elements. Generally, significant amounts of Zn and Mn are measured. An overview of sample WM K4 (Wemyss Mine Tips) in Figure 4.6.a shows 0.5 – 1 mm mudstone clasts, fragments of angular and acicular minerals, and vegetation fragments.

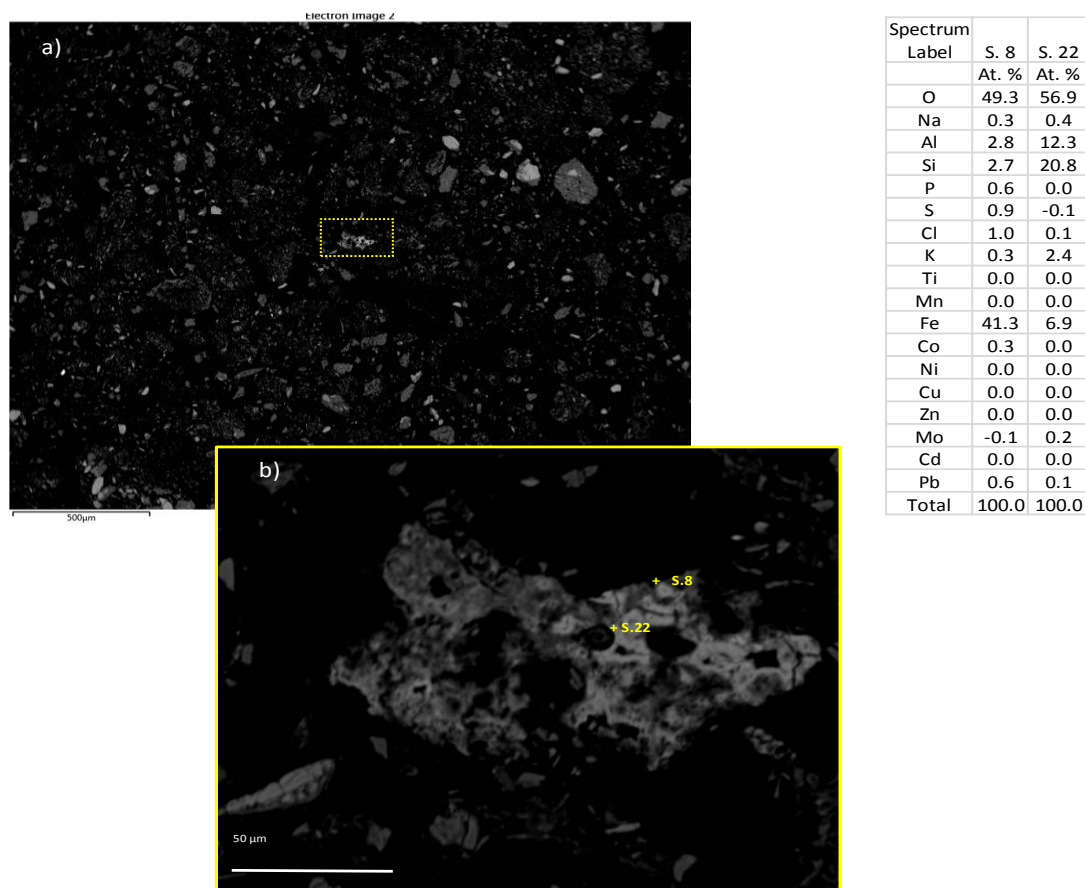


Figure 4.5. Sample T0 M2, upstream mine site. a) Overview of the sample showing plant and shale fragments, angular and acicular minerals (quartz, phyllosilicate, rutile, and zirconium) sometime agglomerate and cemented by a Fe-Oxide paste. b) Detailed image of a phyllosilicate agglomerate cemented by a Fe oxide paste enriched in Pb bearing phases likely represented by anglesite, plumbojarosite, and pyromorphite.

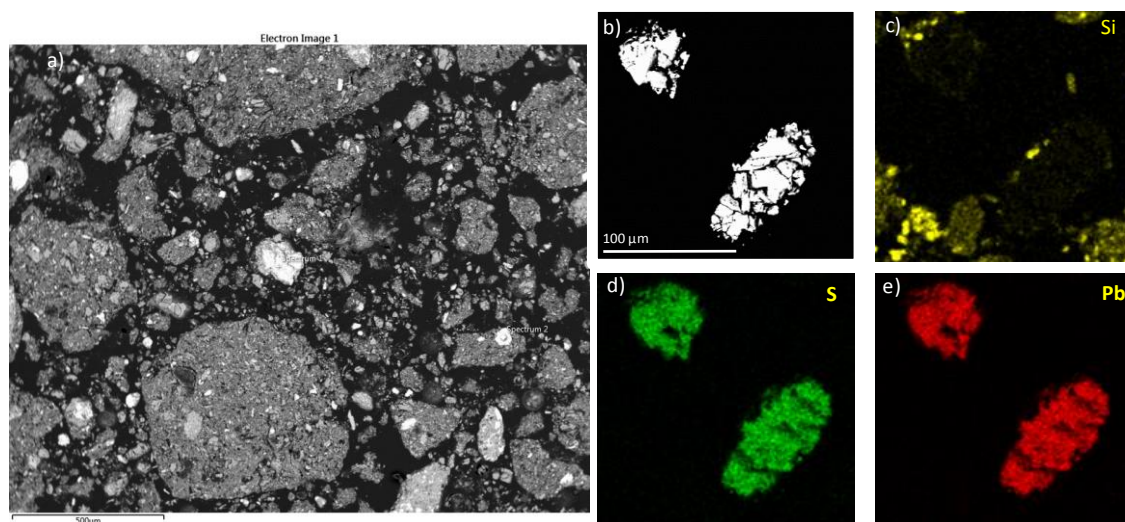


Figure 4.6. Sample WM K4, Wemyss Mine tips. a) Overview of the sample showing angular and acicular minerals (monazite, rutile, feldspar, and phyllosilicate) sometime agglomerate and cemented in 1 – 0.5 mm cluster. Any Pb or Zn bearing metals were observed in this area. b) Low

brightness image of galena grains showing the cubical fractures. c), d) and e) Element map of the galena grain showing respectively Si, S, and Pb intensity.

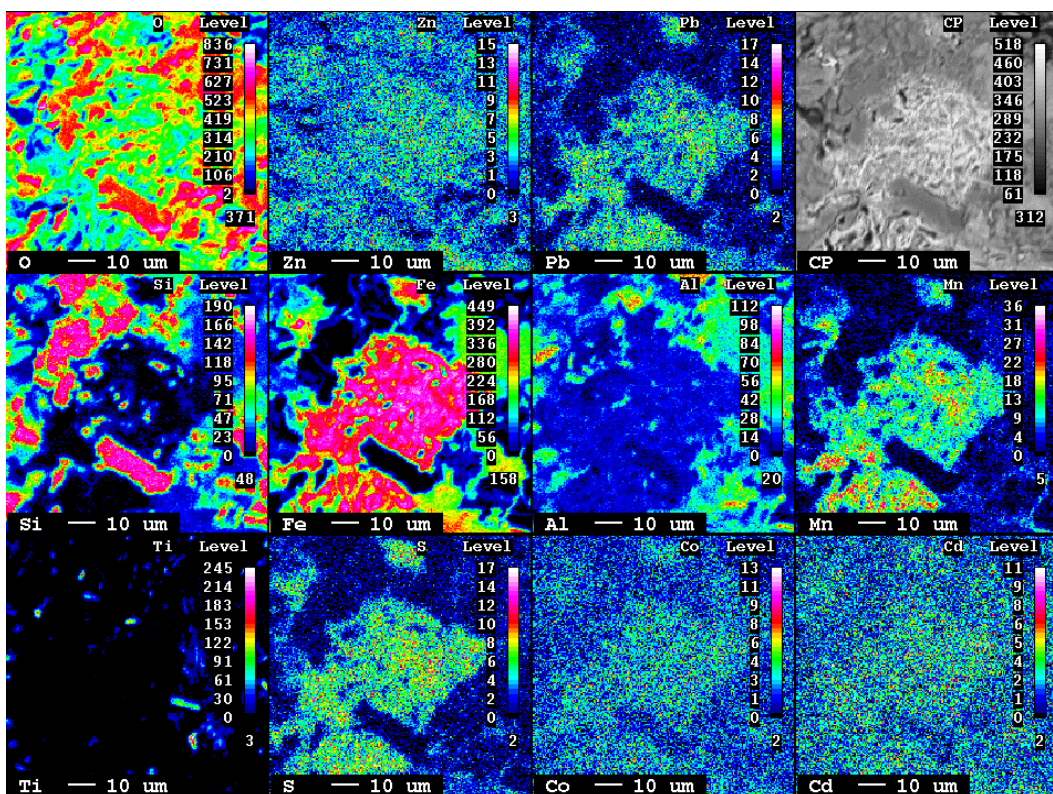


Figure 4.7. Sample WM K4, Wemyss Mine tip. Detailed elementary maps acquired with Jeol8100 Superprobe (WDS) on an amorphous cement phase of Fe Oxide (Fe) enriched in Zn, Pb, S, and Mn. Trapped and surrounding minerals are mainly represented by silicate (Si) and rutile (Ti).

Monazite, rutile, feldspar, and phyllosilicate are identified, and the cement is Fe-oxide with high amounts of Zn, Pb, and sulfate. An EDS map on two 50 – 100 μm elongated bright minerals are enriched in Pb and S, suggesting that these are galena. The cubical fracturing of these grains is highlighted when the brightness is turned down (Figure 4.6.b.c.d.). A further map acquired with the Jeol8100 Superprobe (WDS) shows the composition of the amorphous cement as Fe-oxide (Figure 4.7). The element concentration represented by the colored level bar shows an O – Fe ratio between 1 to 2, indicating a potential goethite or hematite mineralogy. Low amounts of Pb, Zn, S, Mn, Cd, and Co are observed in this mineral phase. The sediment sample from the Mill Race headwater (CW J1) is enriched in bulk minerals observed as single crystals (< 200 μm) or as aggregated clusters (< 1 mm) with plant fragments. Monazite and zircon minerals mainly represent the brightest grains. The monazite grains reach up to 0.5 mm in length. No secondary sulfates or Fe oxides are observed. Iron is generally associated with phyllosilicates. No significant presence of Zn was recorded, but galena grains are occasionally spotted in the sample. A Jeol8100 Superprobe

(WDS) map (Figure 4.8) shows a galena grain and its cubic habit with associated trace Zn, Co and Cd. The edge of the grain is weathered, with secondary Fe-oxide or plumbojarosite observed.

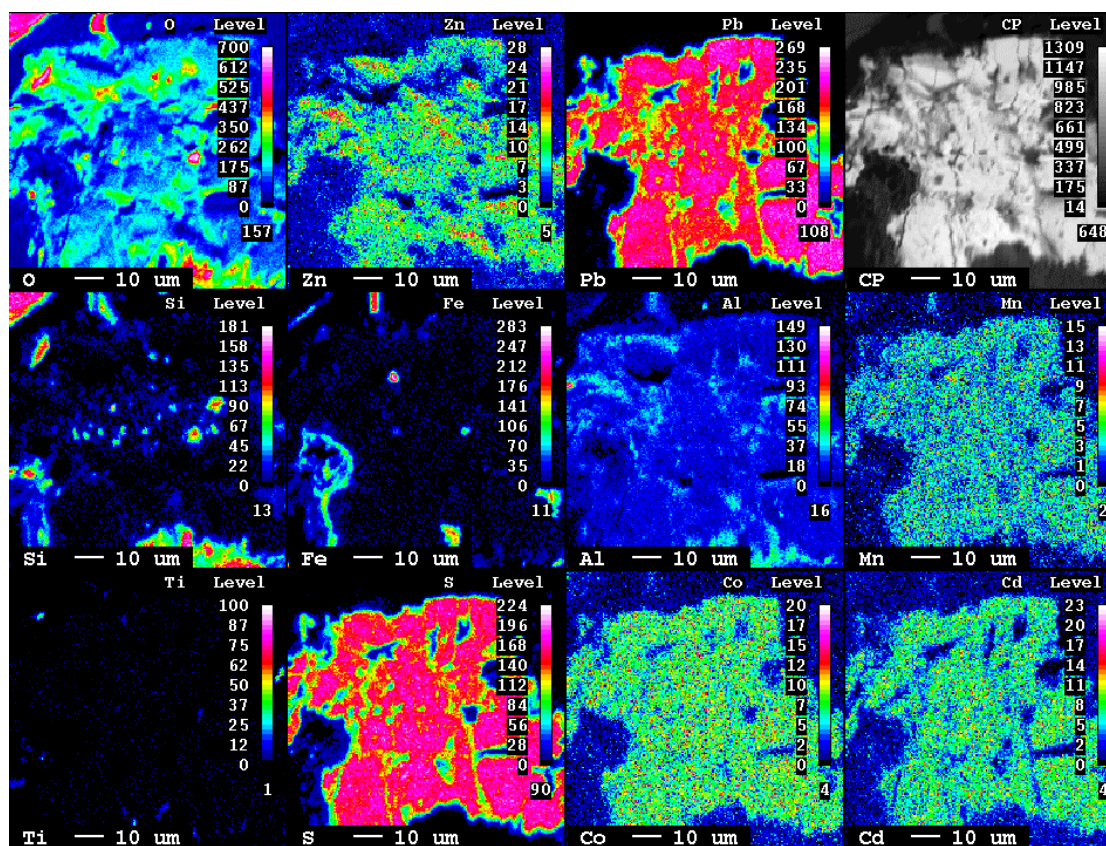


Figure 4.8. Sample CW J1, Mill Race headwater sediment. Detailed elementary maps acquired with Jeol8100 Superprobe (WDS) on a galena grain showing cubical fractures and weathered edges. Zinc, Co and Cd low levels of concentration are associated with the grain.

The Graiggoch Mine sample (GG L1) is represented by mudstone detritus and bulk minerals agglomerated in 0.1 – 0.5 mm clusters or in crystals of various sizes. Plant fragments were also observed. Both primary and secondary minerals are present. A Co-, Cd- and Zn-bearing galena grain was also mapped. Iron and Mn oxides are often observed around the mineral clusters, containing Pb and sometimes Zn. Figure 4.9 shows a weathered edge of a cluster with Fe oxide cement associated with pyromorphite and an Mn - Pb oxide phase (ratio 3 to 1). Numerous spectra of native Cu associated with Zn, Cr, Sn, Ni, and other trace elements were acquired (Figure 4.10). These phases are likely generated by the degradation of anthropogenic detritus possibly linked to mining or to the reprofiling of the riverbank.

Around the middle river length, sample DC E7 was collected on a depositional side of a meander. Bulk minerals and mudstone detritus with rounded shapes are present. Furthermore, several euhedral monazite crystals are observed. Amorphous Fe or Mn oxide phases are found in

association with sphalerite and galena that occur around bulk minerals (Figure 4.11). Some of the sphalerite minerals contains up to 4 wt. % Mo. Further associated secondary minerals are pyromorphite and Zn and Pb sulfides. The EDS analysis also suggests that Cr and Ni are present (Figure 4.11). Samples DC F1d and DC F2 collected on the riverbank show high concentrations of Pb and Zn. In sample F2, collected 60 cm from the river water level, bulk weathered and fragmented bulk minerals and vegetation fragments are observed. Sphalerite grains are spotted showing different degrees of weathering and bearing Mo and Pb (Figure 4.12 and 4.13, respectively). A paste covering a rounded high in C fragment is formed by anglesite associated with Zn sulfur phases (Figure 4.13). At the water level, sample F1d contains angular bulk mineral associated with galena, zircon, and Pb- and Zn-bearing Fe oxides. Lead is present both as primary mineral, galena, and as secondary minerals with compositions matching anglesite and plumbo-jarosite inter-cemented in weathered mudstone detritus (Figure 4.14). Lead-bearing mineral contains about 2 wt. % Co. Both samples contain trace amounts of Ni and Cr.

The samples from the depositional area, RB A1 and C1, are enriched in Pb-bearing Fe oxides (Figure 4.15). No Zn-bearing phases were observed. Phyllosilicate minerals contain trace amounts of Ni and Cr, and occasionally high amounts of Fe. Generally, bulk minerals and mudstone detritus are weathered and fragmented and no plant fragments are observed.

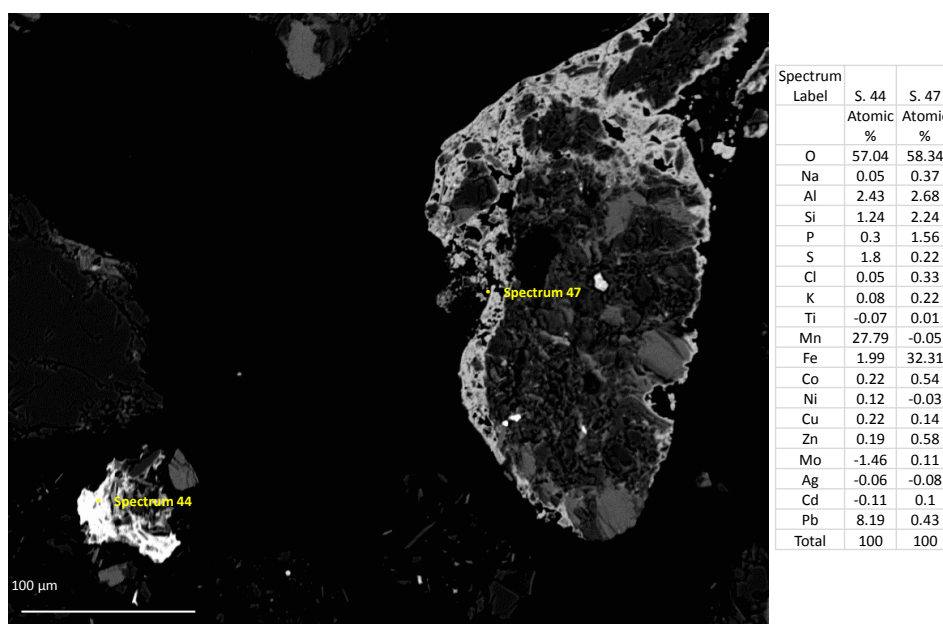


Figure 4.9. Sample GG L1, Graiggoch Mine river bank sediment. On the right, mudstone grain with silicate and monazite minerals covered by Zn-bearing Fe oxides associated with pyromorphite (s.47). On the left, mineral phase of Mn and Pb oxide associated with a low concentration of Fe, Zn, Cu and Co (s.44).

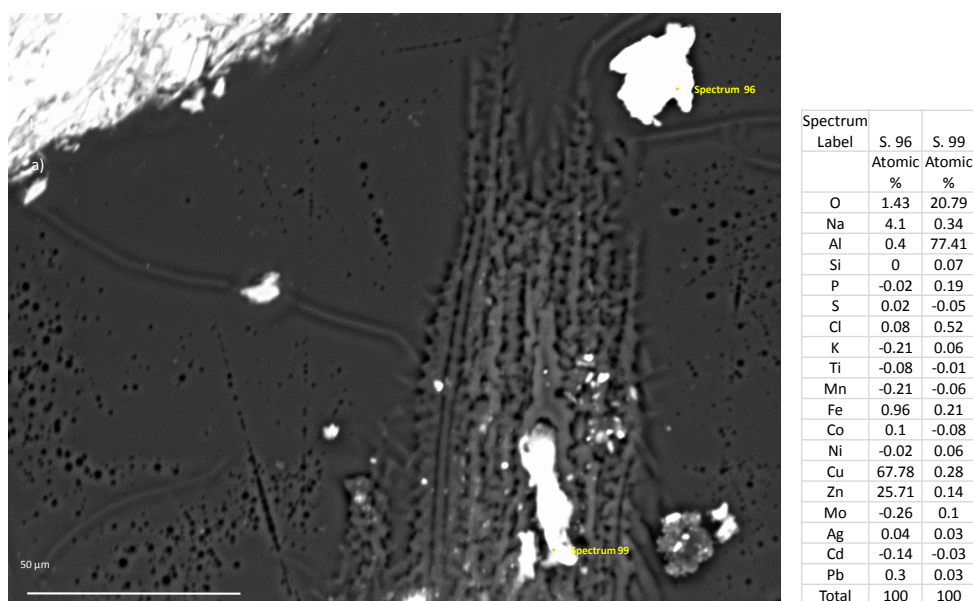


Figure 4.10. Sample GG L1, Graiggoch Mine river bank sediment. a) Image of an anthropogenic fragment of fabric containing aluminum (s. 99) and copper fragments (s.96) surrounded by silicate minerals. Sn, Zn, and Cr are associated with these metals and weathered phases.

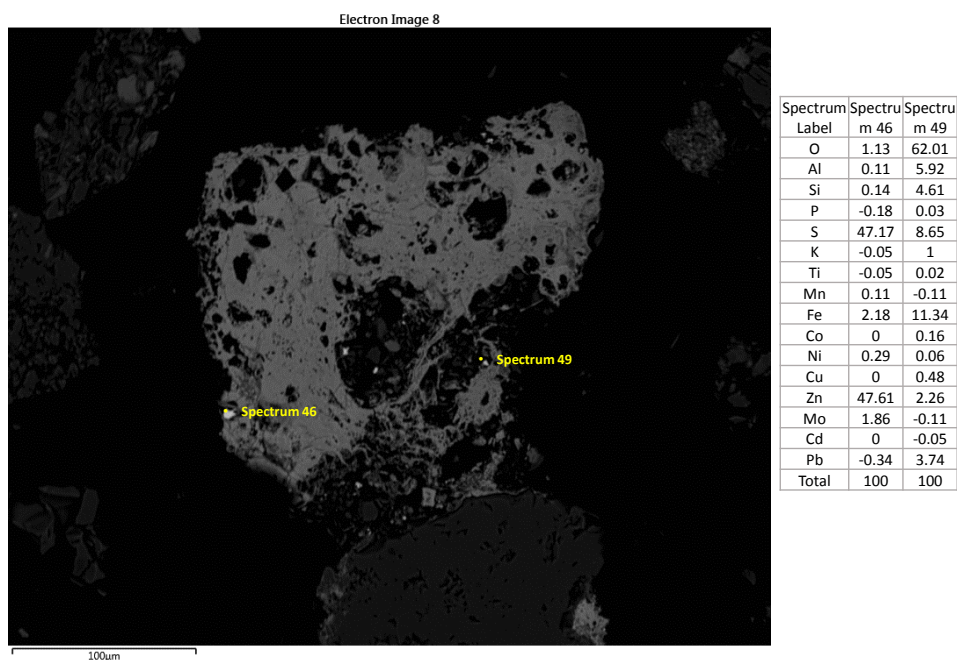


Figure 4.11. Sample DC E7, depositional area at the river middle length. Amorphous Fe-oxide cementation around silicate, rutile, and sphalerite (s.46) minerals. Lead-sulfate (s.49) and trace amount of Ni, Cr, and Zn are often associated with the Fe- oxide cement composition.

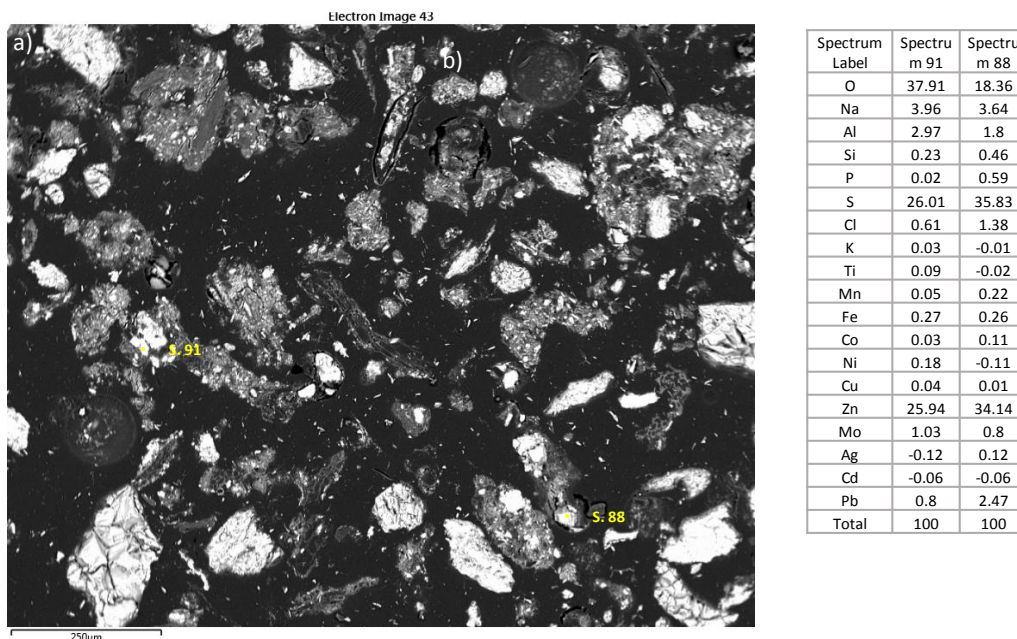


Figure 4.12. Sample DC F2, depositional area at the river middle length. Overview of the riverbank sample collected at 60 cm above the river water level showing plant fragment, weathered detritus, and bulk minerals. Grains of sphalerite (s.91) sometimes associated with lead (s.88) are easily spotted in the sample.

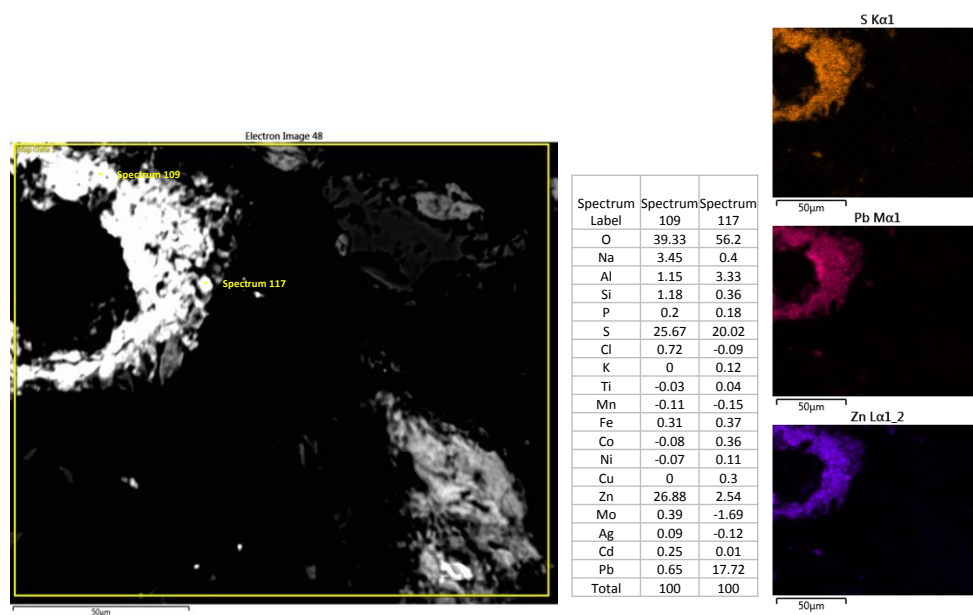


Figure 4.13. Sample DC F2, depositional area at the river middle length. Detail of Pb- and Zn- sulfur grains and weathering processes found in the proximity of a fragment high in carbon concentration (S.109, S.117). On the right, EDS maps show S, Pb, and Zn distribution.

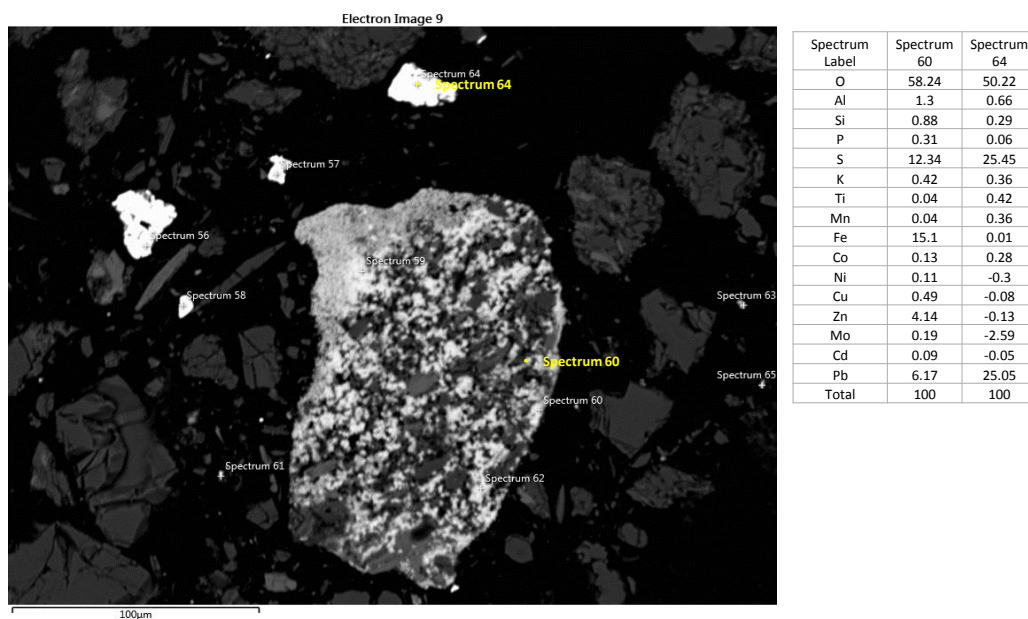


Figure 4.14. Sample DC F1d, depositional area at the river middle length. Details of a riverbank sample collected at the water level showing well shaped galena minerals (s.64) and secondary minerals, likely anglesite and/or plumbojarosite (s.60) formed in the weathered detritus.

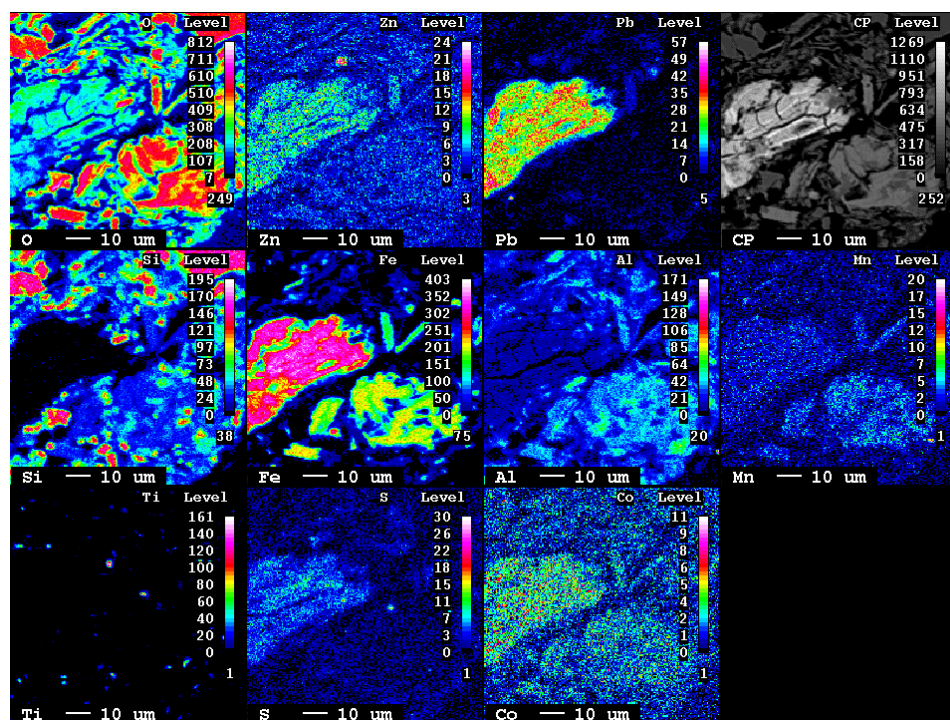


Figure 4.15. Sample RB up/s C1, the upper part of the floodplain. Detailed elementary maps acquired with Jeol8100 Superprobe (WDS) on a Fe oxide associated with Pb concentrations.

4.3.3 River catchment geomorphological description

Height contours and slope of the studied river are presented in Figure 4.16. The river channel at the headwater (0-180 m) has the highest slope of 5.1° . The river segment upstream of the mine area is surrounded by dense vegetation and steep valley sides with a bedrock channel bed. At the mine area, the right bank (facing downstream) of the river crosses loose sandy mine waste and is characterised by low river banks of clay and sand deposits. Occasionally sand is deposited in pools and alcoves of the river channel. Lateral accretions of the channel and erosion of mine waste were observed during site visits. Dense vegetation is present along the left river bank. Around Graiggoch Mine (1110 - 2620 m) the channel crosses a wide valley and has a slope of 1.2° . The river channel is straight at this position, likely imposed by the mine workings, the side road and the farm use of the land. Three bridges (at about 1316, 1820 and 1932 m) for animals or trucks cross the river. The channel bed is 1-2 m wide and is covered by glacial deposits and occasional gravel-sand bars. The vegetation is mainly short grass. At the middle river segment (3000 - 4070 m), the river channel is bedrock-controlled and has a slope of 1.2° . The channel bed is formed alternatively by bedrock and sand pockets. The valley sides are close to the channel and covered by dense wooded and shrub-like vegetation. The river channel here occasionally meanders, creating 0 to 2 m high river banks. Overbank riparian vegetation, such as fern, nettle, and rushes, is abundant. The highest banks are characterised by interlayered clays and sands, whereas the lowest banks contain coarse sand and gravel fluvial deposits. During the three year research period (2015-2017) log cabins, a wooden swing and a pool were built around the river channel for recreational use. The floodplain river segment (5810 – 6740 m) has the lowest slope of 0.6° across the alluvial valley. The river channel meanders, except for the segment crossed by the main road which is channelised using wooden piles. The height of the river bank varies from 0 to 2 m. The area is used mainly as farmland, and channel bed animal crossings occur in the most downstream segment. The channel bed comprises mainly coarse fluvial deposits and the riverbanks, when present, comprise interlayered sand and clay.

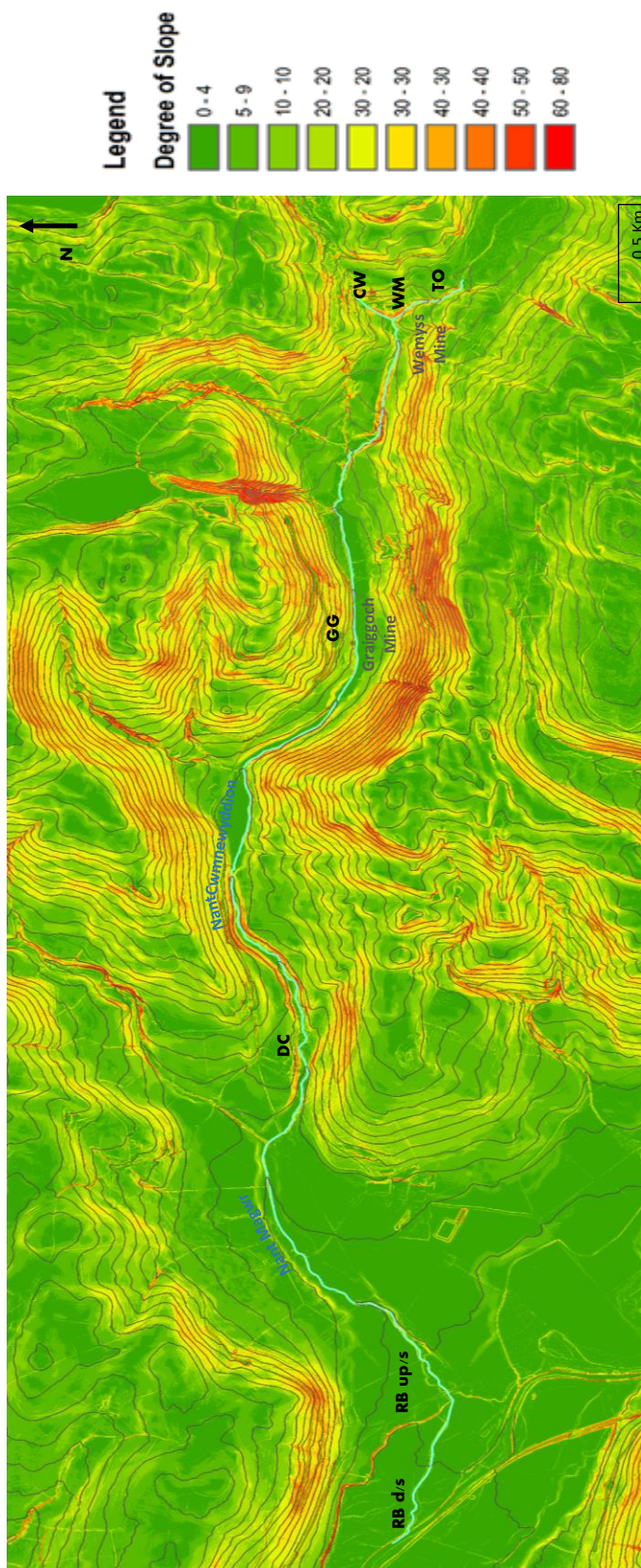


Figure 4.16. Topography and slope map of the research site. Elaborated with ArcGIS from 1 meter resolution LIDAR images (Natural Resources Wales information ©).

4.4 Discussion

4.4.1 Geochemistry of sediments along the catchment

Zinc and Pb concentrations throughout the catchment are higher than the PEL (predicted effect level) values (315 and 91 mg/kg respectively) reported by the Environment Agency (2008b). The only values below the TEL (threshold effect level, 123 mg/kg for Zn and 35 mg/kg for Pb) (Environment Agency, 2008b) are the concentrations measured in a riverbank in the downstream side of the floodplain (Table 4.1). Therefore, according to the PEL system, the channel and overbank sediments are potentially harmful to the surrounding ecosystem. Concentrations of Zn and Pb vary along the river. Upstream of the Wemyss Mine waste piles, Zn and Pb concentrations should reflect the background values, but the values are not the lowest measured along the catchment. The sampled area is situated in proximity of the mineral vein between Wemyss and Frongoch Mines. Therefore, either background values or mine waste transport in the sampling area by erosion or anthropogenic processes can justify the observed values. The mine waste of Wemyss Mine shows among the highest values of Zn and Pb, likely due to the presence of galena and sphalerite grains. Around Graiggoch Mine, Pb concentrations are lower than the upstream mine waste possibly due to reprofiling of the river banks and mixing of mine waste with uncontaminated sediment. Generally, high Pb and Zn concentrations are associated with secondary oxide and phosphate minerals rather than sulfates. Further downstream in the middle reach and the floodplain, high to low concentrations of Zn and Pb are recorded in the sediments, and these can be linked mostly to the presence of secondary minerals bearing these metals. Lead- and Zn-rich sediment in these areas is also locally associated with primary minerals transported downstream.

Lead and Zn concentrations observed in this study are in accordance with the previous literature. Sediment concentrations of Pb from the mine site can be compared to a previous study carried by (Palumbo-Roe et al., 2013). Wemyss Mine concentrations (WM and CW) are similar to the average of values found by Palumbo-Roe et al. (2013). Graiggoch Pb concentrations are lower compared to the average Pb concentrations reported by the Palumbo-Roe et al. (2013) but are included in their Pb concentration range (Table 4.3). Therefore, considering the previous study and the observed clear Pb peaks in EDS SEM and Superprobe spectra acquisitions, higher than observed Pb concentrations at Graiggoch Mine are present. Generally, Zn and Pb concentrations in the Nant Cwmnewyddion and the Nant Magwr, averaged for all the sites, fit into the values of sediment concentrations measured in similar mining-impacted rivers in Wales and England (Table 4.4) (Byrne et al., 2010). Lead concentrations are higher than those in the other sites likely due to the short

length of the river, about 7 km. The comparison among studies is only indicative due to the different measured sediment size fractions and metal concentration analysis methods.

The Zn and Pb minerals in the Cwmnewyddion and Magwr river systems are also typical of Zn and Pb mining areas with low amounts of pyrite and carbonate (Byrne et al., 2010, Palumbo-Roe et al., 2016). Bulk minerals are observed along all the catchment, they are mainly quartz, feldspar, illite, and chlorite, plus associate minerals as monazite, rutile, and zircon. Zinc and Pb primary minerals are galena and sphalerite localised in the upstream part. The secondary mineral geochemistry reflects the presence of phosphate, silicate, and sulfate as anion and Pb, Zn, plus trace metal (Mo, Co, Ni, Cr) as cations. Suggested minerals are anglesite, plumbojarosite, pyromorphite, Pb- and Zn-bearing phyllosilicates. Following the nomenclature reported in Hudson-Edwards et al. (1996) these secondary minerals can be labeled as CSPA (carbonate, silicate, phosphate, and sulfate). Iron- and Mn- hydroxides and secondary sulfates are present as secondary weathering products likely both directly precipitated or forming as replacement of other minerals (Hudson-Edwards et al., 1996). The weathering products occur either at the headwaters with the primary minerals or further downstream, where they are more abundant and varied. A similar mineralogical suite for the Wemyss and Graiggoch Mines was described by Palumbo-Roe et al. (2013).

Table 4.3 Lead concentrations of Wemyss and Graiggoch Mines from this study and previous literature (Palumbo-Roe et al, 2013 modified).

Mining Area	Size Fraction	Pb mg/kg	Reference
Wemyss Mine	<2 mm	24700	This study
Wemyss Mine	<2 mm	23800	This study
Wemyss Mine	<250 um	28059	Palumbo et al 2013
Graiggoch Mine	<2mm	4500	This study
Graiggoch Mine	<250 um	30540	Palumbo et al 2013

Table 4.4 Comparison of Zn and Pb total concentrations measured in river sediment in Wales and England (Byrne et al, 2010 modified).

River	Size Fraction um	Pb mg/kg	Zn mg/kg	Reference
Cwmnwyddion - Magwar, Wales	<2000	8682	1529	This study
Afon Twymin, Wales	<63	3077	230	Byrne et al (2010)
Afon Twymin, Wales	<2000	6411	6955	Wolfenden and Lewin (1978)
Afon Towy, Wales	<2000	949	768	Wolfenden and Lewin (1978)
River Allen, England	<170	2330	1410	Goodyear et al (1996)
River Aire, England	<63	194	506	Walling et al (20033)
River Calder, England	<63	343	907	Walling et al (20033)
Red River, England	<2000	120	630	Yim (1981)
Afon Tawe, Wales	<2000	6993	35796	Vivian and Massie (1977)

Gangue and sulfide mineral weathering processes result in the formation of secondary minerals, such as CSPA, Mn- and Fe- oxyhydroxides, and potentially, or release of metal in the aqueous form (Hudson-Edwards et al., 1996, Nordstrom, 2011, Lynch et al., 2014). The observed mineral suite provides evidence of geochemical settings where these processes occur. Oxidising conditions enhance sphalerite and galena weathering and the release of SO_4 , Zn and Pb. Anglesite is the sulfate mineral formed from galena oxidation, but sphalerite oxidation tends to release Zn as an aqueous phase in circum-neutral river water (Lee et al., 2002). In the studied river system Fe and Mn can be released by oxidative weathering of chlorite and illite minerals (Ross et al., 1982). Iron and Mn oxyhydroxides have formed on weathered surfaces or directly by precipitation depending on redox and pH conditions. During their precipitation these oxyhydroxides can take up trace metals, forming the observed Pb – Mn oxyhydroxides and Pb- and Zn-bearing Fe oxyhydroxides. Plumbojarosite minerals are formed when, as well as Fe concentrations, SO_4 is present as an aqueous species. Phosphate minerals are found mainly as trace minerals associated with plumbojarosite or Mn and Fe oxyhydroxides likely co-precipitating or depositing on their surface.

Primary minerals and the formation of secondary minerals represent a storage system of trace metals into solid phases until changing geochemical conditions trigger mineral instability (Hudson-Edwards et al., 1996). River systems can easily show all these variabilities. Sediment at the headwater of Wemyss Mine can release Zn and Pb from primary minerals both as aqueous or solid phases. Along the river, metals can be trapped physically (deposit) or chemically (precipitate or be adsorbed), as in Graiggoch Mine or in sediment further downstream where both primary and secondary metal-enriched minerals are observed. Along the Nant Cwmnewyddion and the Nant

Magwr, as in similar river systems, mobilisation of metal enriched sediment is expected to occur mainly during high flow conditions at Wemyss Mine (Kincey et al., 2018). Furthermore, chemical metal release or up-take from metal-bearing mineral phases may occur when certain pH or redox settings are reached; this can occur due to streamflow variations, the mixing of water or the soil formation (Wilkin, 2008). Therefore, geochemical and mineralogical investigations of metal-bearing phases are fundamental to anticipate their potential metal release and to inform remediation strategies.

4.4.2 Fluvial morphological control on Zn and Pb bearing minerals distribution

Mining impacted rivers are often subject to active fluvial morphological processes that aim to restore geomorphological equilibrium disturbed by spoil material, use of water and ore extractions (Miller, 1997). Fluvial morphological processes include aggradation and degradation events such as erosion of banks and terraces, deposition and storage of sediments. In this study, areas along the catchment can be classified as erosional, transport or depositional. The geomorphological features (channel, slopes, and meanders, etc.) observed along the river catchment can be associated with different geochemical settings (Ciszewski and Grygar, 2016). Together with hydrological conditions (such as streamflow variations), accumulation, erosion or variations in the permeability of sediment can be significant controllers of pH-redox reactions, metal and minerals residence time (Hudson-Edwards, 2003).

The upstream part of the river is characterised by an accumulation of mine waste at the Wemyss Mine. Over the mine's history, this part of the river was continuously fed with mine waste coming from both Wemyss and the closed Frongoch Mine sites. The capacity to store mine waste could have been limited by the steep valley sides. Therefore, for decades, erosion likely conveyed sediments into the fluvial system. Numerous surveys at the field site showed that erosion of the tips was evident, and this caused changes in the riverbed shape and size. This 0 to 180 m area can be classified as an *erosional area* due to this continuous degradation (Figure 4.17). Here Zn and Pb primary minerals or secondary phases, as anglesite, can be washed downstream by degradation processes. Anglesite minerals, being stable at the given water conditions (Hudson-Edwards et al., 1998), may contribute to the suspended sediment, particularly during high streamflow conditions.

The erosion of the fine-grained waste was observed in the upstream segment, although, accumulation of this material was not observed in the Graiggoch Mine segment. As well known in the literature, dispersion of fine-grained sediment can potentially occur across streamflow

Wemyss Mine area (river segment 0-180 m)

Proposed ruling process: Erosion of Pb- and Zn- enriched sediments.

Sediment geochemistry:

- Pb 24 g/kg
- Zn 4.6 g/kg
- Galena
- Zn- and SO₄-bearing Fe oxide
- Anglesite
- Pb-bearing Fe oxide
- Pyromorphite

Fluvial morphology parameters:

- Steep loose mine waste tips
- Degradation processes observed
- Narrow bedrock river channel
- Small sandy sediment pockets in the channel
- 5.1° slope
- 20 % Silt & Clay

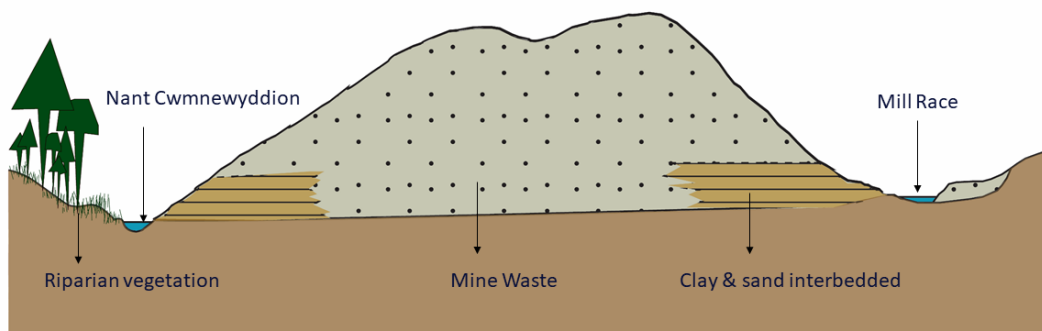


Figure 4.17. Wemyss Mine summary of sediment geochemistry and fluvial morphological parameters to identify the main processes driving Pb and Zn dispersion.

conditions and not only during high energy storm or high flow conditions (Davies et al, 1974). This area has a wide river channel characterised by glacial sand and gravel lens on the riverbed (GG in Figure 4.2) which may enhance the circulation of water (Mayes et al., 2008). Therefore, the river segment from 1110 to 2620 m (which includes the Graiggoch Mine), mainly characterised by downstream passive sediment transport, is classified as a *transport area* (Figure 4.18). In addition, among the geochemical phases, Mn oxides are found associated with Pb, mineral phases found when hyporheic water and river water interact. Their presence, together with the speculated enhanced water circulation due to the sand and gravel lens, may indicate the presence of a hyporheic zone. Here trapped Pb is not likely released in the river water unless reducing conditions are generated, which could occur during prolonged periods of high streamflow (Lynch et al., 2018).

In the geological map (BGS, 2013) a depositional accumulation from glacial and fluvial processes is reported (Figure 4.1) at about 3000 m downstream (DC) where the height contouring describes first a widening followed by a shrinking of the valley side. This morphology of the land forced the river velocity to slow down forming meanders and sediment depositions. For instance, fine-grained sediments, similar to those observed at the Wemyss Mine site, occur in prominent depositions. This area (3000-4070 m) is believed to be a 'trap of sediment' controlled by the bedrock with low

Graiggoch Mine area (river segment 1110-2620 m)

Proposed ruling process: Sediment transport area with hyporheic zone trapping Pb in Mn-oxide minerals.

Sediment geochemistry:

- Pb 5 g/kg
- Pb- Mn Oxide
- Pyromorphite
- Galena
- Pb-bearing phyllosilicates
- Zn 1 g/kg
- Zn- bearing Fe oxide
- Zn- bearing phyllosilicate

Fluvial morphology parameters:

- Wide valley
- Wide straightened river channel
- Glacial and fluvial channel bed
- Sand and gravel lens
- 1.2° slope
- 24% Silt & Clay

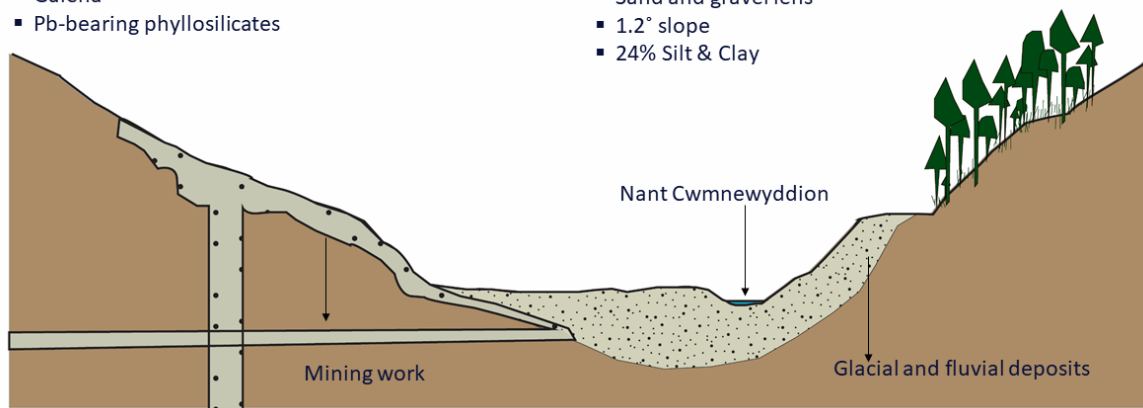


Figure 4.18. Graiggoch Mine summary of sediment geochemistry and fluvial morphological parameters to identify the main processes driving Pb and Zn dispersion.

stream power, and where metal-bearing sediments accumulate and mix with uncontaminated sediments (Hudson-Edwards et al., 2001, Miller, 1997). Therefore, the observed vertical aggradation of river sediment in the valley floor alcove classified this river segment as a *depositional area* (Figure 4.19).

The sand to clay layering (vertical accretions) or sand pockets depositional sediment structures likely control the river bank permeability and interaction with river water. Variation in the water stage can confer a storage control on Pb, also suggested by the variety of Pb- bearing primary and weathering minerals. Lead-bearing sulfate and Fe hydroxide are found in the vertical accretional structures, together with sphalerite grains and Zn associated with Fe, P and S interpreted to be plumbojarosite minerals. Here, reducing conditions can be generated by prolonged flooding conditions promoting Fe oxyhydroxide dissolution and plumbojarosite stability (Forray et al., 2010). Subsequent dry conditions can oxidise sulfide phases (galena and sphalerite) and release associated metals (Lynch et al, 2018) which easily reach the river water through the sandy layers or by forming Pb-bearing secondary Zn sulfate minerals. Furthermore, in the sandy pockets that are characteristic of the low river banks, Pb-bearing Mn oxide may be evidence of small areas of water interaction where hyporheic-type pH and redox conditions likely occur. Secondary Zn sulfate minerals having a high solubility (Lee et al., 2002) may release Zn in an aqueous form when this sediment is washed out during moderate to high streamflow conditions.

Middle river length depositional area (river segment 3000-4070 m)

Proposed ruling process: Pb and Zn enriched sediment are trapped and diluted by valley side sediment deposition. Hyporheic and redox conditions are induced in the river banks.

Sediment geochemistry:

- Pb 20 g/kg, Zn 2 g/kg
- Anglesite
- Sphalerite
- Galena
- Pb- and Zn-bearing Fe oxide
- Plumbojarosite
- Pb 4 g/kg, Zn 1 g/kg
- Pb- Mn oxide
- Pyromorphite
- Sphalerite
- Pb- and Zn- bearing Fe oxide

Fluvial morphology parameters:

- Narrow valley controlled by bedrock
- Deposits in bedrock alcoves
- Meander river path
- Erosional bank with vertical accretional sediments
- Depositional bank with coarse material
- 1.2 ° slope
- 24% Silt & Clay

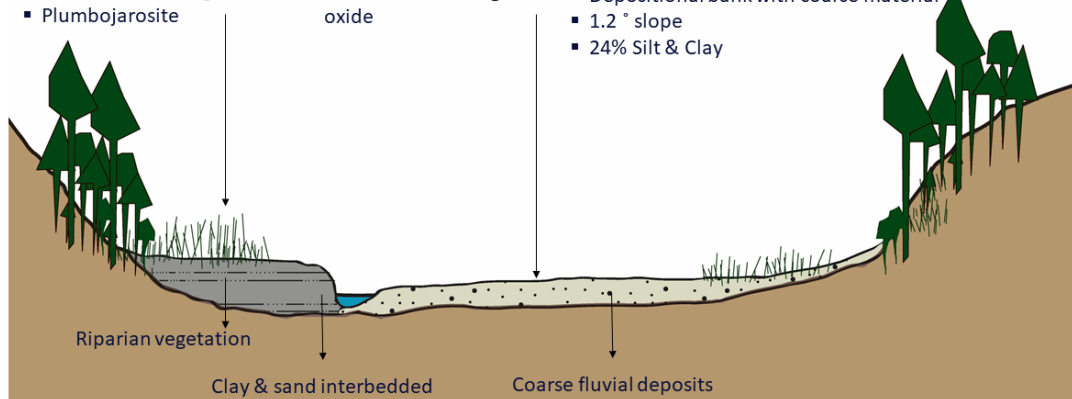


Figure 4.19. Depositional area at the middle river length summary of sediment geochemistry and fluvial morphological parameters to identify the main processes driving Pb and Zn dispersion.

Fine-grained sediments are observed in the floodplain. The alluvium segment is then considered a *depositional area*. The wide depositional valley decreases the water energy, likely enhancing temporal Pb and Zn uptake on mineral surfaces, proved by Pb and Zn mainly associated with phyllosilicate minerals and plant fragments, together with prolonged Pb and Zn storage typical of floodplain depositions (Dennis et al., 2009). Lateral vertical aggradations occurring under moderate to high streamflow conditions can result in the deposition of Pb-enriched sediment transported from the upstream mine sites. Zinc- and Pb- bearing phyllosilicates can be easily dispersed across the whole range of streamflow conditions (Figure 4.20).

These results show how fluvial geomorphological parameters, such as topography, slope, landscape characteristic, and grain size can influence storage of Pb and Zn. As in other studies (Hudson-Edwards et al., 2001, Miller, 1997), metal spatial distribution in mining-impacted rivers can be difficult to understand due to the numerous variables contributing to sediment dispersion. Lead dispersion along the catchment seems to be influenced by the fluvial morphological parameters recognised along the classified areas. Chen et al. (2012) observed a similar Pb behaviour controlled by the topography at the Le'an River floodplain (Jiangxi Province, China). Zhu et al. (2007) explain that slope is a geomorphological and hydrological control on sediment movement, to which Pb fate appears to be linked. On the other hand, the decrease of sediment Zn concentrations is potentially

Floodplain area (river segment 5800 – 6740 m)

Proposed ruling process: Pb is stored in the sediment and likely easily released by phyllosilicate.

Sediment geochemistry:

- Pb 2-11 g/kg
- Pb-bearing phyllosilicate
- Pb-bearing Fe oxide
- Zn 1-3 g/kg
- Zn-bearing phyllosilicate

Fluvial morphology parameters:

- Wide alluvial valley
- Meanders with later and vertical accretions
- River channel occasionally channelled by wooden piles
- 0.6° slope
- 17-36 % Silt & Clay

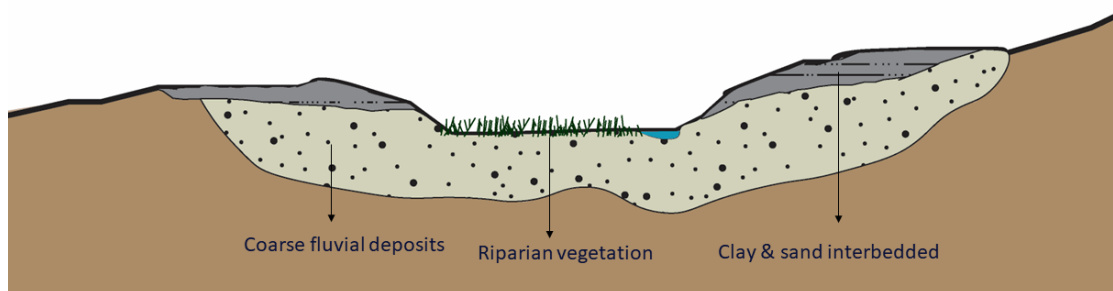


Figure 4.20. Depositional area at the middle river length summary of sediment geochemistry and fluvial morphological parameters to identify the main processes driving Pb and Zn dispersion.

due to the instability of Zn sulfate minerals and Zn high mobility in circum-neutral river systems (Smith, 1999, Lee et al., 2002). In this study, the temporal storage of Zn at 3000 m and in the floodplain may be due to the cation adsorption capacity of Fe oxyhydroxides (Burton et al., 2005).

Finally, the assessment and monitoring of sediment in impacted catchments are often complex, costly and time consuming (Crane, 2003). The use of fluvial morphological parameters is believed to provide a first guide to plan a sampling strategy where depositional area, either alluvial or bedrock controlled are targeted. Fluvial depositional parameters coupled with geochemical and mineralogical investigations can provide information on possible patterns of Zn and Pb release.

4.5 Conclusions

The major conclusions from this chapter are:

- The Zn and Pb concentrations found in the river channel and overbank sediment were higher than PEL values and thus are potentially harmful sources of contamination to the ecosystem.
- Galena and sphalerite are mainly localised in the upstream part of the catchment (0-171 m); their weathering products (sulfates, phosphates, Fe and Mn oxyhydroxides) are present in increased magnitude and variety at the headwaters and further downstream.
- The results show that primary Pb- and Zn-bearing mine waste minerals represent temporary storage of these metals until changing geochemical conditions trigger their instability and formation of secondary minerals.
- River catchment geomorphological parameters such as topography, slope, landscape characteristics, and grain size can help to identify sediment erosional, depositional or transport river areas.
- Erosional areas, such as Wemyss Mine, are exposed to degradation processes, which expose primary mineral to oxidative conditions releasing aqueous or particulate metals downstream.
- At Graiggoch Mine, characterised by the lens of glacial sands and gravels, the river segment has high permeability which potentially facilitates hyporheic – river water interactions where pH and redox conditions allow Mn-oxide precipitation and Pb trapping processes.
- The bedrock-controlled depositional areas trap sediment in clay and sand layering or sandy pockets allowing river water to permeate into the river bank and creating dry-wet sequences; these can enhance a variety of redox conditions where Pb and Zn can co-precipitated or be adsorbed onto various minerals.
- The floodplain can temporarily store Zn and especially Pb sorbed onto phyllosilicate minerals, on top of prolonged storage time enhanced by vertical aggradations which occur under moderate to high streamflow conditions.
- Fluvial geomorphological parameters coupled with geochemical investigations can provide information on the dispersion of Zn and Pb at the catchment scale and guide remediation prioritisation decisions.

Chapter 5. Source apportionment of Zn and Pb metal over the range of streamflows at the catchment-scale

5.1 Introduction

Mine waste weathering and dispersion following rain events continuously threaten and degrade water quality. Metals in such mine wastes are mobilised in the ecosystem and transported in aqueous or solid form by river water or stored in floodplains. Localisation and apportionment of metal sources are current worldwide priorities for reaching good water status.

Mine wastes are often located in river headwaters characterised by high gradient and irregular channel geometry (Moore, 2004b). The interlink between the metal sources and the river channel results in a complex system. Overland water can reach the river after being channelled in smaller inflows or percolating through the surrounding land. In addition, the groundwater can be confined in adits or enter the river bed through the hyporheic zone (Banks and Palumbo-Roe, 2010). Metal-enriched water entering the river through a defined segment is considered a point source; in contrast, diffuse sources are identified as seepages or hyporheic water near the mining inflow mouth or riverbank, runoff washing metal-rich minerals, or by re-suspension of polluted sediment (Mayes et al., 2008). The amount of water moving through the system determines the metal concentration and dispersion. Environment Agency (2012b) identified diffuse sources as significant contributors to total stream loads, up to 50% during baseflow and 90 % during high flows. The development of a methodology that offers high spatial resolution and estimates variation in response to streamflows is fundamental to address metal source apportionment issues, especially in regions characterised by the variable hydrological regime such as those with oceanic temperate climates.

Previous studies illustrated methods to quantify metal sources in mine-impacted catchments. Runkel et al. (2013) used a detailed spatial continuous tracer injection to identify metal sources along Peru Creek, Colorado. This work highlighted that metal loads were underestimated due to the use of common discharge measurements (such as the acoustic doppler current profiler) but captured with the continuous tracer injection capable to quantify hyporheic, groundwater and other diffuse sources. In another study on flow regime and metal concentrations in a remediated stream in Butte, Montana, Runkel et al. (2016) conducted three synoptic sampling campaigns (sweeps) and diel variation measurements to capture high and low flow regime conditions, together with a continuous tracer injection and a rain event. The first sweep sampled the rain event's effect

on the river chemistry, the second sweep, performed during steady flow, was a detailed campaign that identified the positions and nature of the metal sources, and the last sweep was a confirmation of the second. Samples taken during steady flow conditions, coupled with diel results, showed an upstream to downstream decrease in pH and an increase in metal concentration. During the rising of the water stage, most of the metal concentrations were 10-fold the low event values. It is clearly evident that metal source apportionment under low flow conditions can underestimate the metal loads that are transported along the river. Byrne et al. (2013) described six storm events that occurred in the Afon Twymyn, central Wales, captured with automatic samplers. They reported that Zn, Pb and Fe behaviours and sources differentiated among the events. Zinc and Pb concentrations showed a clockwise trend, peaking before discharge maximum, whereas Fe and Cu had the highest concentrations after the discharge wave. Variations of metal patterns among the events were linked to rainfall duration, historical pluviometry, and daily temperature, which together act as a regulator of soil and wastewater metal concentrations. The authors pointed out the necessity to include stormflow sampling during water quality monitoring.

A watershed approach for capturing diffuse sources under different flow conditions was proposed in Mayes et al. (2008). About 30 km of the impacted the River Gaunless catchment, England, were sampled, including inflows, and upstream and downstream confluences in the main river. Under low flow conditions (defined as Q70 or less), sources of Fe were identified as peat deposits, mine seepages, and mine water point sources, with attenuation of Fe due to ochreous precipitation. Groundwater contributions were estimated from Cl load increases noted at particular river segments. High flow Fe load apportionments, observed at Q10, were mostly in particulate form and due to a suite of processes including weathering of lithogeneous and peat sources and partial remobilisation of ochreous mineralisation. The authors reported that the cumulative instream loading, the sum of positive change in load as described in Kimball (2002), was greater during high flow than during low flow conditions stressing the importance of diffuse sources. However, in this study, the exact position and the nature of metal sources were not individuated, suggesting that methods for metal source apportionment need further development.

Studies which address metal sources using continuous tracer injections have been undertaken in areas, such as Montana, Colorado, and Italy, with well-defined seasonal climatic conditions characterised by warm- and dry-summer climate (Runkel et al., 2013, Byrne et al., 2017, De Giudici et al., 2017). Onnis et al. (2018), however, have stressed that it is necessary to estimate metal load contribution in climates characterised by high streamflow variability. Nevertheless, under these climate conditions, studies that used low spatial resolution loading monitoring to identify metal

load variations under a range of streamflows also encountered the problem of diffuse source apportionment (Mayes et al., 2008, Gozzard et al., 2011). A high spatial resolution survey of metal load in an oceanic temperate climate, such as the UK-type climate, seems fundamental to address metal source apportionment issues.

The aim of this chapter is to quantify Zn and Pb point and diffuse sources at the catchment scale across streamflow conditions. The specific objectives are i) to account for metal sources across streamflow conditions with a multi-tracer method approach; ii) to identify Zn and Pb distribution and storage processes and their implications for remediation strategies.

5.2 Method and Materials

To identify streamflow variations and estimate metal loads, streamflow and metal concentrations were measured during several site visits. In the upstream river segment (0-2610 m), a continuous tracer injection was performed to estimate detailed spatial variations of streamflow and metal load. The river was also monitored through slug injections to capture metal loads under a range of streamflow conditions.

5.2.1 Streamflow range definition

Water quality and streamflow data were attributed to streamflow ranges (Q values) which were calculated from the downstream gauge station 63001 (Ystwyth at Pont Llolwyn). The database for the gauge station is available for download at <https://nrfa.ceh.ac.uk/data/station/meanflow>. The entire series of streamflow records were used to calculate the percentile of each site visit (see section 3.2.1 for more details) and rank the Q values, where $Q = 100 - \text{percentile value}$. The Q values were then compared with the streamflow estimates at the downstream point (RB, SN6639273880), where the investigated the Nant Magwr crosses the B4340 road. Following the USGS classification (USGS, 2019), both series of Q values are defined as low flow (LF) when less than Q75, as high flow (HF) when more than Q25 and as moderate flow (MF) when falling between Q25 and Q75. Very high flows (vHF) are Q values less than Q5. The streamflow conditions of the campaign day and measured data are reported as the date of the sampling campaign followed by the Q range (vHF, HF, MF or LF).

5.2.2 Streamflow estimation with the continuous tracer injection method

Detailed streamflow measurements were captured with a continuous tracer injection at the first 2600 m (0 m, or T0, refers to the tracer injection site; Figure 5.1). A solution of 69 g/l NaBr, obtained

by dissolving 35 kg NaBr salt in 370 l of river water, was injected into the river. The NaBr salt was chosen for its conservative behaviour in circum-neutral pH water (Runkel et al., 2013), as per the Nant Cwmnewyddion water, and for its low Br concentrations. The solution was injected with a constant rate of 195 ml/min for 31 hrs starting at 13.00 on the 29/07/2016. Tracer concentration and injection rate consistency were checked six times during injection time by withdrawing samples and measuring the injectate volume after 1 minute intervals. Bromide arrival along the river was monitored at 171 m, 880 m, 1645 m and 2614 m (respectively T1, T2, T3 and T4 in Figure 5.1). These sites, called transport sites, were chosen for their easy accessibility and position related to mining waste locations. Furthermore, the transport site 2614 m (T4) represents the last monitored site during this experiment. At the transport sites temperature, pH and EC variations were recorded at fixed time intervals of 30 min or 1 h. At 880 m and 1645 m transport site pressure transducers (HOBO data logger) were installed to verify that steady flow occurred during the experiment time. In addition, at 880 m the INW TempHion Bromide probe was installed to monitor the Br arrival and the occurring of the plateau in Br concentrations. Once the Br concentration plateau was reached at the most downstream point (2614 m), a detailed grid of samples including 24 river water and 22 visible inflow water were sampled on 30/07/2016 moving from down- to upstream in order to avoid Br cross-contamination (Runkel et al., 2013). To minimise the potential dial signal in the synoptic sampling data EC values were monitored in transport sites and the sampling was conducted in few hours when EC variations were constrained to $\pm 5 \mu\text{S}/\text{cm}$. Samples were processed and returned to the laboratory within three days and then analysed. Furthermore, to monitor chemical and tracer diel variations across three days, two automatic samplers were installed at transport sites T2 and T3. Due to unforeseen technical issues related to the analysis of the samples, data are not available at this time. Bromine analysis was carried out by IC (Ion Chromatography Dionex ICS-25000) and ICP-MS (Inductively Coupled Plasma-Mass Spectrometry Varian 810) at University College of London.

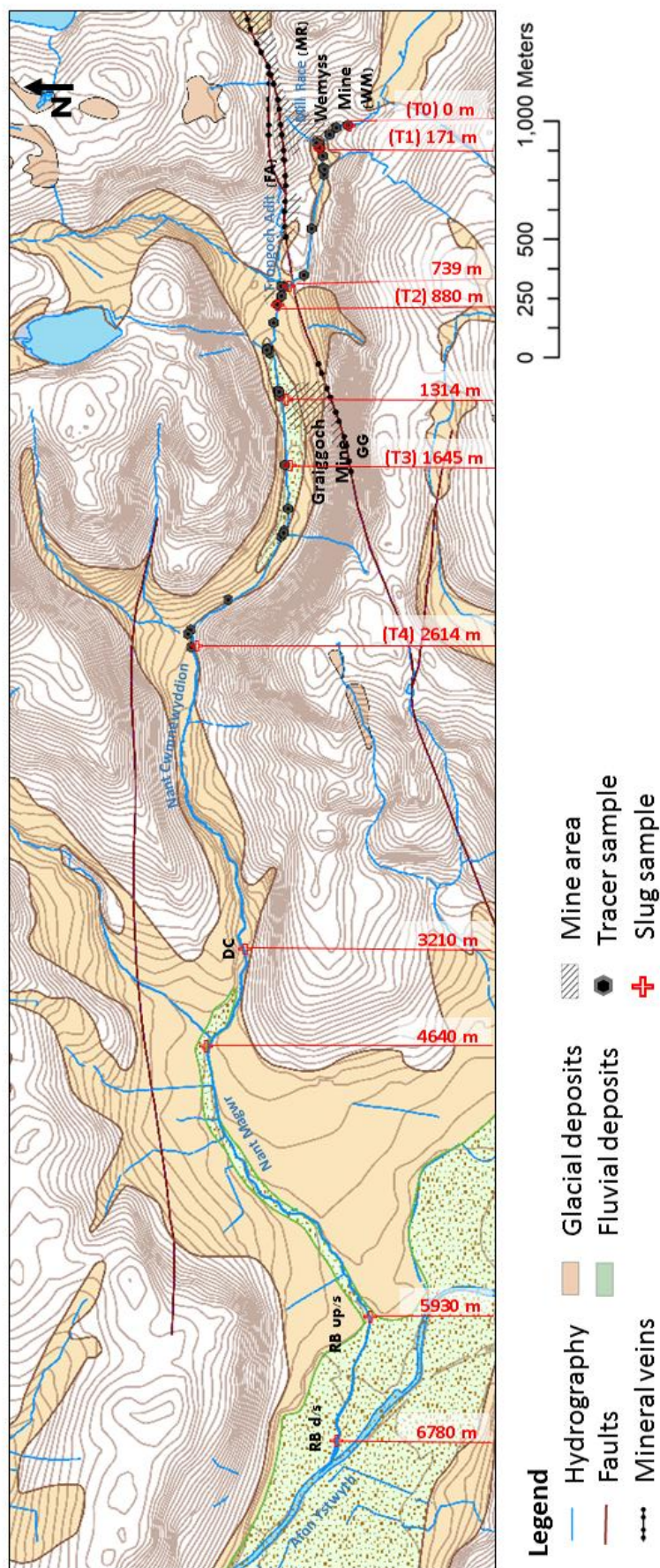


Figure 5.1 Tracer injection and slug sample sites along the Nant Cwmnewyddion and the Nant Magwr. Listed in red the distance from the injection site (T0, 0m) to the tracer transport (T1, T2, T3, and T4) and slug sites. WM: Wemyss Mine; MR: Mill Race; FA: Frongoch Adit; GG: Graiggoch Mine; DC: depositional area at middle river length; RB: floodplain upstream (up/s) and downstream (d/s) areas. DiGMapGB-50 [SHAPE geospatial data], Scale 1:50000, Tiles: ew178, Updated: 1 October 2013, BGS, Using: EDINA Geology Digimap Service (www.digimap.edina.ac.uk, Downloaded: 03-06-2016), modified with ArcGIS v.10.

Streamflows were calculated following the principle of the conservative of mass; the streamflow equals the injection rate and Br concentration product divided by the river Br concentration. Streamflow values were then plotted against the river distance from the injection (0 m) and streamflow variation described as a percentage variation of the final measured streamflow. The uncertainty due to variation in the injection rate during the experiment was measured as the relative standard deviation of the rate measurements and used to generate error bars in the streamflow graphs. Considering the stability in the Br plateau, recorded with the Br probe at 1645 m, the streamflow average was then used in the calculation of metal load and source apportionment. For an extended bibliography please refer to section 3.2.2.

5.2.3 Streamflow estimation using slug injections method

Spatial and temporal streamflow variations were determined during the summers of 2016 and 2017 by undertaking seventeen field visits. Forty-five successful slugs of NaCl salt were executed spread across eleven river sites characterised by irregular channel geometries. Seven sites were located in the first 2640 m, in addition, four downstream river sites were located at 3210 m, 4640 m, 5930 m, and 6780 m to estimate metal load and transport in depositional areas (Figure. 4.1). With the exception of the sites at 739 m, 1645 m, and 4640 m, streamflows were estimated three or more times for each site. Furthermore, occasional seepages and inflows were sampled. Measurements and water samples for chemical analysis were taken from the central part of the river within the current. Tracer injection and monitoring sites were selected in order to allow the full mixing of the injectate along the river. The distance between sites was 10 to 25 times the river width depending on river bed geometry and geomorphology. River segments with inflows or stagnant water pools were avoided (Richardson et al., 2016). Over the two years, two EC multiprobes (Aqua-reader and PCE-PHD 1, PCE Instruments) were used for measuring the tracer dispersion in the river during the slug injection. These were calibrated at the beginning of each field day or when inconsistent results were observed with 1412 $\mu\text{S}/\text{cm}$ standard solution corrected to the ambient temperature. EC variations were recorded each 1 to 5 seconds intervals depending on the type of multiprobes used. In the lab, EC values were then converted to sodium chloride concentration by adding known amount of salt into 200 ml of stream water, measuring the induced EC variation and calculating the angular coefficient (k) linking the two measures. Finally, streamflow values were calculated as the ratio of the salt weight used for the slug and the area under the sodium chloride concentration over the measurement time. For detailed information on the slug injection approach and an extended bibliography refer to section 3.2.3. The range of streamflow is presented as average, minimum and maximum for all the eleven sites.

5.2.4 Metal load analysis

In order to compare metal concentration variations among sites and streamflow conditions, metal load estimations were calculated as the product of metal concentrations and streamflows. For each streamflow measurement, a sample of water was collected at the center of the riverbed where the water was well mixed, avoiding pools and stagnant water. Physicochemical parameters including pH, conductivity, and temperature were monitored during the sampling using the above-mentioned multiprobes. Each sample was then split into three aliquots: i) 0.45 μm filtered and 1% HNO_3 acidified (FA), ii) raw and 1% HNO_3 acidified (RA) and iii) 0.45 μm filtered unacidified (FU). Ultrapure acid (67%) for trace metal analysis and 0.45 μm regenerated cellulose filters (Whatman SPARTAN) were used to process the samples. The complete sample treatment occurred soon after sample collection. Filtered and unfiltered cations (Ca, K, Mg, Na, Si, Zn, Pb, Fe, Mn, Al, Cd, Cu, Al, As, Co, Sr, Ag, Li, Tl, Mo, Ni, Au, Ce) were measured with ICP-AES (Inductively Coupled Plasma - Atomic Emission Spectrometer-Varian 810), ICP-OES (ICP-Optical Emission Spectrometer Thermo Scientific iCAP 6500 Duo) and ICP-MS (ICP- Mass Spectrometer Varian 720 for 2016 and Agilent 7900 for 2017 analysis). Filtered unacidified (FU) samples were filtered at 0.2 μm and analysed for main anions (SO_4 , Cl, F, and PO_4) with an IC (Ion Chromatography Dionex ICS-25000 for 2016 samples and Ion Chromatography Dionex ICS-2000 for 2017 samples). The analysis was carried out using the University College of London facilities in 2016 and using Liverpool John Moores University (cations) and University of Manchester (anions) facilities in 2017.

Alkalinity and nitrate concentrations were determined *in situ* in the field with a Hach Alkalinity Kit and a Hach Pocket Colorimeter™ II: Nitrogen, Nitrate, respectively. Major element water chemistry was displayed using a Piper Diagram elaborated with GW_Chart (software available at the USGS website). Selected samples along the river length were plotted using Ca, Mg and K plus Na for the major cations triangle in the Piper Diagram, and SO_4 , Cl and HCO_3 plus CO_3 for the major anion triangle. Cation and anion concentrations were plotted together in the diamond-shaped graph that shows the water type (USGS, 2008). Accuracy among the instruments was ensured using a series of certificates and laboratory internal standards, such as TMDA 70 (Certified Reference Waters for Trace Elements – Environment Canada, July 2008) and EP-H (Matrix Material Environ MAT Drinking water). The analysis of standards and some samples were repeated to verify precision and instrument drifting. The limit of detection (LOD) was verified with a series of field and laboratory blank. Among the investigated elements, only Fe, Zn, Pb, and SO_4 results are here presented.

5.2.5 Source apportionment

Detailed spatial information on metal sources was generated for the first 2614 m thanks to the continuous tracer injection experiment.

Metal concentrations and load are plotted against the river distance to individuate detailed spatial variations. The spatial variations in concentration give information on likely geochemical processes, and spatial variations in load help to identify source positions. Loads of Zn, Pb, Fe were calculated for both filtered and unfiltered fractions to avoid under- or overestimation of sources that can be generated by sampling execution (Runkel et al., 2013). Sources were identified by comparing metal concentrations and loads at each sample site. The distribution of sampling sites along the river allowed it to be divided into 23 segments.

Load variation between two segments indicates the input or loss of metal occurring in the river segment. In the case of observed inflows, the input due to its presence can be calculated as the measured inflow or the effective inflow. Effective inflow concentrations are calculated as the ratio of load and stream variation occurring at the up- and downstream of an inflow (Byrne et al., 2017). Differences between effective inflow concentration and measured inflow concentration, usually expressed as a percentage on the effective inflow, indicate the presence of hidden sources, attenuation or dilution of sources.

The metal load input (called the cumulative instream load) into the river is calculated as the sum of only positive load variations among river segments. The cumulative instream load does not record load loss and its curve stays constant when a load increase is not present (Kimball, 2002). The contribution of each river segment is calculated as the percentage of the segment load increase divided by the cumulative load at the most downstream point. Contributions can be grouped if a persistent positive percentage is measured. The group of contributions identified the potential sources. Therefore, this data allowed the ranking of Zn and Pb sources along the river.

Average, minimum and maximum load were calculated and plotted against the river length for sites for which streamflow measurements were available four or more times (0, 171, 880, 1645, 2614, 3210, 5930 and 6780 m). River waters at 739 m, 1314 m, and 4640 m were sampled only twice and only those two values were reported. Sources along the river were investigated comparing the instream total and cumulative loads of Zn and Pb, from 17/06/2016 (HF), 30/07/2016 (MF), 28/07/2017 (LF) and 12/09/2017 (MF) from 0 to 5930 m.

Correlations between streamflows and concentrations, and streamflow and load were investigated. Test for normality indicated that the data was not normally distributed and correlation were run with the non-parametric correlation Spearman's Rho. Elements and anions of interest were Zn, Pb, Fe, Cd, and SO₄. As the nature of the relationship between the data was unknown the 2-tailed (non-directional) test was selected to evaluate it. Calculations were performed using SPSS 26.0. The correlations were used as general indicators to identify rise of element loads or concentrations potentially linked to streamflows increases and associate processes.

5.3 Results

5.3.1 Streamflow range definition

Streamflows recorded at Ystwyth gauge station 63001 (Ystwyth at Pont Llolwyn) and estimated at RB are reported together with Q values and Q ranges in Appendix 5.a. Data retrieved at the two streamflow gauges were compared; they showed a correspondence for the 2016 estimates and a discrepancy for the 2017 estimates. Considering that the Nant Magwr is a tributary of the Afon Ystwyth located upstream of the mentioned gauge station, and rainfall may be heterogeneous throughout the catchment, the data are discussed referring to the Q range defined at RB. The intention is to keep consistency in the interpretation of the 2016 and 2017 data. For comparison between Ystwyth gauge station 63001 and RB refer to Appendix 5.a.

5.3.2 Spatially detailed streamflow variations along the river

A continuous tracer injection was conducted during a moderate flow event (30/07/2016, MF), and no water level variation was recorded by the pressure transducer. The in-situ measured Br concentrations exhibited a steady plateau during the synoptic sampling. Detailed streamflow variations were identified in the first 2614 m of the Nant Cwmnewyddion (Figure 5.2). Error bars for streamflow, reported in Figure 5.2, show the relative standard deviation (RSD% = 13.7) of the injection rate. However, considering the stability of the Br plateau and the correction at the injection site of the rate, no error bars are reported for the load estimation. As per the mass balance rule, Br concentrations decreased along the river due to dilution (Figure 5.2). The main peak of streamflow was observed at 880 m after the Frongoch Adit (at 862 m), and it contributed to 23.1% of the total streamflow. The other two main inflows, the Nant Ceunant at 1141 m and the Nant Gilwern at 2554 m, contributed 14.8% and 17.9%, respectively. An increase of 18.3% was observed from 1314 m to 1961 m, but no surface inflows were observed in this reach during the experiment. The streamflow increase may be the result of i) a 20 cm diameter pipe; ii) seven 7 cm diameter

pipes; iii) later seepage and iv) groundwater input. Finally, Mill Race, at 164 m, made only a small contribution to streamflow. Between 162 m and 171 m, a variation of only 1.4% was recorded; in this segment, two water sources (a black culvert located in a weir of the river bed and a later river branch) occur. Both of these sources had Br concentrations that indicate a river connection between the channel and the sub-channel.

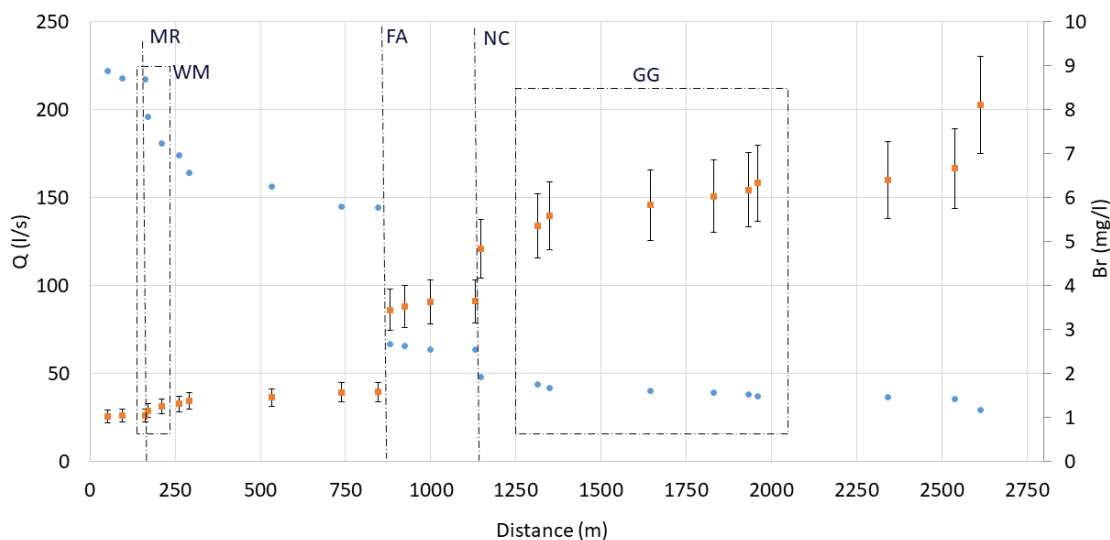


Figure 5.2 Bromide concentrations (blue), streamflow estimations (orange) and relative error bars along the first 0-2614 m where 0 is the continuous tracer injection site (T0). WM: Wemyss Mine; MR: Mill Race; FA: Frongoch Adit; NC: Nant Ceunant; GG: Graiggoch Mine.

5.3.3 Temporal streamflow variations along the river

A complete streamflow dataset is reported in Appendix 5.b. The investigation of streamflow by slug injection highlighted the streamflow temporal variability of this catchment. Streamflow estimations captured a very high flow (vHF, 15/06/2016), two high flows (HF, 17/06/2016 and 27/07/2016), five moderate flows (MF, 19/07/2016, 21/08/2017, 11/09/2017, 16/10/2017, 30/07/2016) and four low flows (LF, 09/06/2016, 15/07/2017, 28/07/2017, 30/07/2017). As shown in Figure 5.3, a general increase in streamflow from upstream to downstream can be observed, and streamflow respects the Q classification defined through Ystwyth gauge station 63001 (Ystwyth at Pont Llolwyn).

In the 0 m to 2614 m reach there were increases in average streamflows from 30 l/s to 146 l/s, with respective minimum and maximum values of 4 l/s (LF, 09/06/2016) - 81 l/s (MF, 16/10/2017) at 0 m and 46 l/s (LF, 15/07/2017) - 203 l/s (MF, 30/07/2016) at 2614 m. In the downstream reach (3210 m to 6780 m), average streamflows increased from 428 l/s to 968 l/s, with minimum and maximum values of 125 l/s (LF, 28/07/2017) - 952 l/s (HF, 17/07/2016) at 3210 m and 309 l/s (LF, 28/09/2016) - 1720 l/s (MF, 19/07/2016) at 6780 m.

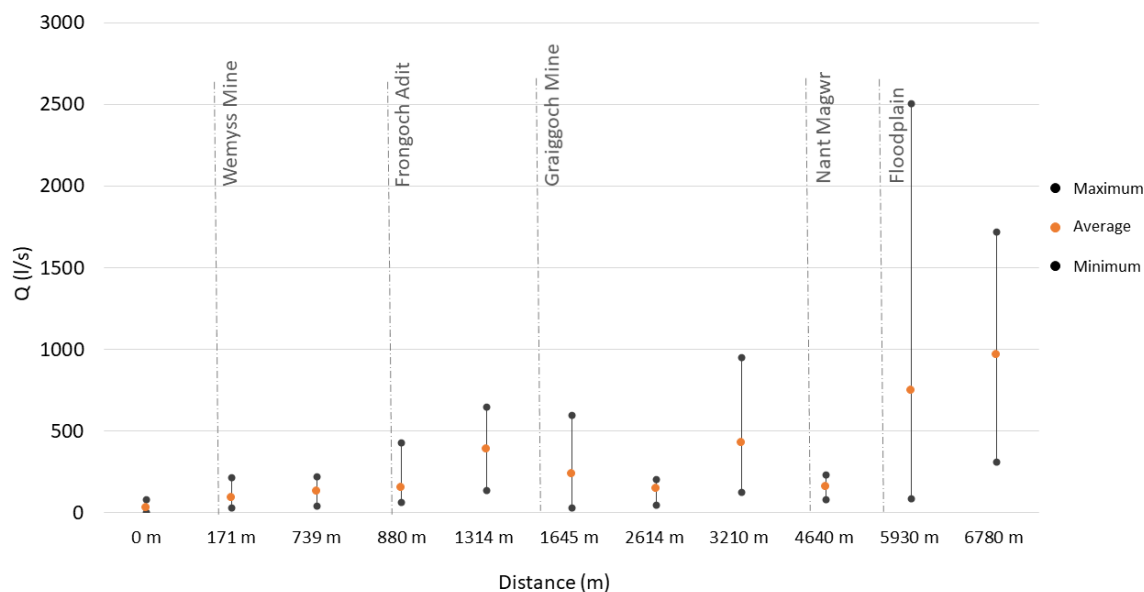


Figure 5.3 Streamflow maximum, minimum and average derived with the continuous tracer and slug injections.

5.3.4 General water chemistry and metal load variations

The river water is circum-neutral with pH 6.9 ± 0.8 and EC 71 ± 25 $\mu\text{s}/\text{cm}$. The river water was more acidic around the mine sites. The highest EC values were recorded at Frongoch Adit and at a culvert nearby Graiggoch Mine (LB pipe at 1321 m). The concentration of NO_3 and HCO_3 were stable along the river measuring respectively 27.1 (± 2.7) mg/l and 0.73 (± 0.37) mg/l . Generally, the bulk water is Ca-sulfate water typical of mine drainage (Appendix 5.c).

Seepage and inflow results

Metal concentrations of the inflows and seepages are reported in Table 5.1. On the 15/06/2016 (vHF) Mill Race was sampled at the headwaters up- and downstream of Wemyss Mine tips (just before entering the Nant Cwmnewyddion). Iron filtered concentrations decreased from 27 to 19 $\mu\text{g}/\text{l}$, and Pb and Zn increased from 368 to 1057 $\mu\text{g}/\text{l}$ and from 1.88 to 2.93 mg/l , respectively. A seepage sampled on the side of the mine spoil showed high concentrations of Pb (8.17 mg/l) and Zn (25.17 mg/l). At 1312 m an ephemeral pipe was sampled under different hydrological conditions; Fe concentrations were consistently <11 $\mu\text{g}/\text{l}$, Pb ranged between 77 and 185 $\mu\text{g}/\text{l}$ and Zn ranged between 4.56 and 5.41 mg/l . In addition, a riverbank seepage, sampled at c. 3210 m (DC) contained high concentration of Fe, Pb, and Zn especially for the unfiltered sample (DC seepage in Table 5.1).

Table 5.1. Inflow and seepage filtered Fe, Pb and Zn concentrations. Filtered and unfiltered concentrations are reported for DC seepage. WM: Wemyss Mine; MR: Mill Race; GG: Graiggoch Mine; DC: depositional area at middle river length; LB: left bank inflow.

Site	Date	Description	Distance m	Fe mg/l	Pb mg/l	Zn mg/l
MR	15/06/2016	MR-headwater	164	0.03	0.37	1.88
MR	15/06/2016	MR-u/s WM tip	164	0.02	0.46	2.09
MR	15/06/2016	MR-ds WM tip	164	0.02	1.06	2.93
WM seepage	15/06/2016	WM seepage	163	0.01	8.17	25.17
GG	15/06/2016	GG LB pipe	1321	0.00	0.19	5.20
GG	31/07/2017	GG LB pipe	1321	0.01	0.07	4.56
GG	30/07/2016	GG LB pipe	1321	0.00	0.08	5.41
DC seepage	17/06/2016	DC seepage (filtered)	3210	0.38	0.44	1.83
DC seepage	17/06/2016	DC seepage (unfiltered)	3210	89.50	3.64	3.57

5.3.5 Metal source apportionment and temporal-spatial variations

For the first 2614 m, detailed spatial variations in concentration and load were captured by continuous tracer injection at moderate streamflow (MF, 30/07/2016). Descriptions of Zn, Pb and Fe chemistry, patterns and sources are reported here. For a complete dataset refer to Appendix 5.d. Iron, Zn, and Pb concentrations, loads and sources were estimated for various streamflow conditions by slug injection investigations for both the upstream (0-2600 m) and downstream (2600-6800 m) reaches. A complete table of streamflows, element concentrations and loads can be found in Appendix 5.e and 5.f.

Detailed spatial concentration and load variations of metals

At the upstream part of the river (0-2614 m), continuous tracer injection showed the variation of Zn, Pb, Fe and SO₄ concentrations for 24 sites at moderate flow conditions (Figure 5.4). Zinc filtered and unfiltered concentrations (Figure 5.4.a) showed similar patterns, increasing from 0.39 mg/l (at 0 m) to 1.66 mg/l (at 2614 m). The highest concentration (2.90 mg/l) was reached around 880–924 m downstream of the Frongoch Adit inflow which has a concentration of 3.91 mg/l of Zn. A rise in Zn concentration (0.70-1.52 mg/l) can be observed from 162 m to 171 m, downstream of a complex section of the river which receives water from Mill Race (0.27 mg/l of Zn), a black culvert (3.70 mg/l) and a later stream branch which may be mixed with a clean seepage (1.14 mg/l of Zn). Unfiltered and filtered Pb concentrations varied. Generally, filtered Pb concentrations rose from 6 to 38 µg/l and unfiltered concentrations rose from 7 to 62 µg/l over the whole river. Two main peak concentrations were observed (Figure 5.4.b): i) at 162-171 m, where concentrations increased from

24 to 171 µg/l for filtered Pb and from 37 to 191 µg/l for unfiltered Pb; ii) at 847-880 m, where concentrations rose from 109 to 127 µg/l for filtered Pb and from 126 to 206 µg/l for unfiltered Pb. In the first segment, Mill Race had a filtered Pb concentration of 1027 µg/l and unfiltered Pb concentration of 1466 µg/l, but only Pb filtered values were then available for the black culvert (280 µg/l) and the lateral stream branch (171 µg/l). In the second segment, concentrations increased downstream of Frongoch Adit which has 123 µg/l filtered and 223 µg/l unfiltered Pb. Although filtered and unfiltered Fe concentrations showed different patterns (Figure 5.4.c), both do not show a rise from 0 to 2614 m. Sulfate concentrations (Figure 5.4.d) increased at 50 – 171 m from 1.00 to 7.11 mg/l, likely due to inputs from the Wemyss Mine tailings and from Mill Race. Another important abrupt jump (6.54 – 12.14 mg/l) is recorded at 880 m. Decreases were then recorded downstream of the Nant Ceunant (1148 m) and around Graiggoch Mine). The most downstream concentration (2614 m) was 9.79 mg/l. Finally, pH and EC varied slightly along the river with a decrease (6.35 to 5.82) of the former and an increase (72 – 111 µs/cm) of the latter (Figure 5.5). A small pH decrease (to 6.12) occurred at 880 m, likely due to inputs from Frongoch Adit, and at 1148 m an increase to 6.24 occurs, likely due to inputs from the Nant Ceunant water. From this site downstream until 2614 m pH varied from 6.24 to 5.82.

Loads for Zn, Pb, Fe, and SO₄ were calculated from 52 to 2614 m and are presented in Figure 5.6.a,b,c,d. For a complete list of loads refer to Appendix 5.d. The Zn load rose from 10 mg/s at 52 m to 336 mg/s at 2614 m. Two steep increases were observed at 162–171 m (18 to 44 mg/s) and at 847–880 m (42 to 249 mg/s). Furthermore, the Zn load increased from 1314 m (258 mg/s) to 1961 m (331 mg/s). Although Pb filtered and unfiltered loads differed, their overall spatial patterns were similar (Figure 5.6.b). In the upstream part (51–2614 m) filtered and unfiltered Pb loads increased from 0.41 to 7.75 mg/s and 1.35 to 12.66 mg/s, respectively (Figure 5.6.b). As observed in the Zn load pattern, two largest Pb load changes were observed at 162–171 m (from 0.63 to 4.96 mg/s for filtered Pb and from 0.96 to 5.55 mg/s for unfiltered Pb) and at 847–880 m (from 4.30 to 10.95 mg/s for filtered Pb and 4.98 to 17.78 mg/s for unfiltered Pb). The ratio of filtered to unfiltered Pb load decreased downstream of Frongoch Adit (862 m). Iron load patterns were different, particularly downstream of Frongoch Adit (862 m) and between 1148 and 1932 m (Figure 5.6.c). Generally, in the upstream part (52 to 2614 m) Fe load increased from 1.55 to 6.57 mg/s for the filtered samples and from 3.09 to 12.71 mg/s for the unfiltered ones. Sulfate loads slowly increased around 95 – 171 m, remained steady around 231 mg/s until 847 m where they sharply increased to 1048 mg/s at 880 m. A small decrease in load was noted around 1316 m. The final Fe load, at 2614 m, was 1985 mg/s (Figure 5.6.d).

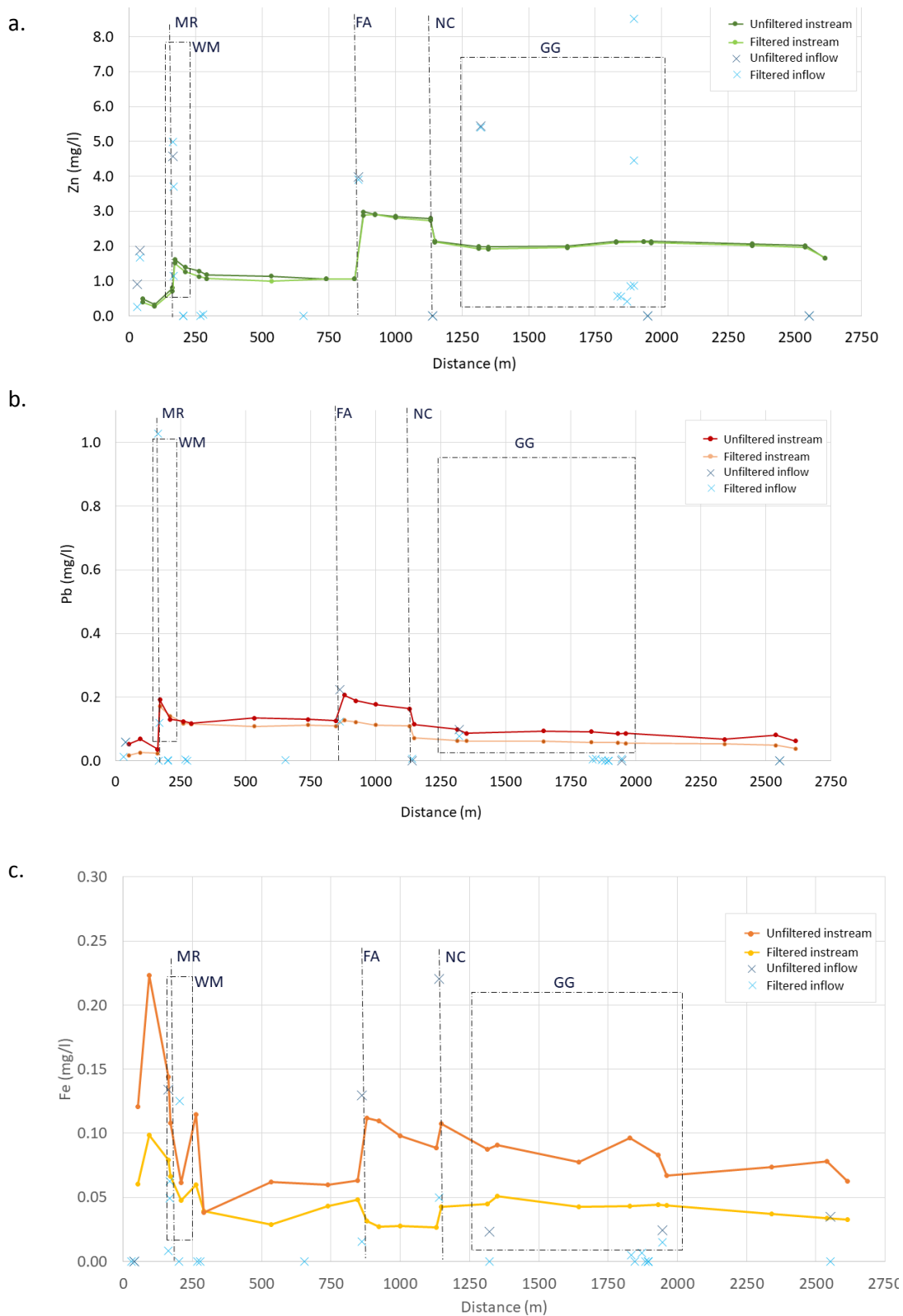


Figure 5.4 Spatial profile of Zn, Pb, Fe and SO_4 concentrations derived with the continuous tracer injection. WM: Wemyss Mine; MR: Mill Race; FA: Frongoch Adit; NC: Nant Ceunant; GG: Graiggoch Mine.

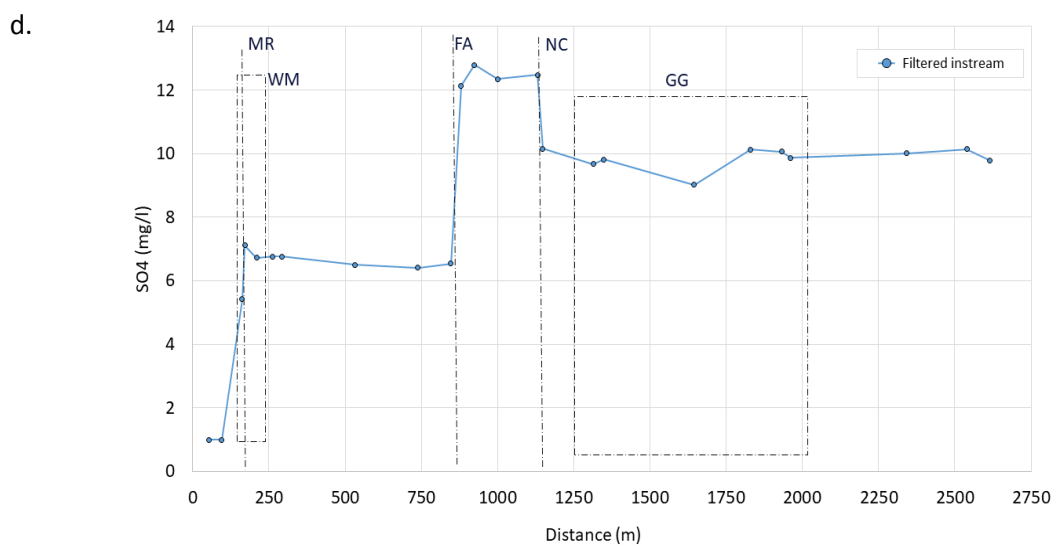


Figure 5.4 (continued)

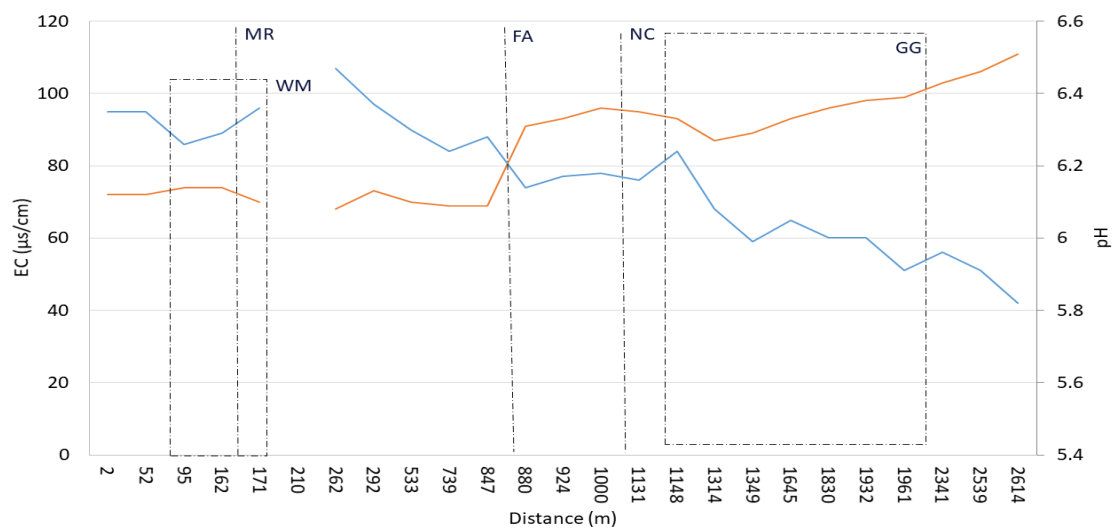


Figure 5.5 Spatial profile of pH (blue) and EC (orange) acquired during the continuous tracer injection.

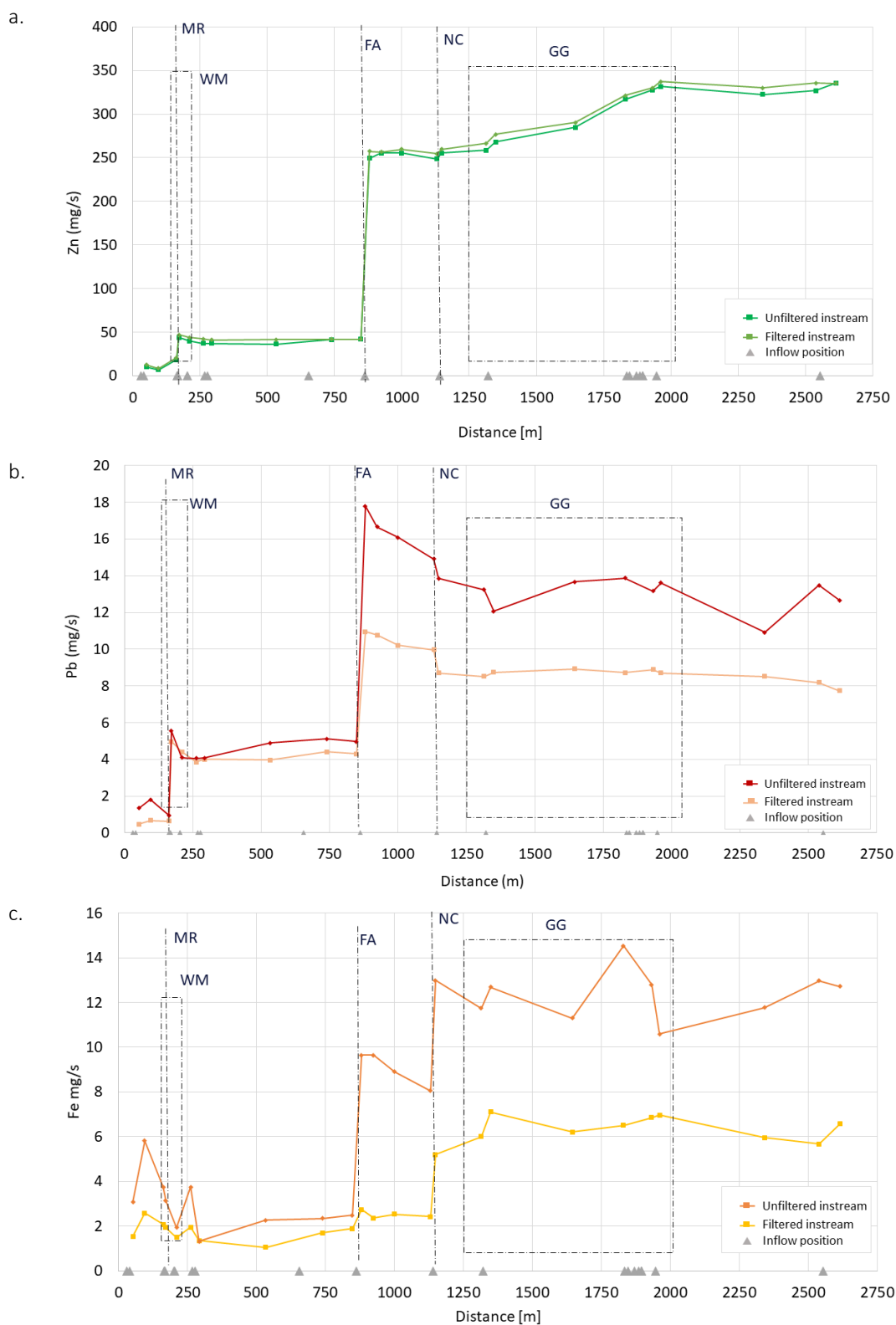


Figure 5.6 Spatial profile of Zn, Pb, Fe and SO_4 concentrations derived with the continuous tracer injection. WM: Wemyss Mine; MR: Mill Race; FA: Frongoch Adit; NC: Nant Ceunant; GG: Graiggoch Mine.

d.

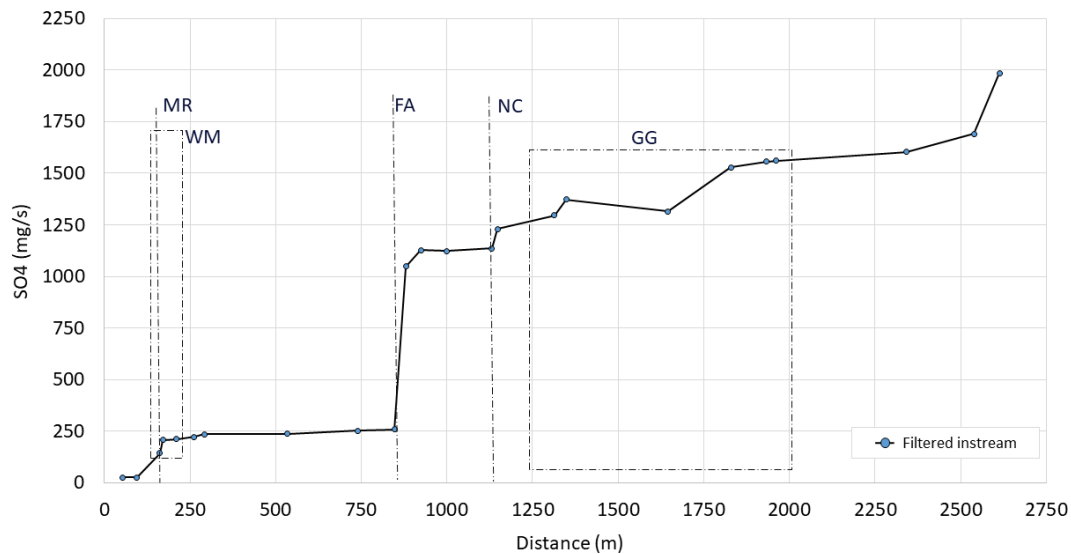


Figure 5.6 (continued)

The high spatial resolution of Zn (filtered), Pb (unfiltered) and Fe (unfiltered) loads were compared to the respective cumulative load to calculate the percentage contributions of each stream segment. When a persistent increase was shown segments were grouped as a whole source area. In Table 5.2 and Figure 5.7 sources are indicated as river segments. The 0 m to 52 m is the upstream Wemyss Mine (u/s WM) segment. Although field observations suggested that from 52 m to 171 m would represent a whole river segment running on the side of Wemyss Mine tips, the segments were left separated for the source apportionment, as different contributions were recorded by Zn, Pb, and Fe. Fifty-two to 95 m is the segment along the upstream part of the Wemyss Mine tip (WM tip); 95–162 m is the segment upstream of Mill Race (WM u/x MR); 162–171 m includes Mill Race, the black culvert and the later stream branch contribution (d/s MR). The 847–880 m segment includes Frongoch Adit coming from the right bank side (FA), followed downstream (880–924 m) by a segment running along shafts (Shafts). The stream segment attributed to Graiggoch Mine covers between 1148 and 1961 m (GG). In addition, three forested areas were recognised from 171 m to 847 m (Forested 1), 924–1131 m (Forested 2), 1961–2539 m (Forested 3). Finally, two river segments include those from 1131–1148 m downstream of the Nant Ceunant (d/s NC) and from 2539 m–2614 m downstream of the Nant Gilwern (d/s NG).

Zinc, Pb and Fe contributions for each segment are reported in Table 5.2. Three main sources were recognised for Zn: 57 % at 847–880 m (FA, Source#1), 21 % at 1148–1961 m (GG, Source#2) and 12 % at 95–171 m (WM u/s MR and d/s MR, Source#3). Lead sources were 51 % at 847–880 m (FA, Source#1), 17 % at 162–171 m (d/s MR, Source#2) and 5 % at 0–52 m (u/s WM, Source#3). As

expected from Fe spatial load curve (Figure 5.6.c), Fe sources differed from those of Zn and Pb, except for the 847–880 m segment (FA, Source#1 with 26 %). Other Fe sources were 18 % at 1131–1148 m (d/s Ceu, Source#2), 11 % at 0–52 m (u/s WM, Source#3), 10 % at 52–95 m (WM tip, Source#4) and 9 % at 1961–2539 m (Forested 3, Source#5). Table 5.2 reports also estimated attenuation percentages. The main attenuation segment, -1.4%, for Zn is linked to 1961–2539 m (Forested 3). Loss of load for Pb and Fe are often related: at 924–1131 m (Forested 2) with -12 % Pb; -6 % Fe, at 95–162 (WM u/s MR) with -5 % Pb and -8 % Fe; at 2539–2614 m (d/s Gilwern) with -3 % Pb and -1 % Fe, and at 171–847 m (Forested 1) with -2 % Pb and -2 % Fe. Two other attenuation segments were observed for Pb at GG (-1 %) and at Shafts (-4.5 %).

Table 5.2 River segment contribution to Zn, Pb and Fe load expressed in %. WM: Wemyss Mine; MR: Mill Race; FA: Frongoch Adit; NC: Nant Ceunant; GG: Graiggoch Mine; NG: Nant Gilwern; Forested: Areas with dense vegetation; Shaft: mining work area with shafts.

Site	Distance (m)	Fe Filtered	Fe Unfiltered	Pb Filtered	Pb Unfiltered	Zn Filtered	Zn Unfiltered
<i>up/s WM</i>	0-52	13.8%	11.3%	3.6%	5.4%	2.7%	3.5%
<i>WM 1</i>	52-95	9.2%	9.9%	1.7%	1.8%	-0.8%	-1.1%
<i>WM 2</i>	95-162	-4.5%	-7.5%	-0.4%	-3.4%	3.1%	3.5%
<i>d/s MR</i>	162-171	3.4%	0.2%	35.0%	16.7%	9.4%	9.6%
<i>Forested 1</i>	171-847	-0.3%	-2.4%	-5.1%	-2.3%	-0.6%	-1.4%
<i>FA</i>	847-880	7.5%	26.1%	51.7%	51.1%	57.1%	60.0%
<i>Shaft</i>	880-924	-3.3%	0.0%	-1.5%	-4.5%	1.7%	-0.2%
<i>Forested 2</i>	924-1131	-2.9%	-5.8%	-7.6%	-11.5%	-0.2%	-0.8%
<i>d/s NC</i>	1131-1148	24.7%	18.0%	-9.9%	-4.2%	1.9%	1.5%
<i>GG</i>	1148-1961	15.8%	-8.8%	0.0%	-1.0%	21.0%	21.6%
<i>Forested 3</i>	1961-2539	-11.6%	8.7%	-4.1%	-0.6%	-1.4%	-0.4%
<i>d/s NG</i>	2539-2614	8.1%	-0.9%	-3.4%	-3.2%	2.5%	-0.1%

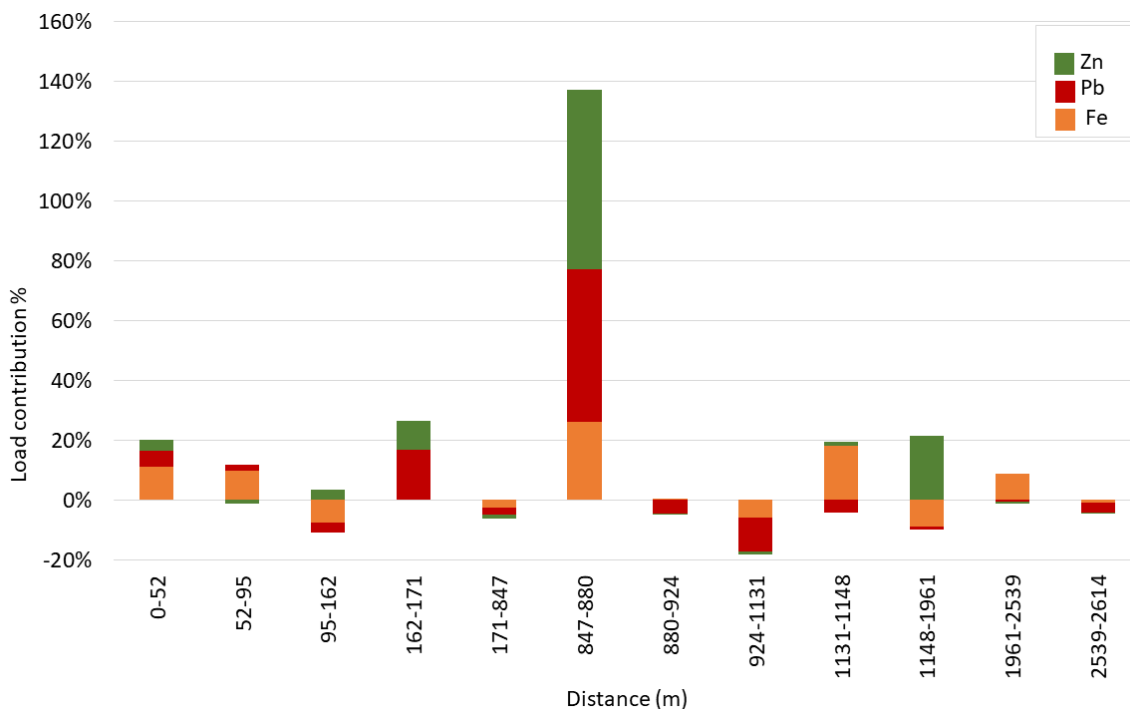


Figure 5.7 River segment contribution and attenuation percentages of Zn, Pb, and Fe derived with the continuous tracer injection.

In order to investigate point sources of contamination, inflow measured concentrations were compared to effective inflow concentrations (Table 5.3). At FA (847-880 m), ranked as Source#1 for Zn and Pb, Frongoch Adit water flowed into the main stream, but the effective inflow concentration indicated higher concentrations (+0.53 mg/l). GG segment acted as Source#2 for Zn and an attenuation area for Pb. The inflow at 1321 m, LB pipe (GG), had a high concentration of Zn and low Pb. The effective inflow indicated a lower concentration for Zn and a loss of Pb. Seven pipes were sampled on the 1830-1932 m river segment, two of them had measured Zn concentrations higher than the effective concentrations, indicating additional water with lower Zn concentration were entering the stream. WM d/s MR (Zn Source#3 and Pb Source#2) was a complex source that compressively showed higher effective concentrations than those for the Mill Race, WM black pipe and later stream branch.

Table 5.3 Effective inflows and measured inflow concentrations (n.d. not measured value).

Inflow name	Distance (m)	Zn		Pb	
		mg/l Filtered	mg/l Unfiltered	µg/l Filtered	µg/l Unfiltered
Effective Inflow	162-171	8.88	9.01	1502	1594
<i>Mill Race (MR)</i>	164	5.00	4.57	1027	1466
<i>WM Black pipe</i>	167	3.70	n.d.	0	n.d.
<i>WM LB lateral stream branch</i>	168	1.14	n.d.	119	n.d.
Effective Inflow	847-880	4.43	4.60	142	274
<i>Frongoch Adit</i>	862	3.91	3.98	123	223
Effective Inflow	1131-1148	0.23	0.18	-42	-35
<i>Nant Ceunant</i>	1141	0.01	0.01	7	0
Effective Inflow	1314-1349	1.64	1.79	38	-202
<i>LB pipe (GG)</i>	1321	5.41	5.44	77	99
Effective Inflow	1830-1932	2.96	2.43	43	-191
<i>LB pipe 7 (GG)</i>	1896	8.51	n.d.	1	n.d.
<i>LB pipe 6 (GG)</i>	1896	4.46	n.d.	1	n.d.
<i>LB pipe 5 (GG)</i>	1896	0.86	n.d.	1	n.d.
<i>LB pipe 4 (GG)</i>	1884	0.85	n.d.	1	n.d.
<i>LB pipe 3 (GG)</i>	1871	0.42	n.d.	1	n.d.
<i>LB pipe 2 (GG)</i>	1846	0.55	n.d.	6	n.d.
<i>LB pipe 1 (GG)</i>	1835	0.57	n.d.	5	n.d.

Metal concentration and load responses to streamflow variations

Metal concentrations and loads captured during several site visits give an indication of metal dispersion related to streamflows (see Appendix 5.e and 5.f for complete results table of 2016 and 2017 campaigns). Zinc, Pb, Fe, and SO₄ average, minimum (min) and maximum (max) values as concentration are plotted against river length, respectively, in Figures 5.8, 5.9, 5.10 and 5.11. Load min, max, and the average of the same elements are reported in Appendix 5.g. Spearman's rho correlations results are reported in Appendix 5.h. Total and cumulative load graphs for unfiltered Zn filtered Pb and unfiltered Pb are reported in Figure 5.12 and 5.13.a, b. Finally, pH variations across streamflows along the river are shown in Figure 5.14.

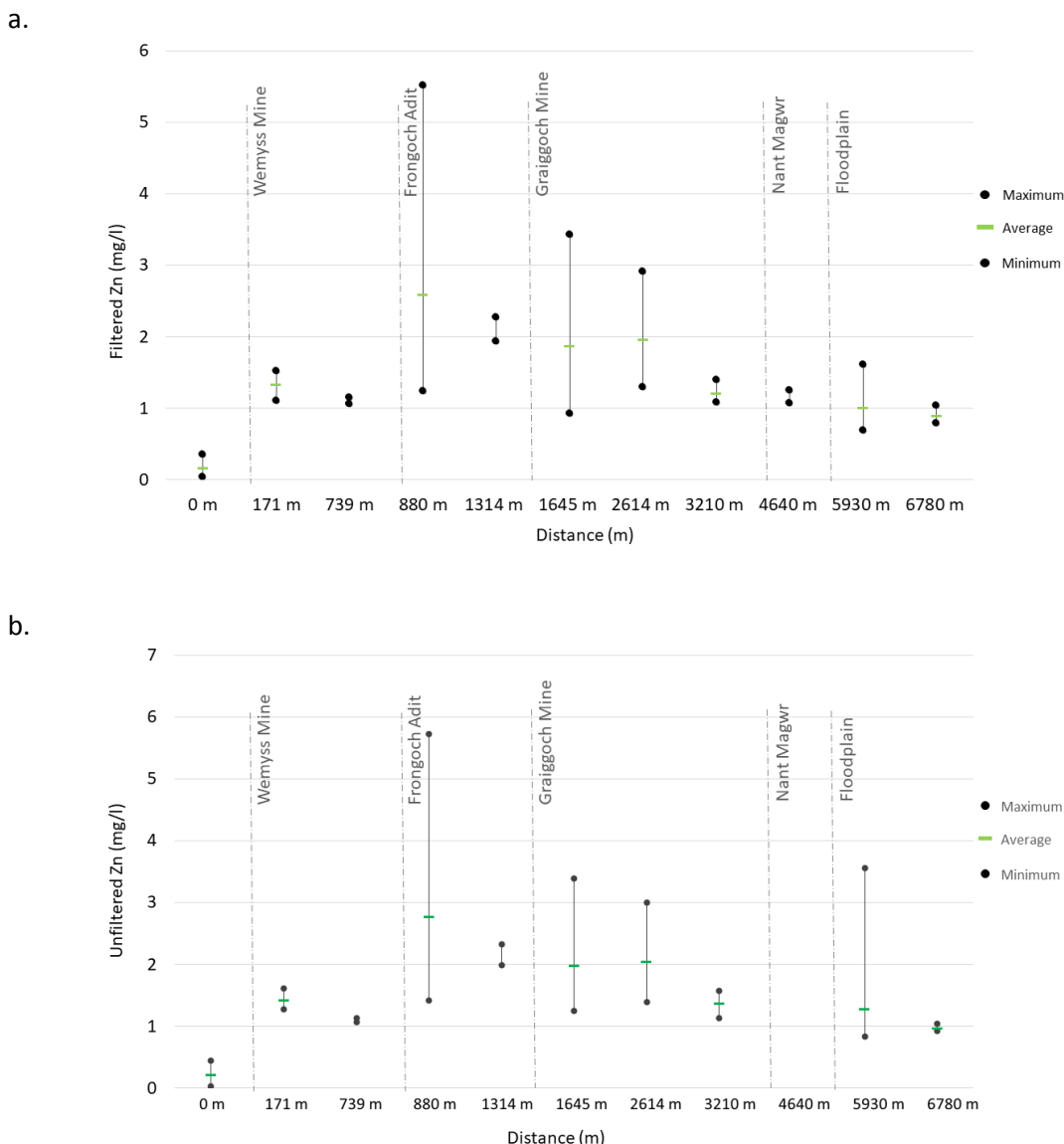


Figure 5.8 Minimum, maximum, and average Zn concentrations along the river.

Filtered and unfiltered Zn showed the same pattern with slightly higher values for the unfiltered results. Zinc average concentrations (Figure 5.8.a,b) increased first at 171 m (from 0.16 to 1.33 mg/l), downstream of Mill Race and the Wemyss Mine tips. A second rise was noted downstream of Frongoch Adit (880 m), recording the highest average concentration of 2.59 mg/l, and further downstream, Zn concentrations decreased to 0.90 mg/l at 6780 m. At 880 m and 1645 m concentrations were more dispersed, indicating a stronger link to streamflows. At 880 m higher concentrations were associated with higher flows, and lower concentrations with low to moderate flows. At 1645 m, the two highest concentrations were associated with both the lowest and highest streamflows (3.43 mg/l and 2.30 mg/l, respectively). Small variations between max and min values were observed at 171, 3210 and 5930 m. At 5930 m higher concentrations were linked

to lower streamflows. Zinc load (Appendix 5.g.1 and 5.g.2) showed an increase in the first 0 – 1314 m, a decrease till 2614 m, and finally an increase toward the downstream part. Minimum values showed a gentle decrease from 880 to 1645 m, but maximum values were consistent upstream, with a significant rise at 5930 m. The lowest load values were recorded at 0 m and the highest at 5930 m (4026 mg/s) during the highest recorded flow (15/06/2016, vHF). Zinc concentration did not show a significant correlation with streamflow ($p < 0.05$), on the other hand, both filtered and unfiltered Zn loads had strong correlations ($p < 0.05$) (Appendix 5.h). For unfiltered Zn the cumulative load curve showed higher values than the total load curve (Figure 5.12). Differences were emphasised downstream 1314 m and during high flows (17/06/2016, HF). Percentages of attenuation processes (Table 5.4) indicated a decrease of 49% in unfiltered Zn under low flow conditions (28/07/2017, LF), and a decrease of 11% under high flow conditions (17/06/2016, HF).

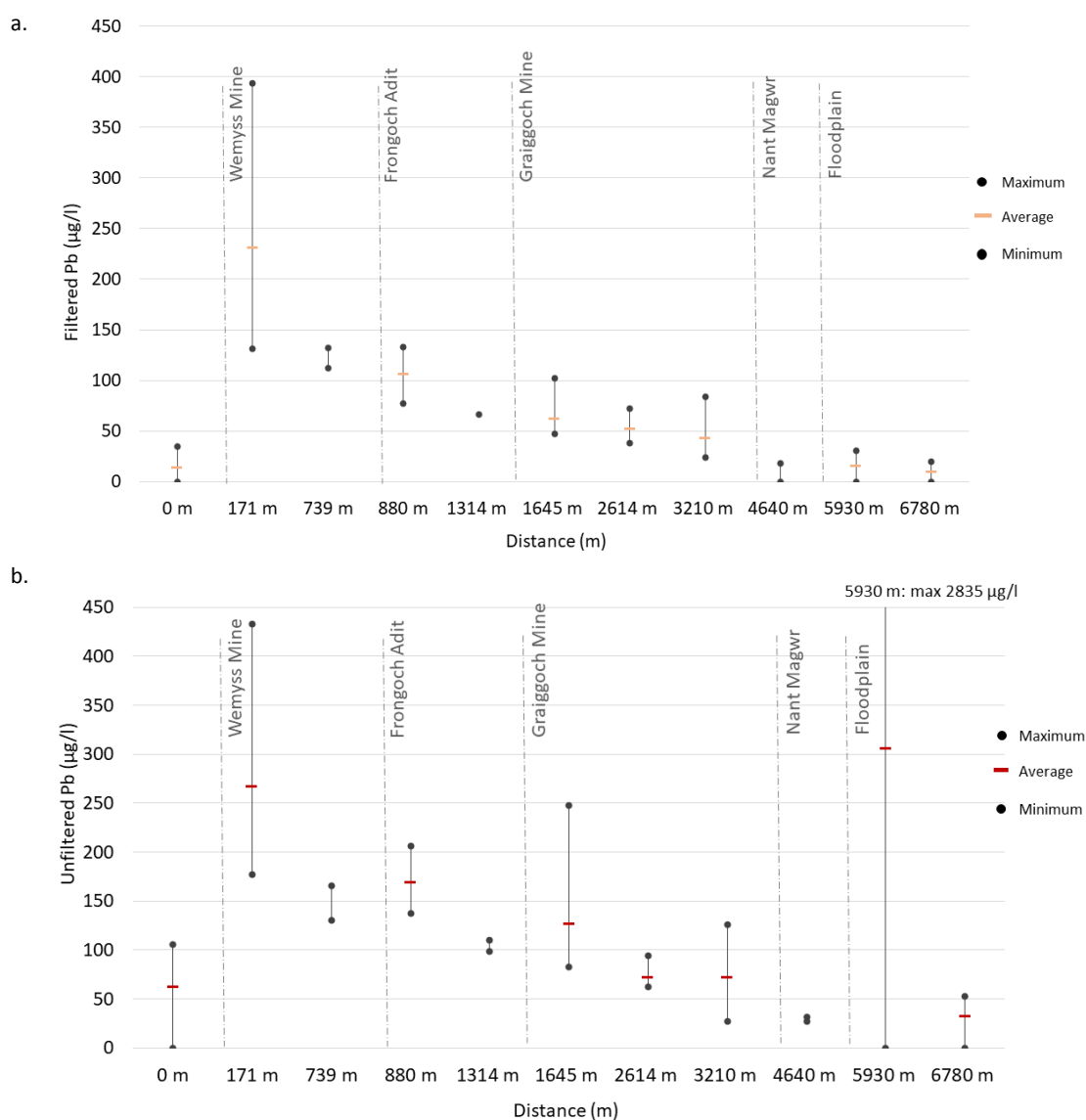


Figure 5.9 Minimum, maximum, and average Pb concentrations along the river.

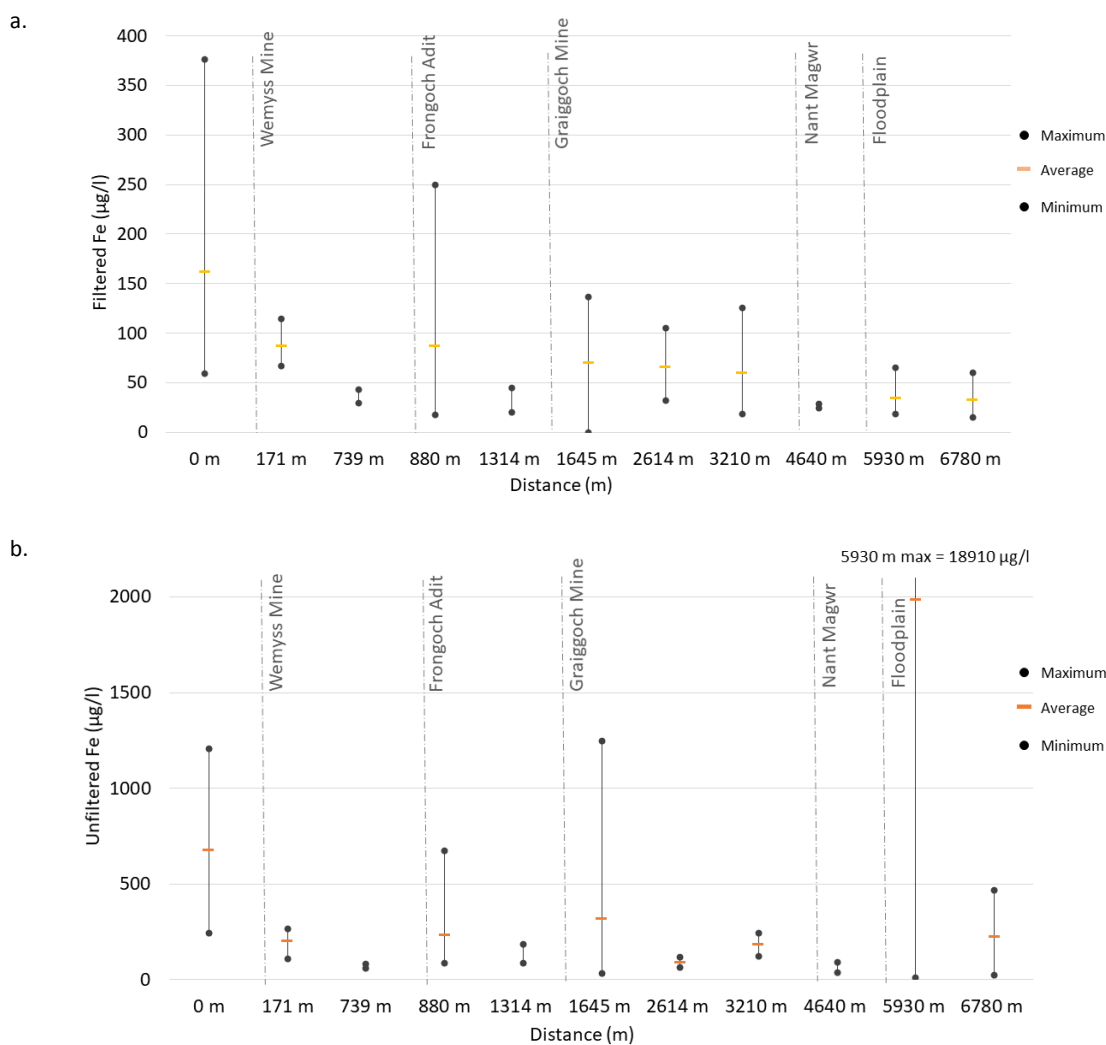


Figure 5.10 Minimum, maximum, and average Fe concentrations along the river.

Filtered and unfiltered Pb concentrations (Figure 5.9.a, b) had generally the same spatial pattern, but unfiltered values showed more dispersion linked to the streamflow. Minimum and averaged values for filtered Pb followed the same trend; unfiltered concentrations showed larger differences between minimum and maximum values compared to those of the filtered concentrations. The first rise was recorded at 171 m with a similar range of average values for filtered (393 $\mu\text{g/l}$, the highest measured value) and unfiltered Pb (432 $\mu\text{g/l}$). A small rise for unfiltered Pb was recorded downstream Frongoch Adit, 880 m. Around Graiggoch Mine unfiltered Pb ranges from 83 $\mu\text{g/l}$ to 248 $\mu\text{g/l}$, whereas filtered Pb varied from 46 $\mu\text{g/l}$ to 102 $\mu\text{g/l}$. Although filtered Pb concentration decreased in the downstream part of the river, unfiltered Pb was highest (2835 $\mu\text{g/l}$) at 5930 m. Similar to 1645 m, at 3210 m Pb concentrations showed variation among streamflows, and this was more accentuated for unfiltered Pb. The load averages for filtered and unfiltered Pb (Appendix 5.g.3 and 5.g.4) rose downstream of Mill Race (171 m), then decreased between 171 and 739 m.

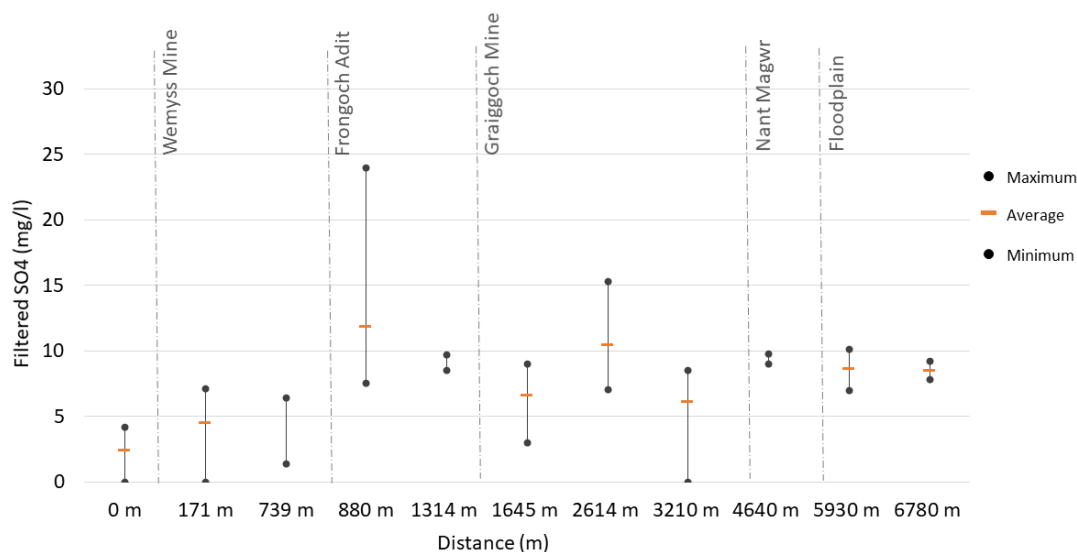


Figure 5.11 Minimum, maximum, and average SO_4 concentrations along the river.

At 880 m average concentrations were slightly lower than at 171 m. Downstream of 880 m the Pb load slightly decreased until 5930 m, where higher averages and a wider range of concentrations were recorded, especially for the unfiltered load. At 3210 m filtered and unfiltered Pb load were between the 1645 m values, with a higher minimum and a lower maximum. No significant correlation was observed between Pb concentration and streamflow. The correlation between streamflow and both filtered and unfiltered Pb load was poor. High significant correlations ($p < 0.5$) were observed at 880 m for the filtered and unfiltered Pb load, at 1645 m for unfiltered Pb and 3210 m for filtered Pb. A poor correlation (0.66) was observed at 5930 m for unfiltered Pb (Appendix 5.h). Cumulative load curves of filtered and unfiltered Pb indicated higher values than total loads curves, which were more accentuated for high flows and low flows (Figure 5.13.a, b) as also observed from the percentage of Pb load attenuation (Table 5.4). Under high flow conditions (17/06/2016, HF) the total load curve for filtered and unfiltered Pb decreased in values between 171-739 m and 1314-3210 m downstream, creating a gap with the cumulative load curves. At low flow condition (28/07/2017, LF) filtered total Pb load decreased after 880 m and unfiltered Pb total load after 1645 m (Figure 5.13.a, b).

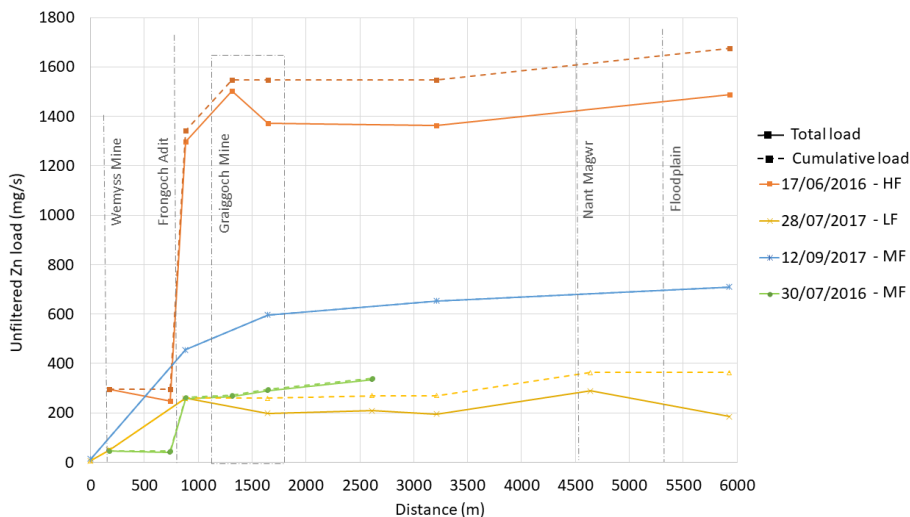


Figure 5.12 Total and cumulative Zn loads under low, moderate and high streamflow conditions.

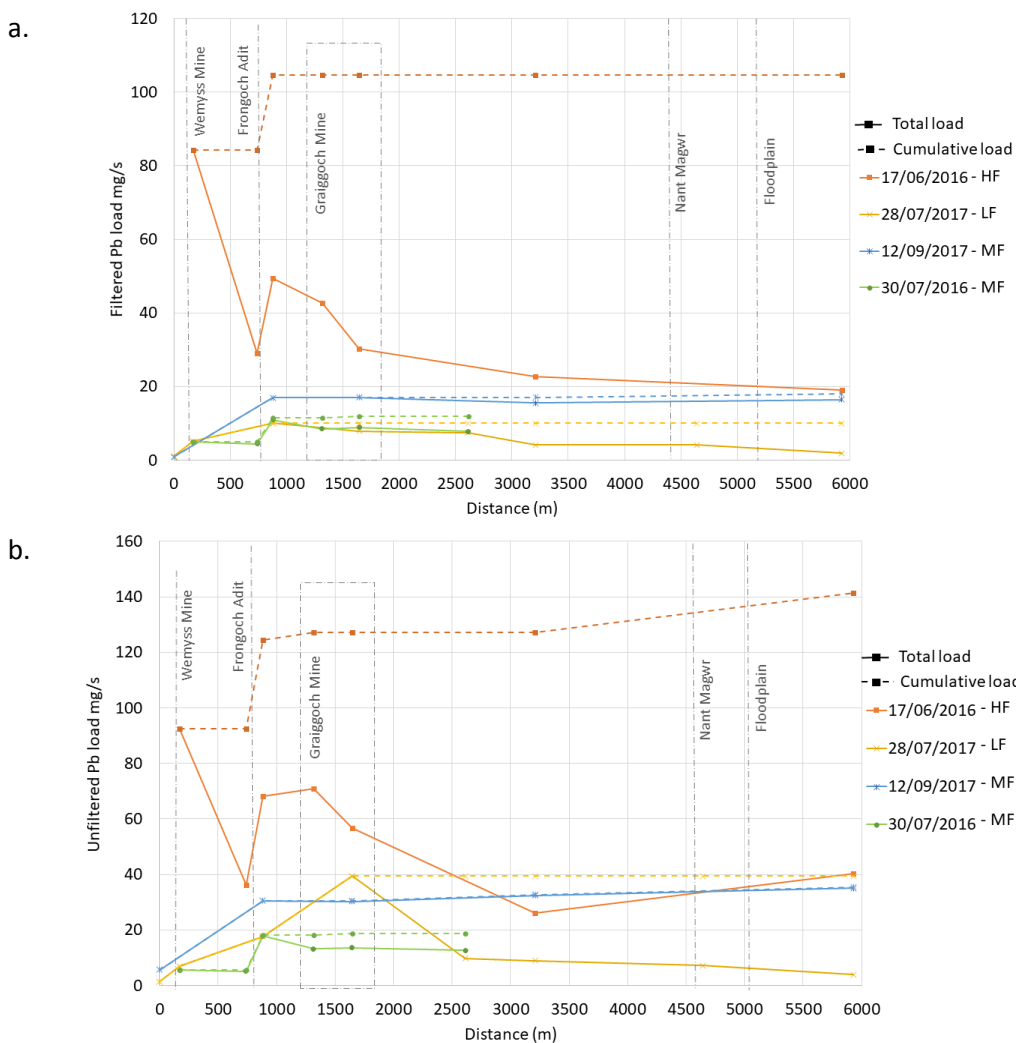


Figure 5.13 Total and cumulative loads of filtered (a) and unfiltered (b) Pb under low, moderate and high streamflow conditions.

Table 5.4 Zinc and lead cumulative loads and attenuation percentages under low (HF), moderate (MF) and high flows (HF).

Date	Distance	Cumulative load			Attenuation %			
		Zn Unfiltered	Pb Filtered	Pb Unfiltered	Zn Unfiltered	Pb Filtered	Pb Unfiltered	
17/06/2016	HF	At 5930 m	mg/s 1674	mg/s 1045	mg/s 141	mg/s 11%	mg/s 82%	mg/s 72%
28/07/2017	LF	At 5930 m	362	10	39	49%	82%	90%
12/09/2017	MF	At 5930 m	709	18	35	0%	9%	1%
30/07/2016	MF	At 2614 m	341	12	19	2%	35%	32%

Iron concentrations and loads are shown in Figure 5.10. The average filtered and unfiltered Fe concentrations displayed similar patterns, whereas the minimum and maximum values showed complex variations. Average Fe concentrations decreased moving downstream (from 162 mg/l to 34 mg/l for filtered and 682 µg/l to 229 µg/l for unfiltered), whereas filtered and unfiltered Fe loads increased from 4.7 mg/s to 22.4 mg/s, and from 15.8 to 170 mg/s, respectively. The load patterns for filtered and unfiltered Fe showed clear increases after 880 m; these were more accentuated with the unfiltered results. Another increase in Fe load is reported after GG, but by contrast, the variation was clearer for filtered Fe. Generally, streamflows did not correlate with the Fe concentrations and only a weak correlation with Fe load is observed (0.80, $p < 0.5$) for filtered and 0.77, $p < 0.05$ for unfiltered, Appendix 5.h). The 0 m, 1645 m and 5030 m streamflows strongly correlated with filtered Fe load; at 3210 m and 5930 m streamflows correlated with unfiltered Fe loads.

Along the studied river, sulfate concentrations (Figure 5.11) increased from 2.42 to 9 mg/l with abrupt rises in average, minimum and maximum values at 880 m. The highest concentrations were registered around 5930 m and 6780 m, with important variations between the minimum and maximum concentrations (Figure 5.11). Streamflows were uncorrelated with SO₄ concentrations and correlated with SO₄ load with the exception of 3210 m (Appendix 5.h).

Finally, the pH showed variations across streamflows with lower pH recorded during medium and high flow conditions (Figure 5.14). Generally, the same spatial pattern was observed across streamflow conditions.

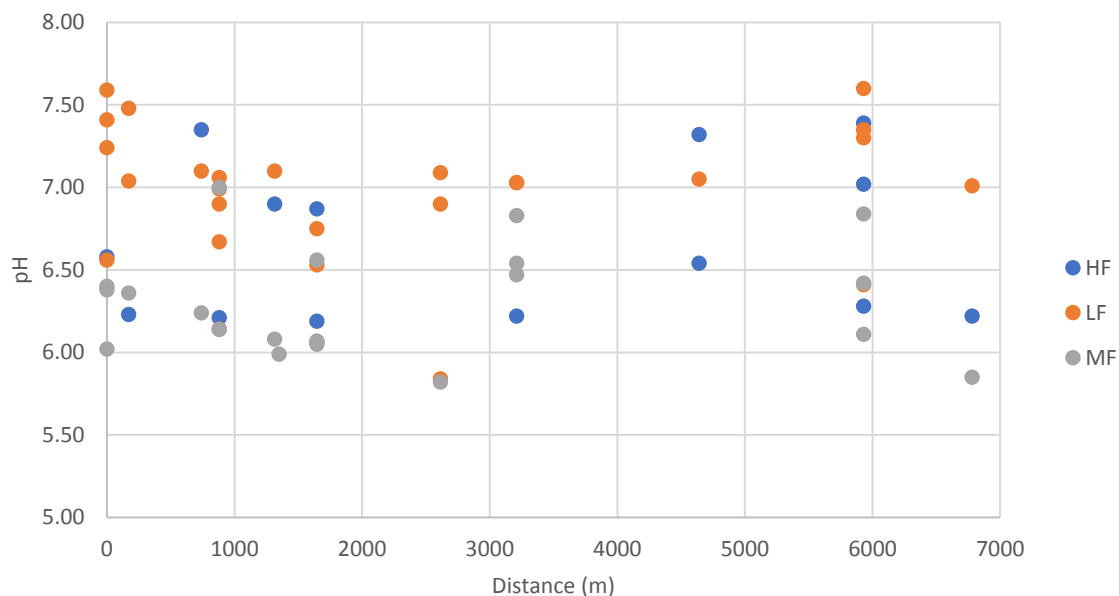


Figure 5.14 pH variations along the river across high (HF), moderate (MF) and low (LF) flows conditions.

5.4 Discussion

5.4.1 Zinc and Pb source apportionment across streamflows

Spatially detailed Pb and Zn load estimations across streamflows enabled accurate Pb and Zn sources to be identified along the catchment. These data, compared with sediment geochemistry results (Chapter 4) helped in recognition of sources, storage areas, and related processes. Zinc and Pb loads responded to streamflow conditions indicating areas of attenuation or sources likely due to the aqueous element geochemistry, sediment geochemistry and fluvial morphological parameters that vary along the Nant Cwmnewyddion and the Nant Magwr. Detailed spatial load data for the upstream reach, where the mining works occur, was determined through continuous tracer (30/07/2016, MF) and slug injection experiments. The downstream reach, which is mostly characterised by floodplain environments with soil deposition and heterogeneous vegetation density, were investigated through slug injections only.

The site upstream of the mine site (0 m) released Zn, Pb and SO_4 responding to streamflow, but the load ranges were the lowest recorded and metal loss likely was due to attenuation processes that occurred just downstream. Therefore, the area is not considered a source of metals under any streamflow conditions.

Wemyss Mine area (52 - 171 m) was recognised as a diffuse source of Zn and Pb and ranked as Source#2 under moderate flow (30/07/2016, MF) conditions. It received inputs from two important point sources: Mill Race and a black culvert emerging from a river weir. The side of the tailings (52-162 m) which includes the WM tip and WM u/s MR was characterised by the mine waste tips that have a steep slope on the left bank of the river. They lie on a thick layer of clay (0.10 to c. 1 m height) which represents impermeable strata stopping the percolation of tailings pore water into the river. In here, Pb and Fe loads decreased significantly (respectively - 3.4% and - 7.5% mg/s during moderate flow conditions, 30/07/2016, MF, Table 5.2), likely trapped by organic matter or Fe-oxide whose production is enhanced by the peat present along the right bank (Lynch et al., 2014, Yang et al., 2006). Less than a litre of water was gained in this segment, likely due to the impermeable clay. Although seepages emanating from the tailings were highly enriched in Pb (Table 5.1), the Pb in these appeared to be sorbed onto Fe hydroxides (Figure 4.7). By contrast, Zn and SO₄ loads increased, possibly due to their greater aqueous mobility at the ambient pH (6.3) of the river in this segment (Lee et al., 2002). Furthermore, at moderate flow (30/07/2016, MF) along 162 – 171 m only 1.4% of water was gained, but additions of 9.4% in Zn and 16.7% in Pb loads were recorded. The increase in load was not justified by the sampled inflows, therefore, this reach contribution likely included seepages and hyporheic water enriched in Zn and Pb. The Mill Race inflow (sampled 15/06/2010 vHF) took up Zn and Pb from the mine tip, whose seepages were enriched in these metals and thus could impact the river especially during moderate to high flow conditions. During the highest recorded flow (17/06/2016, HF), the main Pb source appeared to be located around this river segment (Figures 5.13.a, b). Therefore, even if Wemyss Mine and Mill Race represented the second most important source for Pb at moderate flow, this segment of the river ranked as Source#1 during high flows. By contrast, the Zn load data were not dispersed, suggesting that the contributions of this river segment ranked as the secondary source across low, moderate and high streamflows.

During moderate flow (30/07/2016, MF) the Source#1 for Zn, Pb, and Fe was the Frongoch Adit which flows into the river at 862 m. Although this inflow represented only 23 % of the Nant Cwmnewyddion river water, it contributed to 57% of the Zn, 51% of the Pb and 26% of the Fe (Figure 5.7). Zinc contribution increased across streamflows, reaching high load contribution during high flow conditions (17/06/2016, HF, Figure 5.12). Filtered and unfiltered Pb load strongly responded to streamflow variations (Appendix 5.g.3 and 5.g.4). As a result, the contribution of Frongoch Adit to Pb loading in the catchment increased during high flow events. The measured high flow event (17/06/2016, HF) corroborated this theory. The increase in Pb contribution during high streamflows was important but lower than the contribution gained from Wemyss Mine and Mill Race source.

Under moderate flow conditions (30/07/2016, MF) the river segment along Graiggoch Mine (1148-1961 m) acted as Source#2 for Zn (21%) and as a sink of Pb (-1%) and Fe (-8%). The riverbed in this area was wider than that in the upstream segment and it was mainly characterised by fluvial and glacial deposits (such as diamincton) which induced shallow water levels and a potential hyporheic zone (Figure 4.18). Sources of Zn in this area (1148-1961 m) were probably water infiltration of the hill side (covered by mine waste) which entered the river through the riverbank, and groundwater from underground mining. The groundwater input can be suggested by the streamflow increase estimated by the continuous tracer injection and by the presence of mine levels and shaft in the area and reported in historical maps. At GG, 1148-1961 m, an important water interaction between river water and subsurface water (likely groundwater) was suggested. Effective inflows indicate Zn concentration lower than the measured inflow concentration (LB pipe, LB pipe 7 and LB pipe 6 in Table 5.3) suggesting that more water than observed entered the river in this segment, diluting the Zn pipe concentration. In addition, for both segments, Pb effective concentrations indicate a loss of Pb from the up- to downstream sampling point; this may have been due to geochemical processes that took up Pb from the water. This hypothesis is supposed by the observed Pb load attenuation (Table 5.2) and Pb-bearing minerals found at GG (Figure 4.9). Furthermore, in this river segment, an increase of 18.3% river water was observed from 1314 m to 1961 m, but no surface inflows were observed in this reach during the experiment. The pipe's streamflow was not enough to justify this instream streamflow increase. A possible explanation of Pb load loss behavior is the precipitation of minerals such as plumbojarosite and Pb-bearing Mn and Fe-oxyhydroxides (Figure 4.9), supported also by the decrease in SO_4 and Fe load (Figure 5.6.c, d) (Forray et al., 2010).

The correlation between streamflow and unfiltered Pb load (Appendix 5.h) suggested that re-suspension and dissolution of secondary soluble Pb-bearing mineral can occur during higher flows; runoff from the Graiggoch Mine wastes may have contributed relatively insoluble Pb-bearing minerals to the unfiltered Pb load. Although increases in filtered and unfiltered Pb loads during high flows were observed at the 880-1314 m river segment, minimum and maximum Pb load values (Appendix 5.g.3 and 5.g.4) and total load curve (Figure 5.13.a, b) decreased between 1314-1645 m. Therefore, as a diffusive source, Graiggoch Mine can act as a sink during a range of flow conditions, but it could also release Pb when the river channel and mine side are subject to high flow events.

The river segment around 3210 m, according to the sediment distribution characterisation (Chapter 4), is a depositional area (Figure 4.19) which may trap Zn and Pb enriched sediments. Seepage from the riverbanks yielded large variations between filtered and unfiltered Pb, Zn and Fe, suggesting the presence of metal-bearing fine-grained particles in the river banks. Characterised by the clay

and sand layering, this bank sedimentology structure may promote redox reactions of Pb- and Zn-bearing minerals and subsequent release of metals to waters (Figure 4.13). Compared to the upstream sites, Zn had a similar load but Pb load decreased across all the Q range (Figure 5.12 and 5.13, Appendix 5.g). Therefore, Zn had a mobile, aqueous behaviour, which has been observed in the literature (Smith, 1999), and on the other hand, Pb was trapped in solid form in the sediment. The reasons for Pb load attenuation in this river segment may be the variation in the fluvial parameters that encouraged the deposition of Pb (Figure 4.19). This Pb sink phenomenon has been observed also in other works (Zhu et al., 2007, Chen et al., 2012, Mayes et al., 2013).

Along the floodplain (5800-6740 m) Pb and Zn load are attenuated during low flows (28/07/2017, LF, Figure 5.12 and 5.13). Evidence of Pb- and Zn-bearing minerals were found by Superprobe and SEM images (Figure 4.14, Appendix 4.d), where Pb and Zn were adsorbed onto phyllosilicates and oxyhydroxides (see Chapter 4). During high flows (17/06/2016, HF) the total load of Zn and unfiltered Pb increased in the 3210-5930 m, suggesting the presence of Zn and Pb sources. These sources can be represented by the observed Pb- and Zn- bearing minerals mentioned. On the other hand, the total curve of filtered Pb load indicated a decrease (Figure 5.13 a); this Pb fraction was likely adsorbed to the suspended particles and contributed to the total unfiltered Pb load, or it precipitated in river channel sediments. Correlations between Zn, Pb loads and streamflows highlighted the different mobility of Zn (high correlation coefficient) and Pb (poor correlation; Appendix 5.h). This suggests that Zn was easily dispersed by moderate to high streamflows, and precipitated during low flows, as corroborated by the total and cumulative curves (Figure 5.12). Unfiltered Pb was mostly mobilised under high streamflow conditions.

5.4.2 Distribution and storage processes of Zn and Pb and their implication for remediation strategies

Along the studied river Pb and Zn average concentrations were above the environmental quality standards (EQS) for Zn 0.008 mg/l and Pb 0.007 mg/l (Defra, 2010). Depending on water hardness, Zn EQS can vary between 0.008-0.125 mg/l, but the lowest value is here considered because of the low CaCO₃ concentrations and its likely variation due to streamflows (Gozzard et al., 2011). From upstream of the mine site, at 0 m, averaged values were above the EQS for both Zn and Pb, confirming the high metal background concentrations of these metals already observed (see Table 4.2 Chapter 4). Minimum values of Zn were generally above the EQS; Pb minimum concentrations were above the EQS downstream of Wemyss Mine (171 m), and in the floodplain (5930-6780 m). Zinc concentrations were not correlated with streamflows (Appendix 5.h) with the highest

concentrations recorded under a low flow condition (05/09/2016, LF). On the other hand, maximum Pb concentrations were recorded during high flow (17/06/2016, HF). These results highlight the necessity to monitor metal sources across streamflow conditions and to not rely on a single streamflow event to apportion sources.

Zinc load was well-correlated with streamflow suggesting that Zn load responded to streamflow variations. Zinc load increased under high flow conditions with the main source both at low and high flow being the point source Frongoch Adit (Figure 5.12). Although Frongoch Adit entered the river as a point source, throughout its length, the adit is likely to gain metal load. The involved diffuse sources may be loose material present on the left bank of the adit or water coming from Frongoch Mine (Figure 2.1). In 2011 remediation works were executed at Frongoch Mine, where surface water was diverted to avoid it entering the mine perimeter, reduce the water in the underground mining and limit metal-enriched sediment runoff (NRW, 2015). The remediation generated a decrease in streamflow but increased the Zn and Pb concentrations. Therefore, the remediation effect of the river diversion at Frongoch Mine may be limited during high flows, when water can easily enter the mine work through different paths and flush Zn- and Pb-bearing minerals from the underground workings. Downstream of Frongoch Adit an increase in Pb load was recorded at all streamflows, with higher values for unfiltered Pb. Here suggested, further remediation of Frongoch Adit may be represented by a vertical flow reactor (Florence et al., 2016). Following Byrne et al (2017) the effect of remediation can be estimated using the continuous tracer injection as the cumulative metal load at the most downstream point minus the change of load recorded in the source segment. The remediated concentration would be the ratio of remediated load by the streamflow estimated at the most downstream site. The percentage of remediation effect is the difference between remediated and pre-remediated concentrations divided by the pre-remediate concentration (Table 5.5). For Frongoch Adit remediation may induce a decrease in the concentration of 60% Zn and 52% Pb filtered (Table 5.5). Although, no geochemical variation in the river water is modelled and the remediation strategy may induce downstream Pb and Zn release.

Lead loads did not correlate with streamflow, indicating different patterns of dispersion compared to Zn. Across the range of streamflow conditions, the primary source change occurred from Frongoch Adit, during moderate flow, to Wemyss Mine, during high flow (Figure 5.13). At Wemyss Mine processes of runoff and entrainment could have resulted in the release of Pb to the water which justifies the unfiltered Pb load increase. The filtered Pb load increase suggests the occurring of processes such as Pb-bearing minerals dissolution and de-adsorption from Fe-oxyhydroxides. Indeed, anglesite minerals, observed in the Wemyss Mine (XRD results, section 4.3.3), are stable

Pb-bearing phases until reductive conditions are encountered (Hudson-Edwards et al 1998); local reduction may have caused their dissolution and release of aqueous Pb (Lynch et al., 2018).

Furthermore, as observed in this (Figure 5.14) and other studies, during high flow events aqueous pH can decrease and cause Fe-oxyhydroxide instability and metal release (Byrne et al., 2013). The Wemyss Mine area has been described as an erosional area (Figure 4.17) with important degradation morphological processes witnessed during the presented research. Successful remediation of Wemyss Mine tips can be vegetated surface cover and storm control which can reduce tailing erosion and Pb dispersion (Thurston, 2006). Remediation effects, calculated using the accurate data obtained with the continuous tracer injection (Table 5.5), indicate a decrease of the total concentration of 10% for Zn and up to 35% for filtered Pb. Furthermore, tracer results indicate that caution is necessary for developing the remediation strategy as areas of Pb attenuation are observed on the side of the mine tips (Table 5.2).

Table 5.5 Load contributions of Wemyss Mine (WM), Frongoch Adit (FA) and Graiggoch Mine (GG) and potential remediation effects at 2614 m on loads and concentrations of Zn and Pb. Values are calculated from continuous tracer injection loads estimated under moderate flow (30/07/2016, MF).

	Zn Filtered	Zn Unfiltered	Pb Filtered	Pb Unfiltered
Pre remediation				
<i>Cum load (mg/s)</i>	362.67	359.16	12.85	25.08
<i>Cum concentration (mg/l)</i>	1.79	1.77	0.06	0.12
Load contribution (mg/s)				
<i>WM load</i>	349	34	5	4
<i>FA load</i>	207	215	7	13
<i>GG load</i>	76	78	0	0
Remediated load (mg/s)				
<i>Remediation of WM</i>	328	325	8	21
<i>Remediation of FA</i>	155	144	6	12
<i>Remediation of GG</i>	286	282	13	25
Remediated concentration (mg/l)				
<i>Remediation of WM</i>	1.62	1.60	0.04	0.10
<i>Remediation of FA</i>	0.77	0.71	0.03	0.06
<i>Remediation of GG</i>	1.41	1.39	0.06	0.12
Remediation effect (%)				
<i>Remediation of WM</i>	9%	10%	35%	17%
<i>Remediation of FA</i>	57%	60%	52%	51%
<i>Remediation of GG</i>	21%	22%	0%	-1%

According to the total and cumulative curves (Figure 5.12), the area of Graiggoch Mine (1148-1961 m) represented a source of Zn at moderate flow but decreases in total load were observed at low (28/07/2017, LF) and high flow (17/06/2017, HF). The variation in streamflow in this area is believed to be underestimated. In fact, in this river segment, especially from 1148 to 1961 m, the riverbed was characterised by coarse glacial and fluvial deposits that may enhance hyporheic water paths. Streamflow estimation with slug injection does not necessarily account for all the water due to the low dispersion of the salt through the riverbed. This hypothesis is corroborated by the streamflow average decrease from 1314 to 2614 m (Figure 5.3). On the other hand, the continuous tracer injection estimated a clear increase in the flow (Figure 5.4). This experiment allowed the tracer salt to fully mix and disperse in the river channel enabling most of the water interacting with the river water to be accounted for. Therefore, caution needs to be taken in the interpretation of load estimates through slug injections. Along this river segment, Zn total loads were likely to be underestimated and the observed attenuation was probably an artefact due to these measurements. Finally, the Pb total load decreases at Graiggoch suggested by the slug streamflow estimation was corroborated by the continuous tracer injection (Figure 5.6.b). Remediation of the area 1148-1961 m can decrease Zn concentration up to 22 % (Table 5.5), but care must be taken as the area represents a Pb storage. Change in water chemistry or river hydrology may lead to Pb dispersion. Further study on the hydrological river system, such as geophysical survey, and geochemical modelling for Pb stability are needed first to plan remediation strategies.

5.5 Conclusions

The major conclusions from this chapter are:

- The Nant Cwmnewyddion waters are impacted by Wemyss, Graiggoch and Frongoch Mines working and its water has Zn and Pb concentrations higher than the EQS.
- The multi-tracer method approach allowed spatially detailed Pb and Zn source apportionment and estimated contributions to be made across streamflow variations.
- For the first time, a continuous tracer injection was successfully executed in an oceanic temperate climate under moderate flow. This enabled Zn and Pb point and diffuse sources to be accounted for.
- The Wemyss Mine area (52 - 171 m), characterised mostly by waste tips, was recognised as a diffusive source of Zn and Pb ranked as Source#2 for Zn and Pb under moderate flow conditions and Source#1 for Pb during high flow conditions.
- The Frongoch Adit (862 m), connected to the Frongoch Mine underground workings, was Source#1 for Zn across streamflow conditions and Source#1 for Pb under moderate to low streamflow conditions.
- The Graiggoch Mine (1148-1961 m) acted as a Source#2 for Zn and as a sink of Pb. The diffuse source of Zn in this area was probably water infiltrating mine waste and a potential hyporheic zone connected to the underground mine workings.
- Zinc and Pb loads variations across streamflows must be taken into account when planning remediation and monitoring strategies.

Chapter 6. The role of environmental nanoparticles in metal transport in mining-impacted rivers

6.1 Introduction

Historical and contemporary mining activities generate colloids and nanoparticles as a direct consequence of metal extraction processes or by the release of gangue and waste material into the ecosystem (Mikhlin et al., 2016). These particles, of various sizes (few to thousand nanometers), can be formed by, or adsorb, trace metals (Lead and Wilkinson, 2006). As a consequence, studies of the fate, transport, and toxicology of trace metals in mining-impacted river systems must include colloid and nanoparticle studies. Characterising nanosized particles requires adequate sampling techniques and a multi-method approach for acquiring particle size distribution, surface chemistry, and morphology information. Furthermore, because metal sources can be found throughout the river channel, the input of nanoparticles can occur at different river segments. Therefore, the need to link nano-scale information (chemistry, morphology, and abundance) to the catchment-scale becomes a key step to address trace metal dispersion.

In this study the following definitions have been adopted: *natural colloids* are heterogeneous and polydisperse phases with at least one dimension between 1–1000 nm; *natural nanoparticles* are the colloidal fraction around 1-100 nm (Baalousha and Lead, 2013). Nanoparticles differ from bulk material showing signature chemical and physical characteristics due to the high ratio between surface and volume and to the surface reactivity. Their size influences redox and sorption capacity (Hochella et al., 2008), increases their suspension capacity in a water column and drives aggregation processes (Hotze et al., 2010). Buffle et al. (1998) report that freshwater colloids (1 nm to 1 µm) are formed by aggregates of (i) inorganic phases, (ii) rigid biopolymers and (iii) humic substances or refractory organic matter. The most common inorganic phases are aluminosilicates, silicates, silica, and iron oxyhydroxides. Usually, aluminosilicates are angular thin layers; the other phases can generally be spherical in shape. Natural organic matter in stream systems is mostly represented by fulvic compounds which have a pedogenic origin, a lifetime of several centuries and usually are sized around 0.8-3 nm (Buffle et al., 1998). Inorganic phases can be covered by an adsorbed layer of fulvic compounds or, if smaller in size, be embedded in a gel of fulvic compound (Lead and Wilkinson, 2006).

The capacity of nanoparticles to influence metal dispersion is well known (Hargreaves et al., 2017, Pham and Garnier, 1998). They can modify or induce metal speciation or bioavailability and

enhance metal transport (Baalousha and Lead, 2007). The main nanoparticle characteristics that control their interactions with metals are their morphology, chemical composition, structure and abundance (Buffle et al., 1998, Baalousha and Lead, 2013, Hotze et al., 2010, Christian et al., 2008). Nanostructures, such as organic films around nanoparticles, can influence the reaction kinetics between nanoparticles and trace metals (Aiken et al., 2011, Baalousha and Lead, 2007). Nano-minerals can easily release metals. For example, some microbes (such as *Geobacter sulfurreducens*) can reduce nano- Fe oxide (as hematite and goethite) twice as fast as 20-70 μm sized bulk minerals (Bosch et al., 2010).

Metal-bearing nanoparticle characterisation can provide fundamental knowledge to improve water quality monitoring protocols. In water quality monitoring, 450 nm filters are typically used to separate particulate phases from so-called dissolved elements (American Public Health et al., 2005). Particles with diameters smaller than 450 nm can pass through the filter and account for 'dissolved' elements. The chemistry of nanoparticles is different from the truly dissolved elements. Their toxicology and bioavailability are affected by size and morphology. Some nanoparticles have been found to modify reproduction and physiological conditions, and to create acute toxicology (Baun et al., 2008). In mining-impacted catchments, investigations of naturally occurring nanoparticles can provide a baseline for treatment option planning (Wigginton et al., 2007). Remediation schemes can be limited by the presence of metal-bearing nanoparticles that occur in the reported truly dissolved phase, or they may introduce engineered nanoparticles that may interact with natural nanoparticles, modifying the stability of the latter (Prudêncio et al., 2017, Wigginton et al., 2007).

During the last two decades nanoscale processes involving metal transport, fate and toxicity have captured considerable attention from the scientific community. Different studies focused on the characterisation of nanoparticles and their processes in a different matrix (such as soil, freshwater, groundwater, and air), compared environmental to engineered nanoparticles, investigated their toxicology and developed sampling, filtration or extraction techniques (Baalousha and Lead, 2013, Sharma et al., 2015, Joo and Zhao, 2017).

A multi-method approach was implemented by Lapworth et al. (2013) to characterise suboxic groundwater colloids. The main issue addressed was maintaining the nanoparticle stability during storage and analysis time for which suboxic chambers were tested and implemented. Particle size distribution, morphology, and surface chemistry were analysed with flow fractionation (FIFFF), atomic force microscopy (AFM), scanning electron microscopy (SEM) and transmission electron microscopy (TEM). The data discussion pointed out the complementarity of the different techniques. Plathe et al. (2013) analysed riverbed and bank sediment in a mining-impacted river.

They found trace metals associated with nano-sized Fe and Ti oxides (c.20-400 nm) which may have an important role in metal transport (Zn, Pb, Cu, As, Cr and Co). In their work, samples were collected from 15 and 20 km downstream of a mine waste dam removal site. Nanoparticles were extracted by density, reducing the amount of silica and aluminosilicate which are rarely associated with trace metals (Plathe et al., 2010).

A catchment investigation on waterborne nanoparticles may prove or neglect the importance of these minerals on metal transport. A case study on a Montana (USA) mine area containing As, Fe, and Pb was reported by Wigginton et al. (2007). The mine was subjected to remediation work, but high metal concentrations were still recorded downstream. Solid samples were collected from the riverbed and the floodplain. TEM analysis showed metals attached to or forming nanoparticles. The identified nanoparticles were Zn sulfates, oxides, and sulfides, as well as other nanoparticles with high sorption capacities for Zn, As and Pb such as Mn and Fe oxides. Complementary water samples were collected and analysed with an HR-TEM-EDS, resulting in the observation of metal-bearing nanoparticles. The metals were found to be transported both in the aqueous phases and as sorption complexes on other particles. The authors suggested that during flood events large particles contributed more than smaller particles to the metal load, but long-distance transport could occur only during low flow or slow water velocities (Wigginton et al., 2007).

In Pokrovsky et al. (2010) trace elements and organic carbon seasonal flux were investigated in the Severnaya Dvina River (NW Russia). In-situ filtration (5 μm , 0.22 μm , 100, 10 and 1 kDa) and dialysis (1 and 10kDa) were performed and the results were compared. A similar procedure was used by Pokrovsky and Schott (2002) to investigate trace metal transport associated with iron colloids and organic matter in small boreal rivers (NW Russia). Sampling limitations were encountered in the time-lapse necessary for sampling (few hours per site). Furthermore, data showed disagreement between filtration and dialysis results of the 10 and 1kDa fractions, and a Zn and Pb contamination. The observed organic matter was proposed to be derived from soil horizons or from waterborne organisms (such as bacteria and phytoplankton exudates). Loads of major and trace elements were divided into three forms of suspended (larger than 0.22 μm), total dissolved (smaller than 0.22 μm) and colloidal material (between 1 kDa and 0.22 μm). The colloidal form showed season variations influenced by the organic or organic-mineral colloidal phases originated by the soil. This previous work showed that sources of nanoparticles may be diverse in mining-impacted river systems.

Previous research has highlighted the structural and chemical complexity of the nano-scale phases and processes. For the identification of the role of nanoparticles in metal transport in river water, accurate characterisation of chemical and morphological nanoparticle surface, particle size

dispersion and metal load are fundamental. Inefficient sampling or filtration techniques and analysis based on a singular instrument can generate artifacts in the results and interpretation of occurring processes. Only a few attempts in linking nano-scale to catchment-scale processes to provide information on nanoparticle and metal fate have been made. Therefore, knowledge gaps on metal and nanoparticle fate along impacted rivers are still evident.

The aim of this chapter is to identify the role of nanoparticles in metal transport in mining-impacted rivers at the river catchment scale. The specific objectives are to (i) determine the optimal methods of fluvial sampling, sample treatment and preservation for securing representative nanoparticles; (ii) characterise nanoparticle size dispersion, and morphology following a multi-method approach; (iii) quantify the metal load attributable to suspended particles (> 450 nm), nanoparticle (450 – 2.5 nm) and truly dissolved (< 2.5 nm) and their role in metal transport during moderate streamflow.

6.2 Methods and materials

This experiment was carried out thanks to the grant FENAC/2016/11/008 which allowed access to the Facilities for Environmental Nanoscience Analysis and Characterisation (FENAC). The design of the sampling protocol was carried out at Liverpool John Moores University and then tested in the field with a single sample site test. Samples were then transported to the FENAC laboratory to verify the nanoparticle stability and storage time. Following this trial experiment, the main experiment was then designed, with sampling occurring over two days and all the analyses in the following two weeks. General background information on the used instrument, storage time and filtration unit design are reported in section 3.3.

6.2.1 Sampling protocol and nanoparticles storage time

Along the Nant Cwmnewyddion 5 field sites were chosen at T0 (0 m), T2 (880 m), GG (1645 m), DC (3210 m) and RB (5930 m) following mineralogical characterisation of the riverbank soil, and a review of mine waste locations, the hydrology of the river and site accessibility (Figure 6.1). The nanoparticle sampling protocol consisted of a sequential filtration using i) 63 μ m nylon filters, ii) 1 μ m Merk Millipore capsule filters for metal analysis, iii) 450 nm Nalgene reusable filter units with Whatman Nylon Membrane, iv) Millex[®]10kDA (circa 2-2.5 nm) centrifugal filter. Water samples were prefiltered using 63 μ m and 1 μ m to avoid filter clogging and to partition the phases above and below 450 nm. Nanoparticles were differentiated from truly dissolved metals with the final

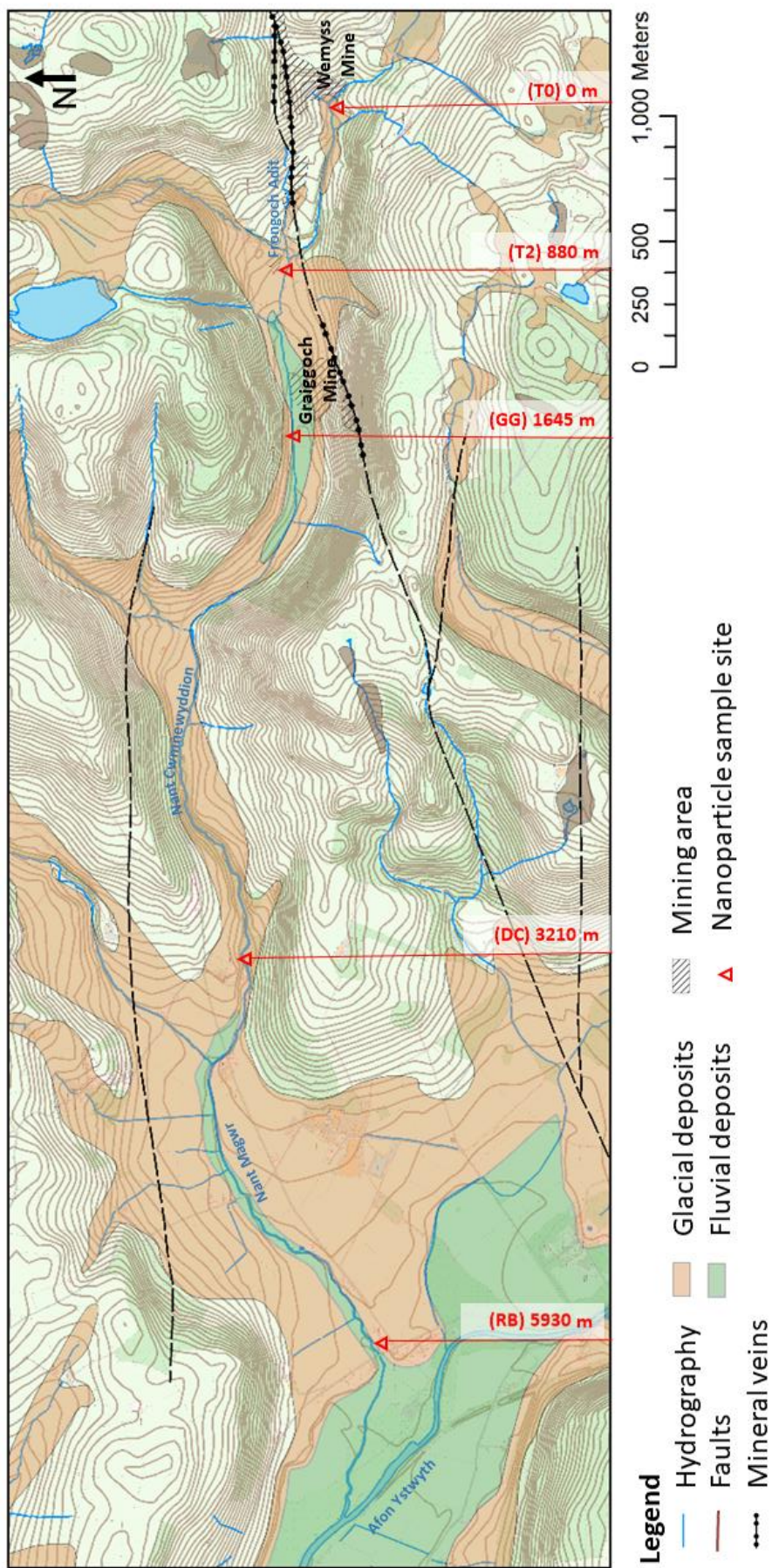


Figure 6.1 The Nant Cwmnewyddion and the Nant Magwr map showing a waterborne nanoparticle sampling site. Listed in red the sampling sites and distance from TO (0m). GG: Graiggoch Mine; DC: depositional area at middle river length; RB: floodplain (upstream site). DiGMapGB-50 [SHAPE geospatial data], Scale 1:50000, Tiles: ew178, Updated: 1 October 2013, BGS, Using: EDINA Geology Digimap Service (www.digimap.edina.ac.uk, Downloaded: 03-06-2016), modified with ArcGIS v.10.

2.5 nm filter step executed with centrifugal filters of regenerated cellulose Amicon Ultracentrifugation (Merckmillipore) and polyethersulfone membrane Vivaspin 500 (SLS) (Figure 6.2). The first three steps were executed in the field with a hand vacuum pump, and the filtration step at 2.5 nm was executed in the laboratory by centrifuging the filters for 30 minutes at 13,300 x g (centrifugal force). From the centrifugal filters, both the filtered and the centrifuged phases were collected. The filtered phase was used to measure truly dissolved metals and the centrifuged phase was prepared for microscopic analysis. To minimise artifacts and nanoparticle weathering the samples were stored under a controlled temperature which reflected the river temperature (13.7°C), and only the 2.5 nm filtered samples were acidified. The equipment used in the filtration system was washed in 10% ultrapure nitric acid and rinsed in ultrapure water (18 MΩ cm⁻¹ MilliQ) to reduce sample contamination. A blank of ultrapure water was collected at each site using the sampling protocol to measure potential contamination. A total time of two hours was spent at each site to complete the filtration procedures. Physicol-chemical water parameters including specific conductivity, temperature and pH were monitored and further samples were collected for dissolved organic carbon (DOC), cation and anion analysis. The water chemistry and nanoparticle investigation were coupled with a salt dilution slug injection in order to estimate streamflow at each site and quantify nanoparticle load (see Chapter 5). Please refer to section 3.3 for a complete description of the sampling procedure.

A trial experiment was conducted to evaluate the nanoparticle sampling protocol and storage time. Water sampling and streamflow measurements were performed on the morning of the 21st of August 2017 at Graiggoch Mine (1645 m). River water samples were collected in duplicate (A – B) and coupled with a blank. Water samples were collected in 250 ml bottles and stored in a Waeco TCX35 cool box at a fixed temperature of 13.7 °C (river temperature). Fifteen ml from samples A and B and the blank were stored separately for the 2.5 nm filtration step. An additional 2 l of river water was collected in case of sample centrifugation was required. The sample was transported to the FENAC laboratories to investigate particle size distribution (PSD) and particle stability after 4, 24 and 48 hours from the sampling. Data acquisition was performed with the Malvern Zetasizer HPPS Nano ZS including DLS (Dynamic Light Scattering) and Zeta potential analysis. The sample fraction subject to analysis was the 450 nm filtered one. DLS system operating procedure (SOP) was set for silica material (the most representative component in the soil), dispersed in water and equilibrated to 13.7 °C for four minutes and run five to seven times depending on the occurrence of precipitation processes. The same procedure (SOP) was used for the Zeta potential measurements (Red Laser 633 nm). The data range was +150 and -150 mV. Due to the high sample heterogeneity, a Zeta Potential Transfer Standard (-42 mV ± 4.2 mV) was run between the first and

second samples. Nanoparticle size and surface charge values were compared among the 4, 24 and 48 hours to establish the sample storage time. As explained in the trial result section 6.3.1, nanoparticle parameters showed consistencies across the 4, 24 and 48 hours and a 48 hours stability window of the nanoparticles was suggested.



Figure. 6.2 Example of river water filtration with 63 and 1 μm pre-filters and 0.45 μm filter.

6.2.2 Nanoparticle characterisation experiment

A nanoparticle stability window of 48 hours allowed two days of sampling followed by characterisation analysis. The sample collection occurred on the 11th and 12th of September 2017 under a moderate flow condition (12/09/2017, MF in Appendix 5.b). The river water was sampled at the five sites following the above protocol. Two ml of the 450 nm filtered sample was centrifuged to obtain the nanoparticles between 450 – 2.5 nm and the truly dissolved fraction (<2.5 nm). DLS analysis for PSD was then carried out, and TEM (transmission electronic microscope) and AFM (atomic force microscope) grids were prepared. The time frame in the laboratory is reported as WI for measurements made immediately after sampling (during the first week) and as WII for those made during the second week of the experiment (Table 6.1).

Table 6.1 Time frame of nanoparticle analysis at FENAC (Facilities for Environmental Nanoscience Analysis and Characterisation) laboratories carried out in September 2017.

	Monday 11th	Tuesday 12th	Wednesday 13th	Thursday 14th	Friday 15th
Week I (WI)	- Sampling	- Sampling	- DLS - 2.5 nm filtration and acidification	- DLS - First slot of grids for TEM and AFM	- Second slot of grids for TEM and AFM
	Monday 18th	Tuesday 19th	Wednesday 20th	Thursday 21st	Friday 22nd
Week II (WII)	- AFM - TEM	- DLS + Zeta	- DLS conc. - Zeta conc.	- DLS	- AFM

DLS and Zeta Potential

DLS analysis was carried out straight after sampling (WI) and after a week (WII) to monitor PSD variations in time. The system operating procedure (SOP) settings used in the trial experiment were employed. The analysis was conducted on samples A and B and their blanks. Elaboration and quality check of the data was performed using Zetasizer software and Excel. The raw correlation data, between signal and particle size parameters, are checked over the *size* workspace of the software. Data quality is indicated by the software and can be verified in the *Intensity PSD* and *Expert Advice* tabs. Cumulant data (Z-average hydrodynamic diameter, polydispersity index PDI) and measure counts (kcps), coupled with the quality report were listed for each run in an Excel file. Good quality data from both of the A and B duplicates were averaged using the Zetasizer software. For each average cumulant and distribution parameters and plots (peaks of the intensity-weighted size distribution) are reported in an Excel file. The repeatability of the measure was checked calculating the standard deviation of the Z-average of each run with Excel. Obtained values of intensity for particle diameters, Z-average (d-nm) could not be converted into a number of particles due to the unknown sample chemistry and shape heterogeneity. Peaks recognised from the software are based on the intensity % of the signal attributed to the Z-average. Small peaks can be ignored by the software and not appear in the peak description table. Therefore, small peak coordinates – expressed as Z-average and Intensity% – were manually extrapolated from the Z-average distribution. Due to the limitations of the data elaboration, results are used for a qualitative comparison among samples and nanoparticle degradation during storage time. Please refer to section 3.3 for background information on DLS analysis.

During WII Zeta potential analysis was performed following the SOP of the trial experiment. The Zetasizer software indicates quality related to *Phase plot* and *Distribution data*. Quality information and Zeta potential parameters for the run averages and main peaks were reported in an Excel file. The resultant data quality was very low due to the low counts and sample heterogeneity (Malvern, 2012). Runs with irregular or inconsistent phase or distribution plots were dismissed; furthermore, the software suggested incompatibility among runs to calculate averages. Due to the low quality of the data, the main experiment Zeta Potential results are not included here.

During WII, RB and DC samples were centrifuged to attempt to increase the quality of the Zeta Potential and DLS data by increasing the instrument counts. The centrifugation process was executed with an Amicon-Millipore ultracell ultrafiltration mounted with a 1 kDa filter membrane of regenerated cellulose. A 20 ml sample was concentrated down to 10 ml under 10 psi nitrogen gas at low stirring in 10 min. Following a DLS result crosscheck between WI and WII, size variations were observed. Therefore, the analysis of further samples was suspended. The results from RB and DC are used to verify the centrifugation effect on the samples.

AFM and TEM

Microscopic analysis was carried out with Atomic Force Mass Spectroscopy (AFM) and Transmission Electronic Microscopy (TEM) in order to acquire nanoparticle shape, size and composition information. Two sets of samples were prepared (i) 10 times concentrated and (ii) 100 times concentrated. The concentration was executed with the centrifugal filters at 40,000 rpm for 20 min. The concentrated sample was dispersed onto AFM and TEM grids following the adsorption on thin layer procedure (Baalousha and Lead, 2013). TEM supports were Formvar/carbon-coated 200 Mesh Cu TEM grids and the AFM supports were freshly cut mica. The supports were placed horizontally, 25 µl drop of the centrifuged sample was deposited onto them and left to rest for 60-90 minutes covered by a glass vessel to keep a clean area. When a thin layer of solution was left on the grid, usually after 60 – 90 mins, the excess of liquid was gently removed and the support was washed by immersing it two to three times in fresh ultrapure water for 30 seconds. The grids were ready to be analysed when they were dry. This method aims to capture and count small nanoparticles easily bound to the mica surface (Lapworth et al., 2013, Baalousha and Lead, 2012).

TEM Images and elementary composition were acquired for nine spots for each of the T2, GG, DC and RB samples with the TEM JEOL 2100 at 200 keV under a range of magnification. The images and chemical results, expressed in weight and atomic percentages, are reported together in excel spreadsheets. Size, shape and electronic density are noted together with the images. The atomic percentages of the most abundant elements are used to identify the most likely mineral phases.

The analysis was limited to collecting semi-quantitative data due to the chemical heterogeneity of the nanoparticles.

AFM analysis was performed with the AFM XE Data Acquisition XE 100 Advance Scanning Probe Microscope PSIA. The analysis was carried out using the topographic source in dry mode and under environment conditions (Baalousha et al., 2014). The nanoparticle height was counted over 20 to 25 images (1x1 μm) per sample. Images were processed by flattening using a polynomial curve; in this case of order four along the Y-axis and 1 along the X-axis, removing the background noise and optimising the contrast (Ratcliff and Erie, 2001). In the processed images, the particles were counted with the transect tool in the EI Image Processing Program. The transect represented the topography of the mica; peaks higher than 5 nm were considered nanoparticles. The threshold of 5 nm was calculated from the noise signal, which usually occurred between 1.5 – 2 nm, and then multiplied by three. When possible a minimum of 200 particle heights were counted to ensure a representative particle distribution (Baalousha and Lead, 2012). The total was then divided by 10 or 100 (depending on the concentration ratio used) to obtain the final concentration of the particles.

Following Baalousha and Lead (2007), the averages were the number averages, $N(z)$, calculated as $\sum n_i z_i / \sum n_i$, and the weighted average, $S(z)$, calculated as $\sum n_i z_i^2 / \sum n_i z_i$. In these equations “z” is the particle height and “n” is the number of particles. The polydispersity (P) is equal to $S(z)/N(z)$. Further parameters reported were the minimum (min), maximum (max) and the standard deviation values. For PSD analysis, the particle heights were divided into 0.5 nm intervals using the *frequency* function in Excel.

6.2.3 River water metal partitioning

The sampling protocol provided unfiltered, filtered 450 nm and 2.5 nm aliquots of river water samples. These aliquots enabled the metal concentrations in suspended particles (> 450 nm), nanoparticle (450 – 2.5 nm) and truly dissolved (< 2.5 nm) to be distinguished. After collection, the samples were acidified using 1% HNO_3 (ultrapure acid). For the truly dissolved range, two types of centrifugal filters at 10 kDa were used for the A and B duplicate samples. Therefore, four centrifugal filters per site were used obtaining 1 to 2 ml volume of samples. A 1 ml portion was diluted up to 10 ml with 0.1 ml HNO_3 and 8.9 ml ultrapure water to run the analysis. The sampling protocol and site contamination were measured by summing metal concentrations in the blank-RB, -DC and -GG 2.5 nm filtered samples and in the 450 nm filtered blank samples.

Water chemical analysis was conducted at LJMU laboratories. Unfiltered samples were analysed with the ICP-OES for Zn, Pb, Al, Fe, and Mn concentrations, and the 450 and 2.5 nm filtered samples were analysed with the ICP-MS for Zn, Pb, Al, Fe, Mn, Cd, and Co. Unfiltered and filtered metal concentrations were described as a function of river length. Metal loads were calculated as the product of streamflow estimation and metal concentrations (see Chapter 5). Loads for each size fractions are expressed as absolute values or percentages of the unfiltered values. The data were plotted using a stacked area graph based on the load size fractions. Anion values were retrieved from Chapter 5.

For dissolved organic matter (DOC) samples processed in the field, 120 ml of river water was passed through 450 nm filters, stored in dark polypropylene Nalgene bottle and acidified with 2M HCl. Samples were analysed at LJMU laboratories with the Total Organic Carbon Analyser (TOC-V) coupled with an autosampler (ASI-V), the Total Nitrogen Unit (TN) and the Sparge Kit. The used software was the TOC Sample Table Editor.

6.3 Results

6.3.1 Evaluation of sampling procedure and storage

For the trial experiment, the samples collected at GG (D26 A, D26 B, and D26 Blank) were analysed by DLS and Zeta potential. The results are reported in Appendix 6.a and 6.b. DLS results show a general polydispersed pattern with a low Z-average difference among the three storage times (4, 24 and 48 hours). Some sample runs show instrument errors reporting the *presence of large or sediment particles, sample too polydispersed for cumulant analysis*. The averages between D26 A and B at 4, 24, and 48 hours have a Z-average value of around 138 nm (SD 1.6 nm). Furthermore, 4, 24 and 48 hours curves of size distribution by intensity (graph in Appendix 6.a) show similar patterns. An analysis of the distribution parameters indicates an averaged Polydispersity Index (PDI) of 44.3 (SD 0.01), with Peak 1 equal to 232 nm (SD 29.2) and Peak 2 equal to 4014 nm (SD 171.5). SD values decrease to 9.6 for Peak 1 and 20.2 for Peak 2 when comparing the 4 to 24 hours data. A window of 48 hours was considered for planning the sampling and the laboratory experiments. The DLS results from the field blank (D26 Blank) showed low signal and no parameters were calculated by the instrument. The Zeta Potential (ZP) dataset reflects the sample heterogeneity; however, the quality of the results was low due to low particle concentration. The SOP halted calculation of D26 A and D26 B averages due to the highly variable results. General qualitative parameters were collected to describe the nanoparticle ZP at 4, 24 and 48 hours. The reported parameters are the arithmetical averages of ZP, Peak 1 ZP, and area (Appendix 6.b). ZP averages are -5.12 mV (SD 2.13)

at 4 hours, -2.72 mV (SD 1.13) at 24 hours and -4.74 mV (SD 1.61) at 48 hours. The low reproducibility of the data discouraged the use of ZP as an indicator of sample stability.

6.3.2 Particle size distribution – DLS and AFM results

DLS elaborated graphs of size distribution by intensity for WI and WII are shown in Figure 6.3. General DLS data from the week I and week II are summarised in Table 6.2. At WI samples from the different sites have an arithmetic average Z-average of 275 nm (SD 13). Figure 6.4 reports the series of graphs from each site at WI, including the peaks recognised manually.

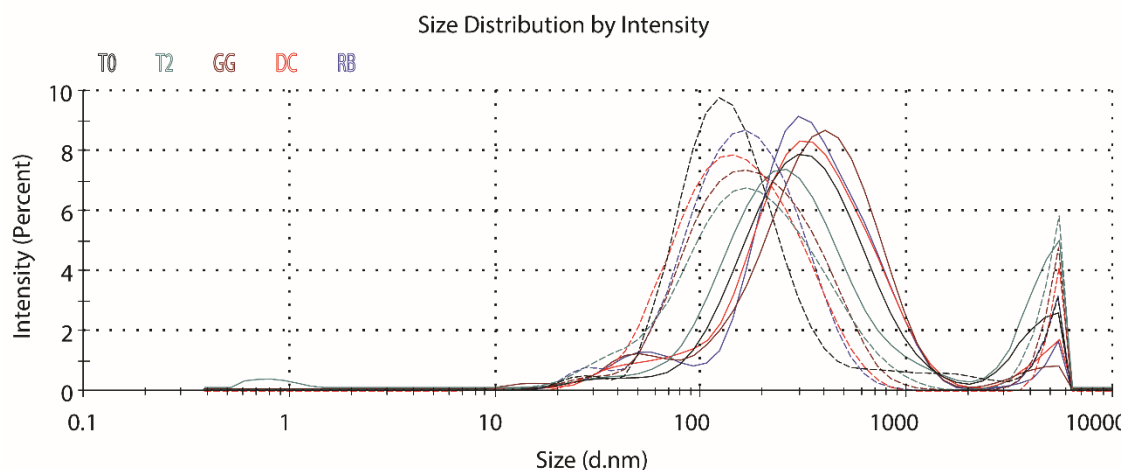


Figure 6.3 DLS size distribution by intensity for sample T0, T2, GG, DC and RB at week I (plain line) and week II (dashed line).

Table 6.2 DLS results from main experiment at week I and week II. Z-ave: Z-average hydrodynamic diameter; SD: standard deviation; PDI: polydispersity index; Peak: intensity-weighted size distribution peak; *, *In range figure low*: instrument expert advice on result quality indicating the presence of large or sedimenting particles; ^, *Cumulative fit error high*: instrument expert advice on result quality indicating the sample is too polydispersed for cumulant analysis.

Sample	Z-Ave		Pdi		Count kcps	Note			
	d.nm	SD		SD					
Week I									
T0	287	32	0.43	0.13	411.1	Good			
T2	283	24	0.5	0.11	87.6	*			
GG	259	70	0.47	0.08	69.9	Good			
DC	264	25	0.44	0.11	71.1	*			
RB	282	32	0.42	0.02	188.2	good			
Average	275								
SD	13								
Sample	Peak 1			Peak 2			Peak 3		
	Size d.nm	Intens. %	SD d.nm	Size d.nm	Intens. %	SD d.nm	Size d.nm	Intens. %	SD d.nm
T0	372	90	266	4291	10.4	9997	0	1.2	0
T2	316	82	255	4452	17	951	1	1.2	0
GG	427	89	253	52	7.3	16	4259	3.2	990
DC	381	95	267	4622	4.8	869	0	0	0
RB	413	89	247	55	8.3	19	4895	3.2	846
Sample	Z-Ave		Pdi		Count kcps	Note			
	d.nm	SD		SD					
Week II									
T0	171	21	0.45	0.1	76	* ^			
T2	239	42	0.58	0.07	53.2	* ^			
GG	225	27	0.44	0.07	55.7	* ^			
DC	196	21	0.39	0.04	58.4	* ^			
RB	195	28	0.42	0.05	90	* ^			
Average	205								
SD	27								
Sample	Peak 1			Peak 2			Peak 3		
	Size d.nm	Intens. %	SD d.nm	Size d.nm	Intens. %	St Dev d.nm	Size d.nm	Intens. %	SD d.nm
T0	189	89	179	4932	6.2	745	1932	3.1	562
T2	222	88	177	4902	12.4	751	0	0	0
GG	217	91	151	5071	8.6	631	0	0	0
DC	182	94	123	5244	6.3	464	12	0.1	2
RB	192	91	116	4962	6.2	738	30	3.1	6

A peak at 5560 nm with an intensity percentage between 0.8-4.9 % is present in all the samples. T0 has a main peak at 295 nm (intensity 7.8%) followed by a tail between 18.2 and 68.1 nm. T2 has a more irregular curve with the main peak at 255 nm (intensity 7.2%), a tail between 21.0 and 51 nm and a small peak at 0.7-1.3 nm. A larger peak size (396 nm at 8.6 % intensity) is noticed for the main GG peak, and a small peak is then recognised at 51 nm, followed by a tail until 11.7 nm. The z-average curve for sample DC shows a main peak at 342 nm and a tail between 105 and 21 nm. The downstream site, RB, has the main peak around 295 nm with a second peak around 59 nm. DLS measurements acquired at WII indicate a shift towards smaller values compared to the WI data. The arithmetic average of the Z-average is 205 nm (SD 27) and the peaks are smaller than WI peaks (Figure 6.3). Furthermore, the SOP reports errors regarding the *presence of large or sedimenting particle* and cumulative fit error (*data quality too poor for distribution analysis and sample too polydispersed for cumulant analysis*). Results from the centrifuged samples RB and DC indicate an increase in counts (kcps) from 58 and 90 kcps to respectively 186 and 258 kcps. In contrast, Z-average values decrease compared to uncentrifuged samples and secondary peaks are not observed in the size distribution by intensity graphs (see Appendix 6.c). DLS results of field blanks report low quality with low reproducibility. This, together with frequent errors in SOP, suggest that these samples may not be suitable for DLS measurement as they are too polydispersed.

The number and weighted averages of the particle size, min, max, polydispersity particle concentration on the mica substrates from the AFM analysis are reported in Table 6.3. A complete list of the acquired images is shown in Appendix 6.d. Figure 6.5 shows particle size distribution (PSD) and cumulative PSD plots. The numerical averages, $N(z)$, for T2, DC, and RB are around 9.1 – 9.7 nm, with the $N(z)$ for GG differing from these with an average value of 7.4 nm. Weighted averages, $S(z)$, for T2, DC, and RB are around 5.6 – 11 nm, with GG showing a higher value of 37.2nm. Polydispersity counts 5.0 for GG and ranges between 0.6 – 1.2 for the other samples. The average of particle per image (NP/um^2) varies from 0.2 to 2.9. Among all the samples the most frequent nanoparticle sizes are between 5 – 11 nm (Figure 6.5 a). A peak of frequency lower than 2 % is observed around 11 – 15 nm; smaller peaks are mostly found around 15 -37 nm and further peaks are spread towards 37 to 69 nm. In the cumulative PSD T2, DC and RB curves follow the same patterns (Figure 6.5 b). The GG curve illustrates a larger contribution of about 6 to 9 nm particles.

Manually identified peaks (Week I)		1°	2°	3°	4°	5°	6°	7°
T0	peak (d.nm)	295.3	5560	18.17	68.06			
	Intensity (%)	7.8	2.5	0.1	0.6			
T2	peak (d.nm)	255	5560	21.04	50.75	1.3	0.6	0.7
	Intensity (%)	7.2	4.9	0.1	0.5	0.1	0.2	0.3
GG	peak (d.nm)	396.1	5560	50.75	78.82	28.21	11.7	
	Intensity (%)	8.6	0.8	1.2	0.9	0.3	0.1	
DC	peak (d.nm)	342	5560	105.7	21.04			
	Intensity (%)	8.2	1.6	1.6	0.1			
RB	peak (d.nm)	295.3	5560	91.28	58.77	21.04		
	Intensity (%)	9.1	1.6	1.8	1.2	0.1		

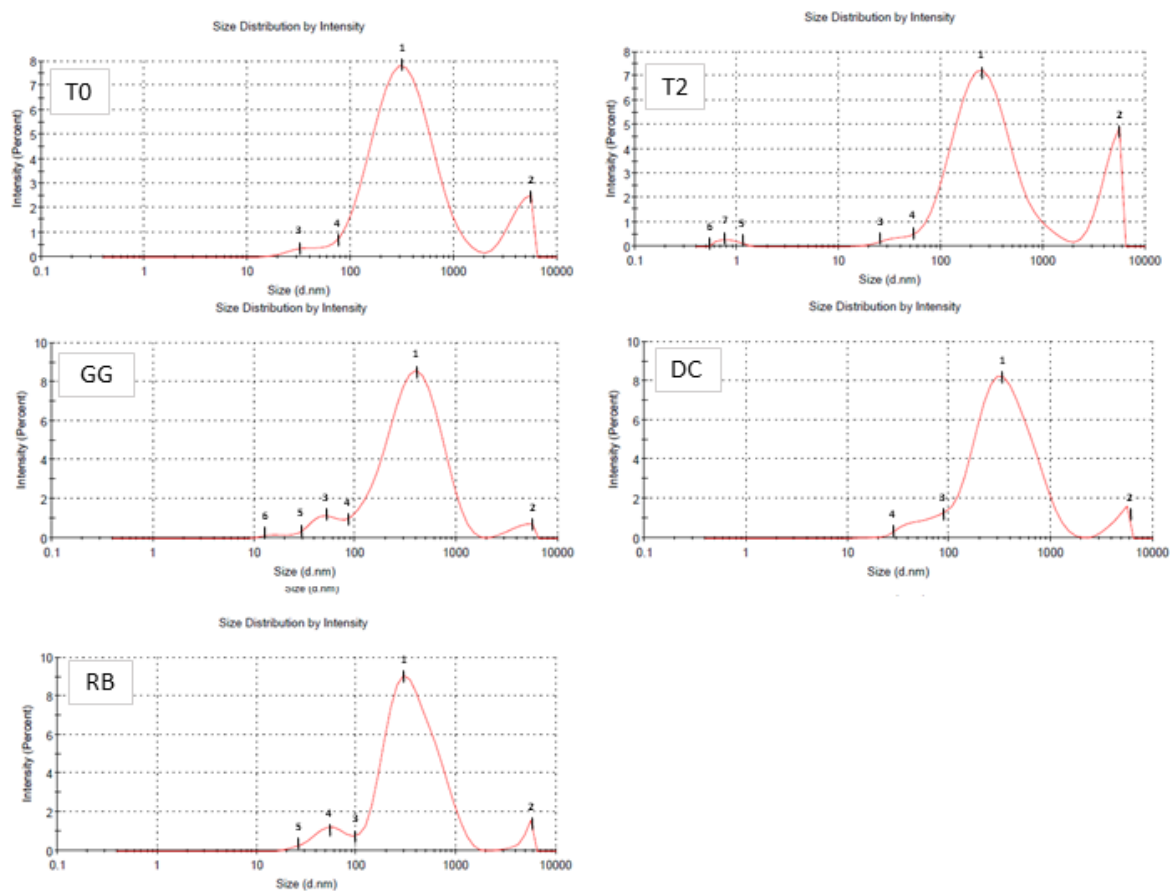


Figure 6.4 Table (on top) reporting the peak size (d.nm) and intensity (%) individuated manually in the DLS graphs of size distribution by intensity reported below (T0, T2, GG, DC and RB).

Table 6.3 AFM results for sample T2, GG, DC, and RB. Reported are the number average, $N(z)$, calculate as $\sum n_i z_i / \sum n_i$ and weighted average, $S(z)$, calculated as $\sum n_i z_i^2 / \sum n_i z_i$ where “ z ” is the particle height and “ n ” is the number of particle; minimum (MIN) and maximum (MAX) particle values; polydispersity (P) equal to $S(z)/N(z)$; concentration of particle on the acquired images ($n/\mu\text{m}^2$).

Sample	T2	GG	DC	RB
N(z)	9.2	7.4	9.1	9.7
S(z)	11.0	37.2	9.3	5.6
MIN	4.7	4.5	4.6	4.5
MAX	60.5	37.3	61.4	70.1
P	1.20	5.04	1.03	0.58
$n/\mu\text{m}^2$	0.2	2.9	0.3	2.3

a.

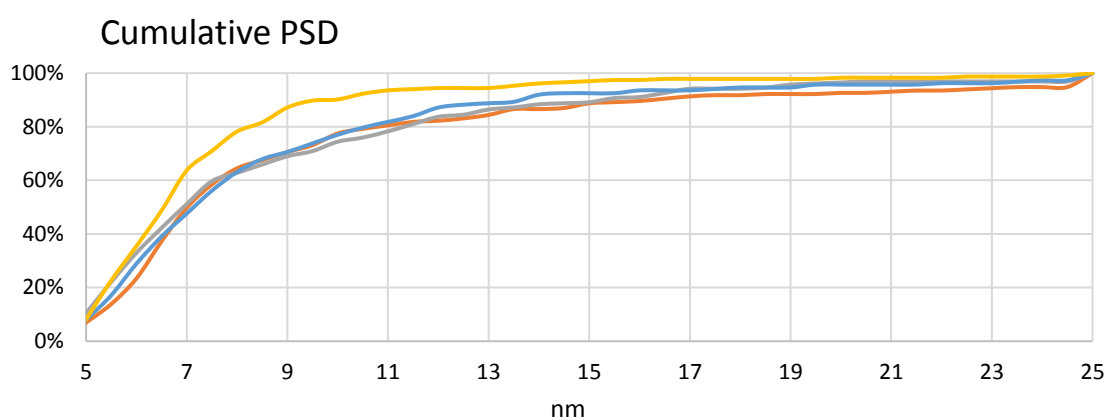


Figure 6.5 AFM results for sample T2, GG, DC, and RB. a) Cumulative PSD curve expressed in percentage. b-e) Histograms of particle size distribution curve for T2 (b), GG (c), DC (d) and RB (e). Particles bigger than 24 nm are counted in 24%.

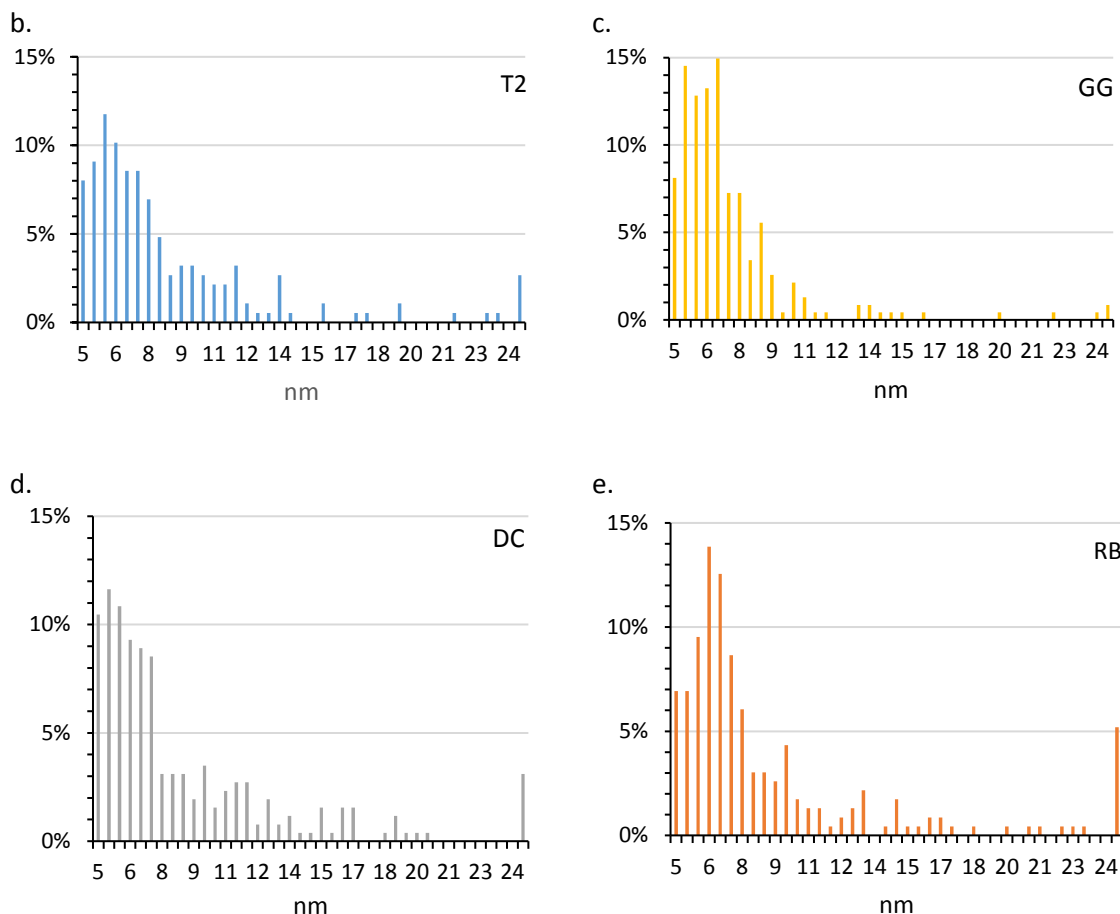


Figure 6.5 (continued)

6.3.3 Geochemical nanoparticle characterisation - TEM results

The complete list of microscopic TEM images and EDS elemental compositions are reported in Appendix 6.e. Particle morphological observations and mineralogical phases are summarized in Table 6.4.

The images acquired for sample T2 show a low variety of particles (Table 6.4 a). Generally, particle or agglomerate size varies from 50x145 nm to 500x1500 nm and shows low to medium electronic density. The most common phases are silicate minerals with high oxygen concentration (average Si:O=0.21 with SD pf 0.06) represented by elongated angular or sub-angular particles that are often agglomerated. A silica particle (image T2.4) with a sub-rounded shape and heterogeneous density, contains Fe (1.1 wt. %) and Co (1.7 wt. %). Low amounts of Co (0.2 wt. %) were found in another sub-rounded particle (image T2.4), likely of illite mineralogy and high density. The presence of other mineral phases is suggested, including gypsum (Ca:S = 1.1) in image T2.8 and an Mg-bearing silicate (Si:Mg = 0.15) in image T2.9.

Sample GG shows particles of various sizes – 15 to 60 nm nanoparticles agglomerated into 70 to 900 nm clusters – and mineralogy (Table 6.4 b). The particles in images GG.1 and GG.3 have a spherical shape and a medium density; they are 15 to 40 nm in diameter and agglomerate into 100 nm clusters. With a Si:O ratio of c. 0.23 they are likely silicates. They contain other metals, such as Fe (1.8 wt. %) and Co (2.3 wt. %) in image GG.1 and Al (1.5 wt. %) in image GG.3. The particles in images GG.2 and GG.4 are sub-angular and irregular with a heterogeneous density. They seem to be formed by well-shaped angular 10 to 60 nm nanoparticles cemented by an amorphous phase. Their chemistry is complex and mainly represented by O, F and Zn (average of Zn:F = 0.9) plus other metals including Au (20.2 wt. %), As (1.5 wt. %), Ni (0.8 wt. %), Co (5.0 wt. %) and Fe (4.8 wt. %) in image GG.1 and Pb (17.4 wt. %), Fe (0.9 wt. %) and Au (9.5 wt. %) in image 4. The particle in image GG.5 has dimensions of 460x600 nm, has a well-shaped hexagonal shape elongated on one side, and is likely a clay mineral (Si:Al = 1.3). The agglomeration of a particle in image GG.6 is formed by 5x100 nm acicular particle of Ni oxide (Ni:O = 0.27) with traces of Si, Cl, and Fe. In image GG.7 two sub-rectangular particles sized about 300x700 and 700x800 nm of medium density are observed. They are formed by smaller particles of silicate composition containing Na, Mg, Al, K and Ca. In image GG.8 two medium dense and sub-rounded particles of 120x230 nm formed by Al oxide are observed (Al:O = 0.55). Sub-angular crystals of various sizes (40x110 – 460x640 nm) and heterogeneous density are captured in image GG.8. Their chemical composition is complex; a Zn-bearing Fe oxide composition is suggested for the particle and a phosphate – sulfate mineralogy for the surrounding phase.

TEM images from DC show small (4 nm) to large (700 nm) particles of various mineralogy (Table 6.4.c). Image DC.1 captures an elongated irregular particle (90x215 nm) of heterogeneous density embedded in an amorphous phase. EDS indicates a Cr- and Ni- bearing Fe oxide, plus silicate and sulfate compositions. Particles in images DC.2, DC.3, DC.4, and DC.9 are agglomerations (about 200x500 nm) of small nanoparticles (30-70 nm) whose chemistry suggests that they are likely a mixture of Fe- bearing Zn oxide, silica, gypsum, and organics. Image DC.5 shows a cluster of nanoparticles with a similar shape to those previously described but with a clay mineralogical composition. The particle in image DC.6 is well-shaped (700x1080 nm), crystalline and dense. Its composition is mainly silicate with 0.4 wt. % Al. The images DC.7 and DC.8 captured 90 nm dense nanoparticles that are clustered to form 300 nm agglomerates cemented by amorphous phases. The chemistry of these nanoparticles suggests that they are Fe and Zn oxides with cement comprising a mixture of silicate, phosphate, sulfate and organic phases. A trace amount of As (1 wt. %) is also indicated (DC.8).

Table 6.4 Description of particles from TEM image observations reporting morphology and potential mineralogy of T2 (a), GG (b), DC (c) and RB (d). The full list of images is reported in Appendix 6.e.

a. T2 (880 m)		Site downstream Frongoch Adit confluence		
N	Overall size	Particle size	Shape and electronic density	Potential mineralogy
	nm	nm		
1	-	500x1500	Elongated sub angular; low medium density.	Silicate mineral; high O conc.
2	-	360x540	Sub rounded well shaped; high density.	Silicate mineral (illite); high O conc.; plus Co.
3	-	50x145	Elongated sub angular; low medium density.	Silicate mineral; high O conc..
4	260x320	n.d.	Agglomeration of plates; low density,	Silicate mineral; high O conc.; plus Co and Fe.
5	420x1180	n.d.	Agglomeration of plates; low density.	Silicate mineral; high O conc..
6	-	100x120	Well defined angular particle; low density.	Silicate mineral; high O conc..
7	-	300x410	Irregular angular plates; low density.	Silicate mineral; high O conc..
8	-	60x150	Elongated particle; medium density	Silicate mineral; gypsum; high O conc..
9	-	175x100 225x150	Dense small rounded particles; plus low density plates.	Mg-bearing silicate; high O conc..

b. GG (1645 m)		Graiggoch Mine		
N	Overall size	Particle size	Shape and electronic density	Potential mineralogy
	nm	nm		
1	100-130	15	Spherical particles; medium density.	Silicate mineral; high O conc.; plus Fe and Co
2	200-300	≤60	Sub-angular high density particles embedded in an amorphous low density phase.	Main chemical composition: O, Zn and F; plus Fe, Co, Ni, As and Au.
3	70 x 90	30 - 40	Spherical particle; medium density.	Silicate mineral; high O conc.; plus Al.
4	200 x 300	10 - 30	Sub-angular particles embedded in an amorphous phase.	Main chemical composition: O, Zn and F; plus Pb, Au and Fe.
5	460x600	-	Hexagonal sub-angular particle; heterogeneous density.	Fe-clay; high O conc..
6	900	5x100	Agglomerate needles; high density.	Ni oxide; plus Fe, Si, Cl.
7	-	300x700; 700x800	Two sub-angular particles.	Silicate minerals.
8	-	120x230	Two sub-rounded particles; medium density.	Al oxide + organic
9	-	40x110; 460x640	Sub-rounded particle; plus sub- angular low density fragments	Zn- bearing Fe oxide particle; phosphate – sulfate fragments.

c. DC (3210 m)		Depositional area at middle river length		
N	Overall size	Particle size	Shape and electronic density	Potential mineralogy
	nm	nm		
1	-	215x95	Elongated irregular particles; heterogeneous density.	Cr and Ni Fe Oxide; silicate; plus S.
2	200x470	30	Agglomeration of small sub- squared particles; heterogeneous density.	Silicate minerals; Fe-bearing Zn oxide; gypsum; high O conc..
3	-	70	Sub-rounded high density particles surrounded by low density phase.	Silicate minerals; Zn-bearing Fe oxide; gypsum; high O conc..

Table 6.4 (continued)

N	Overall size	Particle size	Shape and electronic density	Potential mineralogy
	nm	nm		
4	c. 500	30	Agglomeration of small sub-squared particles; heterogeneous density.	Silicate minerals; Fe-bearing Zn oxide; gypsum; high O conc..
5	50	4	Agglomeration of small rounded particles; heterogeneous density.	Aluminosilicate mineral; high O conc..
6	-	700x1080	Well-shaped crystalline particle; high density.	Aluminosilicate mineral.
7	300	n.d.	Heterogeneous agglomeration of amorphous particles; heterogeneous density.	Fe and Zn oxides; cement comprising a mixture of silicate, phosphate, sulfate minerals; high O conc.
8	-	90	Spherical dense particle surrounded by an amorphous phase.	Fe and Zn oxides; cement comprising a mixture of silicate, phosphate, sulfate minerals; high O conc.
9	-	65x115	Sub-angular particle; medium density.	Silicate minerals; Zn-bearing Fe oxide; high O conc..

d. RB (5930 m)**Floodplain**

N	Overall size	Particle size	Shape and electronic density	Potential mineralogy
	nm	nm		
1	-	1000	Spherical dense particles; amorphous medium density phase.	(Fe,Ni) oxide; plus S and Cl..
2	-	430x1140	Irregular sub rectangular particle; heterogeneous density.	Ce oxide; plus Fe,Ni and Au.
3	370x500	80x410, 110x240	Aggregation of elongated irregular particles; heterogeneous density.	Au oxide; plus Zn.
4	190x150	20X25	Agglomeration of rounded sub-rectangular dense particles; low density phase among particles.	Au oxide; plus Fe.
5	560x640		Amorphous dense phase likely formed by smaller phases.	Au oxide; plus Ca, Fe, Zn As and Au.
6	1000x2000	700?	Elongated agglomeration of dense rounded sub-rectangular particles.	Silicate; sulfate; phosphate; Fe and Zn oxide.
7.a	-	140x260, 160x220	Amorphous sub-rounded phases of various size; high density.	Ce oxide; plus Fe, Cr, Ni and Mo.
7.b	-	300x660, 100x100	Amorphous sub rounded phases of various size; high density.	Ce oxide, plus Au.
8	-	20x20, 80x70, 230x190	Well defined crystalline particles; medium density.	Calcite; plus Si; high O conc..
9	-	100x10	Agglomeration of acicular particles surrounded by an amorphous phase likely formed by spherical particles.	Silicate minerals; high O conc..

TEM images from RB show a range of dense particles and agglomerates of different size and chemistry (Table 6.4.d). The particles in image RB.1 have a perfect circular shape (1000 nm) associated with an amorphous phase. EDS spectra suggest Fe and Ni oxide mineralogy plus sulfur, chloride, and organic phases. Particles in images RB.2 and RB.7 are dense and of irregular shape (from 100x100 nm to 430x1140 nm) with a Ce oxide composition. These contain other metals such as Fe (4.5 wt. %), Ni (1.8 wt. %), Au (1.9 wt. %) and Cr (8.2 wt. %). Image RB.3 captured an agglomeration (370x500 nm) of elongated irregular nanoparticles (e.g. 80x410 nm, 110x240 nm) of Zn-bearing Au oxide. Although image RB.4 has similar chemistry to RB.3 (Fe-bearing Au oxide), its morphology is a cluster (190x150 nm) of small nanoparticle (20x25 nm). Again, image RB.5 shows a 550x650 nm dense particle likely formed by smaller nanoparticles of Au oxide. These contain Fe (0.8 wt. %), Zn (1.3 wt. %) and As (1.4 wt. %). Image RB.6 captures an elongated agglomeration (1x2 μm) of dense particles. Its chemistry is complex and is likely formed by silicate, sulfate, phosphate, and Fe – Zn oxide. Image RB.8 shows crystalline nanoparticles (20x20 nm, 80x70 nm, and 190x230 nm) of calcite and organic phases (Ca:O = 0.18). An agglomeration of acicular nanoparticles (100x10 nm) cemented in an amorphous phase likely formed by spherical particles is found in image RB.9. Its chemistry is represented by silicate and organic phases.

6.3.4 River water metal partitioning

Water metal concentrations, loads and size range percentages are reported in Figure 6.6, and the complete dataset can be found in Appendix 6.f. The reported metals are Zn, Pb, Fe, Al, Mn, Cd and Co. The metals transported in the river water are apportioned to suspended sediment (>450 nm), nanoparticle (2.5-450 nm) or truly dissolved (<2.5 nm). As mentioned above, unfiltered Co and Cd concentrations were not measured due to the low sensitivity of the ICP-OES. Therefore, for those metals only nanoparticle (2-450 nm) or truly dissolved (<2.5 nm) fractions are presented.

Generally, total Zn concentrations vary along the river with the highest concentration (1620 $\mu\text{g/l}$) downstream of Frongoch Adit (T2) and the lowest (110 $\mu\text{g/l}$) upstream of the mine site (T0) (Figure 6.6.a). Zinc loads increase downstream with the major contribution due to Frongoch Adit (Figure 6.6.h). Zinc is mainly contained in the truly dissolved phase with the minimum (min) value of 48% at T0 and maximum (max) of 88% at RB (Table 6.5). The nanoparticle range shows variability of 0-19% Zn, with 17% at T2 and 19% at DC and a null value at RB (Table 6.5). Suspended sediments contribute to the 17 to 40% to the total Zn concentration.

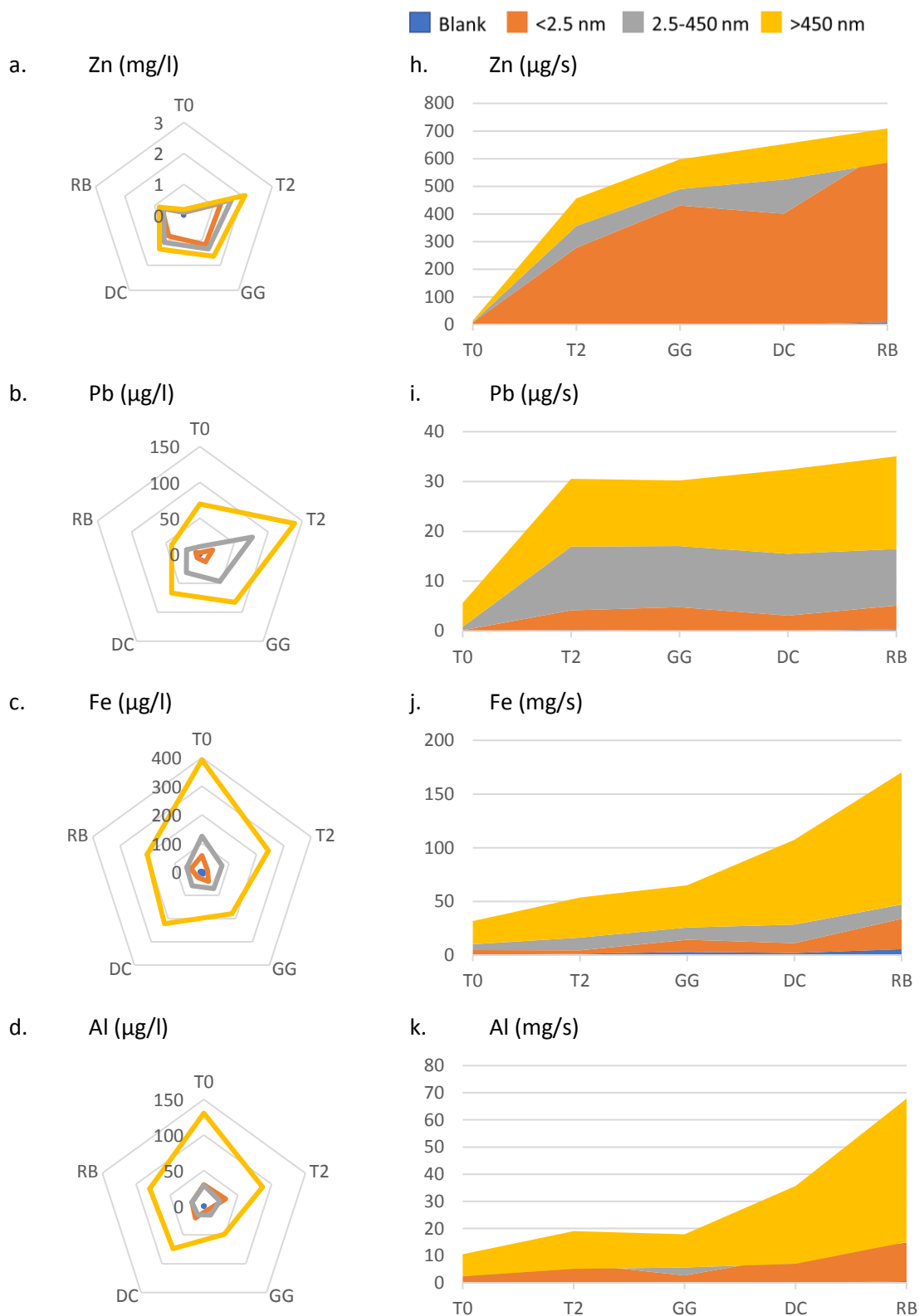


Figure 6.6. Zinc, Pb, Fe, Al, Mn, Cd and Co concentration (on the left) and load (on the right) partitioned as truly dissolved (filtered at 2.5 nm), nanoparticle (2.5-450 nm) and suspended particles (>450 nm).

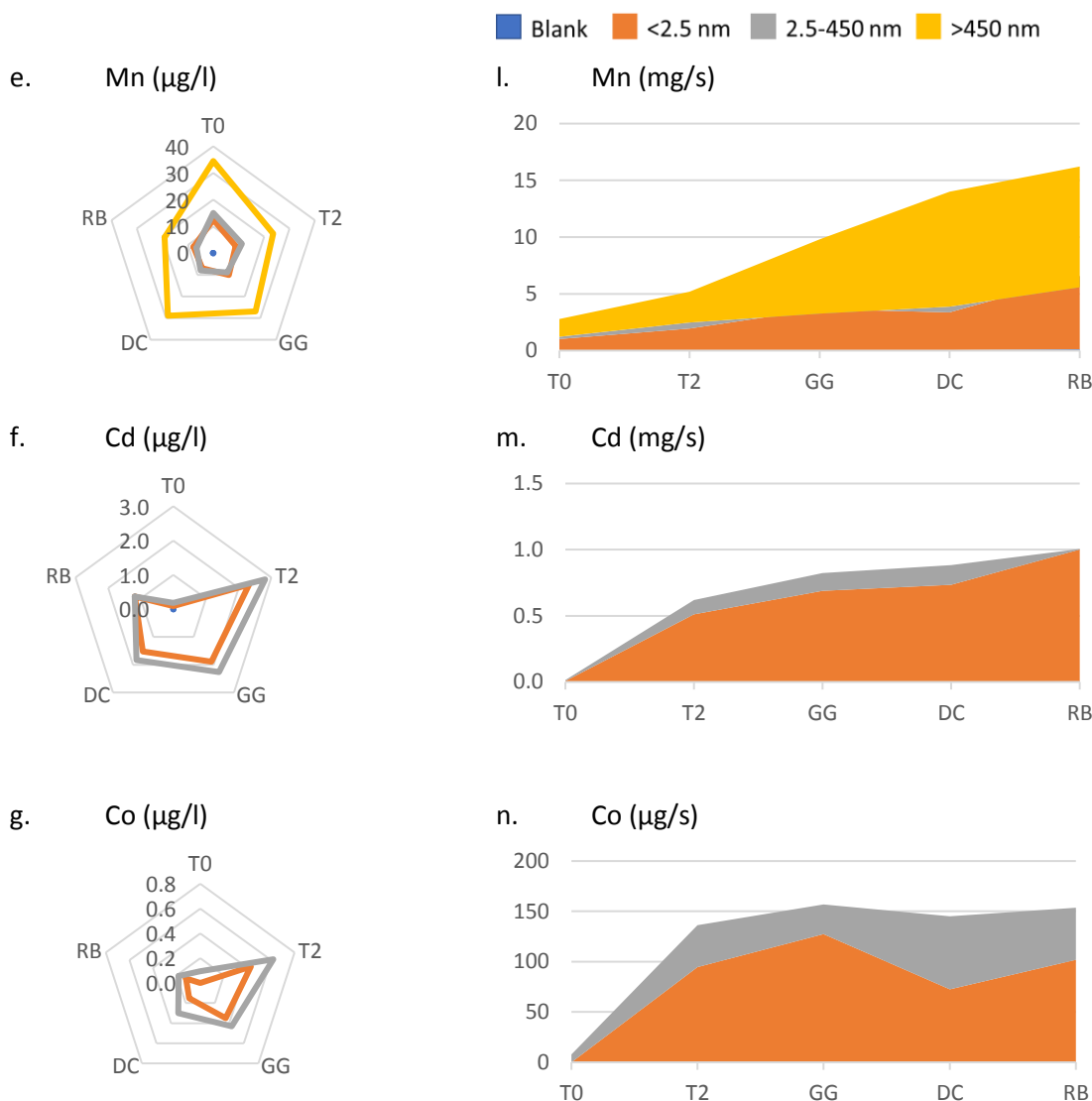


Figure 6.6. (Continued)

The concentrations of total Pb reach a peak at T2 (139 $\mu\text{g/l}$) and decrease downstream until the lowest value is recorded for sample RB (41 $\mu\text{g/l}$) (Figure 6.6.b). Truly dissolved concentrations represent only 3-16 % of the total Pb. Nanoparticle transported Pb is around 32-42%, with the exception of T0 whom nanoparticle contribution is 12%. Most of the Pb is transported in the suspended phase (85%) (Table 6.5). From T2 until RB, Pb moves with suspended particles with an increase in the suspended portion, respectively from 44 to 52%, at the detriment of nanoparticle Pb (Figure 6.6.i). The Pb load increases downstream (Figure 6.6.j).

Total Fe concentrations vary along the river with the maximum concentration recorded at T0 (392 $\mu\text{g/l}$) and the lowest at GG 179 $\mu\text{g/l}$). Iron is mostly transported as suspended particles 61-74%, with

only 8-22% transported as nanoparticles and 6-18% carried in the truly dissolved phase (Table 6.4). From GG to DC the suspended Fe particle contribution increased from 61 to 74%, concomitant with a decrease in the dissolved Fe contribution from 18 to 9 %.

The maximum total Al concentration was measured at T0 (131 µg/l) and the Al load increased from up- to downstream, together with a small decrease from T2 (19074 µg/s) to GG (17836 µg/s) for the total load (Figure 6.6.d, k). Along all the river 68-80% of Al is associated with suspended sediment and, only at GG, a significant portion of Al is transported as nanoparticles (17%) (Table 6.4).

The results suggest that Mn behaves in a similar manner to Fe (Figure 6.6.d, k), as do Cd to Zn (Figure 6.6 f, m). The highest concentration of Co in the 450 nm filtered samples is registered at T2 (0.62 µg/l) and the lowest at T0 (0.10 µg/l, Figure 6.6.g). Values at T0 are too low to attribute percentage concentration to the size range. Nineteen to 50% of the Co is attributed to the nanoparticle size range, with the maximum nanoparticle contribution observed at DC (50%) (Table 6.5). After T2 the Co load increases downstream, but like loads of the other metals, remains steady downstream until RB (Figure 6.6.n).

Finally, dissolved organic carbon decreases from 6.5 mg/l to 5.68 mg/l along the river, with the only outlier value of 4.1 mg/l recorded at GG (Appendix 6.g).

Table 6.5. Partitioned loads of truly dissolved (filtered at 2.5 nm), nanoparticle (2.5-450 nm) and suspended particles (>450 nm).

Range	%	T0	T2	GG	DC	RB	Range	%	T0	T2	GG	DC	RB
Zn	blank	1%	0%	0%	0%	1%	Fe	blank	1%	2%	5%	2%	3%
	<2.5	48%	61%	72%	61%	88%		<2.5	14%	6%	18%	9%	17%
	2.5-450	11%	17%	10%	19%	-7%		2.5-450	17%	22%	17%	16%	8%
	>450	40%	22%	18%	20%	17%		>450	68%	70%	61%	74%	72%
Pb	blank	0%	1%	0%	0%	1%	Al	blank	0%	1%	1%	0%	1%
	<2.5	3%	13%	16%	9%	14%		<2.5	23%	36%	14%	28%	21%
	2.5-450	12%	42%	41%	38%	32%		2.5-450	-1%	-10%	17%	-8%	0%
	>450	85%	44%	44%	52%	53%		>450	78%	73%	68%	80%	78%
Mn	blank	0%	1%	1%	0%	1%	Co	blank	0%	0%	0%	0%	0%
	<2.5	36%	37%	37%	24%	40%		<2.5	0%	69%	81%	50%	66%
	2.5-450	7%	10%	-4%	3%	-6%		100					
	>450	56%	52%	67%	72%	66%		2.5-450	%	31%	19%	50%	34%
Cd	blank	2%	0%	0%	0%	1%							
	<2.5	47%	82%	83%	83%	99%							
	2.5-450	51%	17%	17%	17%	0%							

6.4 Discussion

6.4.1 Optimal methods for fluvial sampling of nanoparticles

The designed method for sampling the nanoparticles and dissolved phases, together with the cleaning protocol ensured limited contamination and did not compromise sample quality. Despite the issue that may occur during sampling (Pokrovsky and Schott, 2002), the use of this designed prewashed filtration unit per site is suggested to reduce contamination issues. Indeed, the DLS results of the blank samples showed no or low signal intensity, meaning low or null particle concentrations could contaminate the samples. Furthermore, the filtration process removed most of the particulates, limiting metal surface sorption and aggregation processes. Only a few larger-sized particles (> 450 nm) were observed due to aggregation, irregular shapes, or less likely filtration failure.

Results from the trial experiment highlighted the difficulty of analysing natural nanoparticles in environmental water samples. To get representative nanoparticles and good quality data, the sample storage time limit was set to 48 hours. The decision was a consequence of (i) the observed Z-average stability among the 4, 24 and 48 hours sampling and (ii) the strong similarity between the 4 and 48 hour curves of particle size distribution versus intensity (Appendix 6.a). A longer time window would have compromised the data quality by enhancing artefacts (Lapworth et al., 2013), and a shorter time would have limited the sampling process. In addition, it is important to acknowledge the occurrence of degradation processes during the 48 hours of storage. The standard deviation of the Z-average increased from 17 nm at 4 hours to 31 nm at 48 hours, suggesting a variation in the nanoparticle distribution. In fact, in the curve on the size distribution versus intensity plot (Appendix 6.a) a shift towards right (representing larger sizes) was observed, and the intensity of the 4 hour tail around 10 – 30 nm decreased. Therefore, as observed in other studies (Johnson et al., 2014), nanoparticle aggregation or bacterial activity are probably the most common degradation processes which can affect nanoparticle characterisation.

Unfortunately, Zeta-potential measurements were affected by the heterogeneity of the samples and the low nanoparticle concentrations. As a consequence, the Zeta-potential analysis produced inconsistent results and low quality phase data (nanoComposix, 2012). The attempt to increase sample concentration was executed during the second week of the main experiment by centrifugation. DLS PSD of the centrifugated and uncentrifuged samples indicated variations in the lower size ranges (Appendix 6.c). Therefore, Zeta-potential analysis for the main experiment was suspended due to observed degeneration of the samples.

Altogether, the trial experiment allowed testing nanoparticle stability, the filtration system and the washing protocol. The developed methods for fluvial sampling of nanoparticles resulted in efficient and easy execution and are therefore proposed for future studies.

6.4.2 Nanoparticle size distribution variations along the river

Curves of size distribution by intensity, derived by the DLS analysis, described polydispersed samples (Figure 6.3). DLS investigations of PSD curves can generate artefacts due to the low performance with polydispersed particles (Baalousha and Lead, 2012). In this study, PSD interpretation was performed by combining SOP output, PSD tails, and secondary peaks. In this study *SOP cumulative parameters* were not considered representative of the samples, they do not highlight variation among sites or the sample polydispersity. Therefore, only the *SOP cumulant parameters* and the curves of size distribution by intensity were used for the semi-quantitative PSD interpretation. The size of the main peak (peak 1) identified by the SOP was preferred to the manually identified peak which is representative of the mode and not of the average peak. The second most intense peak, both in the SOP and manual investigation, was generally around 4-5 μm . This peak could have been a result of sample aggregation, the presence of bacteria or an instrument artefact. Considering its absence in data obtained using the other methods, this peak is not considered representative of the nanoparticle PSD.

PSD curves for each site were used to identify nanoparticle size, transport, and stability along the river (Figure 6.4). Upstream of the mine site (sample T0) can be considered as the starting nanoparticle distribution point to which sourced particles are added along the river. Firstly, downstream of Frongoch Adit (sample T2), particles are added in the low size range at around 40 to 200 nm. Secondly, alongside Graiggoch Mine (sample GG), the PSD shape shows a significant change with new particles appearing (12-80 nm), others decreasing in amount (80-300 nm decrease intensity) or disappearing (0.6-1.3 nm). Decreases in intensity may indicate nanoparticle instability (aggregation or dissolution) potentially due to the lower EC and higher pH encountered in the Nant Cwmnewyddion compared to the Frongoch Adit (Hotze et al., 2010). Further downstream at the middle reach (sample DC), the similarity of the main PSD pattern to that of the T0 PSD may be due to a similar nanoparticle source (such as soil horizons)(Pokrovsky and Schott, 2002). Finally, in the floodplain (sample RB), some nanoparticles are lost, maybe due to diluted water chemistry, light exposure or particle aggregation and deposition (Sharma et al., 2015); others are still present matching the GG peak at 55 nm and supporting the theory of nanoparticle stability at the catchment scales (Wigginton et al., 2007).

Comparison among the DLS, TEM and AFM results can corroborate or question PSD interpretations (Baalousha and Lead, 2012). The nanoparticle size ranges covered by the DLS are the same as those covered by the TEM (Plathe et al., 2010). The TEM size distribution agrees with the PSD obtained with the DLS, also showing that the particles may have aggregated, which can justify DLS signal recorded at ≥ 450 nm. Nevertheless, nanoparticles ranging in size from 5 to about 25 nm were better identified with AFM, likely because those nanoparticles have a stronger affinity with the mica substrate than with larger-sized particles (Lead et al., 2005). Thus, AFM images were able to identify amorphous films (Appendix 6.d) suggesting the presence of amorphous organic phase(s) (Baalousha and Lead, 2013). Furthermore, variations in the AFM polydispersed index can indicate inputs of pore water and hyporheic water to the river water (Lapworth et al., 2013). Therefore, the GG AFM results differ from those from the other sites. GG AFM results show higher polydispersed index, higher percentages of c. 5,5-9 nm and fewer amorphous phases among well-defined particles (Figure 6.5 and Appendix 6.d). These results suggest GG as a potential source of particles which differ from the other sites for their size distribution (DLS results).

This discussion highlights the necessity to characterise nanoparticle sizes and their PSD using different methods to overcome artefacts. Different size ranges, chemistry or morphologies can be either underestimated or overestimated by the use of a single instrument. In fact, small nanoparticles can be overestimated by AFM analysis due to the adsorption time and the bonding ability of the mica substrate (Lapworth et al., 2013). Within addition, height does not always represent the nanoparticle size; irregular shapes and layered mineral (such as silicate and aluminosilicate minerals observed with the TEM) have a dominant dimension which is more likely to lie on the mica substrate. Due to the distortion linked to the topographic measurement, this dimension, or width, can not be measured (Baalousha and Lead, 2007). On the other hand, DLS limitations are due to low nanoparticle concentrations and to the assumption that the nanoparticles are spherical. In most cases, natural nanoparticles are heterogeneous in size and shape (e.g., Appendix 6.e) with polydispersed PSD, contrary to the monodispersed optimal condition required by DLS (Baalousha and Lead, 2012). Compared to AFM measurements, which are conducted for dry particles, the DLS method accounts for a water layer around the particles. As a result, larger sizes can be over-counted. Overall, PSD variation along the river was characterised using the three instruments (DLS, AFM, TEM). The TEM and DLS results were in accordance and the AFM data were used to better describe smaller particles or organic films. As pointed out from other studies (Wigginton et al., 2007, Plathe et al., 2010, Lead and Wilkinson, 2006), these instruments give complementary data and allowed a representative PSD interpretation.

6.4.3 Metal-bearing nanoparticle, sources, and transport along the river

Metals can be transported long distances by nanoparticles (Hochella et al., 2008, Hotze et al., 2010), but identification of nanoparticle surface chemistry and metal presence is often restricted by instruments analysis. In this study TEM data highlight the chemistry of the nanoparticle surfaces, whereas limitations due to the time required for analysing each sample and nanoparticle dispersion on the TEM substrate made it impossible to develop a complete understanding of a potential metal transport driven by nanoparticles. Therefore, the investigation of the river water chemical composition was fundamental to link nanoparticles to their sources and fate, and their potential role in metal transport.

In the circum-neutral rivers of the Nant Cwmnewyddion and the Nant Magwr, Zn was mostly transported as a truly dissolved element (48-88%) and the amount of Zn-bearing nanoparticle varied along the river. When comparing current results to previous studies, it appears that in circumneutral water Zn is mainly found as a dissolved phase (Kimball et al., 1995, Pham and Garnier, 1998). Pham and Garnier (1998) partitioned the seasonal (winter and summer) metal load of the Vienne River, a River Loire tributary (France), and found dissolved Zn (<10kDs) to be 70-80 % of the Zn concentration filtered at 450 nm. In the mining impacted Upper Arkansas River (Colorado, USA), Kimball et al. (1995) found that Zn partitioning was influenced by the presence of Fe- nanoparticles and streamflow variations. In this study, seasonal variation in Zn partitioning among dissolved and nanoparticle were not investigated. However, spatial variations of Zn partitioning were observed along the river likely due to the Zn-nanoparticle bond and the Zn-bearing nanoparticle instability. The increase of Zn load from T0 to T2 is likely due to the Frongoch Adit, recognised as a source of Zn in Chapter 5 (Table 5.2). At GG the amount of Zn-bearing nanoparticle decreased to 10% and dissolved Zn load increased by 11%, suggesting instability of the upstream nanoparticles mainly by dissolution processes or desorption from other particles. Similarly, the abundance of zinc-bearing nanoparticles occurring at site DC (19%) decreased downstream at site RB, also likely due to dissolution and desorption processes (Table 6.5). These observations contrast with the information in the TEM images of sample T2 but in is agreement with DC images. Firstly, the lack of Zn in T2 EDS spectra may be due to the random acquisition of chemical data for 9 spots or may indicate weak Zn adsorption to the nanoparticles. Secondly, Zn-bearing nanoparticles found at DC seem to be formed at the expense of dissolved Zn by adsorption onto Fe-oxides (Table 6.4). Finally, the mineralogical heterogeneity and the difference among sites that emerged with TEM and EDS analysis may indicate weak Zn-nanoparticle bonds and their instability during transport.

The transport of Pb appears to be mostly associated with stable particles, both nanoparticles, and particulate, with only 3-16 % in the truly dissolved fraction (Table 6.5). Being sampled at moderate streamflow condition, these particles are potentially sourced from Frongoch Adit, and partially from the Wemyss Mine area (Chapter 5, Table 5.2). Along the river, the Pb-bearing nanoparticle load indicates a slight decrease, with the Pb-bearing nanoparticle load partitioning into suspended particles at DC and into truly dissolved phase at RB (Figure 6.5.i). Possible reasons for this decrease are firstly an aggregation of upstream nanoparticle into suspended particles, together with an input of Pb-bearing suspended sediment corroborated by the total load increase; secondly a release of Pb into the dissolved fraction. This highlights the capacity of these nanoparticles to transport Pb for kilometers and gradually release Pb in a truly dissolved form or aggregate in suspended particles which can still move downstream or precipitate storing Pb in deposit along the river. Evidence of Pb-bearing nanoparticles in sediment was found in the mining-impacted river system (Duarte et al, 2018, Plathe et al, 2010).

Conversely, an important discrepancy between Pb water load and TEM and EDS investigations emerged; indeed, only one Pb-bearing nanoparticle was found (GG.4 in Appendix 6.e). This may be due to the random and limited acquisition of TEM and EDS data, and to a Pb-organic matter association occurring as a film around nanoparticles. Although this second hypothesis may be speculative, a few pieces of evidence were found. Organic films, observed in the AFM images (as those acquired for T2 and DC in Appendix 6.d), are known to occur around nanoparticles and to influence their reactions with trace metals and to influence metal transport (Aiken et al., 2011). Following this hypothesis, the high O concentration in TEM spectra and the 1 nm peak observed at T2 by DLS PSD (Figure 6.4) can be interpreted as organic matter (generally sized 1-5 nm sized) (Baalousha and Lead, 2007), which agglomerates in film and fibrils around 10-30 nm particles (observed also by Lead et al., 2005). Evidence of Pb-organic matter association is also presented in Pokrovsky et al. (2010). These authors found a positive correlation between Pb-nanoparticle fraction (1 kDa-200 nm) and the organic carbon. However, this speculation requires further characterisation of the organic matter and Pb bonding.

Nanoparticles are found associated with trace metals and their role in metal dispersion appears clear by the results presented here. Along with Zn and Pb also Fe, Co, Al, Ce, Au, Ni, Mo, As and Cr can be transported by nanoparticles (Waychunas et al., 2005). These results agree with other studies in impacted river systems. Duarte et al. (2018) found sediment Fe-oxide nanoparticles (<100 nm) in association with As, Co, Zn, Pb, and Ni. According to their experiments, these nanoparticles can be easily dispersed in the water. In this study, Fe-bearing nanoparticle, silicate, and oxide

minerals contribute to about 20% of the total Fe load (TEM image in Appendix 6.e). In Pham and Garner (1998) study, Fe-bearing nanoparticles accounted for 40-80% of the total Fe filtered at 450 nm. Adopting the same percentage calculation (percentage of the dissolved Fe compared to the Fe filtered at 450 nm), Fe-bearing nanoparticle would count for the 27-72% agreeing with their results. Cobalt nanoparticle loads can account for the same amount of the dissolved fraction (Figure 6.5); nanoparticles can either up-take or release Co from the dissolved fraction (as observed at DC), or be mobilised from riverbank sediment where high-density mineral-bearing Co have been recorder in Plathe et al. (2013). Contrary to the last work, in the studied river, Co is also significantly associated to silicate and complex phases of F and Zn oxides. Other nanoparticles likely remobilised from the sediment are Al-bearing nanoparticles which are mostly silicate and Al-oxide minerals (GG.8 in Appendix 6.e) (Buffle et al., 1998, Schindler and Hochella, 2016).

Metal-bearing nanoparticles were present throughout the river system, contributing to metal transport at the catchment scale. The water quality data expressed in load for each fraction suggests likely sources and instability processes (such as metal release and agglomeration). Furthermore, the limitation in describing nanoparticle-metal interactions based solely on TEM and EDS data is suggested because the metal load data did not correspond with the TEM data. Plathe et al. (2010) noticed a preferential selection of silicate and clay nanoparticles during microscopic sample preparation. Hence, metal-bearing nanoparticles can be prepared by density selection (Plathe et al., 2013). A similar approach would have provided more information on high density nano-minerals, but likely mask the metal contribution of lighter and heterogeneous nano-phases. Therefore, the use of load quantification, easy to implement in the field and laboratory, is proposed as an efficient way to couple nanoparticle surface and metal distribution characterisation.

6.4 Conclusions

The major conclusions from this chapter are:

- The designed filtration system for sampling nanoparticles reduces contamination issues and aggregation processes, and it is easy to execute in field conditions.
- The use of a multi-method approach emerged as fundamental to describe and justify PSD variations among sites and cover the full range of nanoparticle size.
- PSD curves obtained with DLS analysis identified nanoparticle sources along the river (Frongoch Adit and Graiggoch Mine) and can be used to predict nanoparticle stability at the catchment scale.
- TEM results corroborate the size range observed with DLS and justified DLS signal major of 450 nm with aggregate particles.
- AFM analysis highlighted the presence of organic films, together with small nanoparticles (5-25 nm), and indicate Graiggoch Mine as a zone of mixing water and potential nanoparticle source.
- Partitioning of metal load in suspended, nanoparticle and dissolved fractions highlighted the capacity of nanoparticle to transport metals and indicated potential areas where metal-bearing nanoparticle formed.
- Metal load information and TEM-EDS data suggested that Zn-bearing nanoparticles were unstable and that Zn was mainly present as a dissolved phase.
- Metal load partitioning clearly indicate Pb load carried by the nanoparticle fraction through the whole river.

Chapter 7. General Discussion and Conclusions

7.1 Key findings and hypothesised processes

The Nant Cwmnewyddion and the Nant Magwr are typical mining-impacted rivers with high metal concentrations recorded in their river water and sediment (Nordstrom, 2011b). Active geomorphological processes have distributed metal-enriched sediment along the rivers seeking a morphological equilibrium disrupted by the mining activities of Wemyss, Graiggoch and Frongoch Mines (Lewin and Macklin, 1987). Areas of metal-enriched sediment deposition were bedrock alcoves and the floodplain, emulating those described by Foulds et al. (2014) and Dennis et al. (2009). Metal dispersion in the river water showed spatial and temporal variations due to source locations and their potential contribution across streamflows. Similar metal dispersion patterns were observed in other mining-impacted catchments (Gozzard et al., 2011, Jarvis et al., 2019). A close look at the waterborne metals reveals the partitioning of metal in suspended particles (>450 nm), nanoparticles (2.5-450 nm) and truly dissolved metals (<2.5 nm). Similar evidence of metal partitioning has been reported in other rivers, either mining-impacted (Kimball et al., 1995) or not (Pham and Garnier, 1998).

In this context, the multi-disciplinary study presented here directly contributes to the understanding of metal drivers at the nano- and catchment-scale in mining-impacted rivers.

Results from Chapter 4 demonstrated that river catchment geomorphology can influence sediment geochemical processes (such as redox and dissolution) and highlights areas of metal source transformation. Previous studies evaluating the catchment metal distribution have only focused on either the geomorphological or geochemical description. In this novel study, both aspects were investigated, allowing the proposal of potential geochemical processes for different geomorphological settings.

Evidence provided in Chapter 5 stressed the necessity to apportion metal sources across streamflow conditions at a highly resolved spatial scale. For the first time, a multi-tracer approach was applied, allowing point and diffuse metal sources under a variable hydrological regime to be accounted for. This approach proved to be powerful because both linear and temporal metal variations could be estimated. Furthermore, results contributed to the understanding of Zn and Pb hydro-geochemistry. The obtained dataset of river water metal load suggested that Zn load has a strong positive correlation with streamflow, whereas Pb dispersion is controlled by river catchment geomorphology and sediment geochemistry unlike Pb which dispersion is potentially controlled also by river catchment geomorphology and sediment geochemistry, as well as streamflow.

The research presented in Chapter 6 moved another step to understanding the role of nanoparticles in metal transport in mining-impacted rivers. Metal loads were found in suspended particles, nanoparticle and dissolved fraction with different spatial partitioning along the river. This metal partitioning study coupled with the particle size distribution, morphological and chemical characterisations, highlighted potential sources and stability of metal-bearing nanoparticles. This identified the potential role of nanoparticles in metal transport, building on the existing literature. Furthermore, the method developed in this study for sampling and filtering river water proved highly beneficial for preservation of nanoparticle characteristics, and it is hoped it will be adopted for future studies.

7.1.1 Point and diffuse source mechanisms and apportionment along the river

Despite increases in our knowledge of diffuse source mechanisms, understanding of detailed apportionment is still limited. Furthermore, Jarvis et al. (2019) stressed the necessity to adopt a reach-scale investigation to account for shallow subsurface and surface runoff. Gozzard et al. (2011) captured point sources in the River West Allen that accounted for 67% under low flow, with observed diffuse sources identified as spoil seepages and groundwater input. However, the methodology for estimating metal load employed by Gozzard et al. (2011) did not allow a detailed sample grid and diffuse source apportionment. Therefore, as reported also by other authors (De Giudici et al., 2014, Kimball, 2002, Runkel et al., 2013), a better understanding of diffuse source mechanisms and accurate apportionment can be gained by employing the continuous tracer injection method. In this study, continuous tracer injection allowed accurate apportionment of metal sources in the Nant Cwmnewyddion. The Frongoch Adit (862 m) represented a point source of Zn and Pb accounting for about 52% and 60% respectively, meaning that diffuse sources contribute almost half of the metal load at moderate flow. Mine waste tips (loose sand and gravel material at Wemyss Mine, 52-171 m) and a potential hyporheic zone (Graiggoch mine, 1148-1961) represented diffuse Zn sources (respectively Source#3 and Source#2). Similar to this study, the Lion Creek (Colorado) Zn sources were apportioned by a continuous tracer injection (Byrne et al 2017). The authors quantified Zn point sources from an inflow flowing through a denuded area (30%) and the Empire Creek (23%), and the main diffuse source were represented by small seepages and subsurface water, potentially linked to mine shafts (11%).

Diffuse sources such as hyporheic and groundwater are difficult to localise (Mayes et al., 2008) as they are often not visible, or difficult to sample. In the studied river, at Graiggoch Mine (1148-1961 m) the tracer injection captured an increase of streamflow not accounted for by other observed inflows. The sediments in this area are characterised by glacial and fluvial channel bed with sand and gravel lens,

which, together with the presence of Pb-bearing Mn oxide, suggest the presence of a hyporheic zone. Fuller and Harvey (2000) studied the Pinal Creek, a river with similar characteristics (sand and gravel channel, 1% slope, and the presence of mining groundwater), finding a shallow hyporheic zone where Mn oxides affected metal transport by Zn, Co, and Ni uptake. Remaining research gaps concerning hyporheic zone are centred on the quantification of its contribution to overall metal load (Environment Agency, 2006). The source apportionment work in this thesis allowed accurate load quantification (+21% Zn and -1% Pb) at the Graiggoch Mine river segment. Therefore, the continuous tracer injection is proposed as a method to quantify contribution of hyporheic sources.

The temporary storage of metals can be identified by a linear load attenuation (De Giudici et al., 2014). Under moderate flow, attenuation of Pb load in proximity of Wemyss and Graiggoch Mines were found through detailed grid-based sampling. For example, nearby Wemyss Mine, the -3% attenuation on Pb load occurred between 52 and 171 m, identified by 5 sample sites. In addition, attenuation in Zn load was accounted for -2.2% and confined to areas with dense vegetation. Under low flow conditions, the attenuation process of Zn was observed by Gozzard et al. (2011) and Jarvis et al. (2019) finding 41% attenuation of Zn load due to the adsorption on river sediment and benthic algae. The continuous tracer injection allowed identification of attenuation processes that eventually contribute to the metal load under higher flow conditions (Runkel et al., 2016).

7.1.2 Point and diffuse source mechanisms and apportionment across streamflows

Metal sources and their contributions can vary across streamflow conditions due to sediment mobilisation, hydrological connectivity and formation-dissolution of secondary minerals (Nordstrom, 2011). During high streamflow conditions, rising water levels and their infiltration in permeable mine waste and metal-bearing sediment can enhance metal release (Generaux and Hopper, 1998). Furthermore, diffuse and runoff movement of water can take in suspension particles, increasing the total amount of metal loads (Kimball et al., 1995). Byrne et al. (2017) employed continuous tracer injection under low flow to investigate the Lion Creek (Colorado) mining-impact after suspecting variability in source contribution across different streamflow conditions. In particular, among the other sources, they identified a river segment of about 30 m where tailings lay on top of the river bank, and identified them as potential sources of metal under higher flow. A similar situation has been observed at Wemyss mine (52-171 m). This segment, accounting about 20% Pb contribution during moderate flow, became a major source of Pb under high flow conditions, accounting 80% of the cumulative load. In addition, physical erosion of the Wemyss Mine tips was witnessed during the field site visits. Conversely, the dispersion of suspended particles (calculated as the difference between filtered and unfiltered) was higher during low flow conditions (28/08/2017, LF) compared to high flow

conditions (17/06/2016, HF). This may suggest processes of Pb de-adsorption from the suspended particles occur, or that the particles are deposited during high flow conditions.

Different patterns of Zn mobilisations were observed across streamflows. Jarvis et al. (2019) found Zn load was correlated to streamflow, linking the increase of load to the presence of easily extractable Zn in the sediment and a decrease in pH. They found an increase from about 3 kg/day at low flow (100 l/s) to 14 kg/day for high flow conditions (670 l/s). A similar pattern is found in this study, at the Nant Cwmnewyddion and the Nant Magwr, where Zn is positively correlated with streamflow, and the load increased from 16 kg/day at low flow conditions (157 l/s) to 129 kg/day at high flow conditions (1496 l/s). Such variation in river load can be explained by the mobilisation of Zn-enriched sediment and de-adsorption processes. As evidence, Zn attenuation load was apportioned to 49% during low flow, similar to Jarvis et al (2019) which found 41% attenuation of Zn load.

In agreement with previous studies, results in this thesis highlight the variability of Zn and Pb load across streamflows as a result of multiple integrated mechanisms. In this research, source apportionment variations were quantified by the use of a multi-tracer method. Therefore, the coupling of continuous tracer injection with slug injections is strongly recommended to correlate detailed spatial apportionment with metal load variation due to streamflows.

7.1.3 The role of nanoparticles in metal transport in river systems

Conveyance of Zn and Pb load by nanoparticles has been found in other mining-impacted catchments (Kimball et al., 1995). Results from the presented research show that Zn and Pb can be transported in nanoparticle phases far downstream from their sources. These nanoparticles, and their associated metals (Zn, Pb, and also Cd, Cr, Ni, Co, and As), can influence nano-scale water-soil-biota interactions, displaying different chemistry and reactivity to those of dissolved phases (Handy et al., 2008). Therefore, the assumption that metals filtered at 450 (or 200) nm are dissolved, as often adopted in water quality monitoring, is erroneous and overlooks the importance of nanoparticles in metal transport (Baun et al., 2008, Wigginton et al., 2007). The acquisition of metal partitioning approach results beneficial for better predict metal bioavailability and calculate mineral saturation indexes.

Nanoparticles represent a transient phase in the environment that can aggregate, dissolve or adsorb other metals (Sharma et al., 2015). For example, observed Fe-oxide nanoparticles carry metals such as Zn, Pb, Co, Ni, and Cr. In another mining-impacted river near Tauro Mine (Spain), Fe- and Ti-oxides, such as hematite, magnetite, and rutile, were found as nanominerals (Civeira et al., 2016a). These nanominerals can travel longer distances than dissolved particles and can be easily reduced by bacteria releasing metals at a higher rate than bulk minerals (Baalousha and Lead, 2007, Bosch et al.,

2010). Furthermore, iron nanoparticles can adsorb ox-anions such as phosphate, arsenate, and chromate (Civeira et al., 2016b, Waychunas et al., 2005). This behaviour can be suggested for the nanoparticles observed in associations with phosphate and sulfate, particularly abundant at the middle river length site of this study (DC, 3210 m).

The nucleation, growth, and aggregation of nanoparticles depend on factors such as pH, salt presence (NaNO_3 , NaCl and NaSO_4). In sulfate systems, iron hydroxide nanoparticles have fast growth and aggregation rates (Hu et al., 2012). Along the Nant Cwmnewyddion, which has Ca-Sulfate water, sulfate concentrations change linearly, likely affecting the aggregation state of the nanoparticles.

The aggregation of nanoparticles affects their depositions and transport capability. For example, aggregation of nanoparticles with suspended particles (e.g. clay) or low density particles can enhance transport in porous phases (Johnson et al., 2009). Furthermore, agglomerate deposition can occur due to gravity forces taking over Brownian diffusion processes (O'Melia, 1980). Both homo-aggregates, of same particles, and hetero-aggregates, of various particles, were found in the studied river. TEM images show single particles or aggregates of aluminosilicate upstream (T2, 880), a high variety of hetero-aggregates at two sites along the river length (GG, 1645m and DC, 3210 m), and single-particle or homo-aggregate in the floodplain (RB, 5930 m). Hetero-aggregates were complex phases with high concentration of F and Zn or aluminosilicates with Zn or Fe oxides. The characterisation of aggregates is important for better predictions of the metal-nanoparticle fate. For example, clay minerals were observed to be abundant, and can easily aggregate to nanoparticles, influencing their transport and fate (Hotze et al., 2010). In addition, aggregation can alter biological effects, controlling the particle distribution size and the metal dispersion (Buffle et al., 2007). Particle size distribution appears to be important as different nanoparticle sizes can target different organism parts (Swift et al., 1994), or can be phagocytised by macropages and giant cells (Oberdörster et al., 2007). Finally, aggregation can decrease the reactive surface and dissolution rates; for example the decrease of dissolution rate of galena when in an aggregated status (Hotze et al., 2010).

7.1.4 General geochemical and hydrological processes driving Zn and Pb dispersion

Zinc and Pb loads show dissimilar hydro-geochemical behaviours across streamflows and throughout the river. Those differences may be emphasised under high flow conditions when Pb, being sediment-bonded, is more likely to attenuate throughout the river lengths. For example, under high flow conditions, attenuation accounted for 72% of Pb load compared to 11% of Zn load. Conversely, Jarvis et al. (2019) found similar behaviour between the two elements even when the river water displayed similar chemistry. This may be due to the difference in the scale of the studies. Jarvis et al. (2019) investigated about 2 km closer to the former mine, compared to the 6 km of this study which included

potential hyporheic and depositional areas. Therefore, the incorporation of catchment geomorphological descriptions and sediment geochemistry can offer a better understanding of Zn and Pb mobilisation. Furthermore, metal-bearing nanoparticle data, as with metal partitioning and nanoparticle chemistry information, can provide invaluable information into the transport and fate of Zn and Pb in the river water. An excursus on observed Zn and Pb geochemical behaviour is presented below.

The Nant Cwmnewyddion and the Nant Magwr have a circum-neutral pH and low EC, similar to the majority of UK mining-impacted rivers (Jarvis et al., 2019). Under these geochemical conditions, Zn is highly mobile and preferentially exists in an aqueous status (Tame et al., 2017). This research agrees and shows Zn mainly as truly dissolved phase, which represents the most toxic phase (Hem, 1972). In addition, its behaviour is influenced by the streamflows. Jarvis et al. (2019) observed the highest concentration of Zn under low flow conditions. In this study the highest concentration of Zn is also found under low flow conditions, however, no correlation between streamflow and concentration was found. In contrast, a strong positive correlation was found between streamflow and Zn load. Nevertheless, exceptions of Zn high mobility are observed in the depositional areas. At 3210 m (DC), Zn is particularly involved in particle-water geochemical processes; it is found in the water both as dissolved or nano-phases, and in the sediments. On the floodplain, Zn was mostly transported in the truly dissolved fraction, but still Zn-bearing nanoparticles were observed. The low Zn concentration of the sediment in this area suggested that these nanoparticles may adsorb aqueous forms of Zn. Finally, Zn can be mobilised as suspended particles under high flows by the physical erosion of Zn-enriched sediments.

Evidence of Pb sediment-bond behaviour was found at a regional scale with its load positive correlated to the slope (Mayes et al., 2013). This work agrees with this hypothesis, showing areas of low slope involved in Pb attenuation processes, co-precipitation, and adsorption. The estimation of river metal loads together with the geomorphological work indicated that areas of low slope can act as Pb sinks under low flow and Pb sources under high flows. At Graiggoch mine, these sinks of Pb are thought to be in Pb-bearing Mn oxides occurring in the river sediment and were believed to have formed when the river water entered the hyporheic zone, increasing its oxygen content and promoting the formation of oxidised Mn phases (Gandy et al., 2007). Because these minerals have low solubility under the prevailing geochemical conditions, Pb was unlikely to be released to the river water. Further downstream, at 3210 m (DC) and at the floodplain (RB, 5930 m), the reduction of slope angle enhances the deposition of sediments. Herein, sediments have high Pb concentrations and water Pb load is lower compared to the upstream sites under low and moderate flows. Reasons for Pb accumulation

in the sediment can relate to the decrease in river water movement, which increases the chances of metals to be complexed and adsorbed Pb onto Mn and Fe oxides or phyllosilicates at both bulk- and nano-scales (Lynch et al., 2018, Palumbo-Roe et al., 2012). Summarising, this study demonstrates how Pb geochemistry is confounded by water-particle-sediment interactions, which potentially reduces the correlation between the Pb load and streamflow.

7.1.5 Conclusions

The multidisciplinary study here presented addressed the typical issues of mining-impacted catchment by investigating metal dispersion processes at nano- to catchment-scale. Geomorphological processes identified possible areas of metal phases transformation. Zinc and Pb loads showed temporal and spatial variations, with Zn behaviour closely linked to streamflow and Pb dispersion patterns confounded by geochemistry and geomorphology. At a nano-scale, metals are transported by nano-phases showing size, particle size distribution, and chemistry variabilities along the river. Frongoch Adit was identified as the main point source of Zn across streamflow conditions. The Pb main source was represented by the Frongoch adit during low flow condition, and the Wemyss Mine area, under medium and high flows. The multi-tracer method identified diffuse sources of Zn coming from Graiggoch Mine, a potential hyporheic source characterised by the formation of Pb-bearing Mn oxide. Across streamflow conditions, sediment mobilisation, hydro-connectivity, mineral dissolution, and metal de-adsorption were suggested as the main metal dispersion processes.

7.2 Management implications of research findings

This study provides accurate source apportionments along the Nant Cwmnewyddion, together with an indication of source response to streamflow variations. The described multi-disciplinary methods are proven to address metal source apportionment and illuminate Zn and Pb metal dispersion mechanisms. These data are fundamental at a local, regional and global scale. At a local scale, this work provides information on the Wemyss and Graiggoch Mines metal source apportionment and their impact on water and sediment quality downstream of the mining area. At the regional scale, data can be used in modelling metal dispersion in riverine and ocean systems, avoiding a water quality biased toward particular streamflow conditions (Jarvie et al., 1997). Furthermore, observed results can be useful in monitoring Pb and Zn mobilisation in other mining-impacted river systems. On a global scale, due to climate change, high flow and extreme dry events are likely to increase in frequency (Nordstrom, 2009), confounding metal source apportionment and monitoring. Therefore, the proposed multi-tracer method, successful in highly variable weather conditions, can be confidently implemented in a wide range of future climate scenarios.

7.2.1 Water quality management and metal source apportionment

Management strategies to reach good water status and implement EU WFD standards were reported in the River Basin Management Plan (RBMPs) (DEFRA 2006). Past studies and remediation strategies focus mainly on low flow conditions and point sources (DEFRA, 2018). The effort to achieve good quality status should be made at a catchment scale, and focus both on point and diffuse sources (Gozzard et al., 2011). The spatial and temporal variations in metal load captured by this research are aligned with the previous literature and clearly highlight the benefit of a multi-method approach in addressing mining contamination issues.

The planning of remediation strategies requires detailed metal source apportionment in order to achieve the most efficient solution for good water quality (Kimball, 2002). As observed at the Graiggoch Mine, load can be underestimated when the streamflow is measured with slug injection experiments. Other methods, such as those based on the riverbed cross-section area, may further underestimate the streamflow due to irregularity of river channels and subsurface water pathways (Runkel et al., 2013). Therefore, it is evident from this and other work (Byrne et al., 2017, Runkel et al., 2016) that the use of the continuous tracer injection should be part of the metal source apportionment monitoring.

This study, for the first time, has demonstrated the success of accurate point and diffuse source apportionment under moderate flow conditions and has proposed the integration of continuous and slug injections to quantify metal sources with respect to detailed spatial and temporal variations (Onnis et al., 2018). Several works have used a combination of methods, such as sharp-crested V-notch, flat V-weir, slug injections, and flow velocity meters, encountering the limitation of data comparison (Gozzard et al., 2011, Jarvis et al., 2019, Mayes et al., 2008). Although comparison among streamflow investigation is sometimes verified (Jarvis et al., 2019), streamflow estimation errors can affect the apportionment of metal contribution (Runkel et al., 2016). Furthermore, the time required to estimate streamflow at each site affects the total time required to complete synoptic sampling. Consequently, spatially detailed source apportionment cannot reach high accuracy using traditional methods (Mayes et al., 2013). The continuous tracer injection method offers snapshots in time with a detailed sampling grid (Byrne et al., 2017). Once the tracer reaches a steady concentration, the collection of numerous samples can occur in a half-day (or less, depending on the number of operators) covering distances on the scale of kilometers. Such detailed sampling grids allow point and diffuse source apportionment, which can otherwise be under- or overestimated. For example, in this study the streamflow was estimated at 24 sites in about 4 hours covering almost 3 km. The sampling captured detailed load variations of Zn, Pb, Fe, and S along the river, highlighting sources and sinks of

loads. For example, at Wemyss Mine, Pb loads fluctuated and attenuation load was apportioned. Such information indicates potential Pb load variation that can occur due to river water pH or streamflow changes and are fundamental when planning remediation strategies (Palumbo-Roe et al., 2012). This highlights the utility of the continuous tracer injection method, further exemplifying its importance in studies of this nature.

UK weather conditions induce streamflow variations over the entire hydrographic year. This pattern is typical of oceanic temperate climate conditions, which are observed across North Europe (Finlayson et al., 2014). Although high Zn and Pb concentrations were estimated during low flow conditions, even higher concentrations can be measured across a range of streamflows (Nordstrom, 2009). Previous studies have performed continuous injection experiments under low flow conditions (Byrne et al., 2017, Runkel et al., 2013) and shown that high metal concentrations are typical of low flow conditions. However, as stressed by this and previous works (Mayes et al., 2008, Nagorski et al., 2003), in mining-impacted rivers, metal source contributions vary across streamflows. This was observed at the Wemyss Mine, where both point and diffuse Pb sources contributed more during high flow conditions due to runoff and entrainment. The proposed multi-tracer method is a dynamic approach to investigate and plan the remediation of impacted river especially in areas characterised by irregular rainfall events. At present, slug injections are employed in the monitoring routine analysis and the adoption of one to two tracer injections per year would be a worthy and cost-effective investment of resources.

7.2.2 Sediment quality management and metal source investigation

Procedures for assessing sediment quality may benefit from the evidence provided in Chapter 4, where both geomorphological and sediment geochemical studies highlighted the distribution of metal and suggested possible mechanisms of metal-enriched sediment mobilisation or aqueous metal release. As reported in other studies, the geomorphological approach can help in identifying areas of mine waste exposure and deposition (Macklin et al., 2006). River catchment geomorphological description can also identify potential metal sources throughout the river, leading the first steps in mining-impacted river monitoring.

Monitoring of metal contamination is often focused at the headwater, where the mine working is generally located. Unfortunately, centuries of mining activity has produced tons of contaminated waste, which high gradient rivers remobilised downstream along the river (Miller, 1997). Kincey et al. (2018) estimated the loss of 441 t in 18 months through monitoring, and Foulds et al. (2014) identified the spatial distribution of metal-enriched sediment throughout river systems. Although sediment

metal concentrations tend to decrease downstream from the former mine, the estimated metal load variations demonstrated that these secondary sources can still contribute to the metal load, especially under high flow conditions. Therefore, catchment scale identification of metal-enriched sediment distribution is fundamental to localise potential metal sources (Hudson-Edwards et al., 2011). Furthermore, metals comprised in downstream sources are potentially bioavailable. For example, Byrne et al. (2010), using sequential extractions, found an increase in readily extractable Zn and Cd moving downstream from the Dylife Mine, UK. In the presented research, a high variety of metal-bearing minerals were found in the depositional downstream areas (the middle river length and the floodplain). A positive correlation between filtered Zn and Pb load with streamflow suggests a release of those metals under high flow conditions. Hence, a low cost but highly beneficial routine approach would be the study of topography, slope and landscape descriptors (such as vegetation distribution and land use). This could initially be carried out with maps, to help localise potential primary and secondary sources. Once localised, chemical and mineralogical sediment analysis can then help in verifying the source location and metal availability.

7.2.3 The importance of metal-nanoparticles in remediation strategies

Generally, the study of environmental nanoparticles provides precious information on the state of dispersions that can be applied to engineering systems or engineering particles in environmental conditions. Engineering nanoparticles can either move as isolated particles or aggregate in homo-aggregation or hetero-aggregations (Hotze et al., 2010). In impacted river systems, engineered nanoparticles can be introduced by remediation or water treatment techniques (Tafazoli et al., 2017), and possible interactions with autochthonous nanoparticles should be expected (Jones and Su, 2014). Therefore, baseline nanoparticle information (amount, chemistry and sources) can predict potential interactions between them and suggest a metal transport mechanism. For example, in the Nant Cwmnewyddion, the transport of Pb in nanoparticle phase, which amounts to 42% of the total load, is thought to be driven by humic and fulvic acids. Aggregation with this Pb-enriched phase with engineering nanoparticles may influence their ability to be removed by treatment systems (Hotze et al., 2010). At present, controversial results are still found in the literature, indicating either an increase or decrease of remediation effects due to aggregation processes. For example, Ce-oxide which was stabilised with surfactant was not efficiently removed (Limbach et al., 2008), whereas surface coated SiO₂ was removed by flocculation (Jarvie et al., 2009). It is important that future research investigates this matter, and helps in the understanding of aggregation among environmental and engineering nanoparticles.

The investigation of the geochemistry of complex nanoparticles and their ability in transport metals are prerequisites to accurately assess the risks of contamination of the environment and to human health (Handy et al., 2008). Models to quantify metal bioavailability in the filtered phases such as the Free ion activity model, (FIAM) (Morel & Hering, 1983), and the Biotic ligand model (BLM) (Di Toro et al., 2001), generally indicate bioavailable metal concentrations lower than filtered metal concentration, likely due to the presence of organic matter (Lamelas et al., 2005). However, experimental studies found that metal bio-accumulation in the organisms may be higher than those derived from FIAM and BLM (Campbell 1995). For instance, in river systems, Pb uptake by the alga *Chlorella vulgaris* and by the diatom *Stephanodizcus hantzschii* was higher than expected from the FIAM modelling (Mylon et al., 2003). Therefore, metal partitioning studies can contribute to predict metal bioavailability and model mineral saturation index in river water.

As stressed in the existing literature, data on environmental nanoparticles are difficult to collect due to their high instability and variability (Lapworth et al., 2013, Pokrovsky et al., 2010). The approach presented here is powerful because it provides an efficient method for sampling nanoparticles in the fluvial system, obtaining the truly dissolved metal fraction using low cost 10kDa ultracentrifugation filters and, combined with streamflows, metal load partitioning in suspended, nano- and dissolved phases. Furthermore, nanoparticle characterisation via multi-instruments delivered invaluable information on metal-nanoparticle interactions and stability.

7.2.4 Conclusions

The described multi-disciplinary research offered one of the first examples of detailed metal source apportionment identifying drivers of metal dispersion at nano- and catchment-scale. Outputs can inform the local remediation strategy of the area, provide metal data for regional dispersion models, and approach the issues of metal dispersion across high variable streamflows, an emerging problem at a global scale due to climate changes. The proposed multi-tracer approach identified the metal source contributions across streamflows and highlighted the underestimation in streamflow monitoring by slug injections, especially in hyporheic zones. As reported by previous literature, the continuous tracer injection provided an accurate method to estimate detailed load variations along the river, and the slug injections allowed the estimation of the load variations across streamflows. To better understand the impact of metal sources at the catchment scale, soil geochemistry and geomorphological observations can identify potential areas delocalised from the mining up-stream areas and suggest the mechanism of metal release likely to occur across streamflow conditions. Furthermore, metal transport was studied at a nano-scale, a new method to distinguish metal related to dissolved phases, nanoparticle, and suspended particles has been developed. The findings

quantified the metal transport due to nano-phases and suggested metal – nano interactions processes which can be used to investigate metal bioavailability and the potential behaviour of engineered nanoparticles in the environments. Concluding, these dynamic methods can be easily implemented in monitoring routines and provide low-cost data to inform remediation strategies.

7.3 Final remarks and future directions

This thesis goes beyond the metal contamination characterisation of a Welsh catchment. The work has demonstrated that metals can occur within particles of various sizes and travel several kilometres in impacted-rivers. Soil geochemistry and observation of fluvial parameters provided an indication of areas of metal storage or release in the river at a catchment scale. The continuous tracer injection apportioned diffuse and point sources at moderate streamflow conditions, and slug injections quantified metal load variations across streamflows. Zinc was mostly transported in the truly dissolved phase, and its load positively correlated to streamflows. In contrast, Pb load, transported as suspended or nanoparticle phases, responded to physical transport processes and sediment-bound geochemistry, as well as streamflow.

However, data interpretation was partially limited, due to the typical complexity of a mining-impacted river system. Further investigations should be carried out to better quantify and partitioning metal sources across streamflow conditions.

For a better picture of how the contribution of metal sources change across streamflow, the continuous tracer injection should be repeated during low and high flow conditions. Limitations in the execution can derive from the high variability of the rainfall events, which can confound the tracer concentration in the river. Future approaches should focus on the use of continuous tracer injection under non-steady-state conditions, such as during rainfall events. For example, the integration of lysimeters, pluviometers, and pressure-transducers would provide information on water infiltration, rainfall contribution and water level rise. Modelling these data with the tracer concentrations from the river samples would allow estimation of the streamflow and rainfall contribution.

Verifying the presence and extension of diffuse sources such as the hyporheic zone is difficult to achieve. Geophysical investigations, such as Electrical Resistivity Tomography (ERT), may help to identify hyporheic zones (as Graiggoch Mine diffuse source), and its likely connection with mining underground (Uhlemann et al., 2016). Using both continuous tracer injection and ERT in parallel is likely to provide more information on hydro-connectivity between the riverbed and the hyporheic zone.

The successful nanoparticle sampling technique and the multi-instrument nanoparticle investigation identified the role of nanoparticles in Zn and Pb transport. The link between truly dissolved, nanoparticle, and bioavailable phases remains unclear. Comparison studies on metal concentrations among the dissolved phase, FIAM modelling, and bio-uptake are suggested to better understand metal potential toxicity. In this context, a complementary characterisation of the organic matter can add information on nanoparticle stability and metal bioavailability. Finally, the geochemical investigation of sediment nanoparticles may contribute to the understanding of nanoparticle formation and fate.

Multidisciplinary research at the catchment scale, including routine monitoring of streamflows, becomes necessary to understand the real processes, to quantify metal load, and to plan efficient remediation with appropriate priority classifications of contaminated areas (Byrne et al., 2012). This can ensure the achievement of a good quality WFD standard and, consequently, reduce the environmental impact of metal contamination (Environment Agency, 2008).

Present and future generations are facing an environmental crisis consisting of conspicuous contaminated environments, and extreme climate change scenarios such as flooding and drought events. Therefore, the importance of reaching good water status is not only a way to respect the WFD guideline, but a matter of life support for pressured ecosystems. Concerning the mining-impacted river systems, there is an urgent challenge to provide efficient and low-cost strategies for monitoring and reduce the dispersion of contaminants. In this scenario, the presented research contributes to providing information and strategies that can help in reaching a better understanding and quantification of metal dispersion.

7.4 Conclusions

The major conclusion from this chapter are:

- The presented multi-disciplinary study contributed to the understanding of metal drivers at the nano- and catchment-scale in mining-impacted rivers.
- Results show that the river catchment geomorphology can influence sediment geochemical processes (such as redox and dissolution) and point out areas of metal source transformation.
- The proposed multi-tracer method, that combines continuous tracer and slug injections, successfully estimated point and diffuse metal source contributions throughout the river and across streamflows.
- The fluvial nanoparticle investigation revealed that suspended particles, nanoparticles and dissolved phases contributed differently to the metal load. This information, together with metal-

bearing nanoparticle characterisation contributed to shed a light on the role of nanoparticles in metal transport and fate.

- The multi-disciplinary approach contributed to the understanding of Zn and Pb hydro-geochemistry; Zn load has a strong positive correlation with streamflow, unlike Pb which dispersion is confounded by the catchment geomorphology and sediment geochemistry.
- Derived data and methods are fundamental at i) a local scale providing metal source apportionment of the former mines; ii) a regional scale for modelling the metal dispersion in riverine and ocean systems; iii) a global scale given that the multi-tracer method can be implemented confidently in a wide range of climates.
- River catchment geomorphological description can be employed as a low-cost approach to localise potential metal sources and plan catchment-scale monitoring strategies. Then, the integration of chemical and mineralogical sediment analysis can help in verifying the source location and the metal bioavailability.
- The study provided precious information and techniques for the investigation of environmental nanoparticles. Information on chemistry, particle size distribution, and aggregation state can help in modelling metal bioavailability and anticipating possible interactions with engineering nanoparticles often introduced by remediation techniques.
- Ultimately, this study provided information on Zn and Pb dispersion mechanisms and proposed the integration of practical and efficient methods to guide monitoring and remediation of mining-impacted rivers. Much work remains to gain a full understanding of nanoparticle sources and fate and how to better apply the multi-tracer method to apportion metal dispersion under high flow conditions.

Appendices

Appendix 4.a Sediment sample and transect list

	Date	Eastern	Northern	Area	Transect	N° of samples
<i>Upstream of the mine tips - c. 0 m</i>						
1	26/07/2016	271670	273995	TO	M	2
<i>Wemyss mine - c. 171 m and surrounding area</i>						
2	26/07/2016	271611	274198	CW	J	4
3	26/07/2016	271531	274085	WM	K	4
<i>Graiggoch Mine - 1110 - 2620 m</i>						
4	26/07/2016	270410	274241	GG	L	4
<i>Middle reach - 3000-4070 m</i>						
5	19/07/2016	268389	274436	DC	D	6
6	19/07/2016	268397	274449	DC	E	5
7	19/07/2016	268308	274414	DC	F	9
8	20/07/2016	268113	274420	DC	G	5
9	20/07/2016	268113	274420	DC	H	7
<i>Floodplain - c. 5800 m</i>						
10	19/07/2016	266483	273856	RB UP/S	B	2
11	19/07/2016	266488	273860	RB UP/S	C	2
12	19/07/2016	266433	273868	RB UP/S	D	2
13	19/07/2016	266488	273860	RB UP/S	DEP C	2
14	19/07/2016	266453	273860	RB UP/S	I	4
<i>Floodplain - c. 6740 m</i>						
15	18/07/2016	265966	274005	RB D/S	DEP A	7
16	18/07/2016	265966	274005	RB D/S	DEP B	1
17	18/07/2016	265966	274009	RB D/S	A	2
TOT						68

Appendix 4.b pXRF data for sediment samples

Key. VCS: very coarse sand; CS: coarse sand; S:sand; FS: fine sand; VFS: very fine sand; <63: silt and clay

Sample	Fe (wt%)							Zn (wt%)			
	Average	VCS	CS	S	FS	VFS	<63	Average	VCS	CS	S
TANK M1	3.73	2.81	4.06	3.97	4.02	4.08	4.42	0.13	0.13	0.10	0.13
TANK M2	4.04	2.80	4.43	3.52	4.17	4.38	5.33	2.92	3.62	2.97	3.28
CW IJ1	4.37	4.47	4.55	2.22	1.99	4.60	9.53	0.09	0.10	0.09	0.04
CW IJ2	3.61	3.42	2.96	2.32	2.29	2.94	9.18	0.10	0.11	0.11	0.05
CW IJ3	6.30	6.32	5.30	4.72	4.75	8.32	9.55	0.30	0.09	0.47	0.28
CW IJ4	4.28	2.71	2.75	2.33	2.52	4.03	8.67	0.09	0.04	0.06	0.05
WM K1	4.57	2.77	2.98	2.58	2.53	4.75	8.90	0.18	0.12	0.28	0.09
WM K4	4.33	4.90	4.52	3.05	3.05	4.89	5.41	1.33	1.19	1.20	0.75
WM K2	3.44	2.90	2.90	2.46	2.30	2.76	7.36	0.11	0.06	0.09	0.07
WM K3	6.49	6.06	6.69	6.53	6.44	6.96	6.73	0.23	0.17	0.19	0.27
GG L 1	5.02	4.42	4.92	4.28	4.50	6.44	9.76	0.11	0.11	0.10	0.10
GG L 2	8.47	8.05	7.89	8.86	9.46	8.60	9.95	0.09	0.09	0.08	0.11
GG L 3	5.72	6.28	4.38	4.59	5.79	7.69	10.27	0.12	0.11	0.10	0.09
GG L 4	6.67	7.34	6.20	5.20	5.85	7.68	9.48	0.09	0.06	0.08	0.09
DC D 1	7.84	7.42	7.85	7.23	7.73	8.14	8.39	0.28	0.28	0.29	0.28
DC D 2	5.43	5.13	4.32	5.19	5.39	7.64	9.65	0.08	0.10	0.09	0.05
DC D 3	5.25	5.27	5.05	4.90	4.71	5.12	7.59	0.03	0.03	0.03	0.03
DC D 4	7.97	7.09	7.14	7.87	7.56	7.82	11.60	0.02	0.01	0.01	0.01
DC D 5	7.17	6.43	6.67	7.54	8.32	8.19	9.70	0.01	0.01	0.01	0.01
DC E 6	5.91	6.44	5.37	5.05	5.21	6.25	9.77	0.11	0.12	0.07	0.11
DC E 7	5.78	6.07	5.43	5.44	5.28	5.77	7.26	0.08	0.09	0.06	0.10
DC E 8	4.71	2.94	4.99	5.01	5.68	8.75	9.75	0.07	0.03	0.07	0.10
DC E 9	5.74	4.23	5.74	5.78	8.78	9.06	10.51	0.07	0.05	0.06	0.06
DC E 10	6.15	6.48	6.48	5.14	5.06	6.22	9.57	0.09	0.10	0.11	0.10
DC F 1a top	5.73	5.11	6.01	5.47	5.43	5.42	7.58	0.08	0.07	0.07	0.06
DC F 1b 10cm	2.58	1.52	1.81	1.91	2.65	3.75	6.75	0.44	0.42	0.57	0.34
DC F 1c 20cm	4.67	4.01	4.50	4.22	4.32	5.33	7.97	0.24	0.27	0.15	0.28
DC F 1d 30cm	5.01	5.24	4.72	4.72	4.54	5.34	6.74	0.22	0.27	0.25	0.20
DC F2	5.01	4.33	5.09	5.06	5.13	5.09	5.60	n.d.	n.d.	n.d.	n.d.
DC F3	5.13	5.45	5.26	5.05	5.12	4.99	4.60	0.04	0.03	0.03	0.04
DC F4	5.19	5.25	5.01	5.29	5.14	5.28	5.23	0.05	0.05	0.05	0.06
DC F5	6.58	5.32	7.19	7.61	8.49	6.30	6.21	0.09	0.12	0.06	0.06
DC F6	7.94	9.60	8.99	9.70	9.65	7.94	6.65	0.17	0.17	0.18	0.19
DC G 1	4.87	4.10	4.71	4.66	4.96	6.67	9.69	0.10	0.09	0.06	0.12
DC G 2	7.55	7.67	7.20	7.12	6.79	7.82	9.51	0.05	0.05	0.05	0.05
DC G 3	6.10	5.76	6.30	5.76	5.46	6.44	7.57	0.06	0.06	0.06	0.06
DC G 4	6.39	7.98	7.35	6.50	5.99	5.09	6.23	0.19	0.18	0.15	0.15
DC G 5	5.97	5.11	6.16	6.26	5.25	6.31	7.68	0.12	0.12	0.15	0.16

Sample	Zn (wt%)			Pb (wt%)						
	F S	V F S	<63	Average	VCS	CS	S	F S	V F S	<63
TANK M1	0.15	0.13	0.15	0.74	0.75	0.66	0.73	0.81	0.77	0.78
TANK M2	2.34	2.57	2.50	1.84	1.94	1.99	1.93	1.34	1.76	2.11
CW IJ1	0.04	0.10	0.18	4.25	2.81	3.44	0.64	0.78	4.57	12.81
CW IJ2	0.05	0.11	0.25	2.52	0.68	0.97	0.54	0.86	2.91	10.21
CW IJ3	0.38	0.36	0.38	1.15	0.30	0.71	0.72	1.15	2.30	3.16
CW IJ4	0.04	0.09	0.17	1.96	0.47	0.67	0.52	0.50	1.77	5.59
WM K1	0.11	0.17	0.27	2.41	1.13	1.42	0.92	1.00	2.88	4.88
WM K4	0.96	2.23	2.40	3.16	3.34	2.92	2.63	2.69	3.73	4.09
WM K2	0.05	0.07	0.29	3.20	0.46	0.56	0.48	0.59	2.69	14.22
WM K3	0.27	0.27	0.26	0.73	0.65	0.64	0.73	0.78	1.06	0.92
GG L 1	0.11	0.10	0.19	0.29	0.23	0.37	0.23	0.24	0.36	0.52
GG L 2	0.07	0.12	0.13	0.01	0.00	0.00	0.00	0.01	0.01	0.12
GG L 3	0.12	0.17	0.28	0.32	0.15	0.23	0.23	0.51	0.78	1.29
GG L 4	0.12	0.10	0.11	1.18	1.47	1.21	0.76	0.92	1.37	1.43
DC D 1	0.29	0.28	0.28	1.68	1.66	1.77	1.88	1.83	1.64	1.45
DC D 2	0.05	0.08	0.11	0.50	0.34	0.41	0.43	0.67	0.82	1.07
DC D 3	0.04	0.04	0.05	0.47	0.39	0.51	0.46	0.44	0.53	0.61
DC D 4	0.01	0.01	0.05	0.01	0.00	0.00	0.00	0.01	0.00	0.01
DC D 5	0.01	0.01	0.01	0.00	0.00	0.00	0.00	0.00	0.00	0.00
DC E 6	0.07	0.13	0.23	0.39	0.34	0.48	0.25	0.36	0.52	0.69
DC E 7	0.10	0.09	0.07	0.32	0.28	0.34	0.38	0.36	0.25	0.27
DC E 8	0.10	0.08	0.11	0.21	0.05	0.22	0.26	0.34	0.49	0.66
DC E 9	0.12	0.10	0.15	0.26	0.20	0.19	0.26	0.36	0.45	0.66
DC E 10	0.07	0.09	0.14	0.75	0.98	0.95	0.73	0.55	0.67	0.83
DC F 1a top	0.09	0.08	0.11	0.01	0.01	0.01	0.01	0.01	0.01	0.01
DC F 1b 10cm	0.51	0.38	0.41	0.00	0.00	0.01	0.00	0.01	0.00	0.01
DC F 1c 20cm	0.27	0.26	0.27	0.00	0.00	0.00	0.00	0.00	0.00	0.00
DC F 1d 30cm	0.19	0.15	0.19	0.00	0.00	0.00	0.00	0.00	0.00	0.00
DC F2	n.d.	n.d.	n.d.	1.61	1.74	2.07	1.88	1.70	1.32	0.82
DC F3	0.04	0.04	0.04	2.05	1.99	2.07	2.35	2.31	2.05	1.57
DC F4	0.05	0.05	0.04	2.00	2.32	2.10	2.12	2.01	1.88	1.33
DC F5	0.07	0.09	0.09	4.27	3.84	3.86	4.02	4.67	4.76	4.16
DC F6	0.20	0.18	0.15	8.30	6.90	7.67	8.05	9.40	10.06	7.52
DC G 1	0.09	0.16	0.14	0.34	0.26	0.22	0.24	0.49	0.79	1.06
DC G 2	0.05	0.06	0.07	0.33	0.38	0.26	0.34	0.30	0.34	0.40
DC G 3	0.06	0.07	0.08	0.96	0.81	1.07	1.03	0.92	0.98	1.01
DC G 4	0.23	0.20	0.22	3.34	2.44	1.85	2.46	3.77	3.83	4.51
DC G 5	0.08	0.09	0.10	0.65	0.52	0.76	0.79	0.56	0.60	0.69

Sample	Fe (wt%)							Zn (wt%)			
	Average	VCS	CS	S	F S	V F S	<63	Average	VCS	CS	S
DC H 1	4.31	4.20	4.10	4.44	3.99	4.35	5.06	0.12	0.07	0.19	0.08
DC H 2	4.70	4.89	4.53	4.71	4.59	4.53	4.95	0.06	0.05	0.07	0.06
DC H 3	7.04	7.12	6.08	6.60	6.81	8.17	9.04	0.10	0.11	0.10	0.09
DC H 4a top	7.18	6.35	8.74	7.09	5.56	6.72	8.50	0.08	0.10	0.08	0.11
DC H 4b bottom	6.56	5.87	6.82	6.05	6.30	7.08	7.44	0.09	0.08	0.10	0.08
DC H 5	7.95	8.27	8.63	8.14	7.37	5.48	9.51	0.09	0.10	0.07	0.07
DC H 6	9.58	9.92	10.22	9.85	9.86	8.55	9.80	0.09	0.10	0.06	0.06
RB UPS B1	9.45	9.56	9.54	8.92	9.31	9.63	9.71	0.17	0.14	0.15	0.14
RB UPS B2	9.07	9.25	8.79	9.01	8.18	9.62	9.71	0.09	0.10	0.07	0.08
RB UPS C1	7.63	8.84	7.11	6.84	7.16	6.83	8.43	0.28	0.28	0.28	0.27
RB DS A2	7.92	7.18	8.08	7.78	8.37	9.39	11.22	0.01	0.01	0.01	0.01
RB UPS C2	7.76	9.19	7.49	7.50	6.18	7.34	9.61	0.26	0.27	0.27	0.27
RB UPS DEP1C	5.40	4.52	5.17	5.37	6.89	8.38	10.08	0.23	0.27	0.20	0.22
RB UPS DEP2C	6.29	5.12	6.96	5.65	6.04	9.54	9.77	0.16	0.10	0.16	0.17
RB UPS D 1	8.11	8.52	8.75	8.07	6.52	7.44	9.71	0.13	0.27	0.27	0.18
RB UPS D 2	7.73	8.28	8.04	6.32	6.44	7.46	9.68	0.15	0.20	0.19	0.12
RB UPS I 1	7.57	7.39	7.46	7.44	6.61	7.43	9.67	0.15	0.19	0.14	0.16
RB UPS I 2	7.99	7.41	8.11	7.67	6.98	8.60	9.72	0.09	0.06	0.09	0.06
RB UPS I 3 a	8.28	9.20	8.60	7.71	6.71	8.02	9.67	0.10	0.16	0.11	0.09
RB UPS I 3 b	8.95	9.55	8.55	8.65	8.27	8.95	9.64	0.26	0.27	0.26	0.26
RB DS DEPA 1	7.02	5.56	6.07	6.02	6.77	7.95	9.77	0.27	0.28	0.27	0.27
RB DS DEPA 2	6.16	5.34	4.96	6.28	10.63	10.48	7.74	0.13	0.09	0.07	0.15
RB DS DEPA 3	6.91	6.91	5.91	6.08	7.46	9.83	10.89	0.14	0.09	0.12	0.12
RB DS DEPA 4	6.33	5.16	5.78	6.42	6.54	9.58	10.20	0.22	0.19	0.24	0.20
RB DS DEPA 5	6.68	5.63	6.43	5.88	9.76	10.12	11.19	0.12	0.06	0.09	0.12
RB DS DEPA 6	5.97	4.74	5.44	5.89	8.48	11.49	11.11	0.12	0.10	0.09	0.09
RB DS DEPA 7	7.36	7.91	6.00	5.90	7.52	10.00	14.74	0.13	0.08	0.13	0.10
RB DS DEP B 1	6.68	6.51	6.32	5.25	9.74	9.64	10.34	0.16	0.08	0.19	0.16
RB DS A 1	8.47	7.59	8.01	8.12	9.15	9.64	11.64	0.04	0.03	0.03	0.04

Sample	Zn (wt%)			Pb (wt%)						
	F S	V F S	<63	Average	VCS	CS	S	F S	V F S	<63
DC H 1	0.13	0.11	0.12	0.00	0.00	0.00	0.00	0.00	0.00	0.01
DC H 2	0.08	0.07	0.07	0.00	0.00	0.00	0.00	0.01	0.01	0.01
DC H 3	0.09	0.11	0.08	0.81	0.73	0.76	0.79	0.60	1.04	1.27
DC H 4a top	0.06	0.07	0.10	0.59	0.80	0.68	0.69	0.41	0.42	0.47
DC H 4b bottom	0.08	0.11	0.12	0.59	0.51	0.61	0.60	0.53	0.63	0.64
DC H 5	0.07	0.12	0.10	2.17	1.45	1.90	2.08	2.07	2.24	3.00
DC H 6	0.10	0.08	0.10	3.61	2.85	3.61	3.36	4.31	3.27	3.80
RB UPS B1	0.15	0.19	0.23	0.26	0.26	0.26	0.23	0.28	0.26	0.28
RB UPS B2	0.07	0.09	0.12	0.26	0.22	0.28	0.26	0.29	0.26	0.28
RB UPS C1	0.28	0.28	0.27	0.93	0.96	0.95	0.92	1.02	0.90	0.87
RB DS A2	0.01	0.02	0.05	0.00	0.00	0.00	0.00	0.00	0.00	0.01
RB UPS C2	0.26	0.24	0.27	1.27	1.37	1.26	1.49	1.33	1.05	1.18
RB UPS DEP1C	0.27	0.32	0.39	0.22	0.21	0.18	0.22	0.29	0.46	0.54
RB UPS DEP2C	0.27	0.28	0.28	0.22	0.16	0.17	0.21	0.36	0.48	0.51
RB UPS D 1	0.06	0.09	0.07	1.01	1.91	2.13	1.46	0.75	0.65	0.57
RB UPS D 2	0.12	0.12	0.21	0.47	0.54	0.58	0.46	0.53	0.37	0.47
RB UPS I 1	0.15	0.13	0.11	0.84	0.62	0.77	0.88	0.98	0.91	0.94
RB UPS I 2	0.12	0.08	0.10	1.36	1.25	1.29	1.37	1.17	1.42	1.79
RB UPS I 3 a	0.07	0.09	0.10	0.52	0.57	0.62	0.69	0.50	0.39	0.42
RB UPS I 3 b	0.27	0.25	0.26	0.60	0.58	0.61	0.63	0.69	0.57	0.53
RB DS DEPA 1	0.27	0.27	0.27	0.26	0.23	0.26	0.27	0.25	0.29	0.26
RB DS DEPA 2	0.33	0.30	0.24	0.21	0.07	0.18	0.22	0.66	0.62	0.30
RB DS DEPA 3	0.24	0.28	0.30	0.22	0.13	0.16	0.20	0.30	0.57	0.65
RB DS DEPA 4	0.25	0.27	0.28	0.27	0.25	0.23	0.23	0.30	0.38	0.49
RB DS DEPA 5	0.27	0.29	0.29	0.21	0.16	0.15	0.17	0.37	0.59	0.59
RB DS DEPA 6	0.19	0.31	0.29	0.14	0.01	0.15	0.18	0.26	0.54	0.54
RB DS DEPA 7	0.18	0.28	0.38	0.19	0.13	0.16	0.18	0.24	0.46	0.56
RB DS DEP B 1	0.27	0.26	0.27	0.17	0.09	0.16	0.22	0.35	0.28	0.36
RB DS A 1	0.04	0.04	0.09	0.00	0.00	0.00	0.00	0.00	0.00	0.01

Appendix 4.c XRD data for selected sediment samples

TO M2

Accepted	PDF #	Compound Name	I Ratio	I%	I/Ic
TRUE	01-070-7344	Silicon Oxide	1.205	12	3.05
TRUE	00-046-1045	Silicon Oxide	1.166	11	3.41
TRUE	00-035-0748	Manganese Silicate	0.165	2	
TRUE	00-037-0516	Lead Oxide Sulfate	0.592	6	
TRUE	00-033-1486	Lead Oxide Sulfate	0.61	6	
TRUE	01-074-6450	Zinc Titanium Oxide	0.431	4	3.66
TRUE	01-074-0823	Magnesium Aluminum Phosphate Hydroxide Potassium Magnesium Aluminum Silicate Hydroxide	0.308	3	1.25
TRUE	00-010-0495	Sulfur	0.43	4	
TRUE	00-042-1278	Sulfur	0.132	1	
TRUE	00-017-0514	Calcium Aluminum Iron Silicate Hydroxide	0.105	1	
TRUE	00-009-0493	Magnesium Aluminum Silicate Hydroxide	0.071	1	
TRUE	00-040-0508	Yttrium Boron Carbonate Hydroxide	0.163	2	
TRUE	01-072-1234	Magnesium Iron Aluminum Silicate Hydroxide	0.324	3	1.17
TRUE	01-089-2972	Magnesium Iron Aluminum Silicate Hydroxide	0.317	3	1.07
TRUE	01-075-8790	Magnesium Iron Aluminum Silicate Hydroxide	0.237	2	0.8
TRUE	01-089-6454	Magnesium Aluminum Silicate Oxide Hydroxide	0.941	9	3.69
TRUE	01-074-3036	Calcium Aluminum Hydrogen Oxide	0.141	1	1.17
TRUE	01-074-3037	Calcium Aluminum Hydrogen Oxide Potassium Magnesium Aluminum Silicate Hydroxide	0.143	1	1.15
TRUE	00-021-0993	Sodium Titanium Silicate Oxide Hydroxide	0.332	3	
TRUE	01-073-8482	Hydrogen Phosphate	0.578	6	1.16
TRUE	01-075-8791	Magnesium Iron Aluminum Silicate Hydroxide Barium Manganese Titanium Oxide Hydroxide Silicate	0.237	2	0.91
TRUE	01-077-0664	Sodium Barium Strontium Titanium Fluoride Silicate Hydroxide	0.221	2	1.19
TRUE	00-017-0751	Silicate Hydroxide	0.104	1	

CW J1

Accepted	PDF #	Compound Name	I Ratio	I%	I/Ic
TRUE	01-070-7344	Silicon Oxide	1.212	31	3.05
TRUE	00-029-0701	Iron Magnesium Aluminum Silicate Hydroxide	0.275	7	
TRUE	01-074-9742	Lead Sulfate	0.303	8	4.19
TRUE	00-040-1499	Lithium Iron Phosphate	0.234	6	
TRUE	00-020-1084	Sodium Borate Hydrate	0.143	4	
TRUE	00-007-0042	Potassium Aluminum Silicate Hydroxide Potassium Magnesium Aluminum Silicate Hydroxide	0.355	8	
TRUE	00-010-0495	Lithium Aluminum Silicate Hydroxide	0.413	11	
TRUE	00-045-1377	Sodium Iron Silicon Oxide	0.103	3	
TRUE	01-076-9768	Copper Chromium Oxide	0.168	4	0.5
TRUE	00-039-0247	Magnesium Chloride Carbonate Hydroxide Hydrate	0.026	1	2.26
TRUE	00-050-1690	Hydrate	0.621	16	

WM K4

Accepted	PDF #	Compound Name	I Ratio	I%	I/Ic
TRUE	01-071-1080	Magnesium Silicate	0.256	5	0.77
TRUE	00-037-0516	Lead Oxide Sulfate	0.467	9	
TRUE	01-070-7344	Silicon Oxide	1.398	27	3.05
TRUE	00-034-0189	Magnesium Silicate	0.142	3	
TRUE	00-033-1486	Lead Oxide Sulfate	0.475	9	
TRUE	01-070-0287	Calcium Aluminum Silicate	0.574	11	0.59
TRUE	00-029-0701	Iron Magnesium Aluminum Silicate Hydroxide	0.254	5	
TRUE	00-043-0671	Copper Sulfate Hydroxide Hydrate	0.111	2	
TRUE	00-046-1323	Magnesium Aluminum Iron Silicate Hydroxide	0.158	3	
TRUE	00-038-0328	Sodium Aluminum Silicate Hydrate	0.083	2	
TRUE	00-009-0478	Potassium Sodium Aluminum Silicate	0.187	4	
TRUE	00-018-0787	Manganese Hydroxide	0.092	2	
TRUE	01-071-2398	Magnesium Aluminum Silicate	0.578	11	0.44
TRUE	01-086-1521	Manganese Phosphate Hydroxide Hydrate	0.343	7	0.91

GG L1

Accepted	PDF #	Compound Name	I Ratio	I%	I/Ic
TRUE	01-070-7344	Silicon Oxide	1.304	28	3.05
TRUE	00-029-0701	Iron Magnesium Aluminum Silicate Hydroxide	0.323	7	
TRUE	01-073-1133	Manganese Hydroxide	0.186	4	3.69
TRUE	01-075-2545	Titanium Oxide	0.224	5	5.01
TRUE	03-065-3928	Copper Sulfide	0.225	5	0.53
TRUE	00-001-0739	Sodium Aluminum Silicate	0.197	4	
TRUE	01-070-3411	Calcium Titanium Oxide Silicate	0.228	5	1.24
TRUE	01-076-0948	Calcium Aluminum Silicate	0.393	9	0.56
TRUE	01-078-4575	Lead Phosphate Fluoride	0.273	6	5.18
TRUE	01-071-1667	Iron Silicate	0.246	5	1.46
TRUE	01-077-1315	Silicon Oxide	0.454	10	4.83
TRUE	01-076-7141	Potassium Sodium Barium Magnesium Iron Aluminum Silicon Oxide Fluoride Hydroxide	0.557	12	1.21

DC E7

Accepted	PDF #	Compound Name	I Ratio	I%	I/Ic
TRUE	00-012-0242	Magnesium Aluminum Silicate Hydroxide	0.094	2	
TRUE	01-073-1133	Manganese Hydroxide	0.142	3	3.69
TRUE	01-072-1503	Potassium Aluminum Silicate Hydroxide	0.277	6	0.37
TRUE	01-089-8936	Silicon Oxide	1.266	26	2.96
TRUE	01-083-1720	Lead Sulfate	0.419	9	8.11
TRUE	01-075-0581	Cadmium Sulfide	0.699	14	14.06
TRUE	01-089-8918	Magnesium Aluminum Silicate	0.114	2	1.34
TRUE	01-081-0538	Magnesium Aluminum Silicate	0.109	2	1.28
TRUE	01-089-7213	Carbon	1.114	23	2.29
TRUE	01-088-1965	Manganese Iron Oxide	0.169	3	4.93
TRUE	01-076-7776	Aluminum Oxide	0.089	2	0.96
TRUE	00-010-0319	Manganese Iron Oxide	0.11	2	
TRUE	00-009-0485	Manganese Silicate	0.145	3	
TRUE	01-078-4188	Titanium Oxide	0.044	1	3.46

DC F1d

Accepted	PDF #	Compound Name	I Ratio	I%	I/Ic
----------	-------	---------------	---------	----	------

TRUE	00-029-0701	Iron Magnesium Aluminum Silicate Hydroxide	0.314	7	
TRUE	00-046-1323	Magnesium Aluminum Iron Silicate Hydroxide	0.182	4	
TRUE	01-070-7344	Silicon Oxide	1.147	27	3.05
TRUE	00-034-0192	Iron Aluminum Oxide	0.15	4	
TRUE	01-073-1133	Manganese Hydroxide	0.155	4	3.69
TRUE	01-075-2545	Titanium Oxide	0.195	5	5.01
TRUE	01-082-0579	Iron Aluminum Oxide	0.228	5	3
TRUE	01-084-0520	Potassium Hydrogen Phosphate	0.126	3	2.28
TRUE	01-079-2273	Copper Iron Sulfide	0.23	5	2.13
TRUE	01-077-0441	Titanium Oxide	0.049	1	3.53
TRUE	01-078-4188	Titanium Oxide	0.048	1	3.46
TRUE	00-042-1414	Potassium Magnesium Iron Aluminum Silicate Hydroxide	0.734	17	3.3
TRUE	01-082-1301	Manganese Iron Titanium Oxide	0.036	1	4.53
TRUE	01-070-6278	Iron Titanium Oxide	0.351	8	2.61

DC F2

Accepted	PDF #	Compound Name	I Ratio	I%	I/Ic
TRUE	01-073-1133	Manganese Hydroxide	0.139	3	3.69
TRUE	00-034-0192	Iron Aluminum Oxide	0.126	2	
TRUE	01-070-7344	Silicon Oxide	1.2	22	3.05
TRUE	00-037-0481	Iron Phosphate Hydrate	0.459	8	
TRUE	01-082-0579	Iron Aluminum Oxide	0.19	4	3
TRUE	00-046-1323	Magnesium Aluminum Iron Silicate Hydroxide	0.147	3	
TRUE	00-029-0701	Iron Magnesium Aluminum Silicate Hydroxide	0.31	6	
TRUE	00-009-0456	Sodium Calcium Aluminum Silicate	0.231	4	
TRUE	00-012-0242	Magnesium Aluminum Silicate Hydroxide	0.086	2	
TRUE	00-009-0466	Sodium Aluminum Silicate	0.351	6	2.1
TRUE	00-016-0362	Magnesium Aluminum Iron Silicate Hydroxide	0.087	2	
TRUE	00-003-1132	Calcium Magnesium Silicate	0.258	5	
TRUE	00-042-0568	Sodium Calcium Magnesium Aluminum Silicate	0.138	3	
TRUE	00-048-1877	Aluminum Lead Manganese Oxide Silicate Sulfate Hydroxide	0.085	2	
TRUE	01-074-1022	Aluminum Silicate Hydroxide	0.815	15	1.41
TRUE	00-003-0744	Lead Antimony Sulfide	0.073	1	
TRUE	01-079-2192	Sodium Calcium Manganese Arsenic Silicon Vanadium Oxide	0.654	12	2.64

RB D/S A1

Accepted	PDF #	Compound Name	I Ratio	I%	I/Ic
TRUE	00-029-0701	Iron Magnesium Aluminum Silicate Hydroxide	0.427	11	
TRUE	01-073-1133	Manganese Hydroxide	0.158	4	3.69
TRUE	01-070-7344	Silicon Oxide	1.162	30	3.05
TRUE	00-038-0409	Lead Sulfite	0.285	7	
TRUE	01-089-7536	Potassium Aluminum Iron Silicate Hydroxide	0.36	9	0.51
TRUE	00-043-0662	Magnesium Silicate Hydroxide	0.028	1	
FALSE	01-089-0851	Calcium Zinc Sulfate Hydroxide Chloride Hydrate	1.459	38	6.95

RB U/S C1

Accepted	PDF #	Compound Name	I Ratio	I%	I/Ic
----------	-------	---------------	---------	----	------

TRUE	00-012-0242	Magnesium Aluminum Silicate Hydroxide	0.148	4	
TRUE	00-029-0701	Iron Magnesium Aluminum Silicate Hydroxide	0.291	7	
TRUE	00-006-0256	Mercury Sulfide	0.438	11	
TRUE	01-075-4299	Copper Oxide	0.178	4	8.43
TRUE	00-012-0158	Lead Uranyl Phosphate Hydroxide Hydrate	0.1	2	
		Potassium Magnesium Aluminum Silicate Hydroxide	0.136	3	
TRUE	00-021-0993	Hydroxide	0.14	3	3.33
TRUE	01-072-6229	Iron Oxide	0.066	2	
TRUE	00-017-0141	Strontium Aluminum Silicate Hydrate	0.173	4	9.02
TRUE	01-077-4387	Molybdenum Carbide	0.035	1	
TRUE	00-008-0087	Iron Oxide	0.505	12	
TRUE	00-051-2042	4-Aminotoluene-3-sulfonic acid	0.079	2	3.26
TRUE	01-078-4189	Titanium Oxide	0.041	1	4.85
TRUE	01-074-4133	Nickel Titanium Antimony Oxide			
		Potassium Sodium Niobium Titanium Silicate Hydroxide Oxide Hydrate	0.325	8	
TRUE	00-059-0600	Hydroxide Oxide Hydrate	1.399	34	7.43
TRUE	01-070-6796	Bismuth Arsenic Molybdenum Oxide			

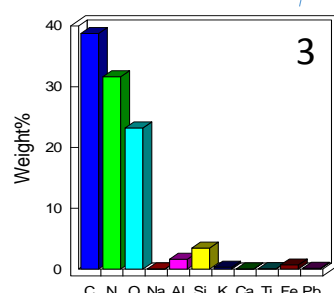
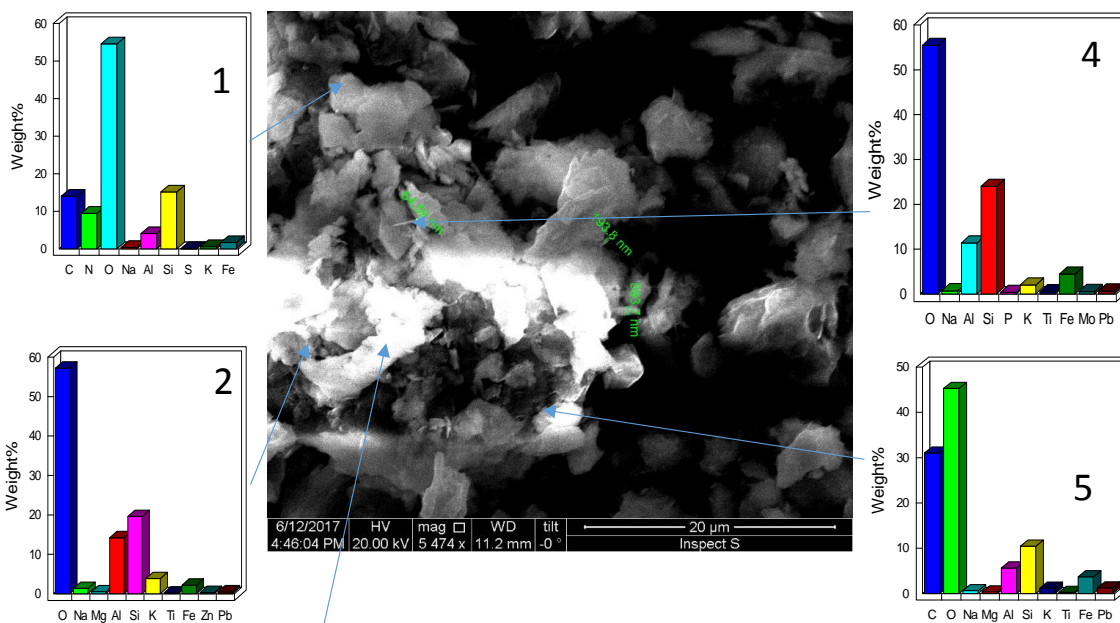
RB U/S C2

Accepted	PDF #	Compound Name	I Ratio	I%	I/Ic
TRUE	00-036-1450	Zinc Sulfide	0.041	1	
TRUE	01-070-7347	Titanium Oxide	0.055	1	3.62
TRUE	01-075-1686	Sodium Calcium Silicate	0.538	11	1.21
TRUE	01-070-7344	Silicon Oxide	1.241	26	3.05
TRUE	00-006-0263	Potassium Aluminum Silicate Hydroxide	0.347	7	
TRUE	00-026-0911	Potassium Aluminum Silicate Hydroxide	0.425	9	
TRUE	00-044-1407	Magnesium Manganese Zinc Hydroxide Hydrate	0.142	3	
TRUE	01-078-2492	Lead Iron Manganese Oxide	0.312	7	3.07
TRUE	01-074-4121	Iron Oxide	0.239	5	2.48
TRUE	00-015-0290	Iron Molybdenum Oxide Hydrate	0.136	3	
TRUE	00-029-0701	Iron Magnesium Aluminum Silicate Hydroxide	0.368	8	
TRUE	01-083-1556	Iron Copper Hydroxide Arsenate Hydrate	0.37	8	1.75
TRUE	01-086-1707	Calcium Aluminum Silicate	0.485	10	0.57

Appendix 4.d Selected SEM data

4.d.1 Sample WM K4

SEM image with foliate particles with a phyllosilicate composition, high content of C, O and sometime N (1 and 3) which may indicate an high content in organic matter. Zinc and Pb are present associated with phyllosilicate composition (2,3 and 5), and high concentration of P and Mo (5). Small particles dimensions are indicated in the image (600 – 64 nm).



Element	Weight%	Weight%	Atomic%
		Sigma	
CK	38.77	7.53	45.17
NK	31.65	8.16	31.62
OK	23.23	3.58	20.31
NaK	0.04	0.03	0.03
AlK	1.61	0.24	0.84
SiK	3.45	0.52	1.72
KK	0.31	0.05	0.11
CaK	0.03	0.02	0.01
TiK	0.07	0.02	0.02
FeK	0.68	0.11	0.17
PbM	0.15	0.04	0.01
Totals	100.00		

1

Element	Weight%	Weight%	Atomic%
		Sigma	
CK	14.03	5.00	19.44
NK	9.48	5.55	11.26
OK	54.57	4.62	56.76
NaK	0.36	0.10	0.26
AlK	4.07	0.36	2.51
SiK	15.14	1.29	8.97
SK	0.06	0.05	0.03
KK	0.61	0.08	0.26
FeK	1.68	0.18	0.50
Totals	100.00		

2

Element	Weight%	Weight%	Atomic%
		Sigma	
OK	57.25	0.63	71.10
NaK	1.36	0.32	1.17
MgK	0.51	0.17	0.42
AlK	14.22	0.29	10.47
SiK	19.62	0.35	13.88
KK	3.86	0.16	1.96
TiK	0.19	0.09	0.08
FeK	2.18	0.17	0.78
ZnK	0.33	0.19	0.10
PbM	0.48	0.22	0.05
Totals	100.00		

4

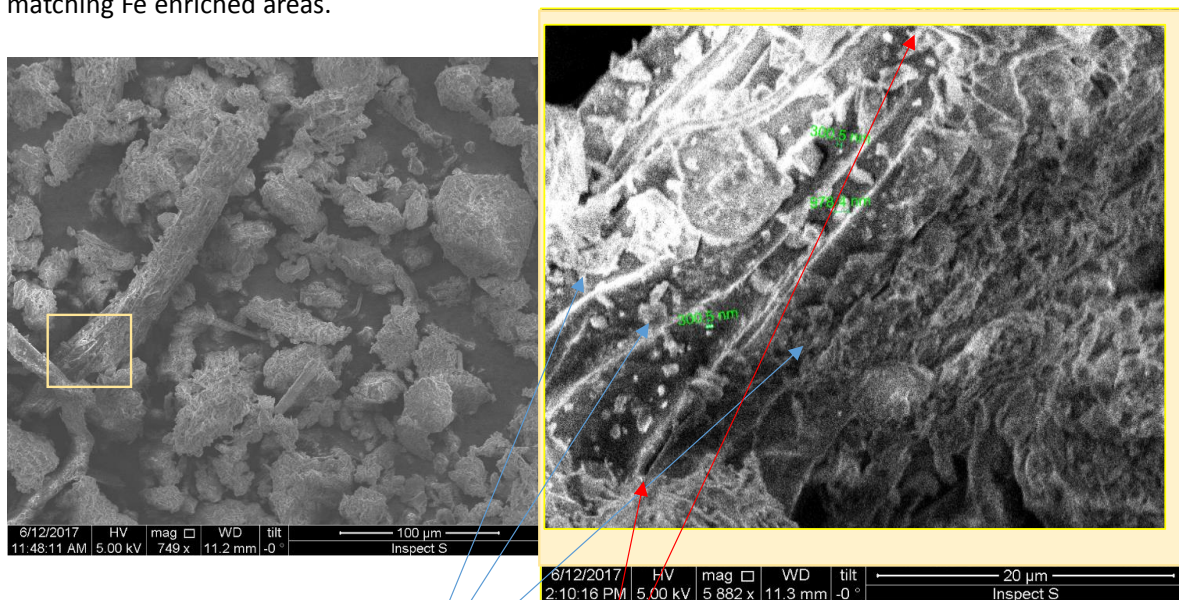
Element	Weight%	Weight%	Atomic%
		Sigma	
OK	55.44	0.68	70.25
NaK	0.70	0.18	0.62
AlK	11.39	0.27	8.55
SiK	23.99	0.42	17.32
PK	0.34	0.15	0.22
KK	1.99	0.13	1.03
TiK	0.52	0.11	0.22
FeK	4.43	0.24	1.61
MoL	0.54	0.32	0.11
PbM	0.66	0.33	0.06
Totals	100.00		

5

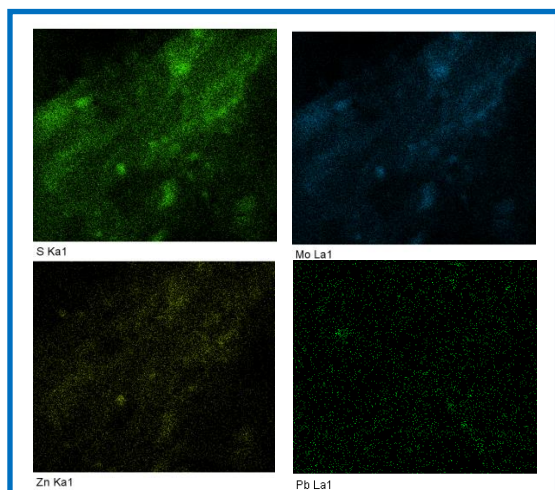
Element	Weight%	Weight%	Atomic%
		Sigma	
CK	31.04	6.06	42.00
OK	45.33	4.09	46.04
NaK	0.64	0.18	0.45
MgK	0.38	0.15	0.26
AlK	5.67	0.55	3.41
SiK	10.48	0.96	6.06
KK	1.20	0.16	0.50
TiK	0.27	0.11	0.09
FeK	3.72	0.41	1.08
PbM	1.27	0.28	0.10
Totals	100.00		

4.d.2 Sample TO M1

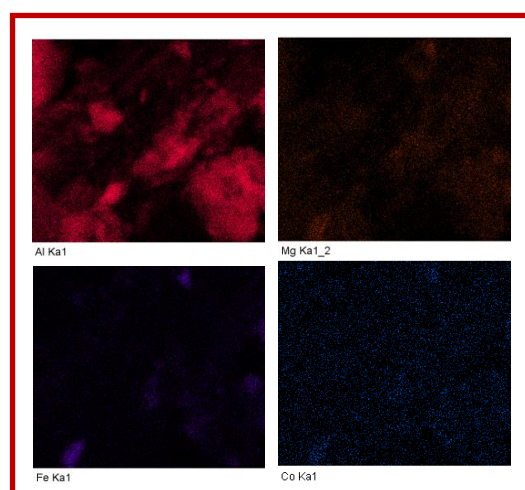
SEM image and chemical map showing a piece of root and grains formed by the agglomeration of small foliate particles or angular grains (such as phyllosilicate and quartz). Zinc and Pb small grains are trapped in the root and associate with Mo minerals likely Mo sulphates. Cobalt is spotted in trace matching Fe enriched areas.



Mo sulphates with Zn, Pb and Na

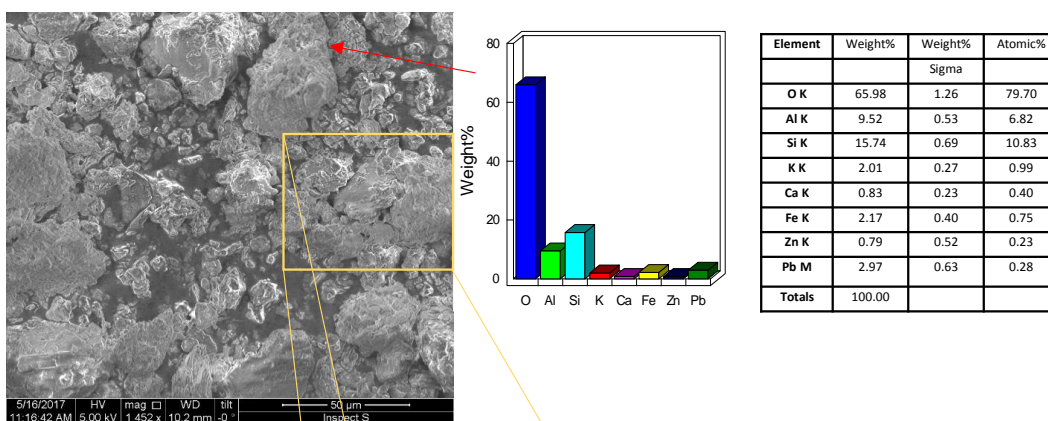


Phyllosilicate showing Co in association with Fe



4.d.3 Sample GG L1

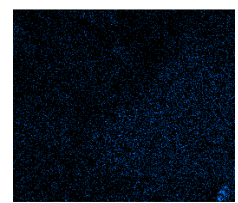
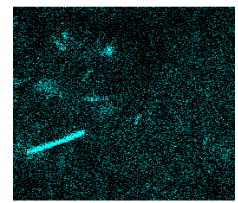
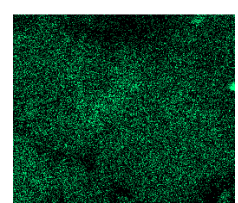
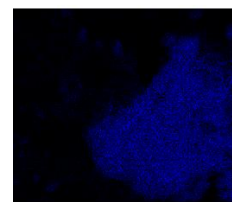
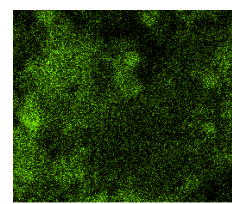
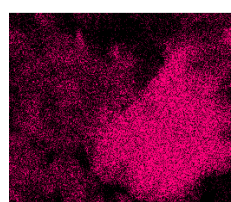
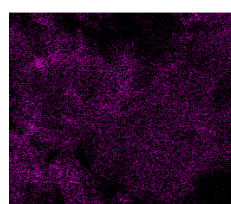
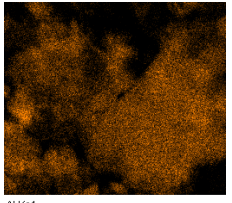
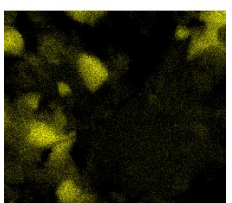
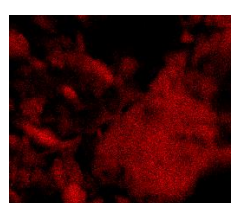
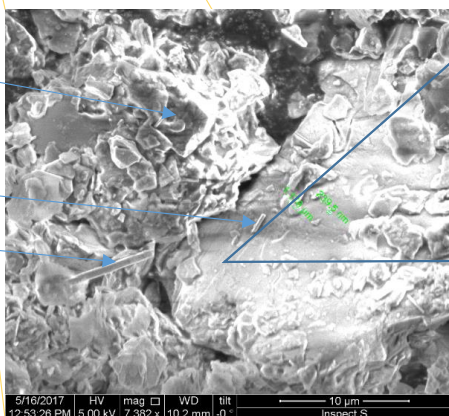
SEM image showing grains of different size and structure: foliate grains (likely K – Mg phyllosilicates) and subangular grains (likely quartz). Moreover, rutile (TiO₂) may be recognised in elongate grains. The composition spotted in a grain, with significant Zn and Pb content, is reported at the top of the sketch.

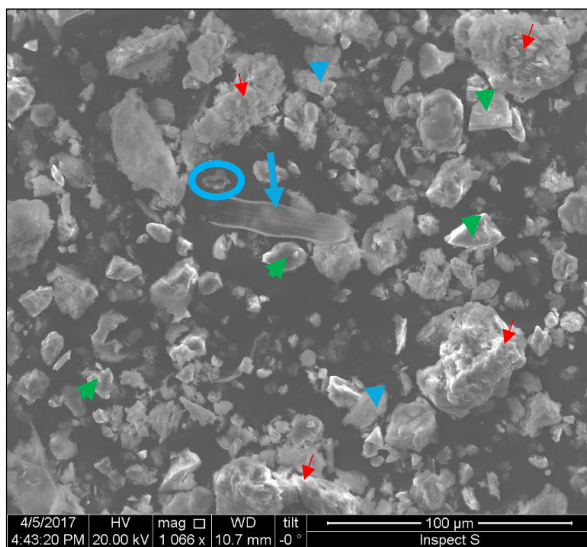


Quartz is present in well shaped grain.

TiO₂ is present as elongated particles of various size (10 μm to sub colloidal size).

Iron and Mn (likely in oxide or sulfate phases) may be covering, as an amorphous layer, clay mineralas.





4.d.4 Sample DC F2

SEM image showing an overview of particles and grains. Three different kind of particles care observed:

i) Particle 1

Organic matter (organism detritus as diatoms)

ii) Particles 2

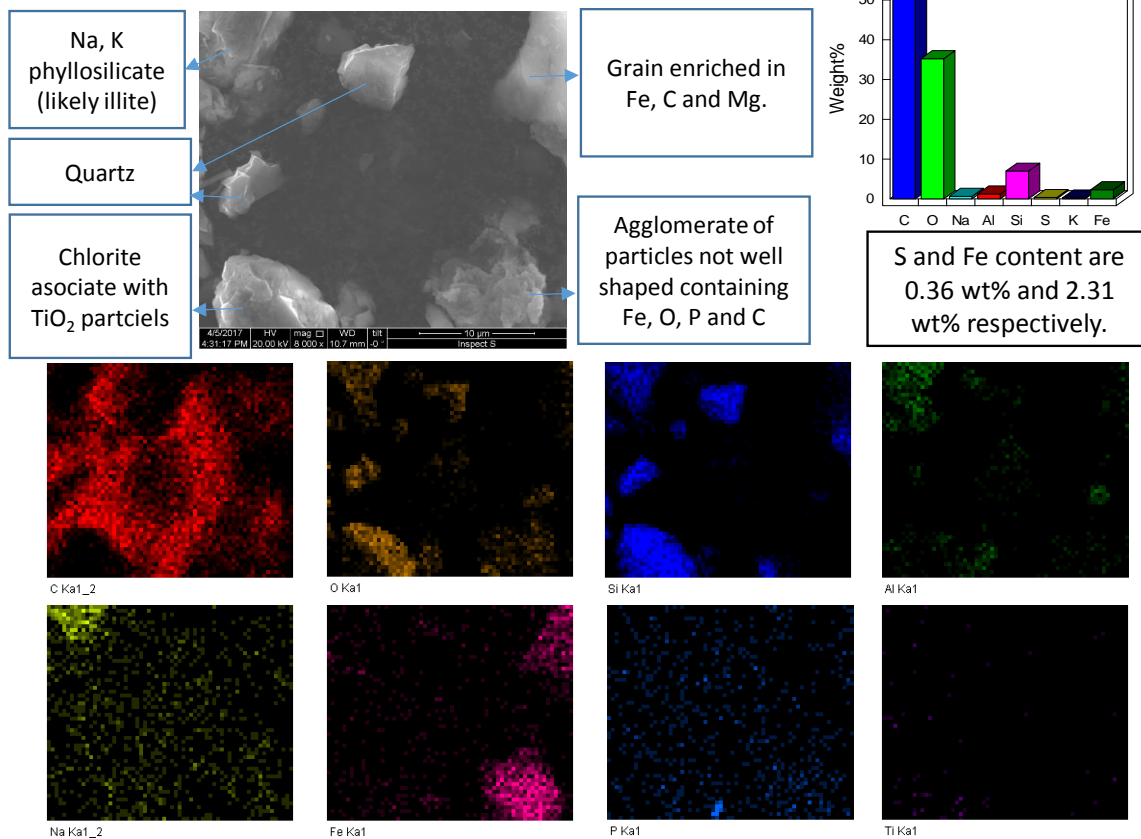
50-100 μm particles composed of small angular and flat particles (likely illite or chlorite minerals)

iii) Particle 3

<50 um angular particles, likely quartz, with few smaller particles (about 5μm) attached on the surface.

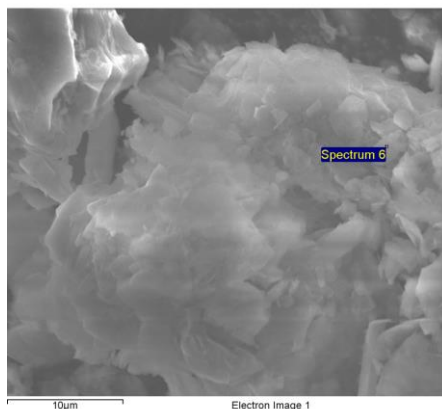
4.d.5 Sample DC F2

Image and chemical map showing element association and mineral morphology.



4.d.6 Sample DC F2

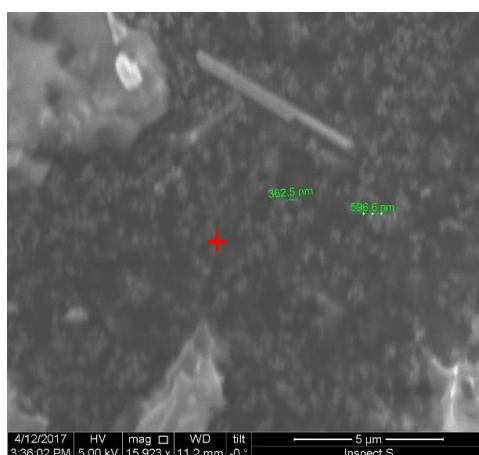
Image showing a foliate grain of clay containing As and Pb. They can be directly associate to the clay mineral or forming nanominerals with S and P which contents are reported in the table.



Element	Weight%	Weight%	Atomic%
		Sigma	
C K	18.25	1.15	27.50
O K	46.04	0.73	52.08
Na K	0.82	0.07	0.64
Al K	10.62	0.19	7.13
Si K	15.94	0.27	10.27
P K	0.22	0.05	0.13
S K	0.50	0.07	0.28
K K	2.10	0.07	0.97
Fe K	2.03	0.10	0.66
As L	0.19	0.10	0.05
Pb M	3.29	0.23	0.29
Totals	100.00		

4.d.7 Sample DC F1d

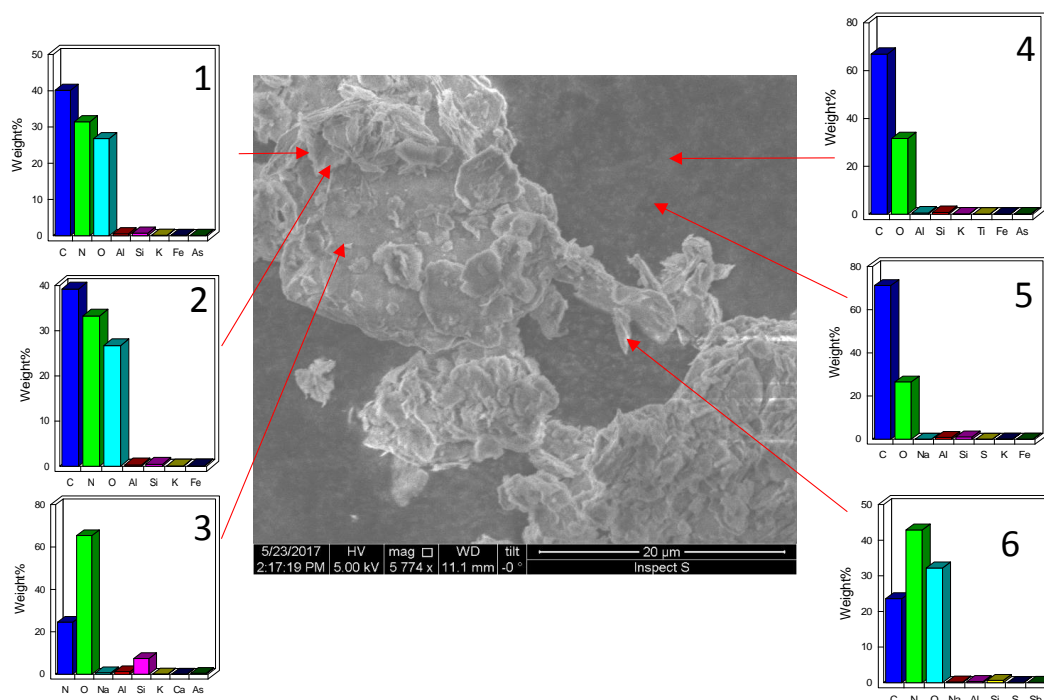
Image showing 1) nanoparticles size (300-500 nm); 2) Table reporting S associate with clay.



Element	Weight%	Weight%	Atomic%
		Sigma	
C K	78.05	0.80	83.89
O K	18.44	0.81	14.88
Na K	0.61	0.10	0.34
Al K	0.11	0.05	0.05
Si K	0.37	0.06	0.17
S K	0.63	0.07	0.26
Fe K	1.80	0.14	0.42
Totals	100.00		

4.d.8 Sample DK BK E7

SEM image showing foliate grains associated with smaller particles. In the background of the image particles of 500- 200 nm are observed (4,5). The EDS analysis suggest the presence of As and Sb within phyllosilicate particles.



1

Element	Weight%	Weight%	Atomic%
		Sigma	
C K	40.15	2.00	45.70
N K	31.44	2.98	30.69
O K	26.80	1.60	22.90
Al K	0.54	0.06	0.28
Si K	0.72	0.06	0.35
K K	0.14	0.03	0.05
Fe K	0.11	0.04	0.03
As L	0.10	0.06	0.02
Totals	100.00		

2

Element	Weight%	Weight%	Atomic%
		Sigma	
C K	39.22	1.50	44.51
N K	33.25	2.21	32.36
O K	26.69	1.23	22.74
Al K	0.29	0.03	0.15
Si K	0.42	0.04	0.21
K K	0.05	0.02	0.02
Fe K	0.07	0.03	0.02
Totals	100.00		

3

Element	Weight%	Weight%	Atomic%
		Sigma	
N K	24.56	4.45	28.31
O K	65.41	3.96	66.01
Na K	0.71	0.26	0.50
Al K	1.22	0.28	0.73
Si K	7.41	0.62	4.26
K K	0.13	0.10	0.05
Ca K	0.10	0.09	0.04
As L	0.46	0.37	0.10
Totals	100.00		

4

Element	Weight%	Weight%	Atomic%
		Sigma	
C K	66.90	0.90	73.34
O K	31.61	0.89	26.01
Al K	0.48	0.06	0.24
Si K	0.71	0.06	0.33
K K	0.10	0.03	0.03
Ti K	0.03	0.03	0.01
Fe K	0.05	0.05	0.01
As L	0.12	0.07	0.02
Totals	100.00		

5

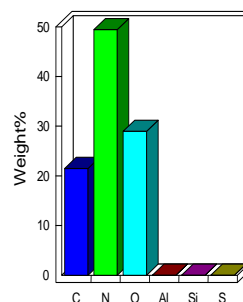
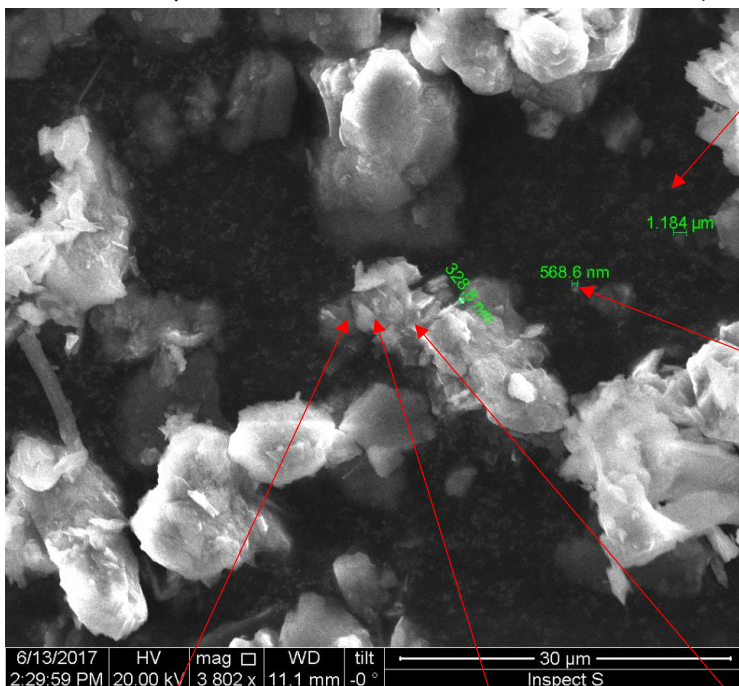
Element	Weight%	Weight%	Atomic%
		Sigma	
C K	71.26	1.11	77.35
O K	26.55	1.10	21.64
Na K	0.05	0.05	0.03
Al K	0.85	0.08	0.41
Si K	1.08	0.08	0.50
S K	0.03	0.02	0.01
K K	0.11	0.04	0.04
Fe K	0.06	0.06	0.01
Totals	100.00		

6

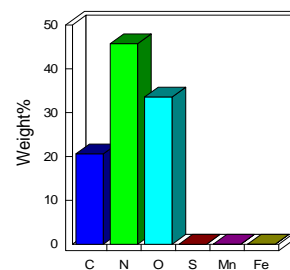
Element	Weight%	Weight%	Atomic%
		Sigma	
C K	23.60	0.96	27.73
N K	42.88	1.10	43.20
O K	32.22	0.91	28.42
Na K	0.21	0.05	0.13
Al K	0.34	0.04	0.18
Si K	0.65	0.05	0.32
S K	0.02	0.01	0.01
Sb L	0.09	0.05	0.01
Totals	100.00		

4.d.9 Sample RB U/S C1

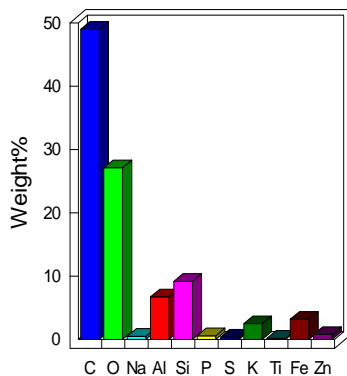
SEM image showing grains formed by the agglomeration of phyllosilicate particles. Their composition appears heterogeneous sometime bearing Zn, Pb and Mo. On the background colloids and nanoparticles may be present and associated to Fe, Mn and S (the element analysis is on the detection limit of the instrument).



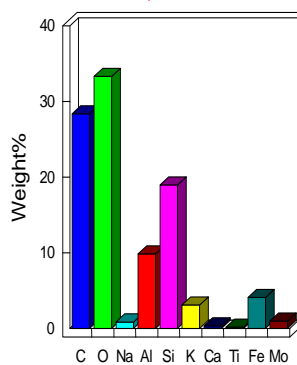
Element	Weight%	Weight%	Atomic%
		Sigma	
C K	21.49	0.20	25.09
N K	49.44	0.22	49.48
O K	28.99	0.18	25.40
Al K	0.03	0.01	0.02
Si K	0.03	0.01	0.02
S K	0.02	0.01	0.01
Totals	100.00		



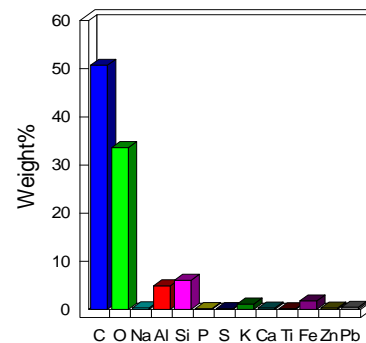
Element	Weight%	Weight%	Atomic%
		Sigma	
C K	20.61	0.53	24.23
N K	45.74	0.52	46.11
O K	33.59	0.40	29.64
S K	0.01	0.01	0.01
Mn K	0.02	0.02	0.01
Fe K	0.03	0.02	0.01
Totals	100.00		



Element	Weight%	Weight%	Atomic%
		Sigma	
C K	48.99	2.27	62.41
O K	27.11	1.38	25.93
Na K	0.49	0.13	0.33
Al K	6.72	0.32	3.81
Si K	9.15	0.43	4.99
P K	0.57	0.08	0.28
S K	0.36	0.06	0.17
K K	2.48	0.14	0.97
Ti K	0.16	0.07	0.05
Fe K	3.19	0.20	0.87
Zn K	0.77	0.17	0.18
Totals	100.00		



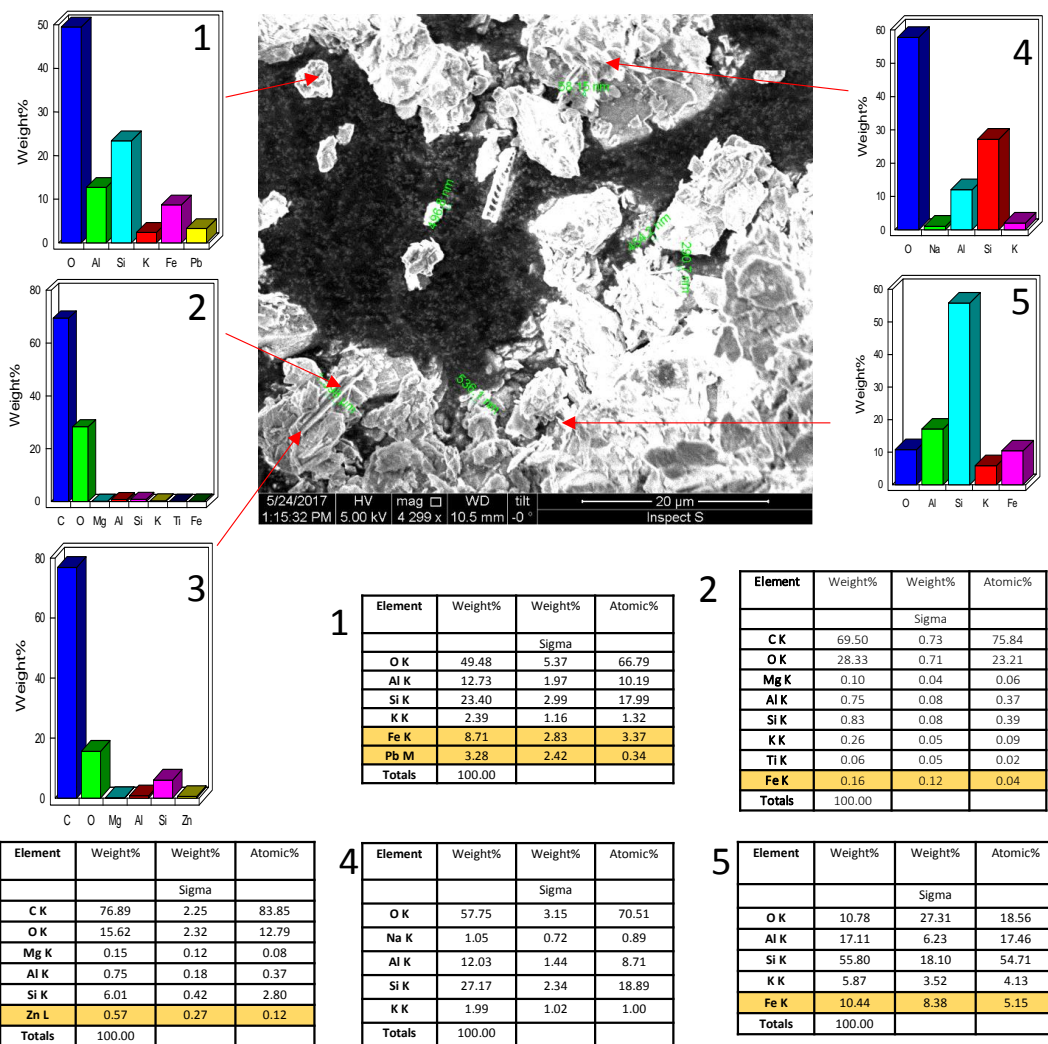
Element	Weight%	Weight%	Atomic%
		Sigma	
C K	28.37	47.30	41.47
O K	33.31	22.02	36.55
Na K	0.85	0.57	0.65
Al K	9.84	6.50	6.40
Si K	18.96	12.52	11.85
K K	3.11	2.05	1.39
Ca K	0.35	0.24	0.15
Ti K	0.16	0.13	0.06
Fe K	4.08	2.70	1.28
Mo L	0.97	0.67	0.18
Totals	100.00		



Element	Weight%	Weight%	Atomic%
		Sigma	
C K	50.75	6.78	61.91
O K	33.62	4.67	30.79
Na K	0.31	0.11	0.20
Al K	4.89	0.68	2.66
Si K	6.05	0.84	3.16
P K	0.16	0.04	0.08
S K	0.16	0.04	0.07
K K	1.12	0.16	0.42
Ca K	0.30	0.05	0.11
Ti K	0.13	0.04	0.04
Fe K	1.77	0.25	0.46
Zn K	0.29	0.09	0.06
Pb M	0.44	0.11	0.03
Totals	100.00		

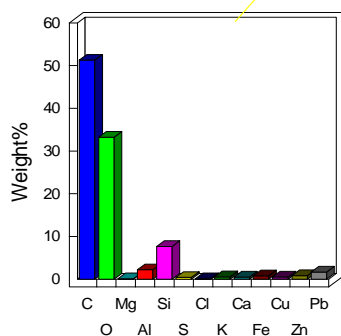
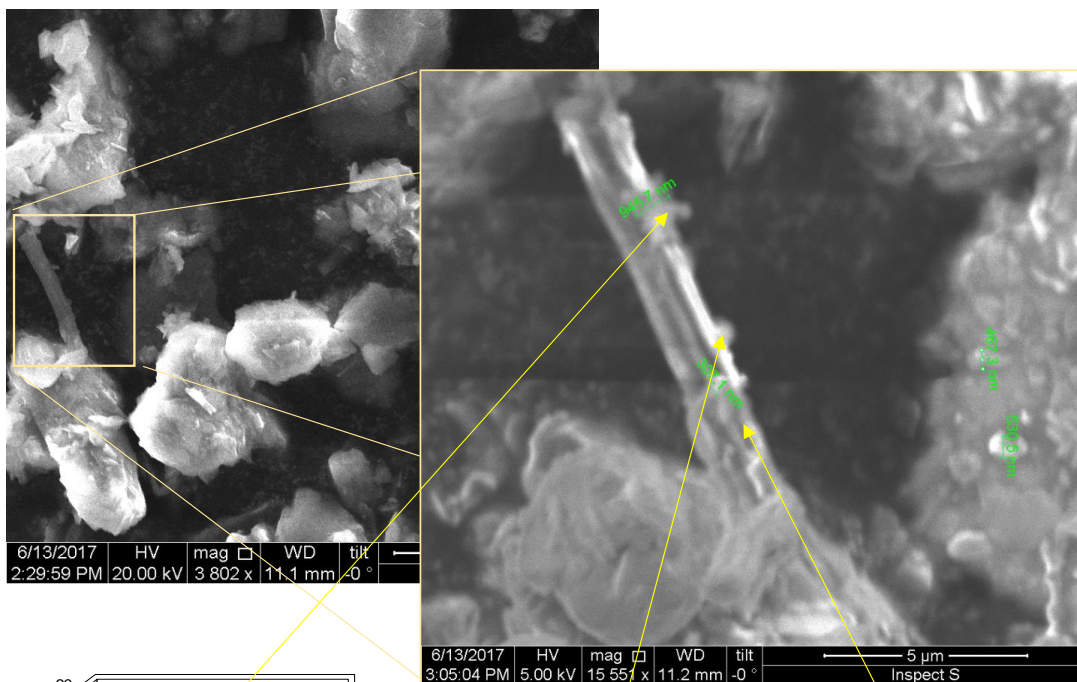
4.d.10 Sample RB U/S C2

SEM image showing different kind of grain from 20 μm to 60 nm including foliate grains, subangular grains, organic matter such as diatomes and pieces of roots. The latest can trap small clay particles (2,3).

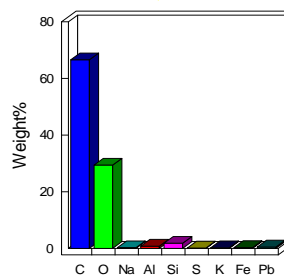


4.d.11 Sample RB U/S C1

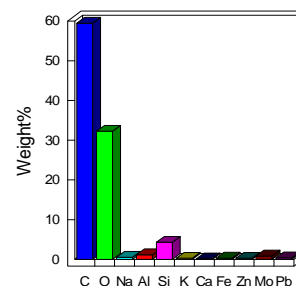
Detail of particles trapped in a piece of root. They are likely to be phyllosilicate associated with S, Mo, Pb, Zn and Cu.



Element	Weight%	Weight%	Atomic%
		Sigma	
CK	51.28	19.21	62.83
OK	33.24	13.15	30.57
MgK	0.12	0.09	0.07
AlK	2.22	0.88	1.21
SiK	7.67	3.03	4.02
SK	0.44	0.19	0.20
ClK	0.13	0.09	0.05
KK	0.56	0.23	0.21
CaK	0.51	0.21	0.19
FeK	0.80	0.33	0.21
ZnK	0.53	0.25	0.12
CuK	0.84	0.38	0.19
PbM	1.68	0.70	0.12
Totals	100.00		



Element	Weight%	Weight%	Atomic%
		Sigma	
CK	66.60	2.41	73.87
OK	29.41	2.29	24.49
NaK	0.24	0.13	0.14
AlK	0.80	0.12	0.39
SiK	1.82	0.17	0.86
SK	0.15	0.09	0.06
KK	0.23	0.08	0.08
FeK	0.27	0.12	0.07
PbM	0.48	0.23	0.03
Totals	100.00		



Element	Weight%	Weight%	Atomic%
		Sigma	
CK	59.47	11.96	68.58
OK	32.27	9.57	27.94
NaK	0.54	0.22	0.32
AlK	1.15	0.35	0.59
SiK	4.31	1.27	2.13
KK	0.29	0.10	0.10
CaK	0.14	0.06	0.05
FeK	0.32	0.12	0.08
ZnK	0.28	0.14	0.06
MoL	0.85	0.30	0.12
PbM	0.39	0.20	0.03
Totals	100.00		

Appendix 5.a Streamflow range (Q) from gauge station and floodplain sample site (RB)

Database name:	UK National River Flow Archive	PhD Research Dataset
Station ID	63001	Floodplain (RB)
Station Name	Ystwyth at Pont Llolwyn	Magwr at B4340
Grid Reference	SN5902477289	SN6639273880
Date first	01/10/1963	09/06/2016
Date last	30/09/2017	16/10/2017

Flow type

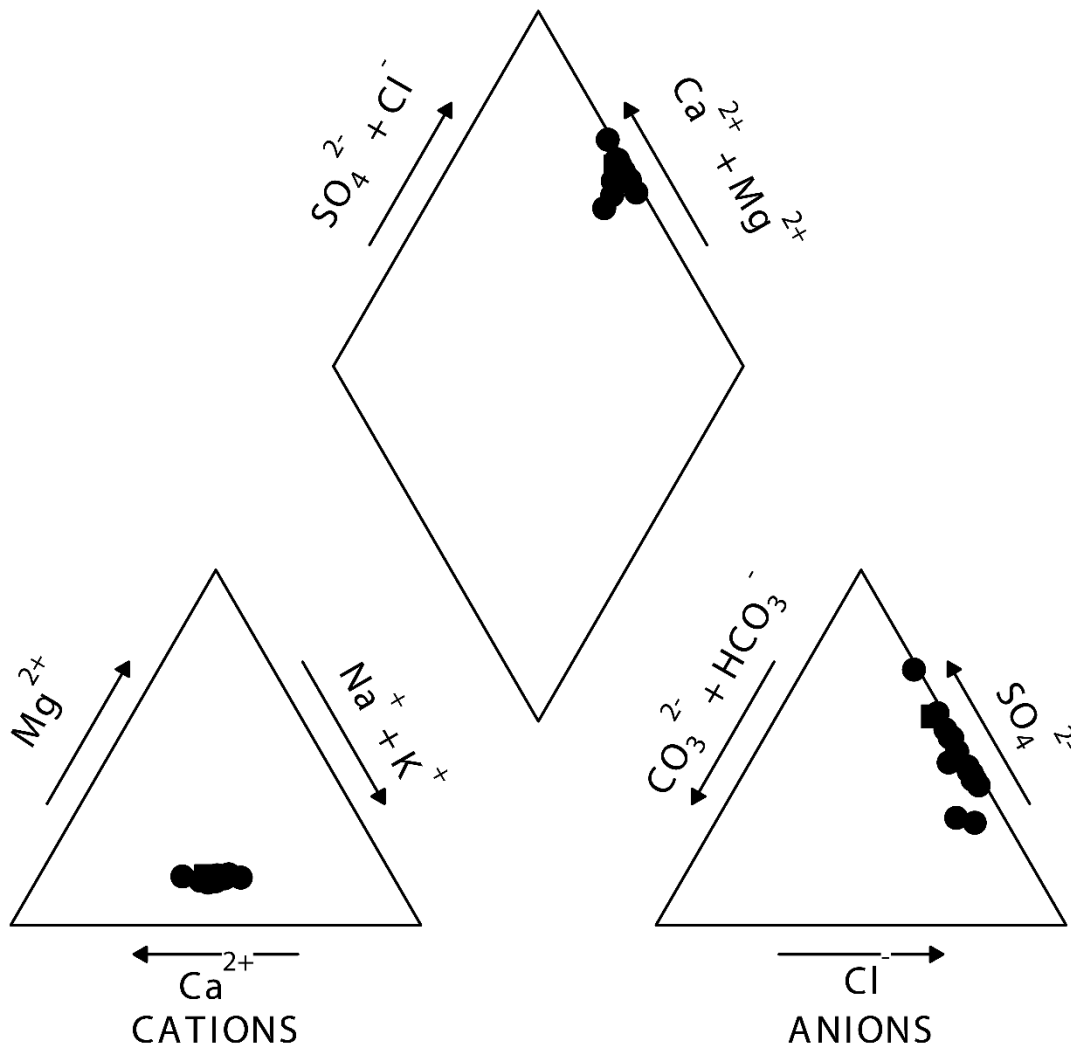
<i>vHF</i>	Very high flow (Q<5)
<i>HF</i>	High flow (Q<25)
<i>MF</i>	Medium flow (Q<75)
<i>LF</i>	Low flow (Q>75)

Date	Station 63001				Station RB				
	m3/s	percentile	Q d/s	Flow	m3/s	Percentile	Q RB	Flow	Used Range
09/06/2016	0.829	0.09	91	LF					LF
15/06/2016	15.5	0.912	8.8	HF	2.506	1	0	vHF	vHF
16/06/2016	14.9	0.905	9.5	HF					
17/06/2016	15.7	0.914	8.6	HF	1.496	0.857	14	HF	HF
18/07/2016	8.78	0.791	20.9	HF					
19/07/2016	5.68	0.671	32.9	MF	0.9	0.714	29	MF	MF
26/07/2016	4.15	0.571	42.9	MF					MF
27/07/2016	13.5	0.887	11.3	HF					
30/07/2016	3.88	0.548	45.2	MF					MF
05/09/2016	12.2	0.866	13.4	HF					
15/07/2017	2.376	0.366	63.4	MF	0.111	0	100	LF	LF
16/07/2017	4.145	0.571	42.9	MF					
28/07/2017	8.043	0.77	23	HF	0.157	0.142	86	LF	LF
29/07/2017	5.051	0.634	36.6	MF					
30/07/2017	5.445	0.657	34.3	MF	0.320	0.241	76	LF	LF
21/08/2017	13.68	0.889	11.1	HF	0.665	0.428	57	MF	MF
11/09/2017	38.75	0.991	0.9	vHF	0.849	0.571	43	MF	MF
12/09/2017	25.58	0.97	3	vHF					
16/10/2017	n/a				0.394	0.285	72	MF	MF

Appendix 5.b Streamflow (l/s) measured at sample sites (m).

DATE	FLOW	0 m	171 m	739 m	880 m	1314 m	1645 m	2614 m	3210 m	4640 m	5930 m	6780 m
09/06/2016	LF	4					32					
16-17/06/2016	HF			219	429	645	599		952		1496	
15/06/2016	vHF		214								2506	
18-19/07/2016	MF										900	1720
27/07/2016	HF				66		124		150			
30/07/2016	MF		29	39	86	134	146	203				
05/09/2016	LF	14			79			184				
15-16/07/2017	LF	20			73			46			111	
					67							
28-29- 30/07/2017	LF	30	39		129	failed	159	150	125	232	320	309
21/08/2017	MF						292				665	
12/09/2017	MF	81			220		364		484		849	
16/10/2017	MF										394	

Appendix 5.c Piper diagram of river water elaborated with GW_chart (USGS website)



Appendix 5.d Metal concentrations and loads derived from the continuous tracer injection (30/07/2016, MF)

Key: FA: filtrated acidifies, RA unfiltered acidified, SD, standard deviation, LOD: limit of detection, St: standard, %RSD relative standard deviation, n.a.: not analysed, LBI: left bank inflow, RBI: right bank inflow.

Sample	Distance m	Zn	Zn	Pb	Pb	Fe	Fe
		mg/l FA	mg/l RA	µg/l FA	mg/l RA	mg/l FA	mg/l RA
<i>River samples</i>							
Correlation Coefficient:		1.000	1.000	1.00	0.999	1.000	1.000
Blank Average		n.a.	n.a.	0.00	0.007	0.005	0.005
SD Blank		n.a.	n.a.	0.00	0.000	0.002	0.002
LOD		n.a.	n.a.	0.01	0.007	0.012	0.012
SD St2		0.044	0.044	0.18	0.014	0.015	0.015
%RSD		4.6	4.6	0.02	7.3	7.8	7.8
D17-CMD 0 A-T0	0	n.a.	0.039	5.66	n.a.	0.082	0.167
D17-CMD 0 B	2	n.a.	0.037	5.79	n.a.	0.079	0.169
D17-CMD 1	52	0.387	0.488	18.02	n.a.	0.061	0.121
D17-CMD 1B	95	0.268	0.321	26.03	0.069	0.099	0.223
D17-CMD 2	162	0.704	0.802	24.19	0.037	0.079	0.144
D17-CMD 3a – T1	171	1.517	1.618	171.16	0.191	0.067	0.108
D17-CMD 3b	210	1.268	1.398	140.43	0.131	0.047	0.062
D17-CMD 4	262	1.131		117.54		0.060	
D17-CMD 5	292	1.071	1.183	115.66	0.118	0.039	0.038
D17-CMD 6	533	0.997	1.142	108.56	0.134	0.029	0.062
D17-CMD 7	739	1.056	1.061	112.43	0.130	0.043	0.060
D17-CMD 8	847	1.063	1.061	108.92	0.126	0.048	0.063
D17-CMD 9 – T2	880	2.888	2.981	126.86	0.206	0.032	0.112
D17-CMD 10	924	2.901	2.915	122.26	0.189	0.027	0.110
D17-CMD 11	1000	2.810	2.856	112.23	0.177	0.028	0.098
D17-CMD 12	1131	2.731	2.795	109.56	0.164	0.027	0.088
D17-CMD 13	1148	2.111	2.148	71.91	0.114	0.043	0.107
D17-CMD 14	1314	1.928	1.988	63.51	0.099	0.045	0.088
D17-CMD 15	1349	1.917	1.980	62.45	0.086	0.051	0.091
D17-CMD 16a-T3	1645	1.953	1.992	61.26	0.094	0.043	0.078
D17-CMD 16b	1830	2.102	2.131	57.87	0.092	0.043	0.096
D17-CMD 17	1932	2.123	2.138	57.52	0.085	0.044	0.083
D17-CMD 18	1961	2.097	2.133	55.04	0.086	0.044	0.067
D17-CMD 19	2341	2.013	2.061	53.16	0.068	0.037	0.074
D17-CMD 20	2539	1.962	2.016	49.12	0.081	0.034	0.078
D17-CMD 21-T4	2614	1.656	1.654	38.20	0.062	0.032	0.063

Sample	Distance	Mn	Mn	Al	Al	Co	Cu	Cd	SO4
	m	µg/l	mg/l	mg/l	mg/l	µg/l	µg/l	µg/l	mg/l
<i>River samples</i>		FA	RA	FA	RA	FA	FA	FA	F
<i>Correlation Coefficient:</i>		1.00	1.000	1.000	1.000	1.000	1.00	1.00	0.989
<i>Blank Average</i>		0.01	0.001	n.a.	n.a.	0.001	0.00	0.00	0.000
<i>SD Blank</i>		0.01	0.000	n.a.	n.a.	0.005	0.02	0.02	0.000
<i>LOD</i>		0.05	0.001	n.a.	n.a.	0.017	0.06	0.06	0.000
<i>SD St2</i>		0.23	0.015	0.011	0.011	0.024	0.27	0.27	0.158
<i>%RSD</i>		0.02	8.0	5.7	5.7	0.0	0.03	0.03	1.6
<i>D17-CMD 0 A-T0</i>	0	5.53	0.013	0.035	0.044	0.070	0.16	0.04	3.058
<i>D17-CMD 0 B</i>	2	5.73	0.014	0.035	0.040	0.070	0.28	0.03	n.a.
<i>D17-CMD 1</i>	52	6.64	0.009	0.033	0.034	0.150	0.31	0.84	0.996
<i>D17-CMD 1B</i>	95	7.00	0.022	0.047	0.051	0.130	0.50	0.58	n.a.
<i>D17-CMD 2</i>	162	7.97	0.014	0.030	0.034	0.170	0.71	1.52	5.418
<i>D17-CMD 3a-T1</i>	171	9.33	0.010	0.043	0.028	0.410	2.27	3.44	7.111
<i>D17-CMD 3b</i>	210	7.94	0.008	0.032	0.031	0.350	1.73	2.96	6.727
<i>D17-CMD 4</i>	262	6.98		0.026		0.300	1.86	2.64	6.767
<i>D17-CMD 5</i>	292	6.56	0.006	n.a.	0.031	0.280	1.43	2.42	6.756
<i>D17-CMD 6</i>	533	5.97	0.007	0.016	0.029	0.270	1.31	2.31	6.499
<i>D17-CMD 7</i>	739	5.37	0.006	0.036	0.037	0.250	1.28	2.43	6.403
<i>D17-CMD 8</i>	847	5.33	0.006	0.035	n.a.	0.250	1.27	2.17	6.540
<i>D17-CMD 9-T2</i>	880	11.29	0.014	0.033	0.053	1.060	1.69	4.90	12.143
<i>D17-CMD 10</i>	924	10.72	0.013	0.037	0.055	1.040	1.48	4.88	12.797
<i>D17-CMD 11</i>	1000	9.83	0.012	n.a.	0.040	0.970	1.31	4.71	12.351
<i>D17-CMD 12</i>	1131	9.57	0.011	0.031	0.031	0.960	1.42	4.74	12.475
<i>D17-CMD 13</i>	1148	8.64	0.021	n.a.	0.038	0.730	1.04	3.61	10.159
<i>D17-CMD 14</i>	1314	8.21	0.021	0.030	0.033	0.660	0.85	3.29	9.673
<i>D17-CMD 15</i>	1349	8.58	0.024	0.037	0.032	0.640	0.81	3.20	9.811
<i>D17-CMD 16a-T3</i>	1645	7.68	0.017	n.a.	0.033	0.590	0.77	3.29	9.024
<i>D17-CMD 16b</i>	1830	7.48	0.016	0.027	0.032	0.550	0.73	3.53	10.135
<i>D17-CMD 17</i>	1932	7.75	0.015	0.019	0.029	0.580	0.80	3.69	10.070
<i>D17-CMD 18</i>	1961	7.57	0.014	0.030	0.026	0.550	0.72	3.57	9.869
<i>D17-CMD 19</i>	2341	7.44	0.014	0.037	0.028	0.530	0.71	3.43	10.013
<i>D17-CMD 20</i>	2539	7.20	0.015	0.018	0.039	0.520	0.71	3.41	10.147
<i>D17-CMD 21-T4</i>	2614	6.12	0.011	0.037	n.a.	0.440	0.67	2.80	9.788

Sample	Distance m	Zn	Zn	Pb	Pb	Fe	Fe
		mg/l FA	mg/l RA	µg/l FA	mg/l RA	mg/l FA	mg/l RA
<i>Inflows</i>							
D17-RBI 1A	31	0.259	0.910	11.88	2.183	n.a.	1.156
D17-RBI 1B	40	1.667	1.865	59.16	0.059	n.a.	n.a.
D17-RBI 2(MR)	164	4.997	4.571	1027.00	1.466	0.009	0.134
D17-WM 1	167	3.700		0.28		0.049	
D17-WM 2	168	1.144		119.17		0.063	
D17-LBI T1 1A	202	n.a.		1.13		n.a.	
D17-LBI T1 B	203	n.a.		1.70		0.125	
D17-LBI 1 A	268	n.a.		4.62		n.a.	
D17-LBI 1 C	277	0.048		0.28		n.a.	
D17-LB POOL	654	0.006		2.44		n.a.	
D17-RBI 3 (FA)	862	3.908	3.977	123.35	0.223	0.015	0.130
D17-RBI 4	1141	0.007	0.010	7.29	n.a.	0.050	0.221
D17-LBI 3	1321	5.406	5.444	77.47	0.099	n.a.	0.023
tube 7	1896	8.514		1.12		n.a.	
tube 6	1896	4.461		0.60		n.a.	
tube 5	1896	0.864		0.95		n.a.	
tube 4	1884	0.849		0.98		n.a.	
tube 3	1871	0.421		1.33		0.007	
tube 2	1846	0.552		5.75		n.a.	
tube 1	1835	0.572		5.04		0.005	
D17-LBI 4	1947	0.009	0.002	5.81	n.a.	0.015	0.025
D17-RBI 5	2554	0.001	n.a.	0.73	n.a.	n.a.	0.035

Sample	Distance m	Mn	Mn	Al	Al	Co	Cu	Cd	SO4
		µg/l FA	mg/l RA	mg/l FA	mg/l RA	µg/l FA	µg/l FA	µg/l FA	mg/l F
<i>Inflows</i>									
D17-RBI 1A	31	0.45	0.371	n.a.	0.886	0.070	0.40	0.60	2.530
D17-RBI 1B	40	2.52	0.002	0.011	0.025	0.370	0.75	3.36	n.a.
D17-RBI 2(MR)	164	5.82	0.005	0.019	0.078	1.180	6.11	11.34	13.634
D17-WM 1	167	14.26		0.036		0.970	4.62	7.86	12.432
D17-WM 2	168	9.46		0.034		0.320	1.70	2.68	n.a.
D17-LBI T1 1A	202	0.98		n.a.		0.050	0.69	0.03	n.a.
D17-LBI T1 B	203	15.38		0.048		0.120	0.29	0.04	n.a.
D17-LBI 1 A	268	0.42		0.029		0.030	<0.06	0.10	n.a.
D17-LBI 1 C	277	0.50		n.a.		0.030	<0.06	0.05	n.a.
D17-LB POOL	654	1.19		n.a.		0.030	<0.06	0.08	n.a.
D17-RBI 3 (FA)	862	15.04	0.019	0.028	0.066	1.580	2.03	6.56	17.523
D17-RBI 4	1141	0.49	0.064	n.a.	0.032	0.030	<0.06	0.02	n.a.
D17-LBI 3	1321	8.69	0.009	n.a.	0.020	1.540	1.34	7.06	n.a.
tube 7	1896	0.59		0.027		0.020	0.26	14.74	20.696
tube 6	1896	0.35		0.020		0.020	0.26	4.14	12.943
tube 5	1896	0.66		0.034		0.030	<0.06	0.55	7.790
tube 4	1884	0.65		n.a.		0.030	<0.06	0.56	7.684
tube 3	1871	0.19		0.026		0.030	<0.06	0.23	n.a.
tube 2	1846	0.88		n.a.		0.040	<0.06	1.12	n.a.
tube 1	1835	1.61		0.029		0.040	0.22	0.36	n.a.
D17-LBI 4	1947	0.89	0.003	0.036	0.039	0.030	0.18	0.06	n.a.
D17-RBI 5	2554	0.26	0.004	0.021	0.032	0.030	<0.06	0.01	8.584

Sample	Distance m	Q l/s	Fe		Zn		Pb		SO4
			mg/s	mg/s	mg/s	mg/s	mg/s	mg/s	
			FA	RA	FA	RA	FA	RA	F
<i>River samples</i>									
D17-CMD 1A	52	25.57	1.55	3.09	9.90	12.48	0.46	0.46	25.45
D17-CMD 1B	95	26.06	2.58	5.82	6.99	8.36	0.68	1.80	83.57
D17-CMD 2	162	26.10	2.07	3.75	18.38	20.93	0.63	0.95	141.42
D17-CMD 3a - T1	171	28.99	1.93	3.14	43.98	46.90	4.96	5.55	206.13
D17-CMD 3b	210	31.38	1.49	1.93	39.78	43.88	4.41	4.10	211.11
D17-CMD 4	262	32.70	1.95	1.63	36.99	42.20	3.84	4.06	221.29
D17-CMD 5	292	34.66	1.36	1.32	37.11	40.99	4.01	4.08	234.15
D17-CMD 6	533	36.45	1.05	2.27	36.34	41.63	3.96	4.90	236.90
D17-CMD 7	739	39.27	1.71	2.34	41.48	41.67	4.42	5.12	251.46
D17-CMD 8	847	39.51	1.90	2.48	41.98	41.91	4.30	4.98	258.40
D17-CMD 9 T2	880	86.31	2.74	9.64	249.22	257.31	10.95	17.78	1048.05
D17-CMD 10	924	88.02	2.37	9.65	255.35	256.56	10.76	16.65	1126.41
D17-CMD 11	1000	90.92	2.53	8.90	255.45	259.70	10.20	16.08	1122.90
D17-CMD 12	1131	91.02	2.42	8.05	248.56	254.44	9.97	14.91	1135.45
D17-CMD 13	1148	121.02	5.19	12.99	255.43	259.89	8.70	13.85	1229.38
D17-CMD 14	1314	134.08	6.01	11.75	258.56	266.56	8.52	13.23	1296.88
D17-CMD 15	1349	139.84	7.10	12.69	268.04	276.86	8.73	12.06	1372.02
D17-CMD 16a T3	1645	145.79	6.21	11.30	284.72	290.46	8.93	13.66	1315.54
D17-CMD 16b	1830	150.75	6.50	14.53	316.83	321.19	8.72	13.86	1527.85
D17-CMD 17	1932	154.47	6.86	12.80	327.86	330.24	8.89	13.15	1555.48
D17-CMD 18	1961	158.19	6.96	10.58	331.72	337.40	8.71	13.62	1561.28
D17-CMD 19	2341	160.19	5.95	11.78	322.43	330.10	8.52	10.91	1604.00
D17-CMD 20	2539	166.54	5.67	12.96	326.80	335.81	8.18	13.47	1689.97
D17-CMD 21	2614	202.76	6.57	12.71	335.82	335.29	7.75	12.66	1984.67

Appendix 5.e Metal concentrations, loads and streamflows estimated with slug injection in 2016

Sample	Date	Distance m	Q l/s	Zn	Zn	Pb	Pb	Fe	Fe	SO4
				mg/l FA	mg/l RA	µg/l FA	µg/l RA	mg/l FA	mg/l RA	mg/l F
D6 S3 MON	09/06/2016	0	4	0.35	0.44	8.4	105.4	0.06	1.05	0.00
D6 S2 MON	09/06/2016	1645	32	3.43	3.39	65.9	88.9	0.00	0.03	7.15
D7 S8 MON	15/06/2016	171	214	1.38	1.38	393.4	432.7	0.08	0.24	0.00
D7 S6 INJ	15/06/2016	5930	2506	1.61	3.55	30.9	2835.0	0.02	18.91	8.89
D7 S5 MON	15/06/2016	6780	875	0.86	0.92	11.1	52.6	0.03	0.47	9.21
D8 S13 MON	16/06/2016	739	219	1.14	1.14	132.3	165.7	0.03	0.08	1.35
D8 S12 MON	16/06/2016	880	429	2.97	3.02	115.3	158.7	0.02	0.13	10.72
D8 S11 MON	16/06/2016	1314	645	2.27	2.33	66.3	109.8	0.02	0.19	8.52
D8 S10 MON	16/06/2016	1645	599	2.30	2.29	50.4	94.9	0.05	0.16	2.96
D9 S16 MON	17/06/2016	3210	952	1.39	1.43	23.9	27.3	0.02	0.12	7.71
D9 S14 MON	17/06/2016	5930	1496	0.97	0.99	12.7	26.9	0.02	0.16	7.00
D10-S1MON	18/07/2016	6780	1720	1.04	1.04	0.0	0.0	0.01	0.02	8.45
D11-S2MON	19/07/2016	5930	900	1.03	1.05	0.0	0.0	0.02	0.01	8.55
D14-S3INJ	26/07/2016	4640	80	1.24	1.25	0.0	27.1	0.02	0.04	9.76
D14-S2MON	26/07/2016	5930	86	1.14	1.17	17.7	24.5	0.02	0.03	9.74
D15-S6MON	27/07/2016	880	66	2.08	2.16	132.9	169.5	0.12	0.19	10.21
D15-S5MON	27/07/2016	1645	124	1.30	1.34	102.0	154.8	0.14	0.23	6.48
D15-S4MON	27/07/2016	3210	150	1.08	1.13	83.8	125.6	0.13	0.24	0.00
D17-CMD 3a - T1	30/07/2016	171	28.99	1.517	1.618	171.2	191.5	0.067	0.108	7.111
D17-CMD 7	30/07/2016	739	39.27	1.056	1.061	112.4	130.3	0.043	0.060	6.403
D17-CMD 9 T2	30/07/2016	880	86.31	2.888	2.981	126.9	206.0	0.032	0.112	12.143
D17-CMD 14	30/07/2016	1314	134.08	1.928	1.988	63.5	98.7	0.045	0.088	9.673
D17-CMD 16a T3	30/07/2016	1645	145.79	1.953	1.992	61.3	93.7	0.043	0.078	9.024
D17-CMD 21	30/07/2016	2614	202.76	1.656	1.654	38.2	62.5	0.032	0.063	9.788
D19-T0A	05/09/2016	0	14	0.03	0.04	0.0	0.0	0.12	0.24	0.00
D19-T2A	05/09/2016	880	79	5.51	5.73	117.6	194.6	0.03	0.09	24.00
D19-T4A	05/09/2016	2614	184	2.91	3.00	49.7	67.3	0.04	0.08	15.26

Sample	Distance m	Zn	Zn	Pb	Pb	Fe	Fe	SO4
		mg/s FA	mg/s RA	µg/s FA	µg/s RA	mg/s FA	mg/s RA	mg/s F
D6 S3 MON	0	1	2	34	422	0	4	0
D6 S2 MON	1645	110	109	2109	2844	0	1	229
D7 S8 MON	171	295	295	84185	92603	17	51	0
D7 S6 INJ	5930	4027	8900	77460	7104510	47	47388	22280
D7 S5 MON	6780	755	805	9695	46043	23	407	8063
D8 S13 MON	739	250	249	28980	36297	7	18	295
D8 S12 MON	880	1276	1297	49464	68062	8	55	4599
D8 S11 MON	1314	1464	1503	42757	70839	13	120	5493
D8 S10 MON	1645	1375	1373	30184	56830	27	94	1770
D9 S16 MON	3210	1324	1363	22753	26034	17	116	7336
D9 S14 MON	5930	1452	1488	18969	40283	35	237	10472
D10-S1MON	6780	1786	1791	0	0	25	41	14533
D11-S2MON	5930	927	942	0	0	19	11	7698
D14-S3INJ	4640	99	100	0	2167	2	3	781
D14-S2MON	5930	98	101	1522	2106	2	2	838
D15-S6MON	880	137	143	8773	11184	8	13	674
D15-S5MON	1645	161	167	12654	19193	17	29	804
D15-S4MON	3210	163	169	12576	18838	19	37	0
D17-CMD 3a - T1	171	44	47	4962	5551	2	3	206
D17-CMD 7	739	41	42	4415	5119	2	2	251
D17-CMD 9 T2	880	249	257	10949	17782	3	10	1048
D17-CMD 14	1314	259	267	8515	13228	6	12	1297
D17-CMD 16a T3	1645	285	290	8931	13657	6	11	1316
D17-CMD 21	2614	336	335	7745	12662	7	13	1985
D19-T0A	0	0	0	0	0	2	3	0
D19-T2A	880	435	452	9292	15373	3	7	1896
D19-T4A	2614	535	553	9139	12381	7	15	2809

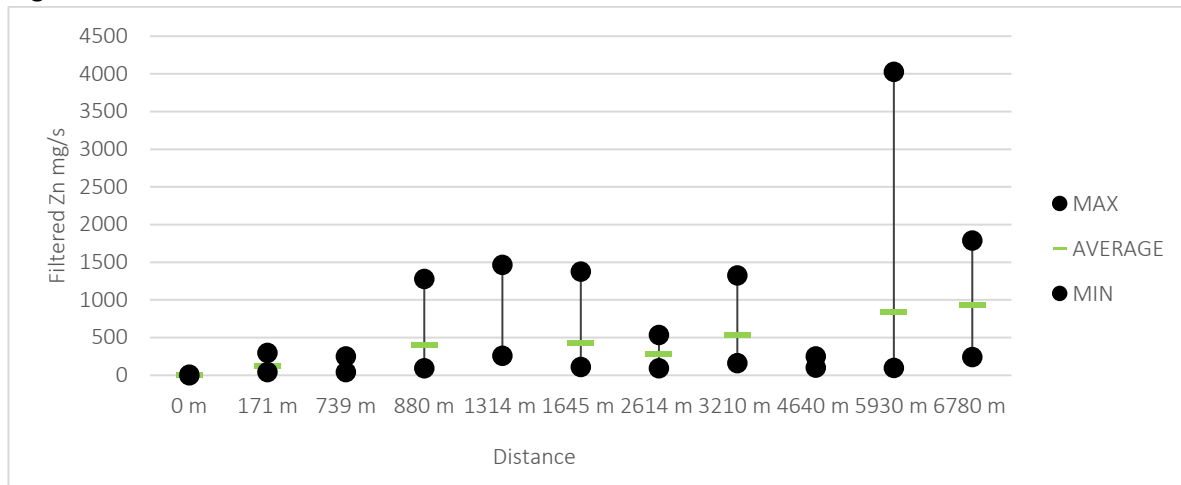
Appendix 5.f Metal concentrations, loads and streamflows estimated with slug injection in 2017

Sample	Date	Distance m	Q l/a	Zn	Zn	Pb	Pb	Fe	Fe	SO4
				mg/l	mg/l	µg/l	µg/l	mg/l	mg/l	mg/l
				FA	RA	FA	RA	FA	RA	F
D20 - S1	15/07/2017	5930	111	1.24	1.31	23.6	31.7	0.04	0.08	10.12
D21 -S5	16/07/2017	0	20	0.14	0.21	19.4	93.7	0.38	1.21	3.89
D21 -S3	16/07/2017	880	73	1.24	1.42	101.1	182.2	0.25	0.67	7.55
D22 -S5	28/07/2017	1645	159	0.92	1.25	49.9	248.0	0.13	1.25	5.67
D22 -S4	28/07/2017	2614	150	1.30	1.40	50.0	65.5	0.09	0.12	7.03
D22 -S3	28/07/2017	3210	125	1.28	1.57	33.3	71.6	0.04	0.16	8.49
D22 -S2	28/07/2017	4640	232	1.07	1.24	17.7	31.2	0.03	0.09	8.98
D22 -S1	28/07/2017	5930	157	1.01	1.18	11.7	24.7	0.03	0.09	9.19
D23 - S11	29/07/2017	0	30	0.19	0.24	34.9	47.7	0.13	0.52	4.04
D23 -S9	29/07/2017	171	39	1.10	1.27	131.2	177.4	0.11	0.26	6.38
D23 -S7	29/07/2017	880	129	1.81	2.01	78.1	137.1	0.09	0.23	9.43
D24 -S13	30/07/2017	5930	320	0.79	0.90	24.1	30.4	0.07	0.11	7.78
D24 -S12	30/07/2017	6780	309	0.79	0.95	19.8	45.2	0.06	0.20	7.84
D26 RB	21/08/2017	5930	665	0.69	0.85	10.8	23.0	0.04	0.14	7.97
D27 - GG	11/09/2017	1645	364	1.35	1.64	46.9	83.0	0.07	0.18	8.26
D27 -DC	11/09/2017	3210	484	1.08	1.35	32.0	67.0	0.06	0.22	8.27
D27 -RB	11/09/2017	5930	849	0.69	0.84	19.4	41.3	0.06	0.20	7.86
D28 - T0	12/09/2017	0	81	0.11	0.18	10.6	69.9	0.13	0.39	4.19
D28 - T2	12/09/2017	880	220	1.62	2.07	77.1	138.9	0.07	0.24	9.21
D29 -RB	16/10/2017	5930	394	0.89	0.96	13.5	26.8	0.04	0.14	9.31

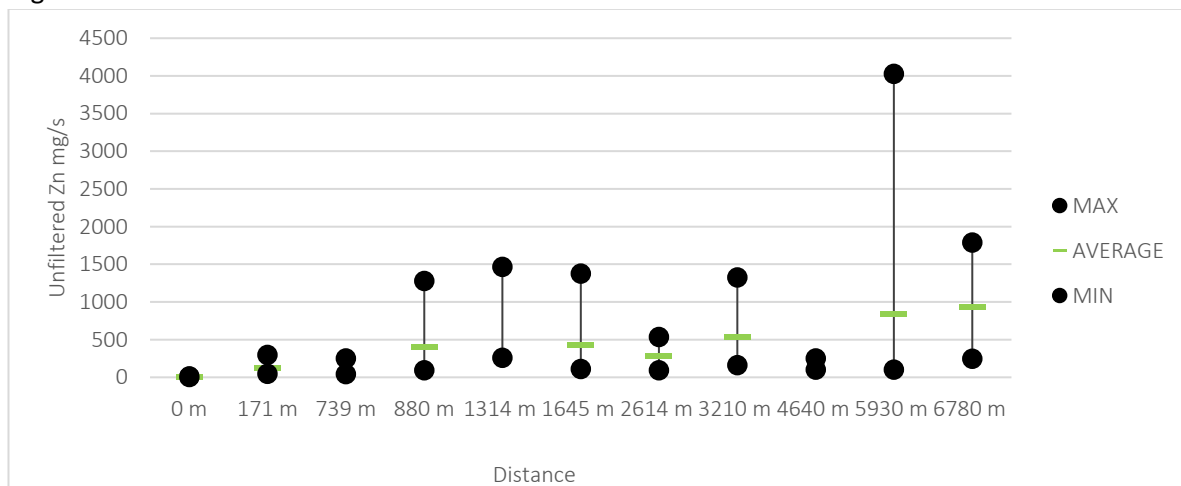
Sample	Distance m	Zn	Zn	Pb	Pb	Fe	Fe	SO4
		mg/s	mg/s	µg/s	µg/s	mg/s	mg/s	mg/s
		FA	RA	FA	RA	FA	RA	F
D20 - S1	5930	138	145	2622	3519	5	9	1123
D21 -S5	0	3	4	387	1874	8	24	78
D21 -S3	880	91	104	7384	13301	18	49	551
D22 -S5	1645	147	199	7937	39432	20	198	901
D22 -S4	2614	195	210	7498	9825	13	18	1055
D22 -S3	3210	160	196	4164	8950	5	20	1062
D22 -S2	4640	248	289	4117	7238	7	21	2084
D22 -S1	5930	158	186	1842	3878	5	14	1443
D23 - S11	0	6	7	1047	1431	4	16	121
D23 -S9	171	43	50	5118	6919	4	10	249
D23 -S7	880	233	259	10078	17686	11	30	1217
D24 -S13	5930	252	288	7718	9728	21	34	2490
D24 -S12	6780	243	293	6114	13967	18	61	2423
D26 RB	5930	457	566	7188	15295	23	95	5298
D27 - GG	1645	490	597	17059	30212	26	65	3007
D27 -DC	3210	525	653	15497	32428	28	107	4004
D27 -RB	5930	586	709	16450	35064	47	170	6674
D28 - T0	0	9	15	858	5662	10	32	340
D28 - T2	880	356	456	16962	30558	16	54	2025
D29 -RB	5930	350	377	5319	10559	15	55	3670

Appendix 5.g Minimum, maximum and average for Zn, Pb, Fe and SO4 loads.

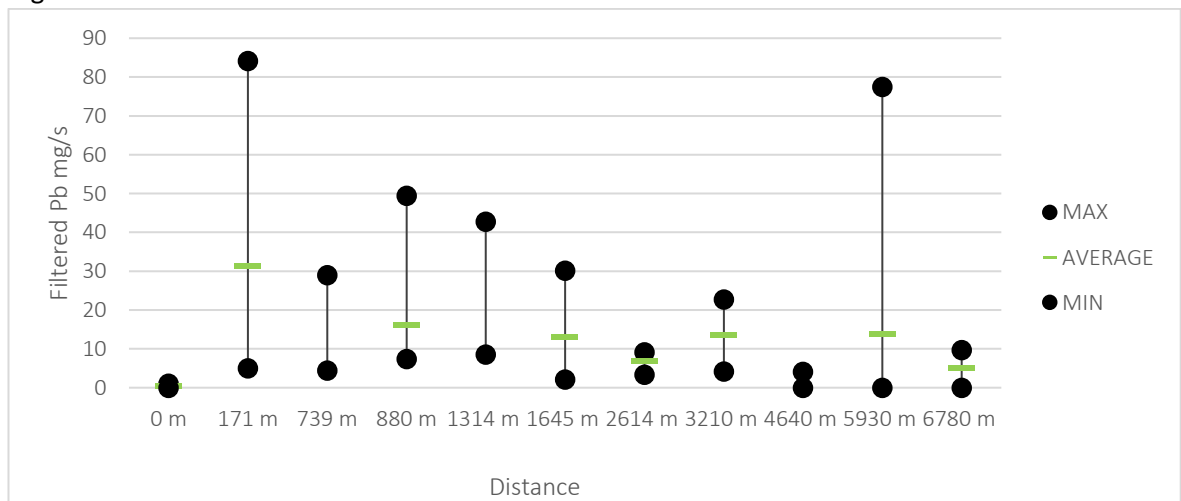
5.g.1



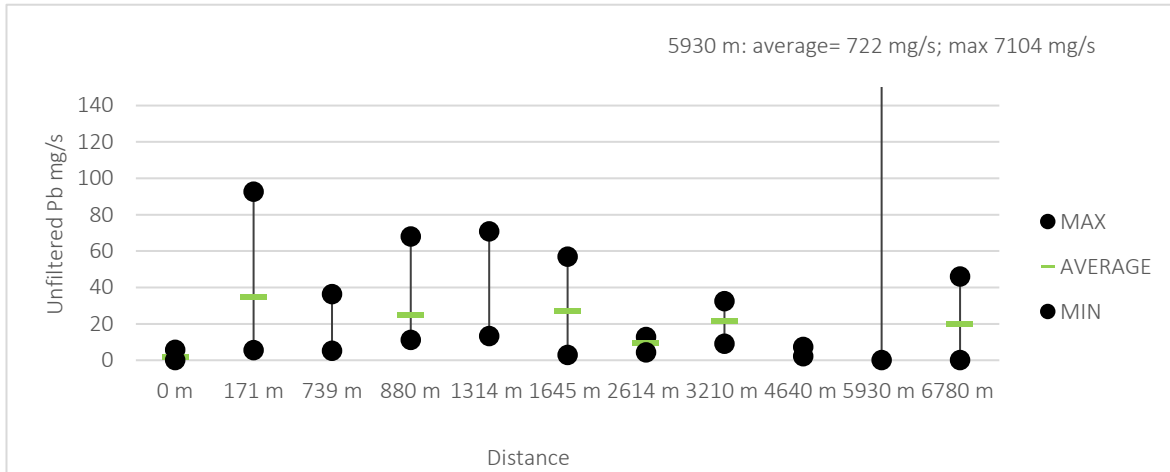
5.g.2



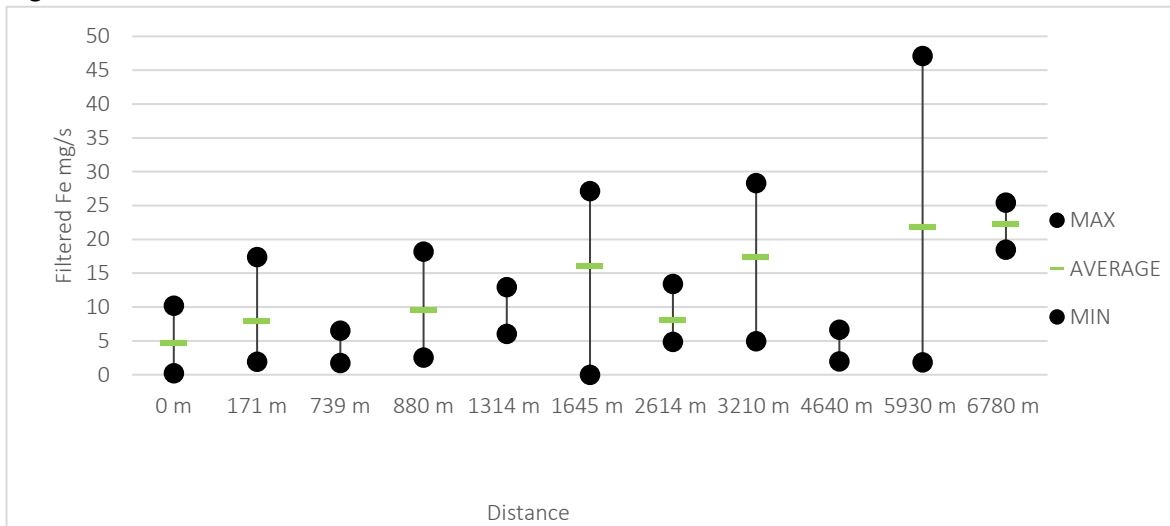
5.g.3



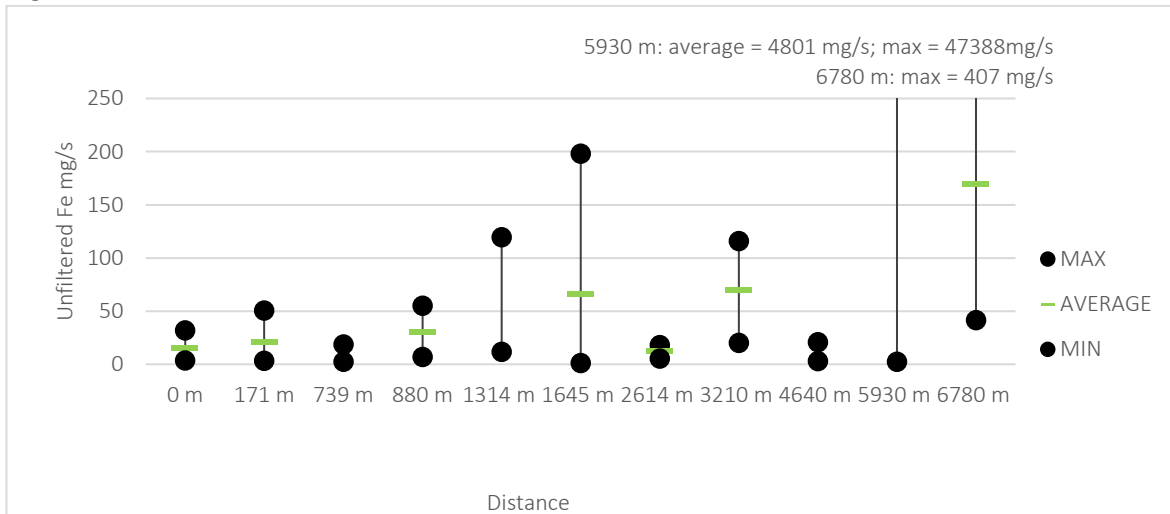
5.g.4



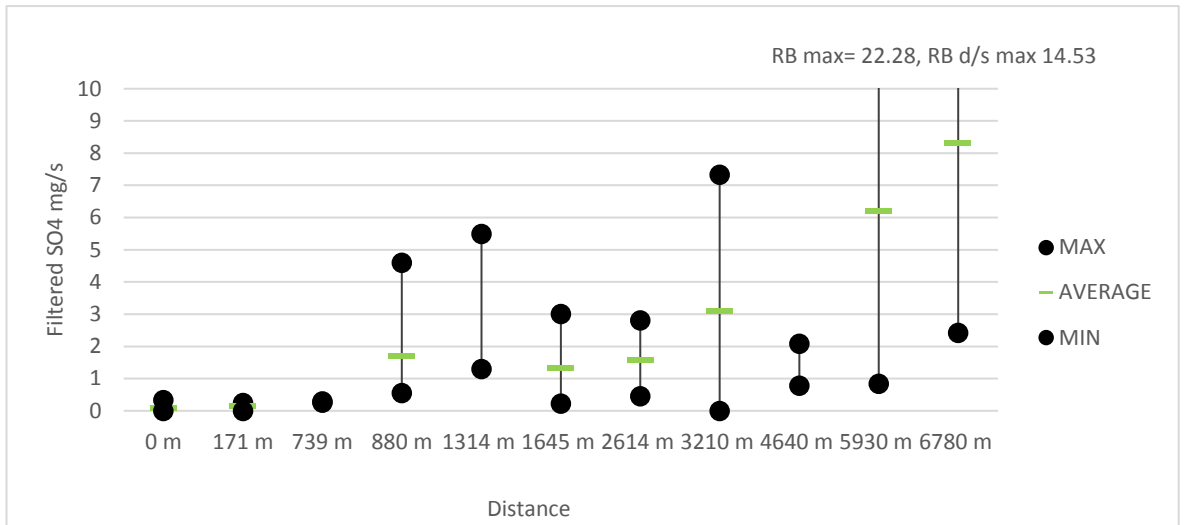
5.g.5



5.g.6



5.g.7



Appendix 5.h Spearman's Rho correlation of Streamflow with concentrations and load.

		Zn FA mg/l	Zn UA mg/l	Pb FA µg/l	Pb UA µg/l	Fe FA mg/l	Fe UA mg/l	SO4 F mg/l
<i>All Site</i>	Correlation Coefficient	0.010	0.047	-0.263	-.290*	-.490**	-0.089	0.177
	Sig. (2-tailed)	0.946	0.752	0.075	0.048	0.000	0.550	0.233
	N	47	47	47	47	47	47	47
		Zn FA mg/s	Zn UA mg/s	Pb FA µg/s	Pb UA µg/s	Fe FA mg/s	Fe UA mg/s	SO4 F mg/s
<i>All Site</i>	Correlation Coefficient	.910**	.926**	.518**	.574**	.802**	.765**	.877**
	Sig. (2-tailed)	0.000	0.000	0.000	0.000	0.000	0.000	0.000
	N	47	47	47	47	47	47	47
<i>T0 0 m</i>	Correlation Coefficient	.900*	.900*	0.800	0.800	.900*	0.800	.975**
	Sig. (2-tailed)	0.037	0.037	0.104	0.104	0.037	0.104	0.005
	N	5	5	5	5	5	5	5
<i>T2 880 m</i>	Correlation Coefficient	0.714	.857*	.929**	.964**	-0.036	0.607	.857*
	Sig. (2-tailed)	0.071	0.014	0.003	0.000	0.939	0.148	0.014
	N	7	7	7	7	7	7	7
<i>GG 1645 m</i>	Correlation Coefficient	.829*	.943**	0.771	.886*	.943**	0.771	.886*
	Sig. (2-tailed)	0.042	0.005	0.072	0.019	0.005	0.072	0.019
	N	6	6	6	6	6	6	6
<i>DC 3210 m</i>	Correlation Coefficient	1.000**	0.800	1.000**	0.800	0.400	1.000**	0.800
	Sig. (2-tailed)		0.200		0.200	0.600		0.200
	N	4	4	4	4	4	4	4
<i>RB 5930 m</i>	Correlation Coefficient	1.000**	1.000**	0.612	.661*	.830**	.818**	1.000**
	Sig. (2-tailed)			0.060	0.038	0.003	0.004	
	N	10	10	10	10	10	10	10

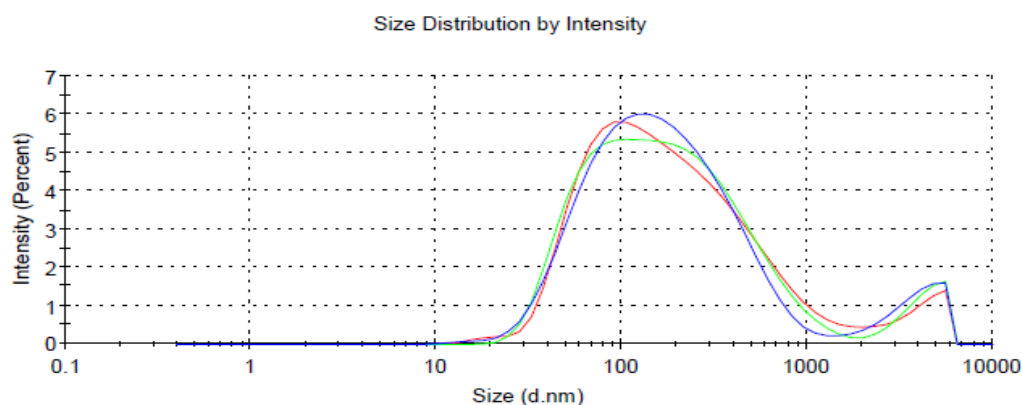
** . Correlation is significant at the 0.01 level (2-tailed).

* . Correlation is significant at the 0.05 level (2-tailed).

Appendix 6.a DLS table and graph of trail experiment data.

Sample	Z-Ave d.nm	Z-ave SD	Pdl	PDI SD	Count kcps	Note		
D26 - 4hs	140	17.90	0.43	0.07	34.20	* ^		
D26 - 24hs	136	19.14	0.46	0.1	38.40	*		
D26 - 48 hs	139	30.68	0.44	0.0	36.40	*		
Average	138		0.44					
SD	1.64		0.01					
Sample	Peak 1 Size d.nm	Peak 1 Intensity %	Peak 1 St Dev d.nm	Peak 2 Size d.nm	Peak 2 Intensity %	Peak 2 St Dev d.nm	Peak 3 Size d.nm	
D26 - 4hs	256	93	292	4011	6.6	1166	0.0	
D26 - 24hs	237	93	245	4226	7.0	1038	0.0	
D26 - 48 hs	207	91	183	3806	9.1	1252	0.0	
Average	232.9			4014				
SD 24h	9.55			107.5			0.00	
SD 48h	20.17			171.5			0.00	

Key. Z-ave: Z-average hydrodynamic diameter; SD: standard deviation; PDI: polydispersity index; Peak: intensity-weighted size distribution peak; *, *In range figure low*: instrument expert advice on result quality indicating the presence of large or sedimenting particles; ^, *Cumulative fit error high*: instrument expert advice on result quality indicating the sample is too polydispersed for cumulant analysis.



Key. Red line: 4 hours; Green line: 24 hours; Blue line: 48 hours.

Appendix 6.b Zeta potential table of trial experiment

Sample	ZP mV	SD (mV)	Peak 1 Mean (mV)	Area (%)	SD (mV)
<i>D26 - 4hs</i>	-3.71	87.4	-14.1	86	13
<i>D26 - 4hs</i>	-9.86	34.6	-15	95.3	12.1
<i>D26 - 4hs</i>	-4.25	46.9	-11.8	93.9	11.2
<i>D26 - 4hs</i>	-4.2	143	-6.46	66.6	19.2
<i>D26 - 4hs</i>	-3.6	75.3	-7.77	90.7	14.3
4h-Ave	-5.12		-11.03	86.50	
4h-SD	2.38		3.38	10.45	
<i>D26 - 24hs</i>	-2.76	14.3	-4.34	98.5	6.11
<i>D26 - 24hs</i>	-0.896	86.7	-11.8	79.7	10.6
<i>D26 - 24hs</i>	-1.56	160	-4.22	54.3	15.2
<i>D26 - 24hs</i>	-3	90	-10	76.7	10.5
<i>D26 - 24hs</i>	-2.54	129	3.97	65.6	13
<i>D26 - 24hs</i>	-4.4	152	-5.77	44.4	13.2
<i>D26 - 24hs</i>	-3.86	160	-1.63	46.9	15.9
24h-Ave	-2.72		-4.83	66.59	
24h-SD	1.13		4.85	18.22	
<i>D26 - 48 hs</i>	-4.73	118	-7.79	75.9	15.2
<i>D26 - 48 hs</i>	-2.41	5.65	-2.41	100	5.65
<i>D26 - 48 hs</i>	-3.88	28.7	-9.21	96	9.86
<i>D26 - 48 hs</i>	-7.27	6.7	-7.27	100	6.7
<i>D26 - 48 hs</i>	-5.42	4.35	-5.42	100	4.35
48h-Ave	-4.74		-6.42	94.38	
48h-SD	1.61		2.34	9.37	

Key. ZP: Zeta potential; SD: standard deviation; Peak: count-weighted Zeta potential distribution peak; Ave: arithmetical average calculated from the reading ZP. On the left graphs of zeta potential distribution by total count for 4, 24 and 48 hours after sampling.

Appendix 6.c Centrifuged and uncentrifuged DLS analysis

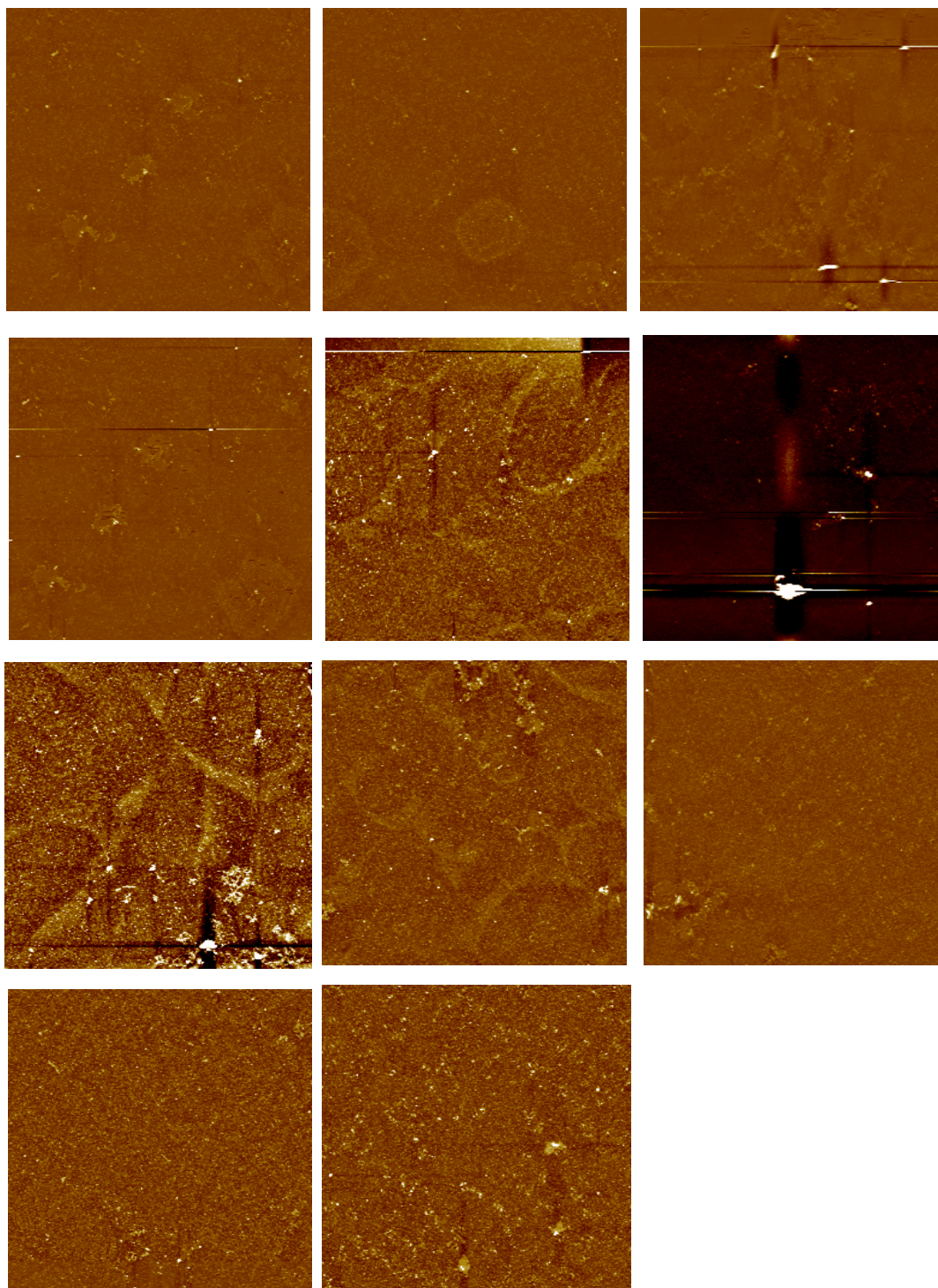
Sample	W LAB	Z-Ave		Pdl		Count kcps	note
		d.nm	SD		SD		
DC	WI	264	25	0.44	0.11	71	*
RB	WI	282	32	0.42	0.02	188	good
DC	WII	196	21	0.39	0.04	58	* ^
RB	WII	195	28	0.42	0.05	90	* ^
RB_conc	WII	164	10	0.41	0.06	259	* ^
DC_conc	WII	171	12	0.48	0.06	186	* ^

Sample	W LAB	Peak 1			Peak 2			Peak 3		
		Size	Intens.	SD	Size	Intens.	St Dev	Size	Intens.	St Dev
		(d.nm)	%	(d.nm)	(d.nm)	%	(d.nm)	(d.nm)	%	(d.nm)
DC	WI	381	95	267	4622	4.8	869	0	0.0	0
RB	WI	413	89	247	55	8.3	19	4895	3.2	846
DC	WII	182	94	123	5244	6.3	464	12	0.1	2
RB	WII	192	91	116	4962	6.2	738	30	3.1	6
RB_conc	WII	186	96	144	5110	3.6	599	21	0.2	5
DC_conc	WII	202	96	160	5283	3.7	425	0	0.0	0

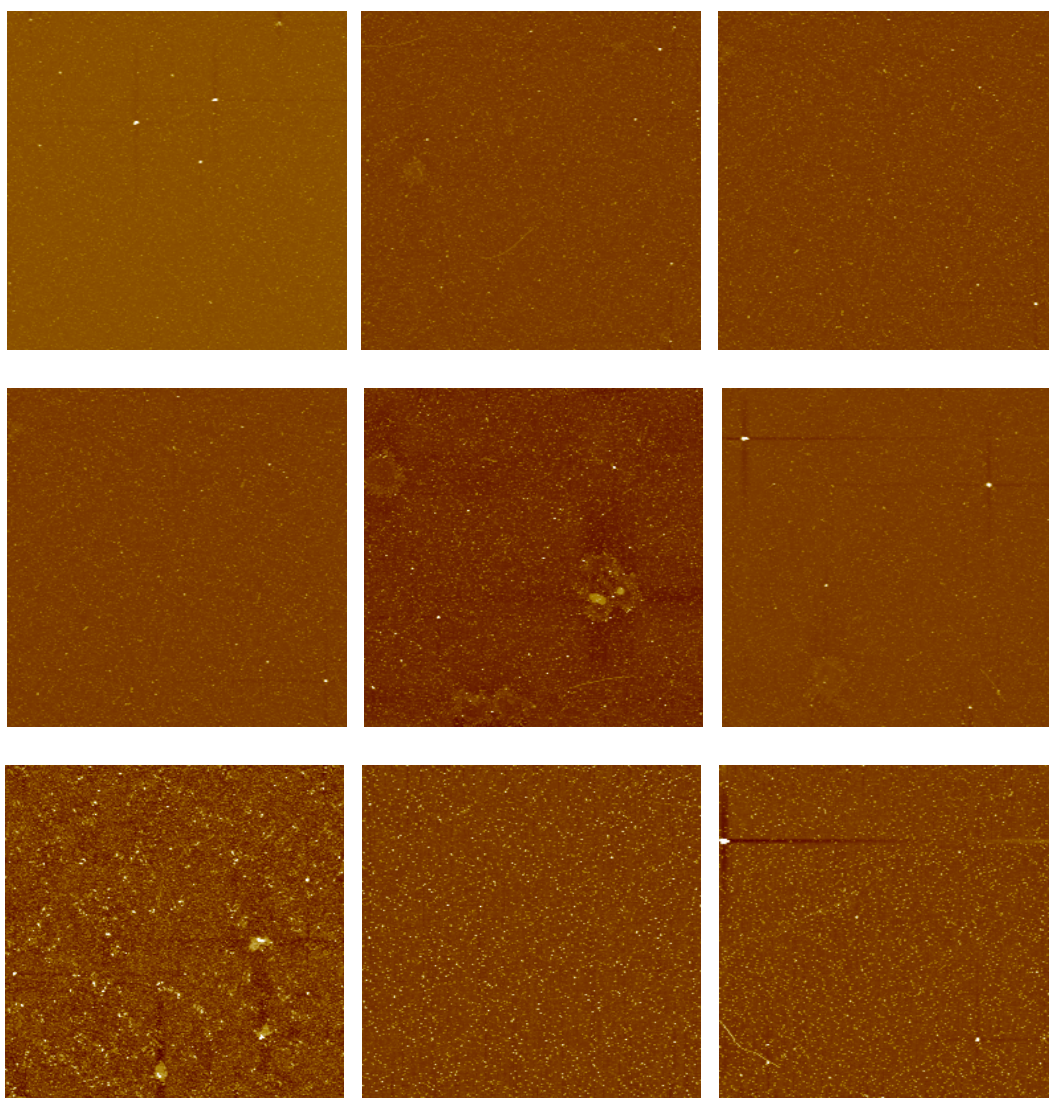
Key. Z-ave: Z-average hydrodynamic diameter; SD: standard deviation; PDI: polydispersity index; Peak: intensity-weighted size distribution peak; *, *In range figure low*: instrument expert advice on result quality indicating the presence of large or sedimenting particles; ^, *Cumulative fit error high*: instrument expert advice on result quality indicating the sample is too polydispersed for cumulant analysis.

Appendix 6.d AFM images

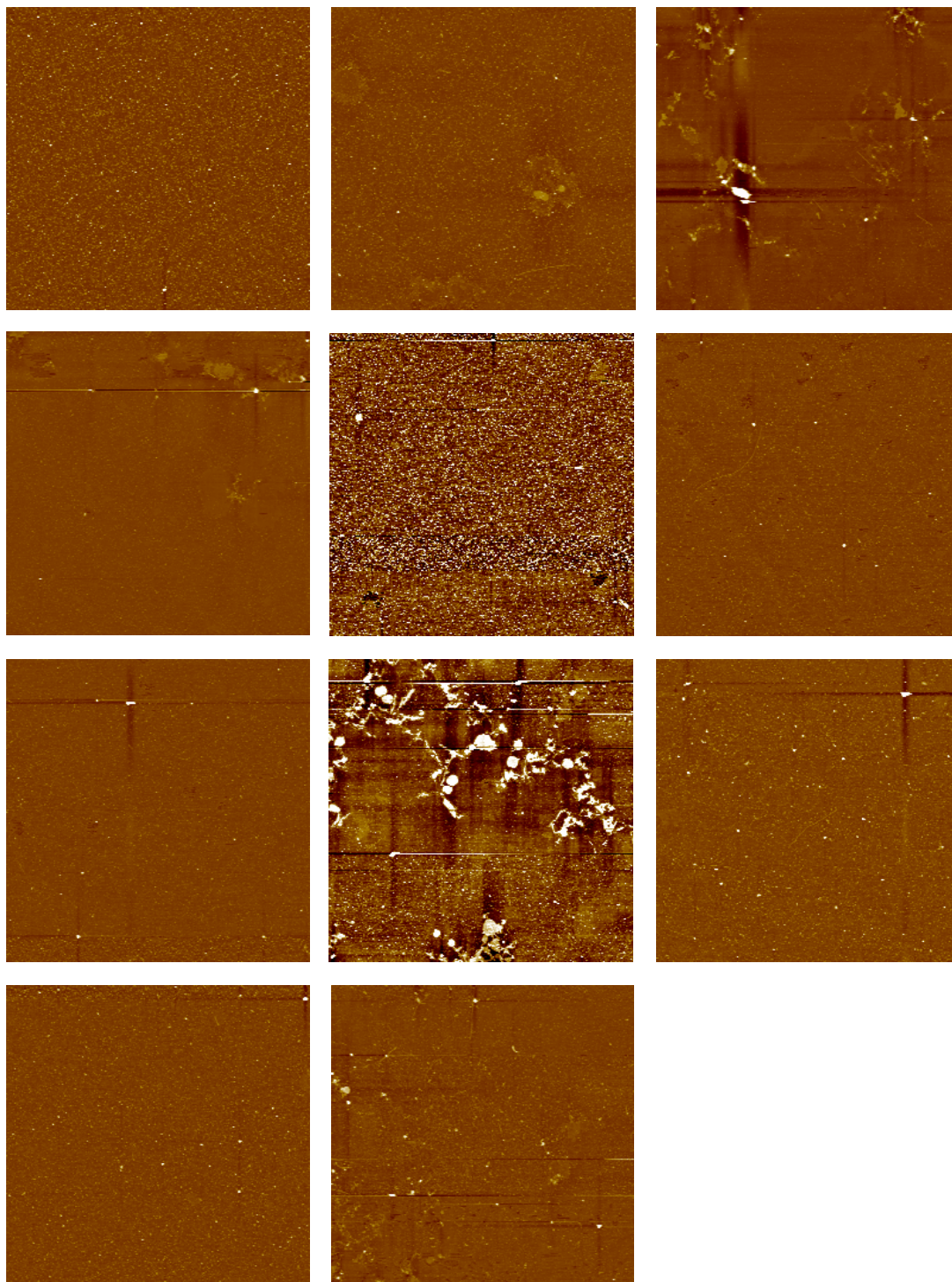
6.d.1 AFM images of sample T2



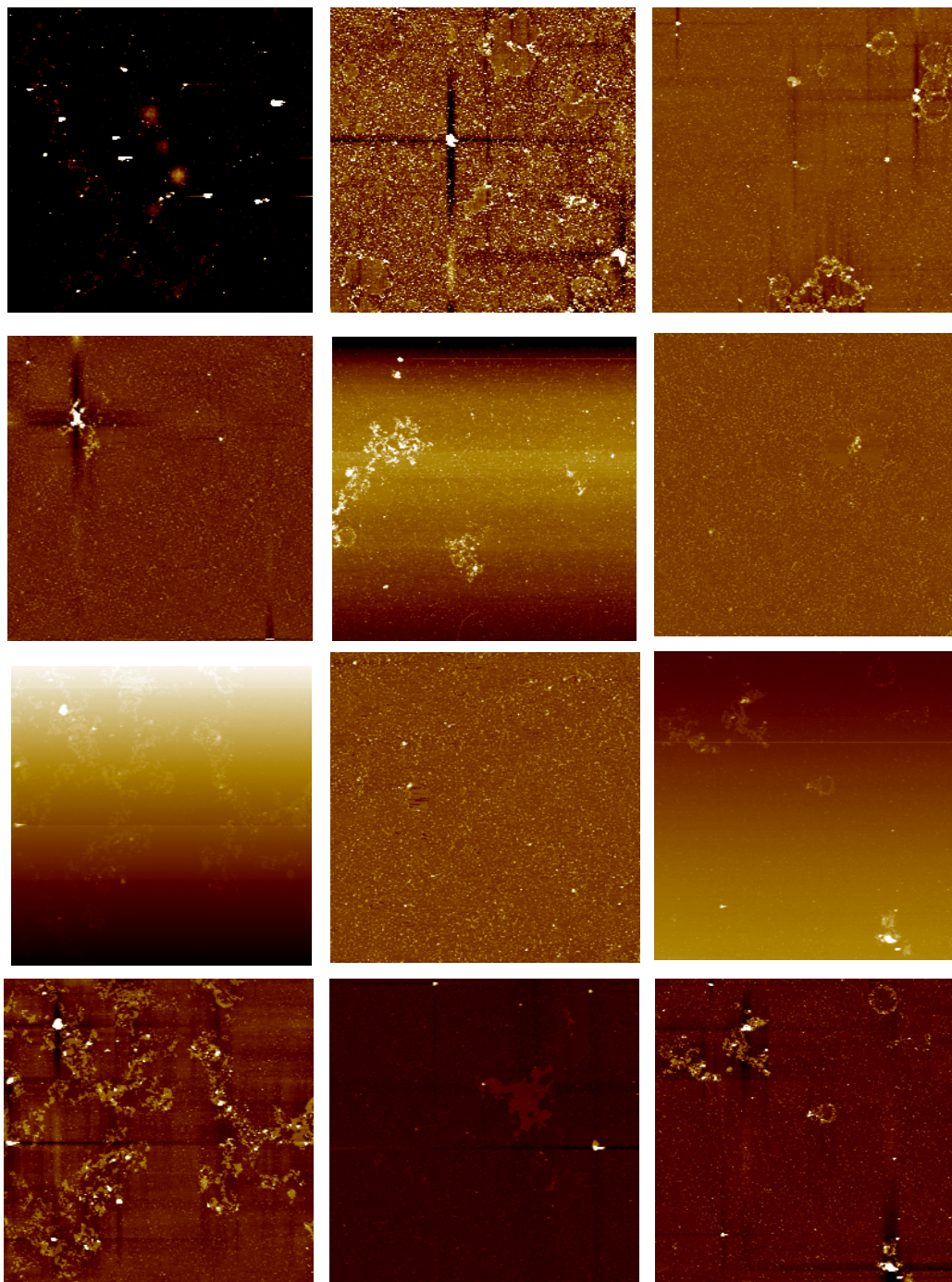
6.d.2 AFM images of sample GG



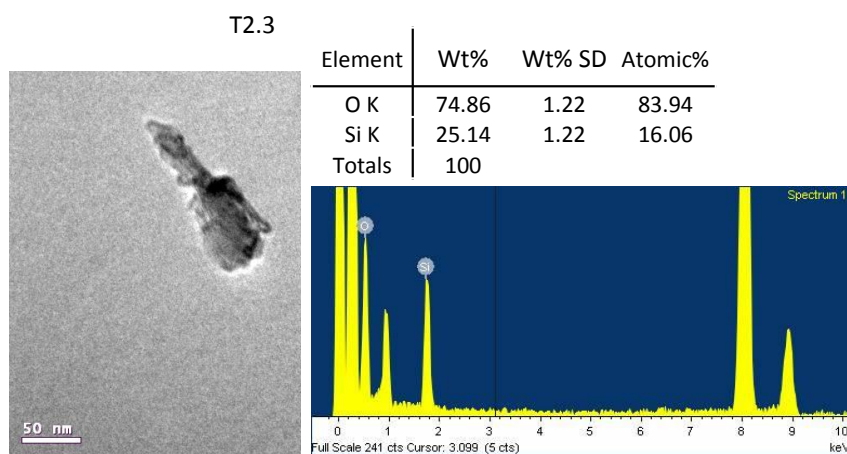
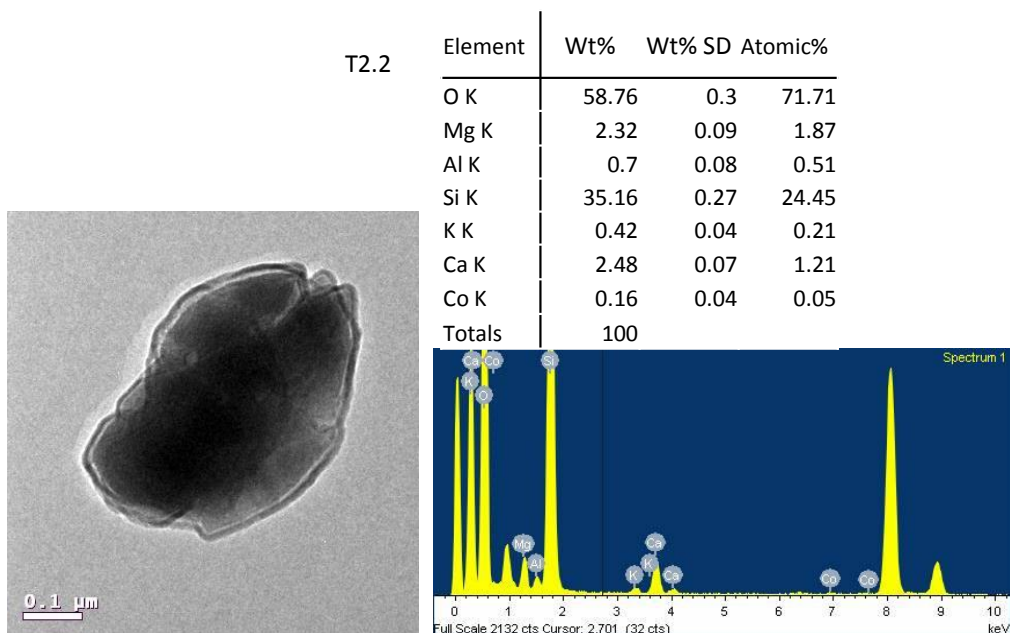
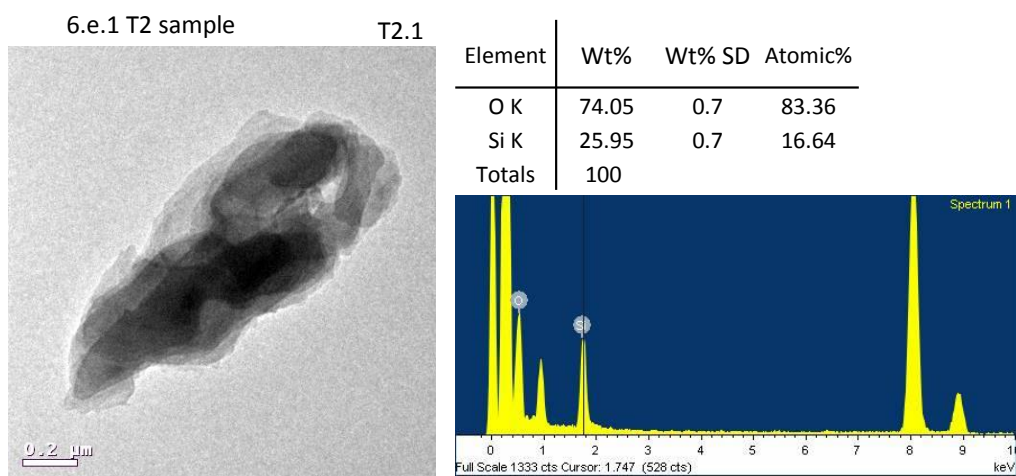
6.d.3 AFM images of sample DC



6.d.4 AFM images of sample RB

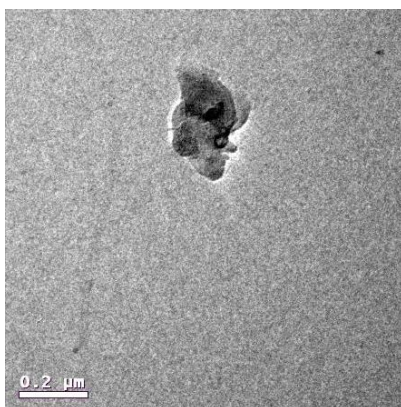


Appendix 6.e TEM and EDS spectra

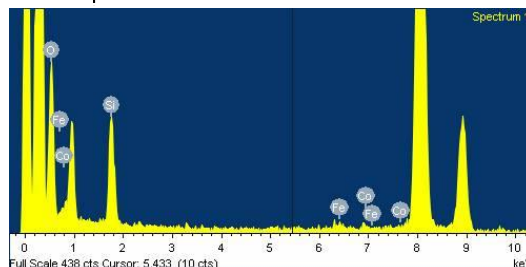


6.e.1 T2 sample

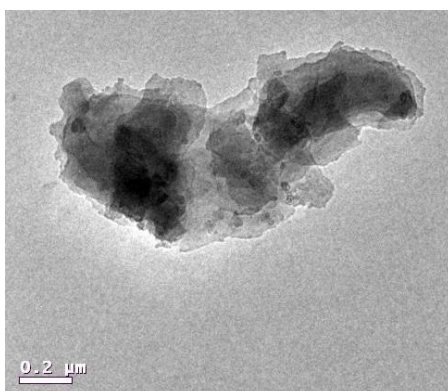
T2.4



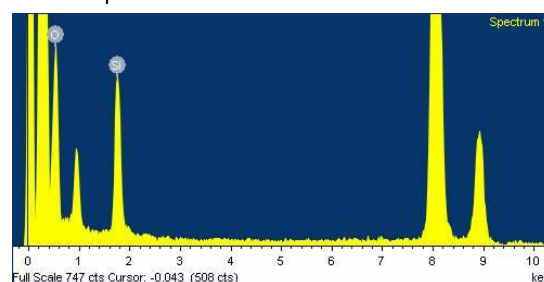
Element	Wt%	Wt% SD	Atomic%
O K	76.43	1.01	85.84
Si K	20.76	0.88	13.28
Fe K	1.11	0.45	0.36
Co K	1.71	0.45	0.52
Totals	100		



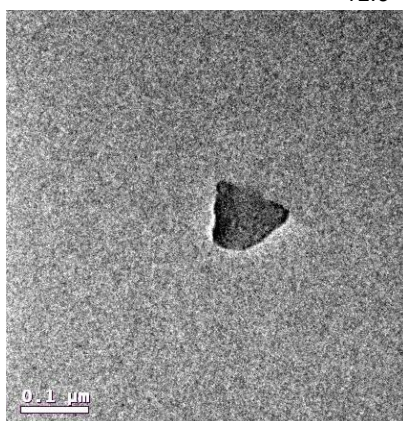
T2.5



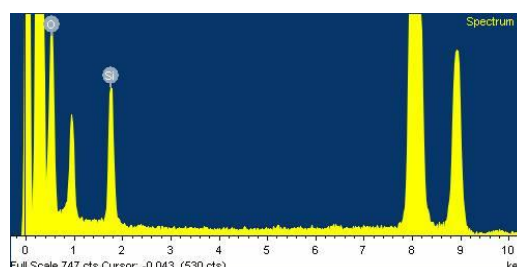
Element	Wt%	Wt% SD	Atomic%
O K	73.53	0.71	82.98
Si K	26.47	0.71	17.02
Totals	100		



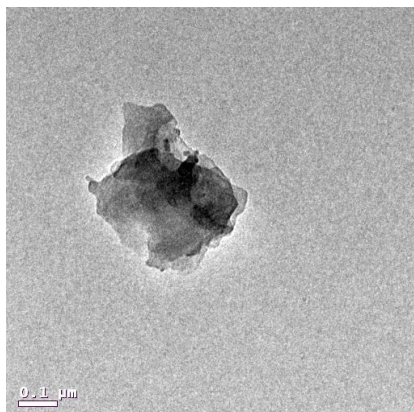
T2.6



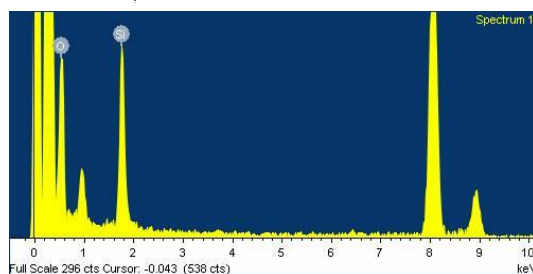
Element	Wt%	Wt% SD	Atomic%
O K	76.98	0.65	85.44
Si K	23.02	0.65	14.56
Totals	100		



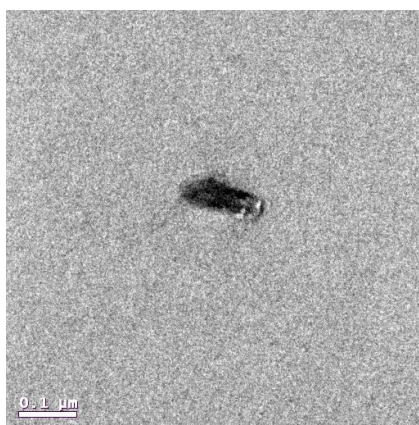
T2.7



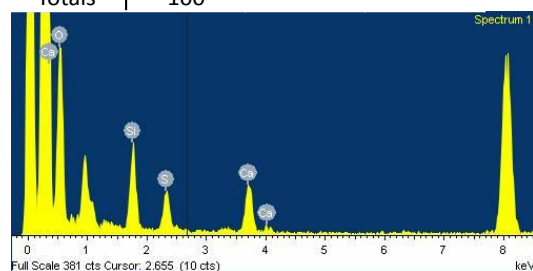
Element	Wt%	Wt% SD	Atomic%
O K	71.51	1.08	81.5
Si K	28.49	1.08	18.5
Totals	100		



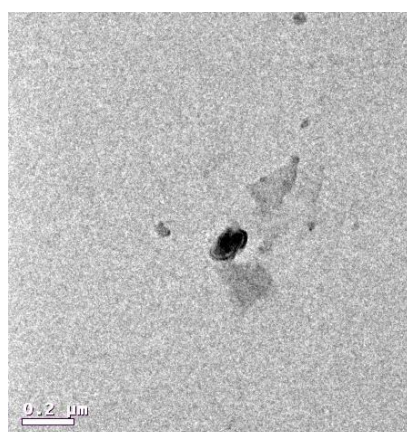
T2.8



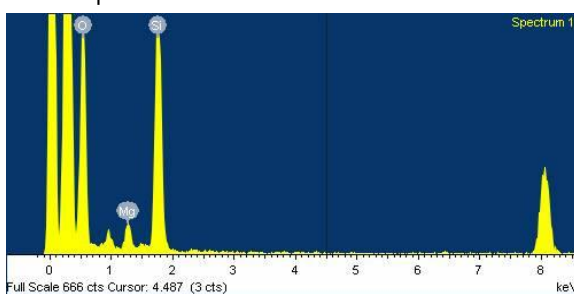
Element	Wt%	Wt% SD	Atomic%
O K	67.69	1.24	80.73
Si K	14.71	0.79	10
S K	7.51	0.62	4.47
Ca K	10.09	0.6	4.81
Totals	100		



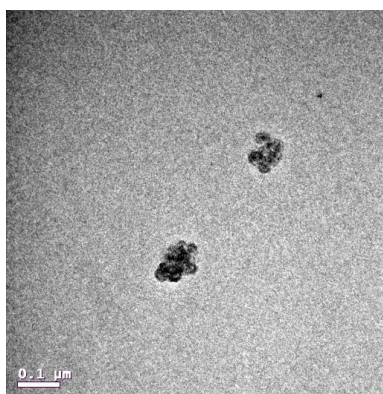
T2.9



Element	Wt%	Wt% SD	Atomic%
O K	66.59	0.67	77.47
Mg K	3.82	0.3	2.92
Si K	29.59	0.62	19.61
Totals	100		

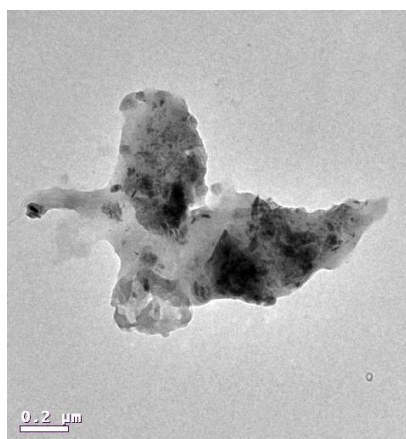
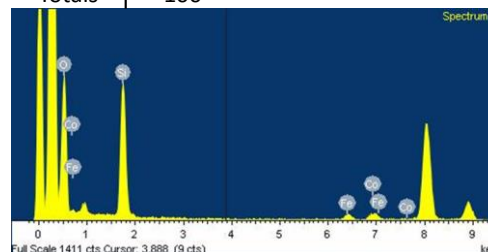


6.e.2 GG sample



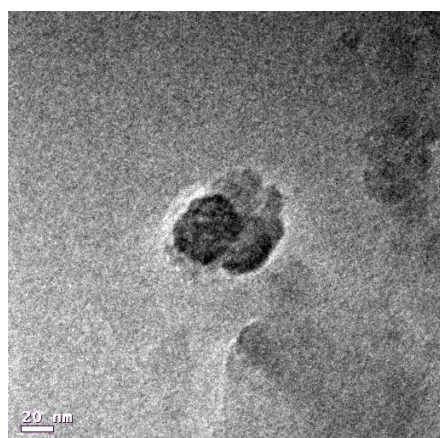
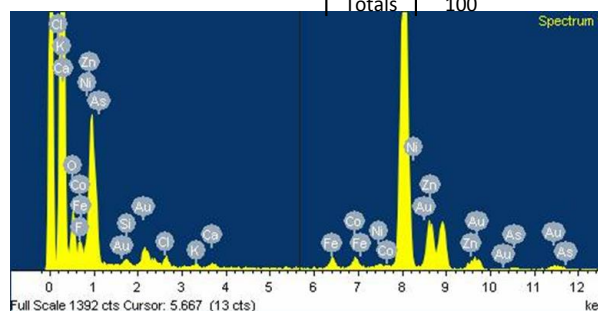
GG.1

Element	Wt%	Wt% SD	Atomic%
O K	68.33	0.57	80.21
Si K	27.62	0.52	18.47
Fe K	1.78	0.18	0.6
Co K	2.26	0.21	0.72
Totals	100		



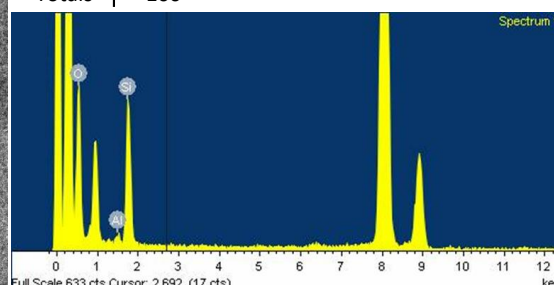
GG.2

Element	Wt%	Wt% SD	Atomic%	Element	Wt%	Wt% SD	Atomic%
O K	27.13	1.49	56.83	Fe K	4.81	0.38	2.88
F K	6.91	1.99	12.18	Co K	5.03	0.42	2.86
Si K	1.77	0.35	2.11	Ni K	0.84	0.36	0.48
Cl K	3.38	0.36	3.19	Zn K	26.1	1.09	13.38
K K	1.06	0.25	0.91	As K	1.5	0.35	0.67
Ca K	1.28	0.25	1.07	Au L	20.2	1.34	3.44
Totals				Totals	100		

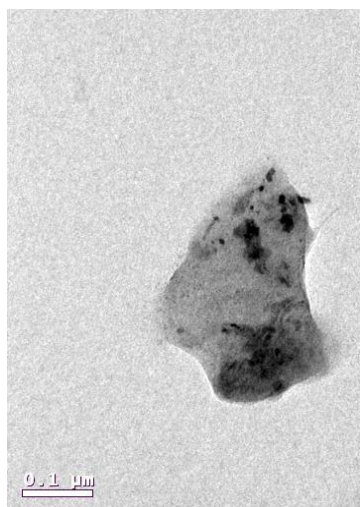


GG.3

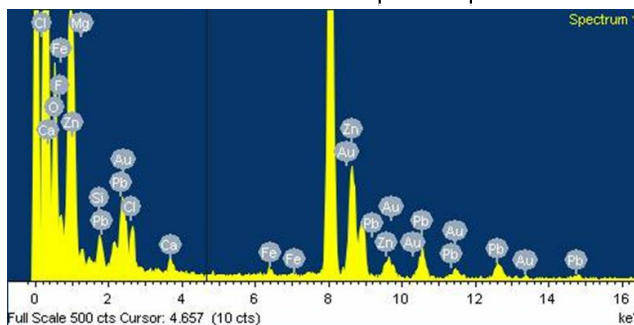
Element	Wt%	Wt% SD	Atomic%
O K	71.08	0.85	81.15
Al K	1.53	0.39	1.03
Si K	27.39	0.8	17.81
Totals	100		



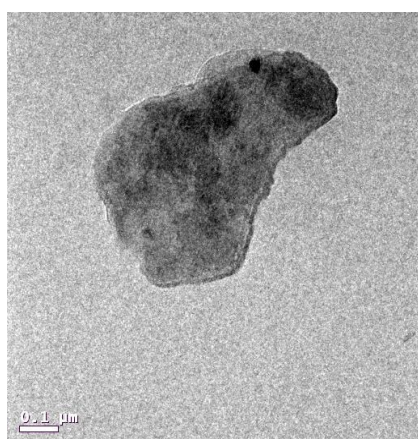
GG.4



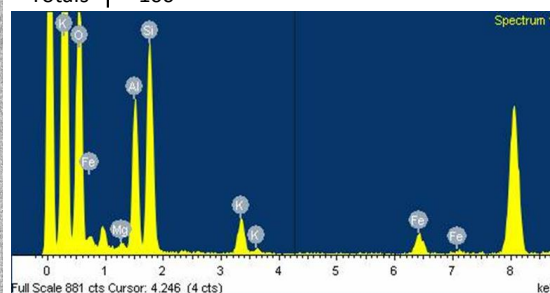
Element	Wt%	Wt% SD	Atomic%	Element	Wt%	Wt% SD	Atomic%
O K	37.53	1.37	68.45	Ca K	1.14	0.21	0.83
F K	5.99	1.64	9.2	Fe K	0.9	0.2	0.47
Mg K	2.37	0.36	2.85	Zn K	18.44	0.76	8.23
Si K	2.59	0.32	2.69	Au L	9.51	0.98	1.41
Cl K	4.16	0.37	3.42	Pb L	17.36	1	2.44
Totals	100						



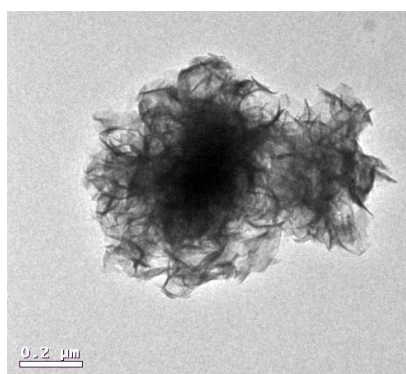
GG.5



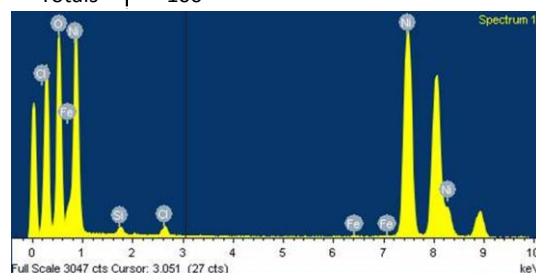
Element	Wt%	Wt% SD	Atomic%
O K	57.32	0.59	71.14
Mg K	0.79	0.16	0.65
Al K	14.67	0.37	10.8
Si K	20.44	0.42	14.45
K K	3.67	0.17	1.86
Fe K	3.1	0.17	1.1
Totals	100		



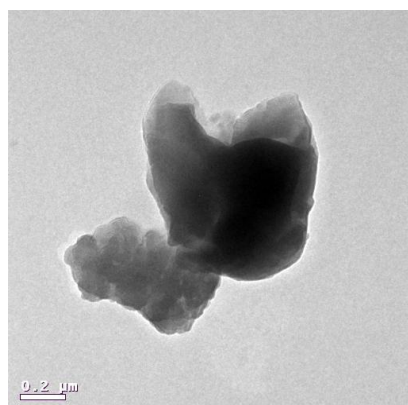
GG.6



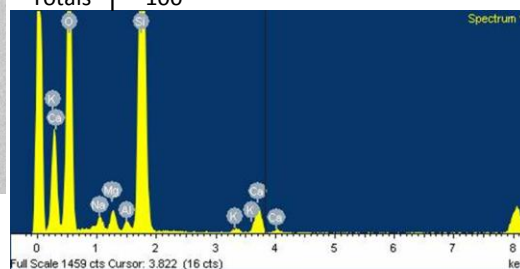
Element	Wt%	Wt% SD	Atomic%
O K	49.17	0.36	77.34
Si K	1.1	0.09	0.98
Cl K	1.28	0.09	0.91
Fe K	0.19	0.06	0.09
Ni K	48.27	0.35	20.69
Totals	100		



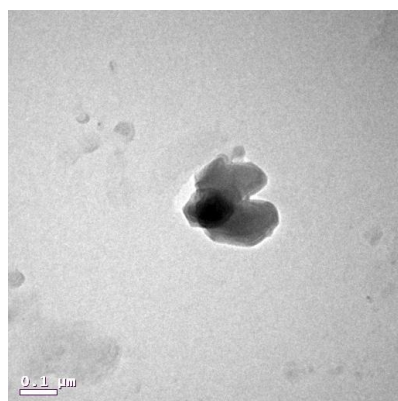
GG.7



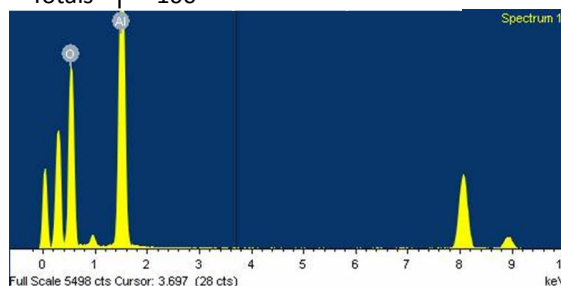
Element	Wt%	Wt% SD	Atomic%
O K	54.88	0.44	68.25
Na K	1.37	0.15	1.18
Mg K	2.07	0.13	1.69
Al K	0.79	0.11	0.58
Si K	37.66	0.4	26.68
K K	0.44	0.06	0.22
Ca K	2.8	0.11	1.39
Totals	100		



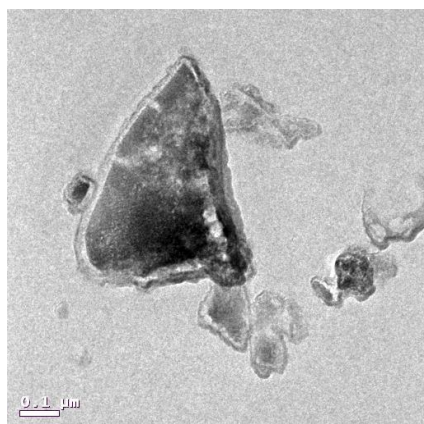
GG.8



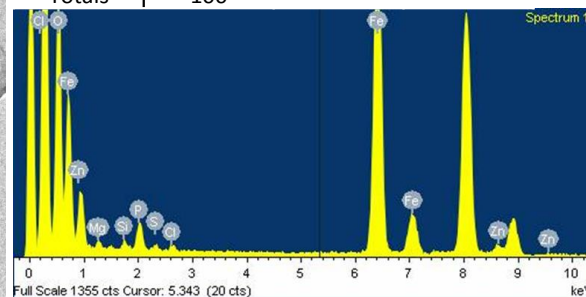
Element	Wt%	Wt% SD	Atomic%
O K	51.84	0.26	64.48
Al K	48.16	0.26	35.52
Totals	100		



GG.9

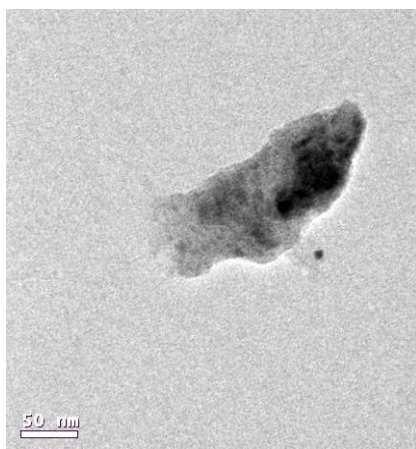


Element	Wt%	Wt% SD	Atomic%
O K	48.66	0.48	75
Mg K	1.12	0.15	1.13
Si K	0.78	0.12	0.68
P K	2.9	0.17	2.31
S K	0.57	0.11	0.44
Cl K	0.69	0.11	0.48
Fe K	44.62	0.45	19.7
Zn K	0.66	0.18	0.25
Totals	100		

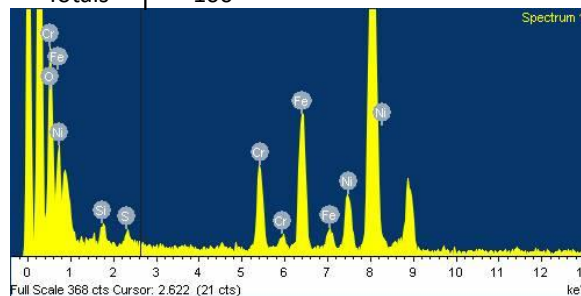


6.e.3 DC sample

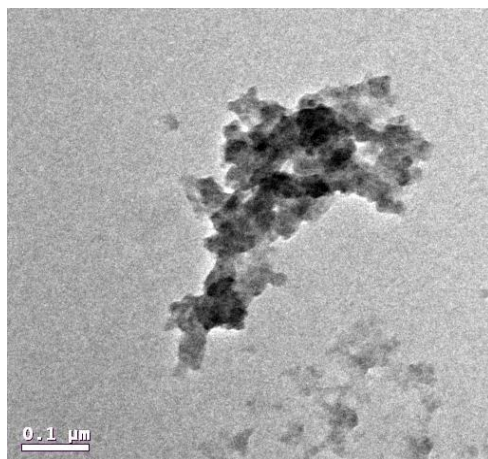
DC.1



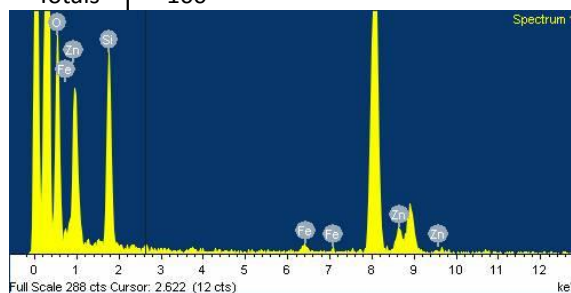
Element	Wt%	Wt% SD	Atomic%
O K	40.43	1.67	68.78
Si K	2.88	0.44	2.79
S K	1.49	0.42	1.27
Cr K	15.08	0.71	7.89
Fe K	28.26	1.03	13.77
Ni K	11.86	0.7	5.5
Totals	100		



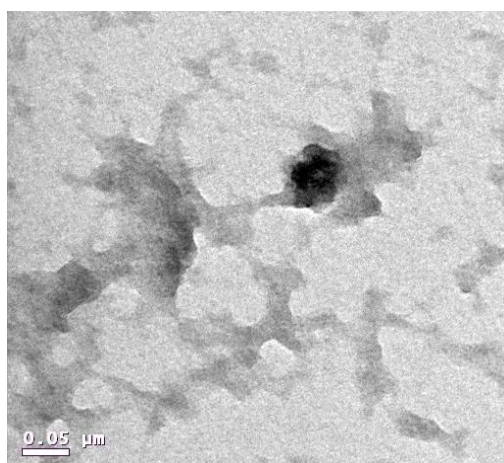
DC.2



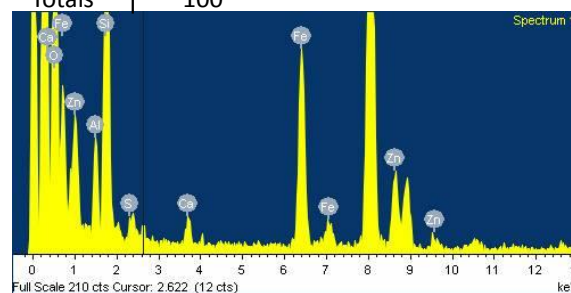
Element	Wt%	Wt% SD	Atomic%
O K	66.73	1.19	79.75
Si K	26.91	1.01	18.32
Fe K	1.39	0.34	0.48
Zn K	4.97	0.72	1.45
Totals	100		



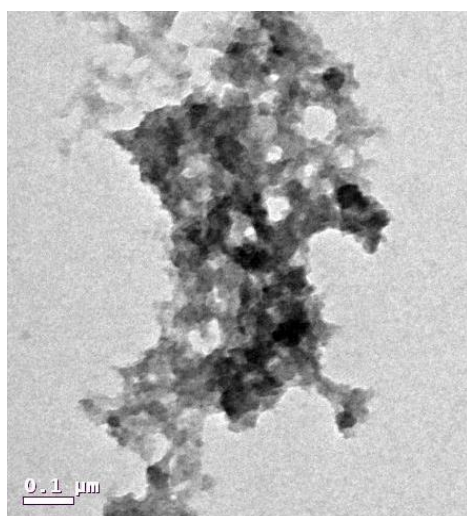
DC.3



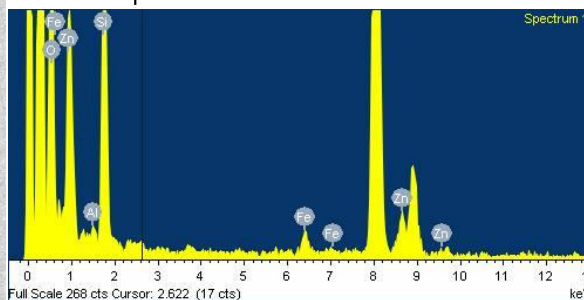
Element	Wt%	Wt% SD	Atomic%
O K	54.37	0.86	72.76
Al K	4.36	0.33	3.46
Si K	20.74	0.57	15.81
S K	0.75	0.21	0.5
Ca K	1.28	0.17	0.69
Fe K	13.07	0.44	5.01
Zn K	5.43	0.39	1.78
Totals	100		



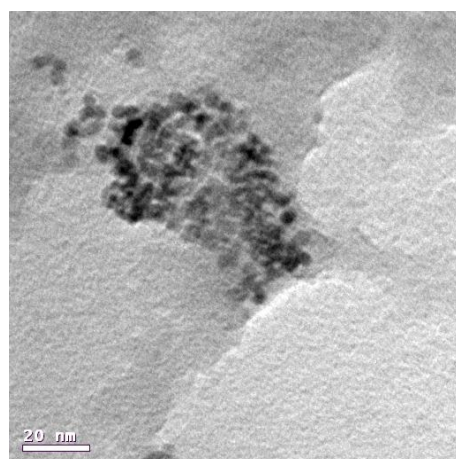
DC.4



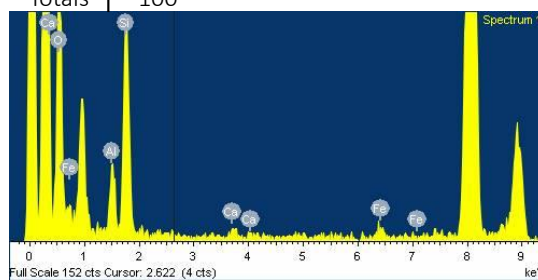
Element	Wt%	Wt% SD	Atomic%
O K	66.93	0.91	79.57
Al K	1.14	0.34	0.8
Si K	26.49	0.75	17.94
Fe K	2.11	0.31	0.72
Zn K	3.34	0.53	0.97
Totals	100		



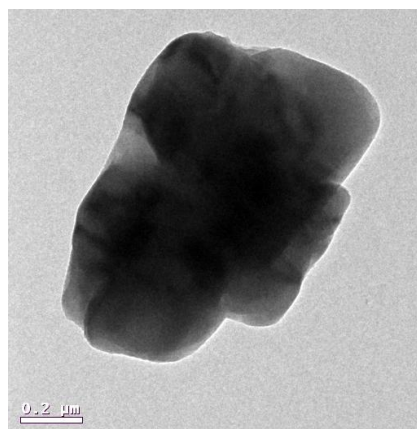
DC.5



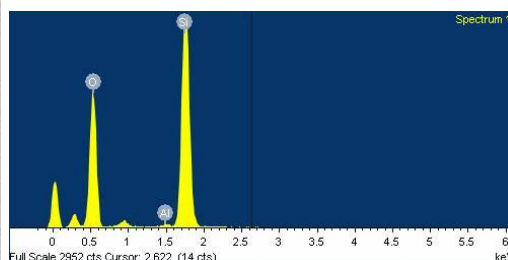
Element	Wt%	Wt% SD	Atomic%
O K	62.1	1.58	74.72
Al K	7.97	0.82	5.69
Si K	26.62	1.28	18.25
Ca K	1.46	0.36	0.7
Fe K	1.85	0.47	0.64
Totals	100		



DC.6

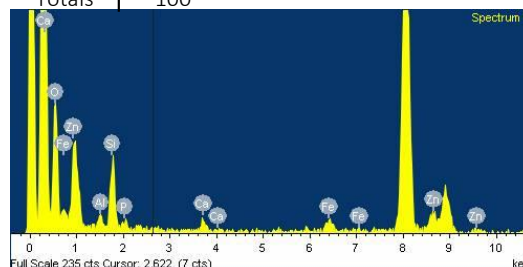
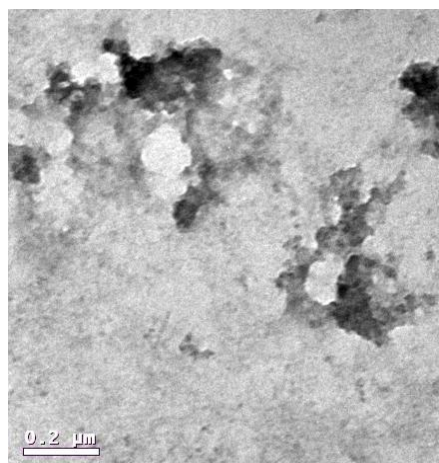


Element	Wt%	Wt% SD	Atomic%
O K	56.36	0.4	69.38
Al K	0.37	0.09	0.27
Si K	43.27	0.4	30.35
Totals	100		



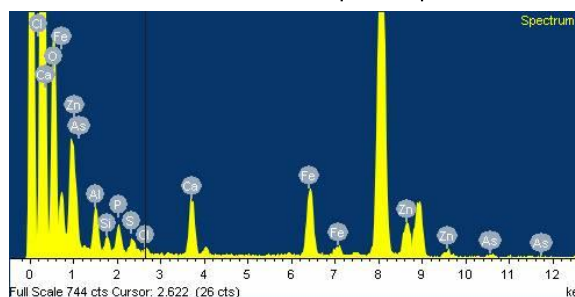
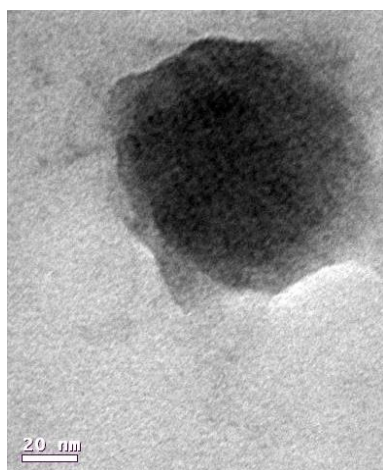
DC.7

Element	Wt%	Wt% SD	Atomic%
O K	61.65	2.21	77.67
Al K	3.57	0.84	2.67
Si K	17.57	1.37	12.61
P K	2.85	0.82	1.86
Ca K	2.63	0.6	1.32
Fe K	4.85	0.8	1.75
Zn K	6.88	1.33	2.12
Totals	100		



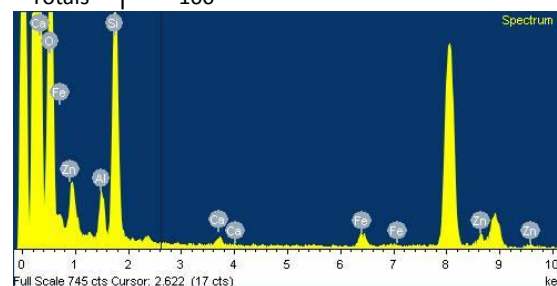
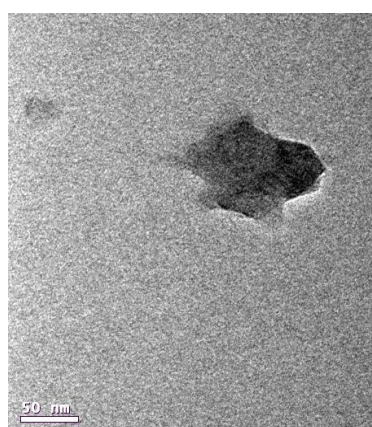
DC.8

Element	Wt%	Wt% SD	Atomic%	Element	Wt%	Wt% SD	Atomic%
O K	58.07	0.83	78.43	Cl K	0.67	0.18	0.41
Al K	5.68	0.33	4.55	Ca K	7.46	0.3	4.02
Si K	1.99	0.24	1.53	Fe K	13.25	0.42	5.13
P K	3.38	0.3	2.36	Zn K	7.11	0.44	2.35
S K	1.39	0.23	0.93	As K	1	0.22	0.29
Totals	100						



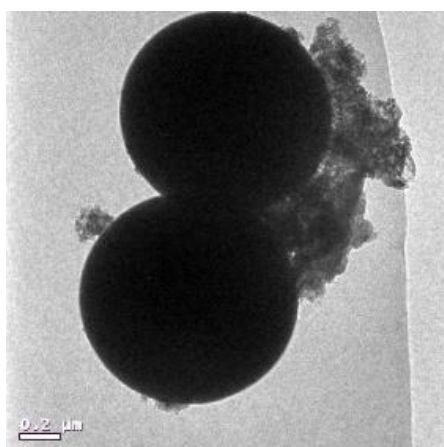
DC.9

Element	Wt%	Wt% SD	Atomic%
O K	63.29	0.72	76.06
Al K	5.01	0.31	3.57
Si K	27.55	0.59	18.86
Ca K	0.98	0.14	0.47
Fe K	2.07	0.19	0.71
Zn K	1.1	0.28	0.32
Totals	100		

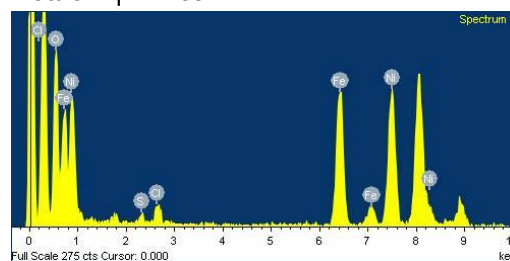


6.e.4 RB sample

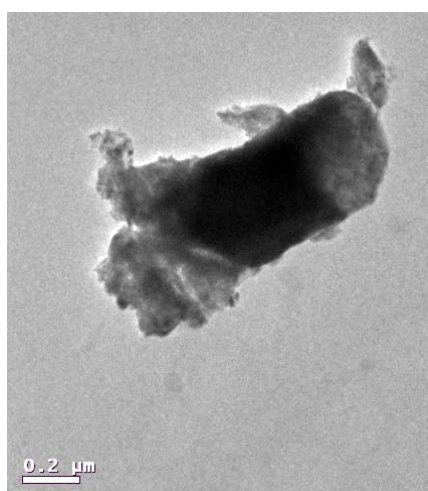
RB.1



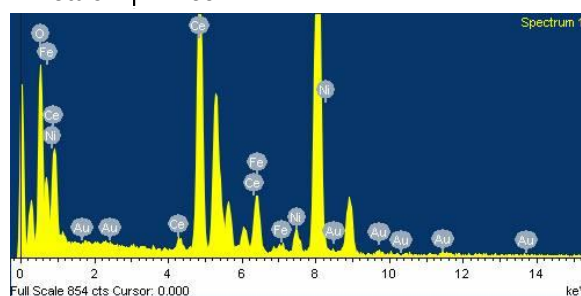
Element	Wt%	Wt% SD	Atomic%
O K	44.2	1.12	73.12
S K	0.98	0.27	0.81
Cl K	2.55	0.33	1.91
Fe K	26.06	0.78	12.35
Ni K	26.21	0.83	11.81
Totals	100		



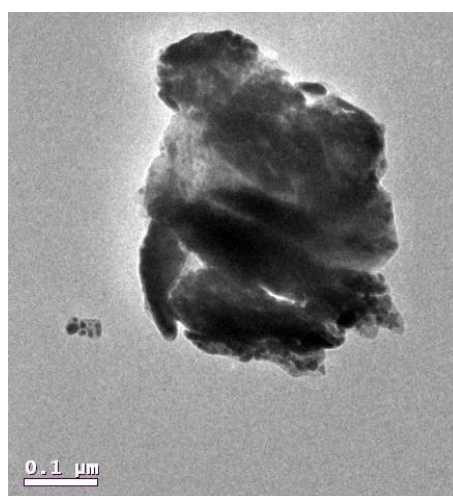
RB.2



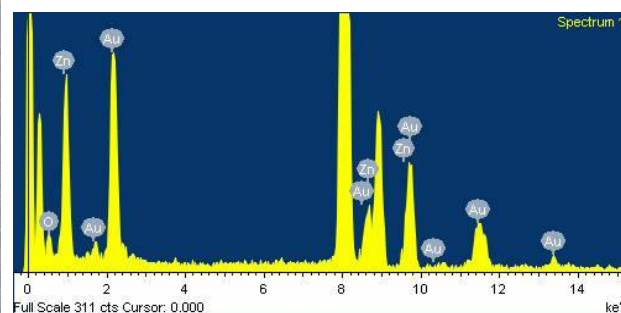
Element	Wt%	Wt% SD	Atomic%
O K	20.94	0.48	67.6
Fe K	4.54	0.18	4.2
Ni K	1.82	0.14	1.6
Ce L	70.74	0.54	26.08
Au L	1.96	0.32	0.51
Totals	100		



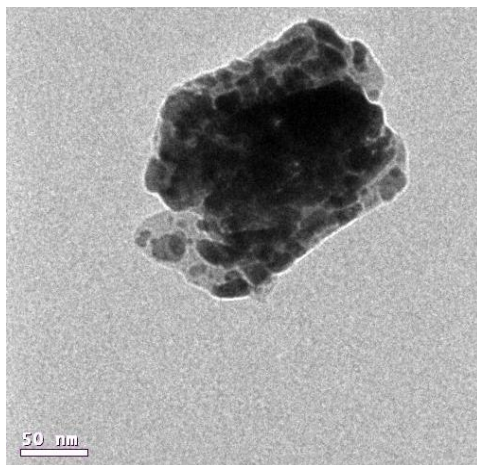
RB.3



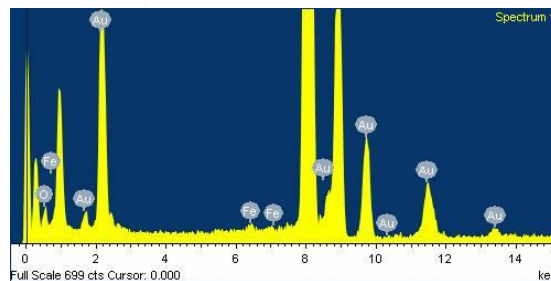
Element	Wt%	Wt% SD	Atomic%
O K	10.42	1.32	55.93
Zn K	5.71	0.87	7.5
Au L	83.87	1.49	36.57
Totals	100		



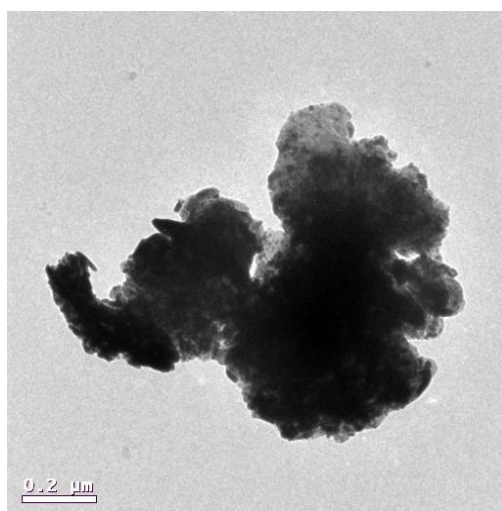
RB.4



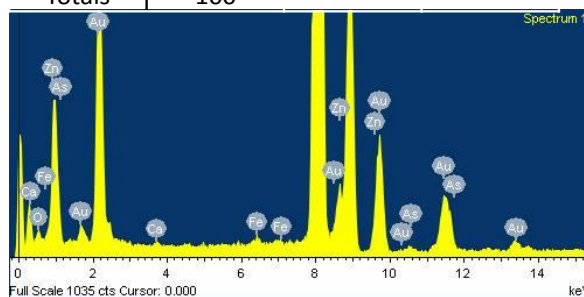
Element	Wt%	Wt% SD	Atomic%
O K	8.9	0.92	53.79
Fe K	1.21	0.28	2.09
Au L	89.89	0.95	44.12
Totals	100		



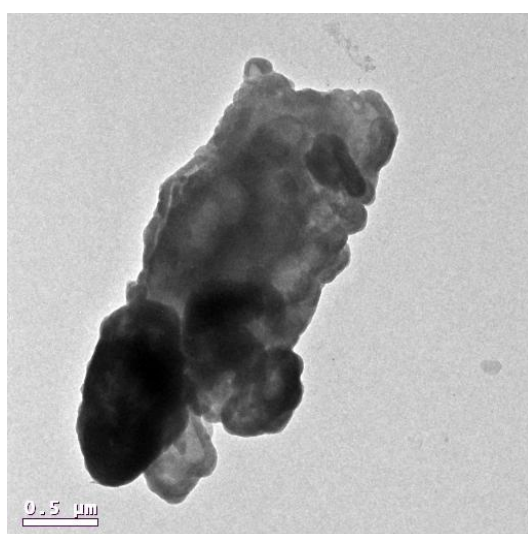
RB.5



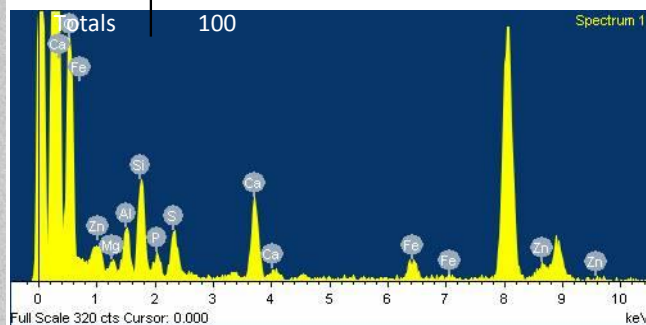
Element	Wt%	Wt% SD	Atomic%
O K	5.87	0.74	41.22
Ca K	0.54	0.17	1.51
Fe K	0.79	0.22	1.59
Zn K	1.26	0.56	2.17
As K	1.41	0.26	2.11
Au L	90.13	0.95	51.4
Totals	100		

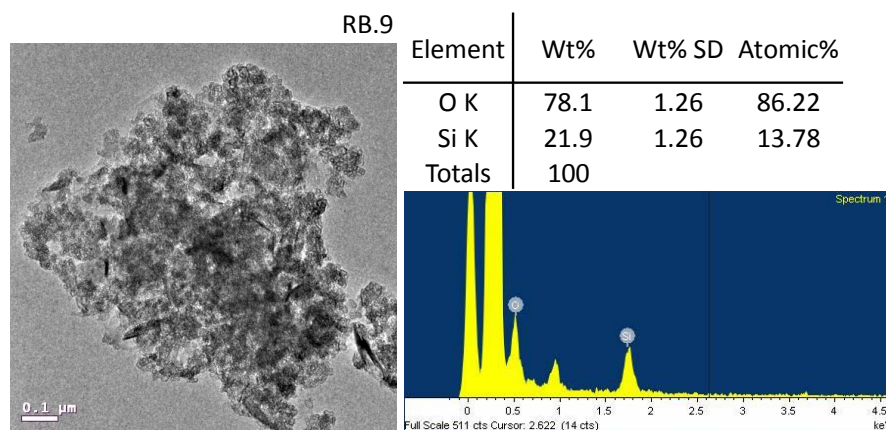
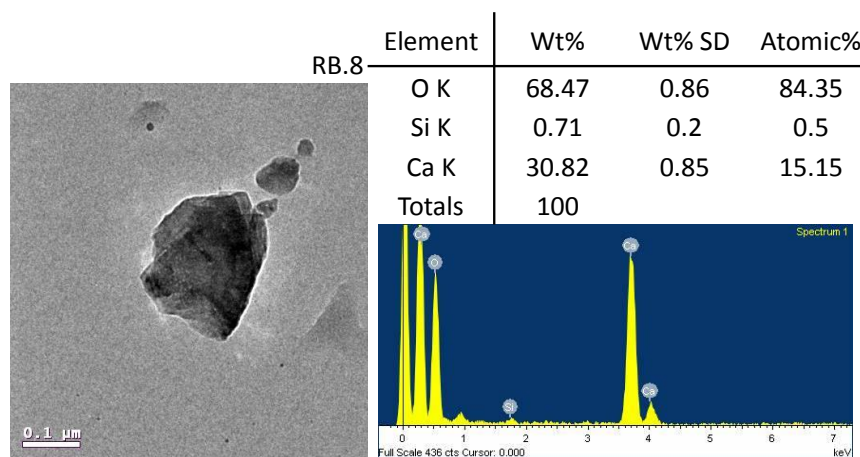
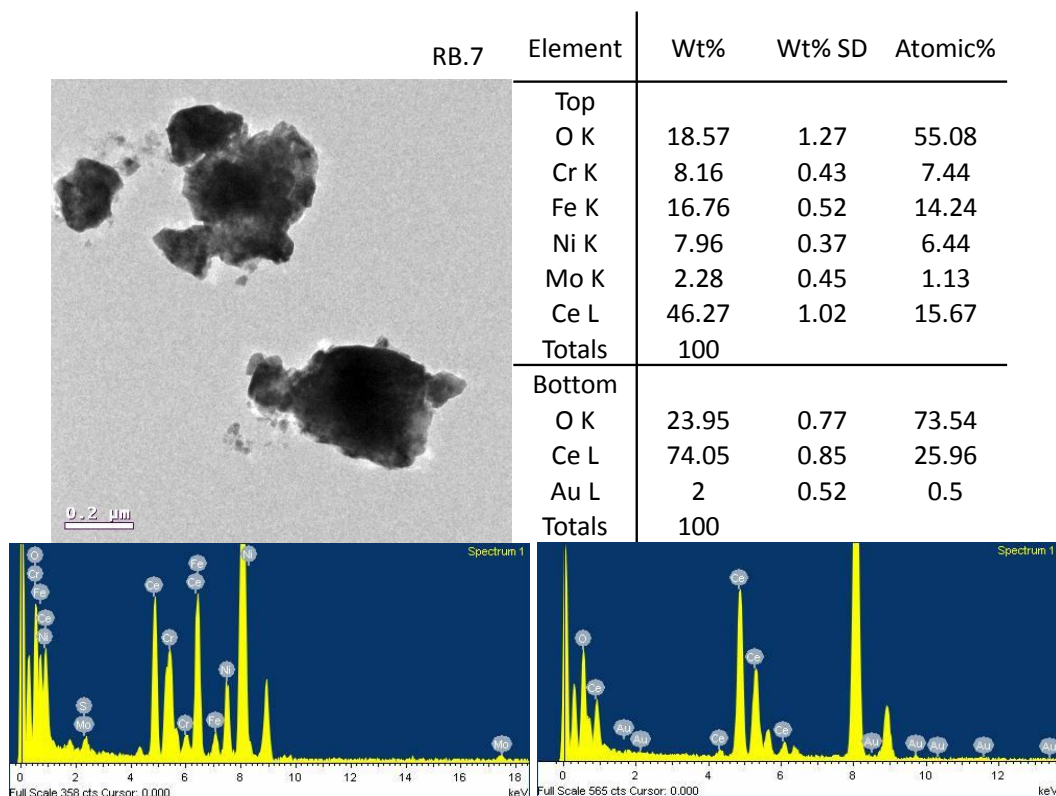


RB.6



Element	Wt%	Wt% SD	Atomic%
O K	62.39	1.13	77.34
Mg K	1.4	0.37	1.14
Al K	4.81	0.45	3.54
Si K	10.44	0.56	7.37
P K	2.37	0.4	1.52
S K	5.09	0.43	3.15
Ca K	8.77	0.44	4.34
Fe K	3.26	0.33	1.16
Zn K	1.47	0.44	0.45
Totals	100		

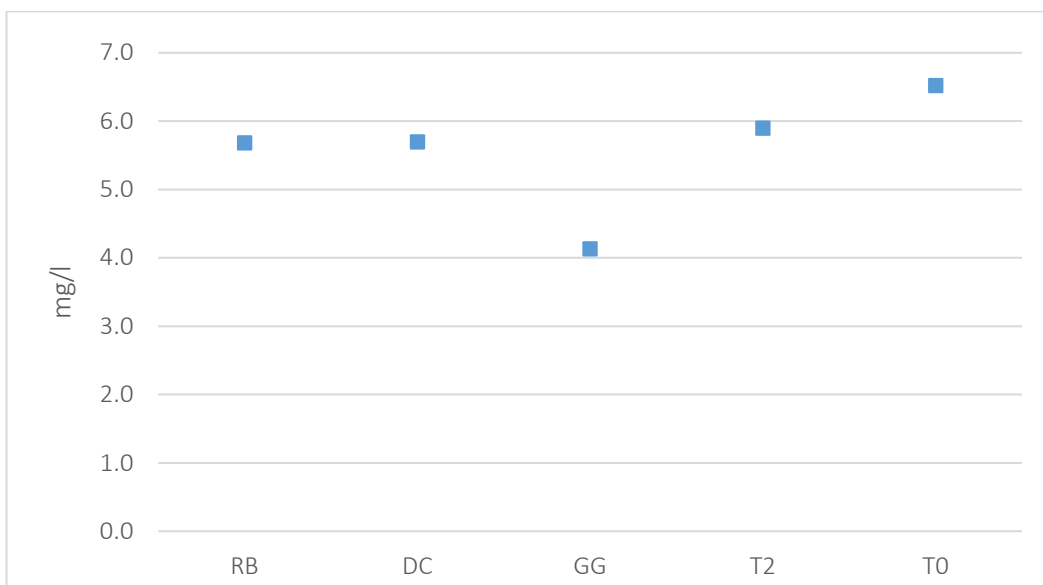




Appendix 6.f Partitioning of metal concentration and load

		<i>T0</i>	<i>T2</i>	<i>GG</i>	<i>DC</i>	<i>RB</i>		<i>T0</i>	<i>T2</i>	<i>GG</i>	<i>DC</i>	<i>RB</i>
blank	Fe	4	6	8	4	6	Fe	315	1218	2929	1954	5506
<2nm	µg/l	58	20	39	23	40	µg/s	4728	4473	14323	11103	33833
<450 nm		126	74	71	59	55		10192	16305	25667	28329	47100
>450		392	244	179	222	201		31736	53680	65047	107254	170225
blank	Mn	0	0	0	0	0	Mn	8	36	53	39	123
<2nm	µg/l	13	9	10	7	8	µg/s	1017	1947	3662	3383	6563
<450 nm		15	11	9	8	7		1221	2483	3245	3868	5569
>450		35	24	27	29	19		2795	5192	9792	13988	16216
blank	Pb	0	1	0	0	0	Pb	15	212	70	73	363
<2nm	µg/l	2	19	13	6	6	µg/s	171	4136	4790	3069	5102
<450 nm		11	77	47	32	19		858	16962	17059	15497	16450
>450		70	139	83	67	41		5662	30558	30212	32428	35064
blank	Zn	2	2	2	1	10	Zn	122	439	602	354	8467
<2nm	µg/l	90	1262	1184	829	747	µg/s	7267	277554	430954	401013	634025
<450 nm		110	1620	1347	1084	690		8922	356473	490349	524581	585543
>450		183	2074	1641	1349	836		14807	456280	597324	652916	709340
blank	Cd	0.00	0.01	0.01	0.01	0.01	Cd	0.2	1.5	3.3	2.9	5.1
<2nm	µg/l	0.09	2.32	1.89	1.52	1.18	µg/s	7.3	510.4	688.0	735.7	1001.8
<450 nm		0.18	2.81	2.26	1.83	1.18		14.9	618.4	824.1	884.3	1005.2
blank	Co	0.00	0.00	0.00	0.00	0.00	Co	0.0	0.0	0.0	0.0	0.0
<2nm	µg/l	0.00	0.43	0.35	0.15	0.12	µg/s	0.0	94.6	127.4	72.6	101.9
<450 nm		0.10	0.62	0.43	0.30	0.18		7.7	136.4	156.9	145.2	153.7
blank	Al	0	1	1	0	1	Al	28	171	255	0	595
<2nm	µg/l	30	32	7	21	17	µg/s	2447	7071	2679	9937	14798
<450 nm		29	24	16	15	18		2382	5176	5671	7031	15012
>450		131	87	49	74	80		10587	19074	17836	35719	67835

Appendix 6.g Dissolved organic carbon (mg/l) plotted by site



References

- AIKEN, G. R., HSU-KIM, H. & RYAN, J. N. 2011. Influence of dissolved organic matter on the environmental fate of metals, nanoparticles, and colloids. *Environmental Science & Technology*, 45, 3196-201.
- AMERICAN PUBLIC HEALTH, A., EATON, A. D., AMERICAN WATER WORKS, A. & WATER ENVIRONMENT, F. 2005. Standard methods for the examination of water and wastewater, Washington, D.C., APHA-AWWA-WEF.
- ATKINS 2008. Frongoch & Wemyss Mine Site Monitoring Summary Report. *Metal Mine Monitoring Project 2006/07*
- BAALOUSHA, M. & LEAD, J. R. 2007. Size fractionation and characterization of natural aquatic colloids and nanoparticles. *Science of Total Environment*, 386, 93-102.
- BAALOUSHA, M. & LEAD, J. R. 2012. Rationalizing nanomaterial sizes measured by atomic force microscopy, flow field-flow fractionation, and dynamic light scattering: sample preparation, polydispersity, and particle structure. *Environmental Science & Technology*, 46, 6134-42.
- BAALOUSHA, M. & LEAD, J. R. 2013. Characterization of natural and manufactured nanoparticles by atomic force microscopy: Effect of analysis mode, environment and sample preparation. *Colloids and Surfaces A: Physicochemical and Engineering Aspects*, 419, 238-247.
- BAALOUSHA, M., PRASAD, A. & LEAD, J. R. 2014. Quantitative measurement of the nanoparticle size and number concentration from liquid suspensions by atomic force microscopy. *Environmental Science: Processes & Impacts*, 16, 1338-47.
- BANKS, V. J. & PALUMBO-ROE, B. 2010. Synoptic monitoring as an approach to discriminating between point and diffuse source contributions to zinc loads in mining impacted catchments. *Journal of Environmental Monitoring*, 12, 1684-98.
- BAUN, A., HARTMANN, N. B., GRIEGER, K. & KUSK, K. O. 2008. Ecotoxicity of engineered nanoparticles to aquatic invertebrates: a brief review and recommendations for future toxicity testing. *Ecotoxicology*, 17, 387-95.
- BGS 2004. British Geological Survey. The geology of the area around Lampeter, Llangybi and Llanfair Clydogau. Integrated Geoscience Surveys South Programme, *Internal Report IR/04/064*.
- BGS 2013. British Geological Survey. DiGMapGB-50 [SHAPE geospatial data], Scale 1:50000, Tiles: ew178, Updated: 1 October 2013, BGS, Using: EDINA Geology Digimap Service [online: www.digimap.edina.ac.uk] accessed 03/06/2016, modified with ArcGIS v.10.
- BOSCH, J., HEISTER, K., HOFMANN, T. & MECKENSTOCK, R. U. 2010. Nanosized iron oxide colloids strongly enhance microbial iron reduction. *Applied Environmental Microbiology*, 76, 184-9.
- BROWN, B. V., VALETT, H. M. & SCHREIBER, M. E. 2007. Arsenic transport in groundwater, surface water, and the hyporheic zone of a mine-influenced stream-aquifer system. *Water Resources Research*, 43.

- BUFFLE, J., WILKINSON, K. J., SERGE, S., FILELLA, M. & ZHANG, J. 1998. A generalized description of aquatic colloidal interactions: the three-colloidal component approach. *Environmental Science & Technology*, 32, 2887-2899.
- BUFFLE, J., ZHANG, Z. & STARTCHEV, K. 2007. Metal Flux and Dynamic Speciation at (Bio)interfaces. Part I: Critical Evaluation and Compilation of Physicochemical Parameters for Complexes with Simple Ligands and Fulvic/Humic Substances. *Environmental Science & Technology*, 41, 7609-7620.
- BURTON, E. D., PHILLIPS, I. R. & HAWKER, D. W. 2005. Geochemical Partitioning of Copper, Lead, and Zinc in Benthic, Estuarine Sediment Profiles. *Journal of Environmental Quality*, 34, 263-273.
- BYRNE, P., REID, I. & WOOD, P. J. 2010. Sediment geochemistry of streams draining abandoned lead/zinc mines in central Wales: the Afon Twymyn. *Journal of Soils and Sediments*, 10, 683-697.
- BYRNE, P., WOOD, P. J. & REID, I. 2012. The Impairment of River Systems by Metal Mine Contamination: A Review Including Remediation Options. Critical Reviews in *Environmental Science and Technology*, 42, 2017-2077.
- BYRNE, P., REID, I. & WOOD, P. J. 2013. Stormflow hydrochemistry of a river draining an abandoned metal mine: the Afon Twymyn, central Wales. *Environmental Monitoring & Assessment*, 185, 2817-32.
- BYRNE, P., RUNKEL, R. L. & WALTON-DAY, K. 2017. Synoptic sampling and principal components analysis to identify sources of water and metals to an acid mine drainage stream. *Environmental Science and Pollution Research*, 24, 17220-17240.
- CABOI, R., CIDU, R., CRISTINI, A., FANFANI, L., MASSOLI-NOVELLI, R. & ZUDDAS, P. 1993. The abandoned Pb-Zn mine of Ingurtosu, Sardinia (Italy). *Engineering Geology*, 34, 211-218.
- CAMPBELL, P. G. C. 1995. Interactions between trace metals and aquatic organisms: A critique of the free-ion activity model. In *Metal speciation and bioavailability in aquatic systems*; Tessier, A., Turner, D. R., Eds.; John Wiley & Sons: Chichester.
- CÁNOVAS, C. R., OLÍAS, M., NIETO, J. M. & GALVÁN, L. 2010. Wash-out processes of evaporitic sulfate salts in the Tinto river: Hydrogeochemical evolution and environmental impact. *Applied Geochemistry*, 25, 288-301.
- CÁNOVAS, C. R., RIERA, J., CARRERO, S. & OLÍAS, M. 2018. Dissolved and particulate metal fluxes in an AMD-affected stream under different hydrological conditions: The Odiel River (SW Spain). *Catena*, 165, 414-424.
- CHEN, Y., LIU, Y., LIU, Y., LIN, A., KONG, X., LIU, D., LI, X., ZHANG, Y., GAO, Y. & WANG, D. 2012. Mapping of Cu and Pb contaminations in soil using combined geochemistry, topography, and remote sensing: a case study in the Le'an River floodplain, China. *International Journal of Environmental Research & Public Health*, 9, 1874-86.
- CHILLERI, E. 2019. Trace metal contents and mobility in mine wastes of the Central Wales mine district: environmental implications. Master Thesis, University of Florence.
- CHRISTIAN, P., VON DER KAMMER, F., BAALOUSHA, M. & HOFMANN, T. 2008. Nanoparticles: structure, properties, preparation and behaviour in environmental media. *Ecotoxicology*, 17, 326-43.

- CISZEWSKI, D. & GRYGAR, T. M. 2016. A Review of Flood-Related Storage and Remobilization of Heavy Metal Pollutants in River Systems. *Water Air & Soil Pollution*, 227, 239.
- CIVEIRA, M. S., OLIVEIRA, M. L., HOWER, J. C., AGUDELO-CASTANEDA, D. M., TAFFAREL, S. R., RAMOS, C. G., KAUTZMANN, R. M. & SILVA, L. F. 2016a. Modification, adsorption, and geochemistry processes on altered minerals and amorphous phases on the nanometer scale: examples from copper mining refuse, Touro, Spain. *Environmental Science & Pollution Research*, 23, 6535-45.
- CIVEIRA, M. S., RAMOS, C. G., OLIVEIRA, M. L., KAUTZMANN, R. M., TAFFAREL, S. R., TEIXEIRA, E. C. & SILVA, L. F. 2016b. Nano-mineralogy of suspended sediment during the beginning of coal rejects spill. *Chemosphere*, 145, 142-7.
- COURT, A. 2014. River contamination at the Dylife mine site, Mid-Wales: sources and seasonal patterns within surface and underground water. MPhil Thesis, University of Aberystwyth.
- CRANE, M. 2003. Proposed development of Sediment Quality Guidelines under the European Water Framework Directive: a critique. *Toxicology Letters*, 142, 195-206.
- CRAVOTTA, C. A. 2008. Dissolved metals and associated constituents in abandoned coal-mine discharges, Pennsylvania, USA. Part 2: Geochemical controls on constituent concentrations. *Applied Geochemistry*, 23, 203-226.
- DAT ARCHEOLOGICAL SERVICES 2016. Metal Mine Remediation Project Part 3: WEYMSS, Archaeological Assessment. Report ERN109181.**
- DAVIS, A., DREXLER, J. W., RUBY, M. V. & NICHOLSON, A. 1993. Micromineralogy of mine wastes in relation to lead bioavailability, Butte, Montana. *Environmental Science & Technology*, 27, 1415-1425.
- DE GIUDICI, G., WANTY, R. B., PODDA, F., KIMBALL, B. A., VERPLANCK, P. L., LATTANZI, P., CIDU, R. & MEDAS, D. 2014. Quantifying biomineralization of zinc in the Rio Naracauli (Sardinia, Italy), using a tracer injection and synoptic sampling. *Chemical Geology*, 384, 110-119.
- DE GIUDICI, G., PUSCEDDU, C., MEDAS, D., MENEGHINI, C., GIANONCELLI, A., RIMONDI, V., PODDA, F., CIDU, R., LATTANZI, P., WANTY, R. B. & KIMBALL, B. A. 2017. The role of natural biogeochemical barriers in limiting metal loading to a stream affected by mine drainage. *Applied Geochemistry*, 76, 124-135.
- DEFRA 2006. Department for Environment, Food and Rural Affairs, UK. River Basin Planning Guidance.
- DEFRA 2010. Department for Environment, Food and Rural Affairs, UK. River Basin Districts Typology, Standards and Groundwater threshold values (Water Framework Directive) (England and Wales) Directions 2010.
- DEFRA 2018. Department for Environment, Food and Rural Affairs, UK. A Green Future: Our 25 Year Plan to Improve the Environment; HM Government: London, U.K., [online: <https://www.gov.uk/government/publications/25-year-environment-plan>] accessed 01/08/2019.
- DENNIS, I. A., COULTHARD, T. J., BREWER, P. & MACKLIN, M. G. 2009. The role of floodplains in attenuating contaminated sediment fluxes in formerly mined drainage basins. *Earth Surface Processes and Landforms*, 34, 453-466.

- DI TORO, D. M., ALLEN, H. E., BERGMAN, H. L., MEYER, J. S., PAQUIN, P. R. & SANTORE, R. C. 2001. Biotic ligand model of the acute toxicity of metals. 1. Technical Basis. *Environmental Toxicology and Chemistry*, 20, 2383-2396.
- DUARTE, A. L., DABOIT, K., OLIVEIRA, M. L. S., TEIXEIRA, E. C., SCHNEIDER, I. L. & SILVA, L. F. O. 2019. Hazardous elements and amorphous nanoparticles in historical estuary coal mining area. *Geoscience Frontiers*, 10, 927-939.
- ECHIGO, T., ARUGUETE, D. M., MURAYAMA, M. & HOCELLA, M. F. 2012. Influence of size, morphology, surface structure, and aggregation state on reductive dissolution of hematite nanoparticles with ascorbic acid. *Geochimica et Cosmochimica Acta*, 90, 149-162.
- ENVIRONMENT AGENCY 2002. Metal Mine Strategy for Wales.
- ENVIRONMENT AGENCY 2006. Attenuation of mine pollutants in the hyporheic zone. *Science Report: SC030155/SR6*
- ENVIRONMENT AGENCY 2008a. Assessment of Metal Mining-Contaminated River Sediments in England and Wales. *Science Report: SC030136/SR4*.
- ENVIRONMENT AGENCY 2008b. Abandoned mines and the water environment. *Science Project: SC030136-41*.
- ENVIRONMENT AGENCY 2012a. Prioritisation of abandoned non-coal mine impacts on the environment. *Science Report: SC030136/R13*.
- ENVIRONMENT AGENCY 2012b. WFD Investigation: Abandoned Mines Project, Afton Ystwyth. *Science Report: SC030155/SR6*.
- EUROPEAN COMMISSION, 2012. Commission Staff Working Document, European Overview (1/2) Accompanying the Document: "Report From the Commission to the European Parliament and the Council on the Implementation of the Water Framework Directive (2000/60/EC) River Basin Management Plans". COM (2012) 670 Final.
- FINLAYSON, B. L., PEEL, M. C. & MCMAHON, T. A. 2014. Climate and Rivers☆. Reference Module in Earth Systems and Environmental Sciences.
- FORRAY, F. L., SMITH, A. M. L., DROUET, C., NAVROTSKY, A., WRIGHT, K., HUDSON-EDWARDS, K. A. & DUBBIN, W. E. 2010. Synthesis, characterization and thermochemistry of a Pb-jarosite. *Geochimica et Cosmochimica Acta*, 74, 215-224.
- FOULDS, S. A., BREWER, P. A., MACKLIN, M. G., HARESIGN, W., BETSON, R. E. & RASSNER, S. M. 2014. Flood-related contamination in catchments affected by historical metal mining: an unexpected and emerging hazard of climate change. *Science of Total Environment*, 476-477, 165-80.
- FRAU, F., CIDU, R. & ARDAU, C. 2012. Short-term changes in water chemistry in the Baccu Locci stream (Sardinia, Italy) affected by past mining. *Applied Geochemistry*, 27, 1844-1853.
- FULLER, C. C. & HARVEY, J. W. 2000. Reactive Uptake of Trace Metals in the Hyporheic Zone of a Mining-Contaminated Stream, Pinal Creek, Arizona. *Environmental Science & Technology*, 34, 1150-1155.

- GANDY, C. J., SMITH, J. W. & JARVIS, A. P. 2007. Attenuation of mining-derived pollutants in the hyporheic zone: a review. *Science of Total Environment*, 373, 435-46.
- GENERAUX, D. P., & HOOPER, R. P. 1998. Oxygen and hydrogen isotopes in rainfall-runoff studies. In C. Kendall & J. J. McDonnell (Eds.), *Isotope tracers in catchment hydrology*. New York: Elsevier, 319–346.
- GOZZARD, E., MAYES, W. M., POTTER, H. A. & JARVIS, A. P. 2011. Seasonal and spatial variation of diffuse (non-point) source zinc pollution in a historically metal mined river catchment, UK. *Environmental Pollution*, 159, 3113-22.
- GUTIERREZ, M., MICKUS, K. & CAMACHO, L. M. 2016. Abandoned PbZn mining wastes and their mobility as proxy to toxicity: A review. *Science of Total Environment*, 565, 392-400.
- HAMMARSTROM, J. M., SEAL, R. R., MEIER, A. L. & KORNFELD, J. M. 2005. Secondary sulfate minerals associated with acid drainage in the eastern US: recycling of metals and acidity in surficial environments. *Chemical Geology*, 215, 407-431.
- HANDY, R. D., OWEN, R. & VALSAMI-JONES, E. 2008. The ecotoxicology of nanoparticles and nanomaterials: current status, knowledge gaps, challenges, and future needs. *Ecotoxicology*, 17, 315-25.
- HARGREAVES, A. J., VALE, P., WHELAN, J., CONSTANTINO, C., DOTRO, G., CAMPO, P. & CARTMELL, E. 2017. Distribution of trace metals (Cu, Pb, Ni, Zn) between particulate, colloidal and truly dissolved fractions in wastewater treatment. *Chemosphere*, 175, 239-246.
- HELSEN, D. R. & HIRSCH, R. M. 2002. Statistical Method in Water Resources Book 4, Hydrologic Analysis and Interpretation Techniques of Water-Resources Investigations of the United States Geological Survey Chapter A3.
- HEM, J. D. 1972. Chemistry and occurrence of cadmium and zinc in surface water and groundwater. *Water Resources Research*, 8, 661-679.
- HOCELLA, M. F., JR., LOWER, S. K., MAURICE, P. A., PENN, R. L., SAHAI, N., SPARKS, D. L. & TWINING, B. S. 2008. Nanominerals, mineral nanoparticles, and Earth systems. *Science*, 319, 1631-5.
- HORIE, M. & FUJITA, K. 2011. Toxicity of Metal Oxides Nanoparticles. *Advances in Molecular Toxicology*, 5.
- HOTZE, E. M., PHENRAT, T. & LOWRY, G. V. 2010. Nanoparticle Aggregation: Challenges to Understanding Transport and Reactivity in the Environment. *Journal of Environment Quality*, 39.
- HU, Y., LEE, B., BELL, C. & JUN, Y.-S. 2012. Environmentally Abundant Anions Influence the Nucleation, Growth, Ostwald Ripening, and Aggregation of Hydrated Fe(III) Oxides. *Langmuir*, 28, 7737-7746.
- HUDSON-EDWARDS, K. A., MACKLIN, M. G., CURTIS, C. D. & VAUGHAN, D. J. 1996. Processes of Formation and distribution of Pb-, Zn-, Cd-, and Cu-bearing Minerals in the Tyne Basin, Northeast England: Implication for Metal-Contaminated River Systems. *Environmental Science and Technology*, 30, 72-80.

- HUDSON-EDWARDS, K. A., MACKLIN, M. G., CURTIS, C. D. & VAUGHAN, D. J. 1998. Chemical Remobilization Of Contaminant Metals Within Floodplain Sediments In An Incising River System: Implications For Dating And Chemostratigraphy. *Earth Surface Processes and Landforms*, 23, 671-684.
- HUDSON-EDWARDS, K. A., MACKLIN, M. G., MILLER, J. R. & LECHLER, P. J. 2001. Sources, distribution and storage of heavy metals in the Rio Pilcomayo, Bolivia. *Journal of Geochemical Exploration*, 72 229-250.
- HUDSON-EDWARDS, K. A., JAMIESON, H. E. & LOTTERMOSER, B. G. 2011. Mine Wastes: Past, Present, Future. *Elements*, 7, 375-380.
- HUDSON-EDWARDS, K. A. 2003. Sources, mineralogy, chemistry and fate of heavy metal-bearing particles in mining-affected river systems. *Mineralogical Magazine*, 67, 205-217.
- HÜRKAMP, K., RAAB, T. & VÖLKEL, J. 2009. Lead Pollution of Floodplain Soils in a Historic Mining Area—Age, Distribution and Binding Forms. *Water, Air, and Soil Pollution*, 201, 331-345.
- IPCC 2013. Intergovernmental Panel On Climate Change. Summary for Policymakers. In: Stocker TF, Qin D, Plattner G-K, Tignor M, Allen SK, Boschung J, Nauels A, Xia Y, Bex V, Midgley PM, editors. *Climate Change 2013: The Physical Science Basis. Contribution of Working Group I to the Fifth Assessment Report of the Intergovernmental Panel on Climate Change*. Cambridge: Cambridge University Press; 2013.
- JARVIE, H. P., NEAL, C. & TAPPIN, A. D. 1997. European land-based pollutant loads to the North Sea: an analysis of the Paris Commission data and review of monitoring strategies. *Science of The Total Environment*, 194-195, 39-58.
- JARVIE, H. P., AL-OBAIDI, H., KING, S. M., BOWES, M. J., LAWRENCE, M. J., DRAKE, A. F., GREEN, M. A. & DOBSON, P. J. 2009. Fate of Silica Nanoparticles in Simulated Primary Wastewater Treatment. *Environmental Science & Technology*, 43, 8622-8628.
- JARVIS, A. P., MOUSTAFA, M., ORME, P. H. A. & YOUNGER, P. L. 2006. Effective remediation of grossly polluted acidic, and metal-rich, spoil heap drainage using a novel, low-cost, permeable reactive barrier in Northumberland, UK. *Environmental Pollution*, 143, 261-268.
- JARVIS, A. P., JOHNSTON, D., MAYES, W. M. & POTTER, H. A. B. 2008. Application of a new methodology for assessing the priorities for abandoned mine water pollution remediation at a national scale: results and implications from a study across England and Wales. In: Rapantova, N. & Hrkal Z. (eds) *Proceedings of the 10th International MineWater Association Congress: mine water and the environment*.
- JARVIS, A. P., DAVIS, J. E., ORME, P. H. A., POTTER, H. A. B. & GANDY, C. J. 2019. Predicting the Benefits of Mine Water Treatment under Varying Hydrological Conditions using a Synoptic Mass Balance Approach. *Environmental Science & Technology*, 53, 702-709.
- JOHNSON, D. B. & HALLBERG, K. B. 2005. Acid mine drainage remediation options: a review. *Science of The Total Environment*, 338, 3-14.
- JOHNSON, R. L., JOHNSON, G. O. B., NURMI, J. T. & TRATNYEK, P. G. 2009. Natural Organic Matter Enhanced Mobility of Nano Zerovalent Iron. *Environmental Science & Technology*, 43, 5455-5460.

- JOHNSON, C. A., FREYER, G., FABISCH, M., CARABALLO, M. A., KÜSEL, K. & HOCELLA, M. F. 2014. Observations and assessment of iron oxide and green rust nanoparticles in metal-polluted mine drainage within a steep redox gradient. *Environmental Chemistry*, 11, 377-391.
- JOHNSON, C. A., FREYER, G., FABISCH, M., CARABALLO, M. A., KÜSEL, K. & HOCELLA, M. F. 2014. Observations and assessment of iron oxide and green rust nanoparticles in metal-polluted mine drainage within a steep redox gradient. *Environmental Chemistry*, 11, 377-391.
- JONES, E. H. & SU, C. 2014. Transport and retention of zinc oxide nanoparticles in porous media: effects of natural organic matter versus natural organic ligands at circumneutral pH. *Journal of Hazardous Materials*, 275, 79-88.
- JOO, S. H. & ZHAO, D. 2017. Environmental dynamics of metal oxide nanoparticles in heterogeneous systems: A review. *Journal of Hazardous Materials*, 322, 29-47.
- KALNICKY, D. J. & SINGHVI, R. 2001. Field portable XRF analysis of environmental samples. *Journal of Hazardous Material*, 83, 93-122.
- KENNEDY, S. 2002. Speciation and Characterization of Heavy Metal-Contaminated Soils Using Computer-Controlled Scanning Electron Microscopy. *Environmental Forensics*, 3, 131-143.
- KILPATRICK, F. A. & COBB, E. D. 1985. Measurement of discharge using tracers. *Techniques of Water-Resources Investigations of the United States Geological Survey Book 3*, Chapter A16.
- KIMBALL, B. A., CALLENDER, E. & AXTMANN, E. V. 1995. Effects of colloids on metal transport in a river receiving acid mine drainage, upper Arkansas River, Colorado, U.S.A. *Applied Geochemistry*, 10, 285-306.
- KIMBALL, B. A., RUNKEL, R. L., CLEASBY, T. E. & NIMICK, D. A. 1998. Quantification of Metal Loading by Tracer Injection and Synoptic Sampling, 1997–98. *Integrated Investigations of Environmental Effects of Historical Mining in the Basin and Boulder Mining District, Boulder River Watershed, Jefferson County, Montana*, Chapter D6, Professional Paper 1652–D6.
- KIMBALL, B. A. 2002. Assessment of metal loads in watersheds affected by acid mine, drainage by using tracer injection and synoptic sampling, Cement Creeck Colorado USA. *Applied Geochemistry*, 17, 1183–1207
- KIMBALL, B. A., BIANCHI, F., WALTON-DAY, K., RUNKEL, R. L., NANNUCCI, M. & SALVADORI, A. 2007. Quantification Of Changes In Metal Loading From Storm Runoff, Merse River (Tuscany, Italy). *IMWA Symposium 2007: Water in Mining Environments*, R. Cidu & F. Frau (Eds), 27th - 31st May 2007, Cagliari, Italy.
- KINCEY, M., WARBURTON, J. & BREWER, P. A. 2018. Contaminated sediment flux from eroding abandoned historical metal mines: Spatial and temporal variability in geomorphological drivers. *Geomorphology*, 319, 199-215.
- KOSSOFF, D., DUBBIN, W. E., ALFREDSSON, M., EDWARDS, S. J., MACKLIN, M. G. & HUDSON-EDWARDS, K. A. 2014. Mine tailings dams: Characteristics, failure, environmental impacts, and remediation. *Applied Geochemistry*, 51, 229-245.

- LAMELAS, C., WILKINSON, K. J. & SLAVEYKOVA, V. I. 2005. Influence of the Composition of Natural Organic Matter on Pb Bioavailability to Microalgae. *Environmental Science & Technology*, 39, 6109-6116.
- LAPWORTH, D. J., STOLPE, B., WILLIAMS, P. J., GOODDY, D. C. & LEAD, J. R. 2013. Characterization of Suboxic Groundwater Colloids Using a Multi-method Approach. *Environmental Science & Technology*, 47, 2554-2561.
- LARSON, L. N., FITZGERALD, M., SINGHA, K., GOOSEFF, M. N., MACALADY, J. L. & BURGOS, W. 2013. Hydrogeochemical niches associated with hyporheic exchange beneath an acid mine drainage-contaminated stream. *Journal of Hydrology*, 501, 163-174.
- LEAD, J. R., MUIRHEAD, D. & GIBSON, C. T. 2005. Characterization of Freshwater Natural Aquatic Colloids by Atomic Force Microscopy (AFM). *Environmental Science & Technology*, 39, 6930-6936.
- LEAD, J. R. & WILKINSON, K. J. 2006. Aquatic Colloids and Nanoparticles: Current Knowledge and Future Trends. *Environmental Chemistry*, 3.
- LEE, G., BIGHAM, J. M. & FAURE, G. 2002. Removal of trace metals by coprecipitation with Fe, Al and Mn from natural waters contaminated with acid mine drainage in the Ducktown Mining District, Tennessee. *Applied Geochemistry*, 17, 569-581.
- LEWIN, J. & MACKLIN, M.G. 1987. Metal mining and floodplain sedimentation in Britain. In: V. Gardiner (Editor), *International Geomorphology*. Wiley, London, 1009-1027.
- LIMBACH, L. K., BEREITER, R., MÜLLER, E., KREBS, R., GÄLLI, R. & STARK, W. J. 2008. Removal of Oxide Nanoparticles in a Model Wastewater Treatment Plant: Influence of Agglomeration and Surfactants on Clearing Efficiency. *Environmental Science & Technology*, 42, 5828-5833.
- LYNCH, S., BATTY, L. & BYRNE, P. 2014. Environmental Risk of Metal Mining Contaminated River Bank Sediment at Redox-Transitional Zones. *Minerals*, 4, 52-73.
- LYNCH, S. F. L., BATTY, L. C. & BYRNE, P. 2017. Critical control of flooding and draining sequences on the environmental risk of Zn-contaminated riverbank sediments. *Journal of Soils and Sediments*, 17, 2691-2707.
- LYNCH, S. F. L., BATTY, L. C. & BYRNE, P. 2018. Environmental risk of severely Pb-contaminated riverbank sediment as a consequence of hydrometeorological perturbation. *Science of The Total Environment*, 636, 1428-1441.
- MACKLIN, M. G., BREWER, P. A., HUDSON-EDWARDS, K. A., BIRD, G., COULTHARD, T. J., DENNIS, I. A., LECHLER, P. J., MILLER, J. R. & TURNER, J. N. 2006. A geomorphological approach to the management of rivers contaminated by metal mining. *Geomorphology*, 79, 423-447.
- MACKLIN, M.G., RUMSBY, B.T., AND NEWSON, M.D. 1992. Historical floods and vertical accretion of fine-grained alluvium in the lower Tyne valley, northeast England. In: P. Billi, R.D. Hey, C.R. Thorne and P. Tacconi (Editors), *Dynamics of Gravel-bed Rivers*. Wiley, New York, 573-589.
- MALVERN, I. 2012. Zeta Potential an introsuction in 30 minutes. *Zetasizer Nano Series technical note*, MRK654-01.

- MARCUS, W.A., 1987. Copper dispersion in ephemeral stream sediments. *Earth Surface Processes & Landforms*, 12, 217-228.
- MAYES, W. M., GOZZARD, E., POTTER, H. A. & JARVIS, A. P. 2008. Quantifying the importance of diffuse minewater pollution in a historically heavily coal mined catchment. *Environmental Pollution*, 151, 165-75.
- MAYES, W. M., POTTER, H. A. & JARVIS, A. P. 2010. Inventory of aquatic contaminant flux arising from historical metal mining in England and Wales. *Science of The Total Environment*, 408, 3576-83.
- MAYES, W. M., POTTER, H. A. B. & JARVIS, A. P. 2013. Riverine Flux of Metals from Historically Mined Orefields in England and Wales. *Water, Air, & Soil Pollution*, 224.
- MEDAS, D., CIDU, R., LATTANZI, P., PODDA, F. & DE GIUDICI, G. 2012. Natural Biomineralization in the Contaminated Sediment-Water System at the Ingurtosu Abandoned Mine. In E. Kothe and A. Varma (eds.), *Bio-Geo Interactions in Metal-Contaminated Soils*, Soil Biology 31, Springer-Verlag Berlin Heidelberg., 113-129.
- MET OFFICE 2020 Statistic ad Excel Dara file ID 61003. [Online: www.statista.com/statistics/610083/monthly-rainfall-in-wales accessed 15/02/2020]
- MIGHANETARA, K., BRAUNGARDT, C. B., RIEUWERTS, J. S. & AZIZI, F. 2009. Contaminant fluxes from point and diffuse sources from abandoned mines in the River Tamar catchment, UK. *Journal of Geochemical Exploration*, 100, 116-124.
- MIKHLIN, Y., VOROBYEV, S., ROMANCHENKO, A., KARASEV, S., KARACHAROV, A. & ZHARKOV, S. 2016. Ultrafine particles derived from mineral processing: A case study of the Pb-Zn sulfide ore with emphasis on lead-bearing colloids. *Chemosphere*, 147, 60-6.
- MILLER, J. R. 1997. The role of fluvial geomorphic processes in the dispersal of heavy metals from mine sites. *Journal of Geochemical Exploration*, 58, 101 - 118.
- MOORE, R. D. 2004b. Introduction to Salt Dilution Gauging for Streamflow Measurement Part 2: Constant-rate Injection. *Streamline Watershed Management Bulletin*, 8/No.1 Fall 2004.
- MOORE, R. D. 2004a. Introduction to Salt Dilution Gauging for Streamflow Measurement: Part 1. *Streamline Watershed Management Bulletin*, 7/No. 4 Winter 2003/04.
- MOORE, R. D. 2005. Slug Injection Using Salt in Solution: Part 3. *Streamline Watershed Management Bulletin*, 8/ No 2 Spring 2005.
- MOREL, F. M. M., HERING, J. G. 1983 Principles and applications of aquatic chemistry; *Wiley Interscience*: New York.
- MYLON, S. E., TWINING, B. S., FISHER, N. S. & BENOIT, G. 2003. Relating the Speciation of Cd, Cu, and Pb in Two Connecticut Rivers with Their Uptake in Algae. *Environmental Science & Technology*, 37, 1261-1267.
- NAGORSKI, S. A., MOORE, J. N., MCKINNON, T. E. & SMITH, D. B. 2003. Geochemical response to variable streamflow conditions in contaminated and uncontaminated streams. *Water Resources Research*, 39, 1044-1057.

- NAIDU, G., RYU, S., THIRUVENKATACHARI, R., CHOI, Y., JEONG, S. & VIGNESWARAN, S. 2019. A critical review on remediation, reuse, and resource recovery from acid mine drainage. *Environmental Pollution*, 247, 1110-1124.
- NANOCOMPOSIX 2012. Zeta Potential Analysis of Nanoparticles. *Nano Composix*, September 2012, V 1.1.
- NIMICK, D. A., GAMMONS, C. H. & PARKER, S. R. 2011. Diel biogeochemical processes and their effect on the aqueous chemistry of streams: A review. *Chemical Geology*, 283, 3-17.
- NORDSTROM, D. K. 2009. Acid rock drainage and climate change. *Journal of Geochemical Exploration*, 100, 97-104.
- NORDSTROM, D. K. 2011a. Hydrogeochemical processes governing the origin, transport and fate of major and trace elements from mine wastes and mineralized rock to surface waters. *Applied Geochemistry*, 26, 1777-1791.
- NORDSTROM, D. K. 2011b. Mine Waters: Acidic to Circumneutral. *Elements*, 7, 393-398.
- NRFA 2019. National River Flow Archive, [online: www.nrfa.ceh.ac.uk/data/station/meanflow/63001] accessed 01/08/2019.
- NRW 2016. Natural Resources of Wales. Abandoned Mine Case Study, Wemyss Lead and Zinc Mine.
- OBERDÖRSTER, G., STONE, V. & DONALDSON, K. 2007. Toxicology of nanoparticles: A historical perspective. *Nanotoxicology*, 1, 2-25.
- O'MELIA, C. R. 1980. ES Features: Aquasols: the behavior of small particles in aquatic systems. *Environmental Science & Technology*, 14, 1052-1060.
- ONNIS, P., BYRNE, P., HUDSON-EDWARDS, K. A., STOTT, T. & HUNT, C. 2018. Source Apportionment of Trace Metals Over a Range of Stream Flows Using a Multi-method Tracer Approach. In: Wolkersdorfer, C., Sartz, L., Weber, A., Burgess, J. & Tremblay, G. (Eds), *Proceedings of the 11th International MineWater Association Congress: risk to opportunity*, 843-848.
- OSPAR 2019. Oslo Paris Commission website [online: www.ospar.org] accessed 1/08/2019.
- OXFORD INSTRUMENTS, 2008. INCA Energy Applications training notes. *Bucks: Oxford Instruments*.
V
- PALUMBO-ROE, B., WRAGG, J. & BANKS, V. J. 2012. Lead mobilisation in the hyporheic zone and river bank sediments of a contaminated stream: contribution to diffuse pollution. *Journal of Soils and Sediments*, 12, 1633-1640.
- PALUMBO-ROE, B., WRAGG, J., CAVE, M. & WAGNER, D. 2013. Effect of weathering product assemblages on Pb bioaccessibility in mine waste: implications for risk management. *Environmental Science and Pollution Research*, 20, 7699-7710.
- PALUMBO-ROE, B. & DEARDEN, R. 2013. The hyporheic zone composition of a mining-impacted stream: Evidence by multilevel sampling and DGT measurements. *Applied Geochemistry*, 33, 330-345.

PALUMBO-ROE, B., ANDER L., JOHNSON C. & M., C. 2016. Stream sediment background concentrations in mineralised catchments in Northern Ireland: assessment of 'pressures' on water bodies in fulfilment of Water Framework Directive objectives. In: Young, M. E. (ed.), *Unearthed: impacts of the Tellus surveys of the north of Ireland*. Dublin. Royal Irish Academy.

PHAM, M. K. & GARNIER, J.-M. 1998. Distribution of Trace Elements Associated with Dissolved Compounds (<0.45 µm–1 nm) in Freshwater Using Coupled (Frontal Cascade) Ultrafiltration and Chromatographic Separations. *Environmental Science & Technology*, 32, 440-449.

PLATHE, K. L., VON DER KAMMER, F., HASSELLÖV, M., MOORE, J., MURAYAMA, M., HOFMANN, T. & HOCELLA, M. F. 2010. Using FIFFF and aTEM to determine trace metal–nanoparticle associations in riverbed sediment. *Environmental Chemistry*, 7.

PLATHE, K. L., VON DER KAMMER, F., HASSELLÖV, M., MOORE, J. N., MURAYAMA, M., HOFMANN, T. & HOCELLA, M. F. 2013. The role of nanominerals and mineral nanoparticles in the transport of toxic trace metals: Field-flow fractionation and analytical TEM analyses after nanoparticle isolation and density separation. *Geochimica et Cosmochimica Acta*, 102, 213-225.

POKROVSKY, O. S. & SCHOTT, J. 2002. Iron colloids/organic matter associated transport of major and trace elements in small boreal rivers and their estuaries (NW Russia). *Chemical Geology*, 190, 141-179.

POKROVSKY, O. S., VIERS, J., SHIROKOVA, L. S., SHEVCHENKO, V. P., FILIPOV, A. S. & DUPRÉ, B. 2010. Dissolved, suspended, and colloidal fluxes of organic carbon, major and trace elements in the Severnaya Dvina River and its tributary. *Chemical Geology*, 273, 136-149.

PRUDÊNCIO, M. I., VALENTE, T., MARQUES, R., BRAGA, M. A. S. & PAMPLONA, J. 2017. Rare Earth Elements, Iron and Manganese in Ochre-precipitates and Wetland Soils of a Passive Treatment System for Acid Mine Drainage. *Procedia Earth and Planetary Science*, 17, 932-935.

RADU, T. & DIAMOND, D. 2009. Comparison of soil pollution concentrations determined using AAS and portable XRF techniques. *J Hazard Mater*, 171, 1168-71.

RATCLIFF, G. C. & ERIE, D. A. 2001. A Novel Single-Molecule Study To Determine Protein–Protein Association Constants. *Journal of the American Chemical Society*, 123, 5632-5635.

RAYBOULD, J.G. 1974. Ore textures, paragenesis and zoning in the lead-zinc veins of mid-Wales. *T I Min Metal B*, 112-119.

RICHARDSON, M., MOORE, R. D. & ZIMMERMANN, A. 2016. Variability of tracer breakthrough curves in mountain streams: Implications for streamflow measurement by slug injection. *Canadian Water Resources Journal / Revue canadienne des ressources hydriques*, 42, 21-37.

RIVER POLLUTION COMMITTEE 1874. Fifth Report, Volume 1, *Oral and Written Evidence*. London: Her Majesty's Stationary Office.

ROSS, G. J., WANG, C., OZKAN, A. I. & REES, H. W. 1982. Weathering of chlorite and mica in a new Brunswick Podzol developed on till derived from chlorite-mica schist. *Geoderma*, 27, 255-267.

RUNKEL, R. L., WALTON-DAY, K., KIMBALL, B. A., VERPLANCK, P. L. & NIMICK, D. A. 2013. Estimating instream constituent loads using replicate synoptic sampling, Peru Creek, Colorado. *Journal of Hydrology*, 489, 26-41.

- RUNKEL, R. L., KIMBALL, B. A., NIMICK, D. A. & WALTON-DAY, K. 2016. Effects of Flow Regime on Metal Concentrations and the Attainment of Water Quality Standards in a Remediated Stream Reach, Butte, Montana. *Environmental Science & Technology*, 50, 12641-12649.
- SCHMID, B. H., INNOCENTI, I. & SANFILIPPO, U. 2010. Characterizing solute transport with transient storage across a range of flow rates: The evidence of repeated tracer experiments in Austrian and Italian streams. *Advances in Water Resources*, 33, 1340-1346.
- SCHINDLER, M. & HOCELLA, M. F. 2016. Nanomineralogy as a new dimension in understanding elusive geochemical processes in soils: The case of low-solubility-index elements. *Geology*, 44, 515-518.
- SHARMA, V. K., FILIP, J., ZBORIL, R. & VARMA, R. S. 2015. Natural inorganic nanoparticles--formation, fate, and toxicity in the environment. *Chemical Society Reviews*, 44, 8410-23.
- SKOUSEN, J., ZIPPER, C. E., ROSE, A., ZIEMKIEWICZ, P. F., NAIRN, R., MCDONALD, L. M. & KLEINMANN, R. L. 2017. Review of Passive Systems for Acid Mine Drainage Treatment. *Mine Water and the Environment*, 36, 133-153.
- SMITH, K. 1999 Metal sorption on mineral surfaces: an overview with examples relating to mineral deposits vol 6A. The environmental geochemistry of mineral deposits part a: processes, techniques and health issues. *Society of Economic Geologists*, Colorado, USA
- STOKES, M. 2012. Assessing the water quality impacts of abandoned metal mines on the Ystwyth catchment, Wales. MSc dissertation, Swansea University.
- SWIFT, D. L., CHENG, Y. S., SUT, Y. F. & YEHI, H. C. 1994. Ultrafine Aerosol Deposition in the Human Nasal and Oral Passages. *Annals of Work Exposures and Health*, 38, 77-81.
- TAFAZOLI, M., HOJJATI, S. M., BIPARVA, P., KOOCH, Y. & LAMERSDORF, N. 2017. Reduction of soil heavy metal bioavailability by nanoparticles and cellulosic wastes improved the biomass of tree seedlings. *Journal of Plant Nutrition and Soil Science*, 180, 683-693.
- TAME, C., HUDSON-EDWARDS, K. A. & POTTER, H. A. B. 2017. Weathering of Zinc-(Zn)-bearing Mine Wastes in a Neutral Mine Drainage Setting, Gunnerside Gill, Yorkshire. *Procedia Earth and Planetary Science*, 17, 284-287.
- THURSTON, H. W. 2006. Opportunity Costs of Residential Best Management Practices for Stormwater Runoff Control. *Journal of Water Resources Planning and Management*, 132, 89-96.
- TORDOFF, G. M., BAKER, A. J. M. & WILLIS, A. J. 2000. Current approaches to the revegetation and reclamation of metalliferous mine wastes. *Chemosphere*, 41, 219-228.
- UHLEMANN, S. S., SORENSEN, J. P. R., HOUSE, A. R., WILKINSON, P. B., ROBERTS, C., GOODDY, D. C., BINLEY, A. M. & CHAMBERS, J. E. 2016. Integrated time-lapse geoelectrical imaging of wetland hydrological processes. *Water Resources Research*, 52, 1607-1625.
- USGS 2008. United State Geological Survey, Water Chemistry 2: Sampling and Presenting Water Analysis [online: http://inside.mines.edu/~epoeter/_GW/18WaterChem2/WaterChem2pdf.pdf] accessed 01/08/2019.

USGS 2019. United State Geological Survey, [online: <https://help.waterdata.usgs.gov/faq/surface-water/what-is-a-percentile>] accessed 01/08/2019.

VAN DAMME, A., DEGRYSE, F., SMOLDERS, E., SARRET, G., DEWIT, J., SWENNEN, R. & MANCEAU, A. 2010. Zinc speciation in mining and smelter contaminated overbank sediments by EXAFS spectroscopy. *Geochimica et Cosmochimica Acta*, 74, 3707-3720.

VASYUKOVA, E., POKROVSKY, O. S., VIERS, J. & DUPRÉ, B. 2012. New operational method of testing colloid complexation with metals in natural waters. *Applied Geochemistry*, 27, 1226-1237.

WATTS, G., BATTARBEE, R. W., BLOOMFIELD, J. P., CROSSMAN, J., DACCACHE, A., DURANCE, I., ELLIOTT, J. A., GARNER, G., HANNAFORD, J., HANNAH, D. M., HESS, T., JACKSON, C. R., KAY, A. L., KERNAN, M., KNOX, J., MACKAY, J., MONTEITH, D. T., ORMEROD, S. J., RANCE, J., STUART, M. E., WADE, A. J., WADE, S. D., WEATHERHEAD, K., WHITEHEAD, P. G. & WILBY, R. L. 2015. Climate change and water in the UK – past changes and future prospects. *Progress in Physical Geography: Earth and Environment*, 39, 6-28.

WAYCHUNAS, G. A., KIM, C. S. & BANFIELD, J. F. 2005. Nanoparticulate Iron Oxide Minerals in Soils and Sediments: Unique Properties and Contaminant Scavenging Mechanisms. *Journal of Nanoparticle Research*, 7, 409-433.

WELSH MINE PRESERVATION TRUST, 2009. Presentation Ceredigion Archeology Dayschool 28th February 2009 [online: http://orapweb.rcahms.gov.uk/coflein//M/MLPC_10_01.pdf accessed 15/02/2020.

WIGGINTON, N. S., HAUS, K. L. & HOCELLA JR, M. F. 2007. Aquatic environmental nanoparticles. *Journal of Environmental Monitoring*, 9.

WILKIN, R. T. 2008. Contaminant Attenuation Processes at Mine Sites. *Mine Water and the Environment*, 27, 251-258.

YANG, J. Y., YANG, X. E., HE, Z. L., LI, T. Q., SHENTU, J. L. & STOFFELLA, P. J. 2006. Effects of pH, organic acids, and inorganic ions on lead desorption from soils. *Environmental Pollution*, 143, 9-15.

ZHU, Y.-M., LU, X. X. & ZHOU, Y. 2007. Suspended sediment flux modeling with artificial neural network: An example of the Longchuanjiang River in the Upper Yangtze Catchment, China. *Geomorphology*, 84, 111-125.